Experimental and Analytical Investigations of Reinforced Concrete Beam-Column Joint Subjected to Shock and Impact Loading

A thesis submitted in fulfilment of the requirements for the degree of

DOCTOR OF PHILOSOPHY

by

Anupoju Rajeev

DEPARTMENT OF CIVIL ENGINEERING
INDIAN INSTITUTE OF TECHNOLOGY GUWAHATI
JULY 2020

Dedicated to my

Mother Mrs. Anupoju Vijayalakshmi

and

Father Mr. Anupoju Paidilingachari

Declaration

I hereby certify that the work compiled in this thesis is the outcome of the research work, performed by myself, else stated, under the guidance of Dr. Amit Shelke.

Any part of this work has not been submitted for the award of any degree, diploma, associate-fellowship, fellowship or its equivalent to any university or institution.

Anupoju Rajeev

Registration No. 146104035

Department of Civil Engineering

Indian Institute of Technology Guwahati

Certificate

It is certified that the work contained in the thesis entitled "Experimental and Analytical Investigations of Reinforced Concrete Beam-Column Joint Subjected to Shock and Impact Loading" by Mr. Anupoju Rajeev, a student, in the Department of Civil Engineering, Indian Institute of Technology Guwahati, India, for the award of the degree of the Doctor of Philosophy, has been carried out under my supervision and, that this work has not been submitted elsewhere for the degree.

Date:

Dr. Amit Shelke
Associate Professor
Department of Civil Engineering
Indian Institute of Technology Guwahati
Guwahati-781039, Assam, India

Acknowledgements

This dissertation marks the inception of my professional career as a researcher as well as the culmination of my 25 years long student career. It is not possible without the support of numerous people, including my supervisor, family, colleagues, and friends. I would like to acknowledge everyone who has made this thesis possible either directly or indirectly, and I'm thankful for every little help and encouragement during this journey.

Firstly, I would like to thank my supervisor, Dr. Amit Shelke, without whom this thesis would not have been possible. His persistent guidance, motivation, and recommendations have shaped my basic understanding of this domain to a great extent during my research work. I have learned a lot from him during this short research career so far, and I hope to learn furthermore in the forthcoming years.

Besides my supervisor, I would like to acknowledge the doctoral committee members, Prof. Arbind Kumar Singh, Prof. Niranjan Sahoo, Prof. Konjengbam Darunkumar Singh, and Dr. Hrishikesh Sharma, for their valuable recommendations and insightful remarks throughout research activities, which has encouraged me continuously towards undertaking a meaningful thesis work. Further, special appreciation for the senior technician and support staff of the Department of Civil Engineering namely, Mr. Biswajit Debnath, Mr. Pranab Hazarika, Mr. Saurabh Mudoi, Mr. Suresh Boro, Mr. Pankaj Khakhalary, and Mr. Bipul Boniya. Also, Mr. Sanjib Sarma, a senior technician from the Department of Mechanical Engineering.

I would also like to acknowledge the financial support provided by the Department of Science and Technology (SERB/F/2242/2015-2016) and Defence Research and Development Organization (Grant No. ARMREB/CDSW/2017/192), Government of India. I take this opportunity to sincerely acknowledge Dr. Anugrah Singh (IIT Guwahati) for providing the high-speed camera system. I would like to extend my sincere gratitude to the Ministry of Human Resource Development and Indian Institute of Technology Guwahati for providing financial assistance, which reinforced me to study comfortably.

I would sincerely appreciate all my fellow lab-mates-friends: Mr. Parsi Sai Sharath, Mr. Lavish Pamwani, Mr. Dharmendra Dhaka, Mr. Shekhar Singh, Mr. Ayush Maheshwari, Miss Joane Mathew, Mr. Ajeeth Prabhu, Miss Ann Mathew Sheryl, Mr. Mussa Kalimullah, Mr. Shivam Ojha, and Mr. Devasish Lahkar for their contributions

towards my dissertation: be it preparing drafts or assisting me in experiments/ coding. Without this group, my journey perhaps would have been of less fun.

My sincere obligations to Mr. Rohith Padyana (Tesscorn) is indeed for helping in the post-processing of high-speed camera data. I would like to show my due respect to Mr. Debnath in the development of the shock and impact testing simulator.

I also owe thanks to my seniors as well as fellow mates: Dr. Sumit Agarwal, Dr. Soumya Ranjan Nanda, Mr. Saibal Kanchan Barik, Dr. Sritam Swapnadarshi Sahu, Mr. Kintada Maharshi, Mr. Suresh Modalavalasa, Dr. Trishna Choudhury, Mr. Suman Mushahary, Mr. Suman Kumar, Mr. Anyam Vamsi Krishna Reddy, Mr. Jagan Mohan Rao, Miss Evangleen, Mr. Vimalathithan, and Mr. Mayur kedare.

Special thanks to the following people: Mary, Tulika, Muskan, Uday Kiran, Sai Swetha, Triveni, Hari, Sony, Vaibhav, Varaprasad, A.C. Bhaktivedanta Swami Prabhupada, Mahasundar Dasa Prabhuji, Chaitanya Dasa Prabhuji, Shiva, and Syed Habibunnisa for always being available to share my feelings and for providing the emotional support when I was feeling low.

Last but not least, special gratitude is due to my parents Mr. Anupoju Paidilingachari and Mrs. Anupoju Vijaya Lakshmi, who have sacrificed a lot for me. I wouldn't have reached so far without their love and constant support. I dedicate this thesis to my parents. You two are the reason why I wanted to pursue PhD, and your motivation is well placed, well-structured, and inspiring. I thank my sister and brother-in-law, Mrs. Revathi and Mr. Madhanmohan in believing me and keeping me focused on both happy as well as tough times in my life. Lastly and most importantly, I would like to thank my beloved Lord Shivakeshava for not letting me down at a time of crisis and showing me the silver lining in the dark clouds.

Anupoju Rajeev
Indian Institute of Technology Guwahati
July 2020

Abstract

This dissertation reports the experimental and analytical investigation of exterior beam-column joints subjected to shock and impact loading. Further, the study is extended towards the development of a sacrificial the structural system for the mitigation of damage induced by impact and blast loading.

In recent years, numerous terrorist attacks occurred all over the world that has revealed the vulnerability of the building structure from blast explosions and missile impacts. The global behavior of the structure is governed by the strength and deformation capacity of individual structural elements such as beam, column, slab, and shear wall. Therefore, it is important to investigate the behavior of individual members considering its stiffness, strength, and boundary conditions. Beam-column joints are the vital structural element in the load path mechanism of the framed structural buildings due to their significant role in uniting the overall skeletal system of the building. Studies on beam-column joint subjected to seismic and cyclic loading have been researched extensively over the past four decades through the experimental, analytical, and numerical investigations. However, there is a lack of systematic research on beam-column joints subjected to shock and impact loading. Especially the available studies on the joints protected using composite shielding material to resist shock and impact is limited. Prior to this study, a detailed study on the Aluminum honeycomb composite shield was conducted.

The first part of the research is devoted to the development of the shock and impact testing simulator at IIT Guwahati. A shock tube simulator is capable of mimicking the blast loading by generating a high magnitude of shock waves. In the current research work, it is employed for conducting shock and impact experiments on reinforced concrete beam-column joints. Prior to the conducting of this experimental research on the structure, a detailed experimental and numerical investigation was carried out to calibrate and characterize the behavior of the shock tube.

The second part of the research explores the response of the exterior reinforced concrete beam-column joints under quasi-static and dynamic loadings. In the current study, dynamic loadings refer to shock and impact loading. The design consideration followed for the exterior beam-column joints in this study are gravity design (IS 456:2016) and seismic design criteria (IS 1893:2016, IS 13920:2016) respectively.

The main aim of the dissertation is to develop an impact resistive sacrificial protective system using honeycomb composite that acts as an energy absorber under

extreme loadings scenarios, i.e., shock and impact. Towards this broad objective, initially, the honeycomb is tested under quasi-static compression loading to evaluate energy absorption capability. The hierarchal progressive plastic deformation of the thin honeycomb wall provides stable energy absorption by maintaining constant plateau stress at an increasing strain. Further, a low-velocity drop test was conducted on honeycomb composite to investigate the dynamic force and failure patterns due to impact. The experimental results were used to validate and develop an analytical model to determine the peak contact force. The analytical model accounts for uncertainties in geometric as well as material properties. The knowledge gained through the experimental and analytical investigation of low-velocity impact was used to design and develop laminated composite material to resist high-velocity impact.

The current research effort advances the experimental and numerical investigation of reinforced concrete structures by enabling a sacrificial protective system using honeycomb composite to minimize impact damage in the beam-column joint assembly. Shock tube experimental setup was used to impact high-velocity impact on the proposed experimental test structure. Systematic high-velocity impact testing was conducted on an external beam-column joint to investigate the structural response. The external beam-column joint was further protected with honeycomb composite to resist impact loading. The enhancement of ballistic performance due to honeycomb composite was compared with the bare external beam-column joint. The ballistic performances were evaluated using displacement and acceleration response. Furthermore, the response of the structural member shielded with honeycomb composite was examined based on the ballistic limit velocity, perforation energy, impact morphology, evaluation of target damage, failure modes, and evolution of cracks. These energy absorbers offer a sustainable solution to shield and safeguard the parent structure against the blast and impact loading. The energy absorption performance of the structure was enhanced when shielded with honeycomb energy absorbers.

Findings in the current dissertation can be employed as a protective façade system to the structural members to safeguard the infrastructure against blast and impact threats. The application of the honeycomb protective sacrificial system can be widespread for safeguarding existing defense and public buildings by enhancing energy absorption capabilities. Future research can be carried out on the structural optimization of honeycomb for enhancing its performance against extreme loadings. Furthermore, investigations need to be extended on the application of honeycomb composite in other structural elements such as piers and shear wall subjected to extreme loadings. This will give insights on the behavior of the composite to safeguard bridge piers and high rise buildings.

Keywords: Aluminum honeycomb shielding; Ballistic limit; Beam-column joints; Crack propagation; Impact loading; Seismic detailing; Shock loading; Shock tube.

Contents

List of Figures

List of Tables

Nomenclature

α	angle of incidence
α_{om}	maximum transversal indentation
γ_1	specific heat ratio for air
γ_4	specific heat ratio for nitrogen gas
$\dot{\varepsilon}$	strain rate
$\dot{\varepsilon}_{sc}$	strain rate for concrete in compression
ε_{tu}	ultimate tensile strain in concrete
$\dot{\varepsilon}_{st}$	reference strain rate of concrete in tension
ε_{syd}	strain corresponding to the dynamic yield strength
$\varepsilon_{c,\lim}$	ultimate limit strain in concrete
ε_y	yield strain at the beginning of the plateau region
ε_r	strain in radial direction
ε_θ	strain in tangential direction
ε_D	densification strain
φ	diameter of impactor
φ_y	yield curvature
φ_u	ultimate curvature
δ	total deflection
δ_u	total plastic deformation
σ_{alu}	yield strength parent Aluminum material
σ_o	plateau stress
ρ_c	effective density of honeycomb core
ρ_{alu}	density of parent Aluminum material

ρ_i	density of the impactor
Π	total potential energy
η	energy absorption efficiency
a	contact radius
b	decay coefficient of the waveform
BS	beam weak in shear
BF	beam weak in flexure
BSNS	beam weak in shear with non-seismic detailing
BSS	beam weak in shear with seismic detailing
BFNS	beam weak in flexure with non-seismic detailing
BFS	beam weak in flexure with seismic detailing
c	cell size
CF	charge factor
CS	column weak in shear
CSNS	column weak in shear with non-seismic detailing
CSS	column weak in shear with seismic detailing
C_o	speed of sound wave
d_c	damage variable in compression
d_t	damage variable in tension
D	bending stiffness of sandwich panel
D_m	membrane rigidity
D_f	flexural rigidity
DNT	dinitrotoluene
E_O	static elastic modulus of concrete
E_S	elastic modulus of reinforcing steel
E_{SP}	strain hardening modulus of reinforcing steel
E_c	young's modulus of core
E_f	young's modulus of facesheet
E_P	perforation energy
f_{cr}	mean characteristic compressive strength of concrete

f_{tr}	mean split tensile strength of concrete
f_y	yield strength of longitudinal reinforcing steel bar
f_t	ultimate strength of longitudinal reinforcing steel bar
f_{syd}	dynamic yield strength at any strain rate
f_{sys}	static yield strength
FPS	frames per second
G_C	shear modulus
h	impact drop height
h_f	thickness of facesheet
h_C	height of core
i_s	positive time impulse
i_s^-	negative time impulse
$\bar{I}$	impulse
K_{el}	equivalent elastic stiffness
K_{pl}	plastic stiffness
K_{LM}	load mass factor
K_L	load factor
K_M	mass factor
$K_{LM,el}$	load mass factors in the elastic case
$K_{LM,pl}$	load mass factors in the plastic case
K_m	membrane stiffness
K_{bs}	combined bending and shear stiffness
l	cell width
l_p	length of plastic hinge
LVDT	linear variable differential transformer
m_i	mass of the projectile
M	mach number
M_S	shock mach number
M_y	resisting bending moment at yield
M_u	ultimate bending moment

M_{el}	equivalent mass in elastic regime
M_{pl}	equivalent mass in plastic regime
M_E	mass of the equivalent system
MRF	moment resisting frame
$M1$	mass of impact system
$M2$	mass of sandwich panel
p	contact pressure
p_i	initial momentum
P_{SO}	peak overpressure
P_{SO}^{-}	minimum pressure value
P_{atm}	atmospheric pressure (=103.25 kPa)
P_o	ambient pressure
P_r	reflected pressure
P_C	axial load at inflection points in column
P_1	atmospheric pressure
P_2	pressure in region 2 of driver section
P_4	pressure in region 4 of driver section
q	crushing strength of honeycomb core
q_o	initial peak dynamic pressure
Q_e	explosives specific energy
Q_{TNT}	TNT specific energy
R	standoff distance from the detonation source to the target point in metre
R_C	radius of contact circle
RDX	cyclonite
SS	stainless steel
SDOF	single degree of freedom
t	cell wall thickness
t_d	positive phase duration

t_d^-	negative phase duration
T	temperature of gas
TNT	trinitrotoluene
u	radial displacement
U	velocity of gas particle in medium (m/s)
ν	Poisson's ratio
v_i	impactor velocity
V_C	shear force at inflection points in column
V_o	impact velocity
V_B	strain energy due to bending
V_M	membrane stretching energy
V_b	ballistic limit
w_S	shear deflection
W	weight of the TNT equivalent charge of explosive in kilogram
X_y	depth of neutral axis
Z	scaled distance
'$W_{TNT_{eq}}$'	TNT equivalence

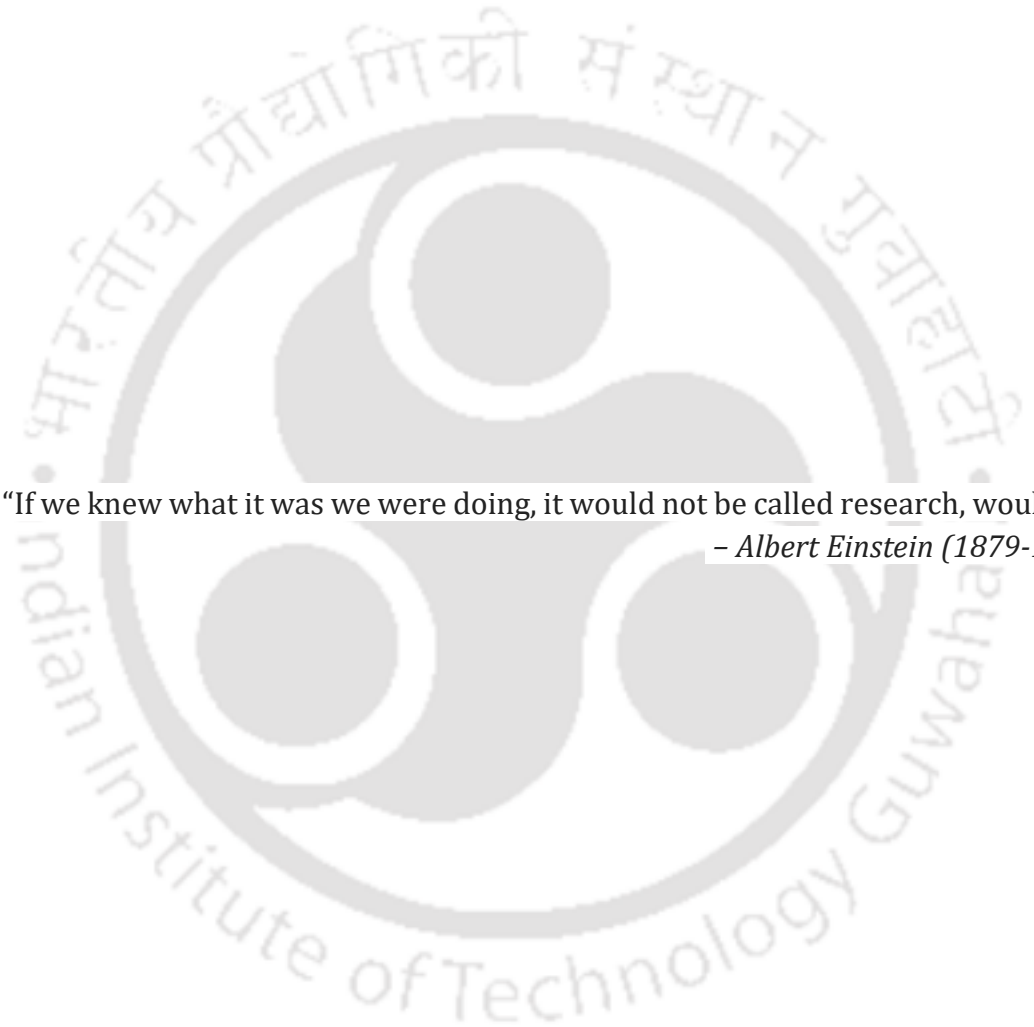

"If we knew what it was we were doing, it would not be called research, would it?"

– Albert Einstein (1879-1955)

Chapter 1
Introduction

1.1 Background

The entire world is witnessing a sudden surge in terrorist activities after the September 11 attacks in New York City and Washington D.C in 2001. Terrorism has been used by various left-right wing political organizations such as nationalists, religious groups, revolutionaries, and the ruling government to achieve their strategic goals and objectives. Terrorist often uses explosives to cause maximum destruction to the civilian, residential, and government building to generate fear for exploiting the political message. Several terrorist attacks on civil infrastructure and military have raised alertness by revealing the vulnerability of reinforced concrete (RC) structures subjected to shock, blast, and impact loading. These deliberate terrorist attacks have resulted in casualties and caused tremendous damage to the structures (Baker et al. 2012). Some explosions lead to the collapse of the entire structure and surge casualties.

According to the Global Terrorism Database of the National Consortium for the Study of Terrorism and Responses to Terrorism (START) at the University of Maryland (USA) (Global Terrorism (Database 2017), and recent publications (Edwards et al. 2016; Shvetsov et al. 2017; Williams et al. 2010) during the period between 2006 and 2019, the total recorded terrorist activities around the world are more than 126,713 with a total casualty of more than 216,915. Observing at the trend of recent terrorist attacks in Pentagon and World Trade Center (WTC 2001), Marriott Hotel in Jakarta (2003), Australian Embassy in Indonesia (2004), Night Clubs and Restaurants in Bali (2005, 2002), United States (Boston in 2013), Iraq (2017, 2016, 2014), Afghanistan (2018), and Kenya (2019) it can be seen that predominantly the public buildings, hospitals, theatres, government infrastructure, and bridges, etc. are targeted.

Seldom, important structures are likely to be situated in the highly seismic prone areas and their design is governed by respective country seismic codes (ACI 318-14, ASCE 7-10, EC 8, NZS 1170-2004). Furthermore, such important structures identified in the seismic prone area were designed based on the current seismic codes provided by the Indian Standard (IS 1893:2016, IS 13920:2016). An exterior Beam-Column joint plays a vital role in the RC framed buildings and are probably the most exposed structural components during the bomb explosions and impact of terrorist attacks (Krauthammer 2008). The shear failure, anchorage and bond failure within these vital beam-column assemblies may lead to the progressive collapse of the entire structure which ends with the huge loss of causalities and property (Choi and Kim 2011; Yu and Tan 2013). A significant amount of research on structural members such as slabs, beams and columns under extreme loading scenario such as blast and impact has been

carried out (Bangash 2006; Mays et al. 1995). Only a few studies were conducted on the influence of seismic design criteria on blast resistance of RC frames structures (Hayes Jr et al. 2005; Parisi and Augenti 2012; Saatcioglu et al. 2009). Hence, the key motivation of the current research work is to study the impact behavior of the beam-column assemblage.

1.1.1 Motivation

In the past few decades, extensive research has been conducted to investigate the behavior of existing RC structures subjected to seismic loading. However, the structures that are built-in between 1970-1990 in high seismic regions have inherent deficiencies in structural designing and detailing. Investigations conducted by Ghobarah et al. (1997); Hakuto et al. (2000), concluded that the moment-resisting frame (MRF) designed based on gravity load consideration exhibit extremely poor performance under seismic loading. The poor performance of the MRF attributed to the following deficiencies: i) inadequate transversal reinforcement for efficient confinement at beam-column joint, ii) insufficient amount of longitudinal and transversal reinforcement in the column at joints, iii) inadequate anchorage detailing at beam-column joint, iv) inadequate lap splices in the column, and v) lower quality of materials. The major concern was related to the weakness and deficiencies at beam-column joints viz-a-viz beam weak in shear, column weak in shear and beam weak in flexure at the beam-column junction. Therefore, considering these limitations, the thesis is focused on the investigation of the behavior of beam-column subassembly subjected to lateral loading.

After the September 11, 2003 attacks in New York City, the world is witnessing ever-increasing threats from blast and impact loading. Government building, hospitals, a military installation that have superior structural design and detailing are always the preferred targets by the terrorist. However, recently residential buildings and other low importance structures are increasingly getting targeted using low-intensity IED and blast. The structures designed and constructed pre-1990 era in the high seismic region has already been exposed to severe ground shaking in the past. Prolonged seismic loading on these structures leads to the deterioration of structural capacity and its integrity that increases the vulnerability to the blast loading. The structural deficiency with regards to seismic loading is equally adverse for blast loading. Therefore, the motivation of the thesis is to investigate the behavior of the structural elements with inherent structural deficiency at the beam-column joint when subjected to shock and impact loading.

Acknowledging the fact that the nature of seismic and blast wave loading are entirely different phenomena. However, the provision for ductile detailing with special confinement adopted for seismic loading has proven to exhibit superior performance for the structures subjected to blast load. However, the efficiency of the provision of ductile detailing that applies to seismic loading is not thoroughly investigated in regards to blast loading and impact loading. The motivation of the present research is to

investigate the performance of the RC structure designed with ductile designing subjected to blast and impact loading.

Seldom, there is some misconception that the blast resistance to the building can provide from the earthquake-resistant design. However, there is a remarkable overlap between the two loadings in the common area of progressive collapse prevention, earthquake-resistant buildings are uncertain about mitigating the direct effects of a blast loading acting on the building envelope (refer Figure 1.1). The brief representation of the blast and seismic loading time histories along with the response of the structure for the same is shown in Figure 1.2.

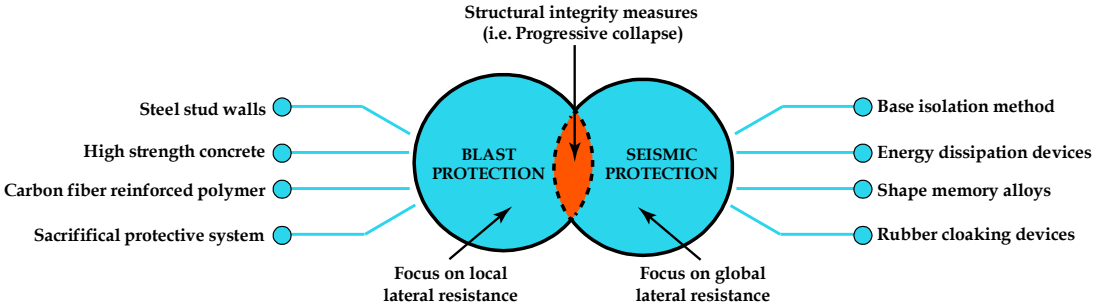

Figure 1.1 Overlap of blast vs seismic and various protection scheme

There is a fundamental difference between blast loading and seismic loading and the behavior of the structure under their influence. Blast loading usually occurs on the exterior envelope of the structure whereas seismic loading induces base excitation.

i) The blast load is usually caused out of plane loading, whereas seismic excitation causes in-plane vibrations.
ii) Blast loads are characterized by high-pressure impulse loading of few milliseconds duration, unlike seismic excitation that is non-stationary lasting for few seconds.
iii) Low-intensity blast loading usually causes localized damage, whereas seismic loading excites global mode of vibrations.
iv) The mass facilitates to resist the blast loading, whereas the inertial load attracts earthquake force intensifies the damage.

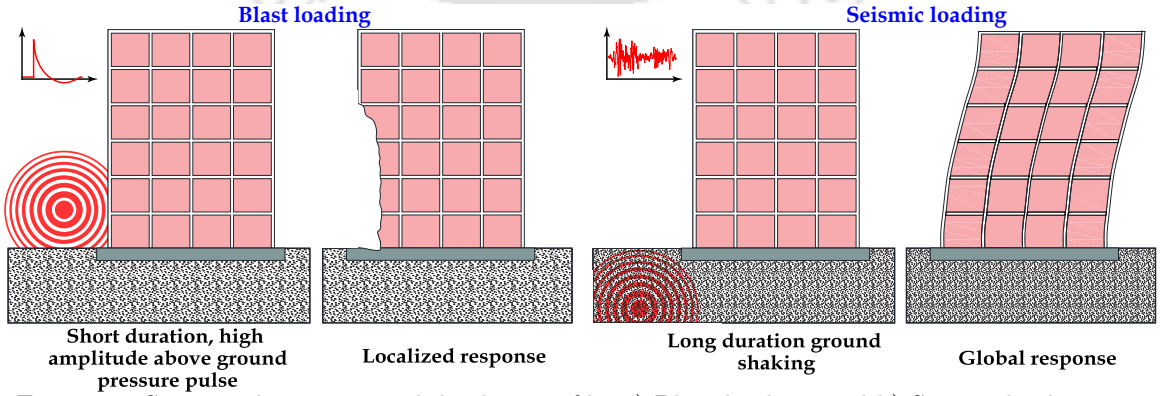

Figure 1.2 Structural response with loading profile: a) Blast loading, and b) Seismic loading

The various methods for the mechanical characterisation of the materials and the corresponding range of its strain are illustrated in Figure 1.3.

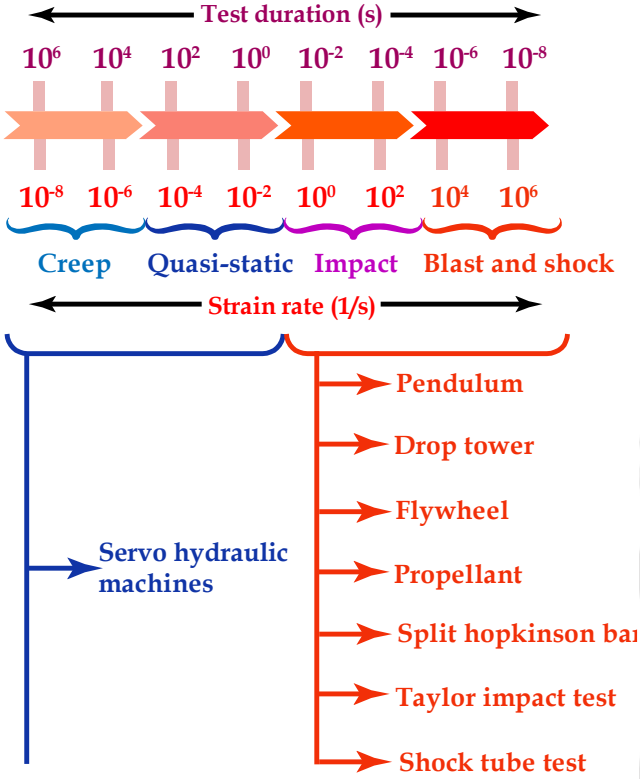

Figure 1.3 Methods of mechanical characterisation and corresponding strain

1.1.2 Blast loading

Blast is defined as an enormous release of energy due to rapid chemical or nuclear reaction that converts explosives material to high temperature and dense high-pressure gas. The explosive gas expands at very high-velocity to attain equilibrium with atmosphere resulting in the formation of a shock wave. The shock waves expand radially outwards and travel with supersonic velocities, and when these waves get amplified upon experiencing confined boundaries due to back wall reflections. The detonation causes an instantaneous rise in pressure in the scale of few milliseconds. The blast wave suddenly releases its energy, and the peak pressure attenuates exponentially in space and time. The magnitude of the blast wave depends on the a) explosive (type, quantity), b) standoff distance, and c) confining boundaries (air-blast/ground blast/rigid boundaries) causing blast amplification. The typical profile of the blast pressure wave generated from the ideal explosion along with the various loadings in terms of amplitude and frequency that determine the design of structural components is shown in Figure 1.4.

The severity of damage caused to the buildings not only depends on the explosive parameters but also on architecture layout, type of framing system, construction methodology, and construction materials. In a building system, the blast load is directly resisted by a) primary structural frame (beam, column, and shear wall), b) secondary structural elements (slab, diaphragms), and c) building envelops (protective wall, masonry, and cladding). The primary structural frames mainly resist blast loads by

undergoing inelastic deformation. Based on the blast parameters, the structural members fails under flexure and/or shear mode. Any discontinuity in the primary structural members leads to ineffective force redistribution within the structure resulting in domino type collapse mode. From aesthetic consideration, the building envelop is often comprises of laminated glass cladding or unreinforced masonry that is directly exposed to the blast. The positive phase of the blast wave shatters the glass, but the negative blast pressure causes defragmentation and disperses the fragments to a significant distance. The high-velocity flying glass debris causes laceration and induces significant injuries. The façade at the ground floor is most vulnerable due to its ease in accessibility and exposure to peak pressure intensity. Structurally strengthen façade can act a first protective measure to resist blast load, thereby protecting the primary structure. Several innovative designs of protective cladding and façade have been studied to isolate the primary structural frame from the direct incident from peak blast pressure (ASCE 2011; Hetherington and Smith 2014; Krauthammer 2008).

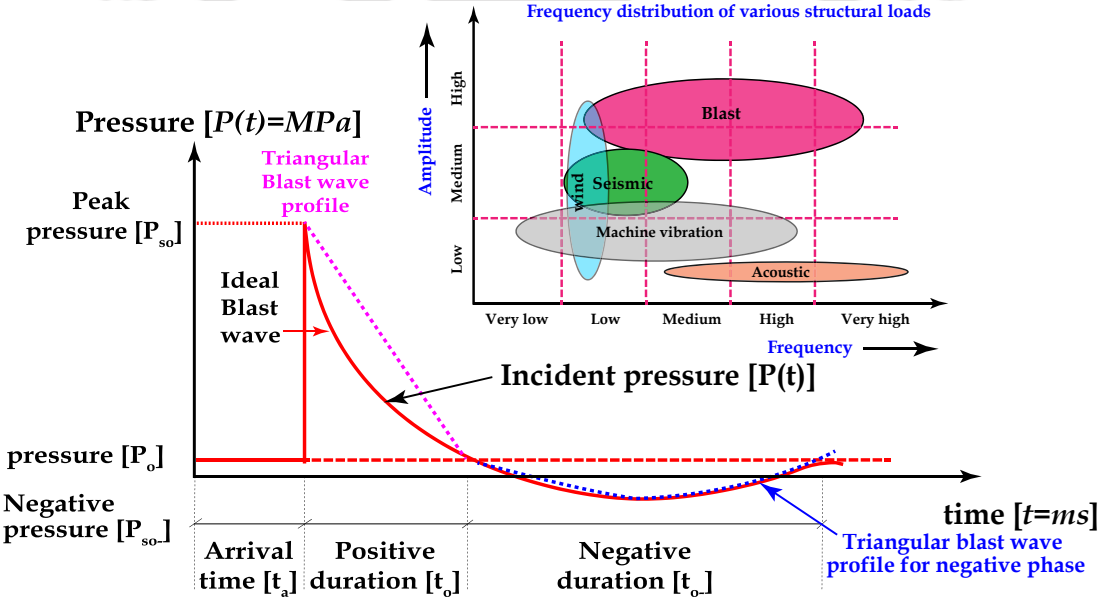

Figure 1.4 Blast wave and amplitude-frequency relations of different structural loadings

Based on UFC 4-010-01 (2018), the level of protection to the structure is based on the response of the building to blast loading. The level of protection or extent of damage is quantified in terms of deformation and rotation capacity. Table 1.1 summarizes the performance of the building in terms of the level of protection and damage induced in the structure (Defense 2001). Performance-based design (PBD) approach is widely accepted framework that relates postulated threats with structural vulnerability and quantifies the risk associated with the proposed level of protection. The PBD approach acknowledges that not all structures could be design and constructed to resist the maximum intensity of blast loading due to postulated threats due to enormous economic burdens and lack of space in the highly populated urban environment. Based on the structural utility and its importance, the acceptable risk is associated with the

building. However, for a given level of risk, PBD strictly enforces that the building should be protected against progressive collapse. Moreover, ISC Physical Security Criteria for Federal Facilities (DHS 2010) added that the exterior building envelops unlike glass façade should contribute in resisting blast load and in turn, protect the primary structure.

Table 1.1 DOD Minimum Antiterrorism Standards for Buildings (FEMA-426 2003)

Level of protection	Potential Building Damage /Performance[2]	Potential Door and Glazing Hazards[3]	Potential Injury
Below AT standards[1]	Severe damage. Progressive collapse likely. Space in and around damaged area will be unusable.	Doors and windows will fail catastrophically and result in lethal hazards. (High hazard rating)	Majority of personnel in collapse region suffer fatalities. Potential fatalities in areas outside of collapsed area likely.
Very Low	Heavy damage - Onset of structural collapse, but progressive collapse is unlikely. Space in and around damaged area will be unusable.	Glazing will fracture, come out of the frame, and is likely to be propelled into the building, with the potential to cause serious injuries. (Low hazard rating) Doors may be propelled into rooms, presenting serious hazards.	Majority of personnel in damaged area suffer serious injuries with a potential for fatalities. Personnel in areas outside damaged area will experience minor to moderate injuries.
Low	Moderate damage –Building damage will not be economically repairable. Progressive collapse will not occur. Space in and around damaged area will be unusable.	Glazing will fracture, potentially come out of the frame, but at a reduced velocity, does not present a significant injury hazard. (Very low hazard rating) Doors may fail, but they ill rebound out of their frames, presenting minimal hazards.	Majority of personnel in damaged area suffer minor to moderate injuries with the potential for a few serious injuries, but fatalities are unlikely. Personnel in areas outside damaged areas will potentially experience a minor to moderate injuries.
Medium	Minor damage –Building damage will be economically repairable. Space in and around damaged area can be used and will be fully functional after cleanup and repairs.	Glazing will fracture, remain in the frame and results in a minimal hazard consisting of glass dust and slivers. (Minimal hazard rating) Doors will stay in frames, but will not be reusable.	Personnel in damaged area may suffer minor to moderate injuries, but fatalities are unlikely. Personnel in areas outside damaged areas will potentially experience superficial injuries.
High	Minimal damage. No permanent deformations. Facility will be immediately operable.	Glazing will not break. (No hazard rating) Doors will be reusable.	Only superficial injuries are likely.

Note: 1. This is not a level of protection, and should never be a design goal. It only defines a realm of more severe structural response, and may provide useful information in some cases.
2. For damage/performance descriptions for primary, secondary, and nonstructural members, refer to UFC 4-020-02, DOD Security Engineering Facilities Design Manual (2007b).
3. Glazing hazard levels are from ASTM F 1642.

Apart from strengthening the structure against blast loading, another vital consideration to minimize the hazard associated with blast loading is architectural design and planning. Architecture considerations significantly contribute to reducing the risk of blast loading without taxing the project cost. Two crucial aspects of architecture considerations for mitigating blast effects are i) building size and configuration, and ii) layout design. The building aspect ratio, presence of reentrant corners, concavity in the plan, and building irregularity significantly influence the blast hazard to the building. Low rise building with low aspect ratio reduces the sudden collapse of the structure. Also, the requirement of glass façade and architectural cladding are not needed that directly reduces risk from glass fragmentation. However, the low height building is notoriously vulnerable to collapse due to exposure of blast overpressure onto the roof. High rise building usually demand excessive protective

measure at lower floors due to direct blast exposure. The high aspect ratio seldom causing trapping of blast pressure and reflects nearby structure enhancing the devastating blast effects. The geometry of the building plays a significant role in dictating the performance of the structure. The reentrant corners in the building having "U" and "L" shape or overhanging canopy tends to trap the blast energy and amplify them due to strong near field back reflection. The structure with circular and convex shape is efficient to mitigate the blast effects on the structure. ASCE 7-05 (2006) state the convex shape causes diversion of wind loads, thereby reducing the drag coefficient up to 65%.

1.1.3 Structural design considerations

The blast resistance design of the building aims towards mitigating the blast-related damage incurred to structure and reduce the fatalities by avoiding sudden collapse. Previous blast experience has demonstrated the maximum human life had lost due to

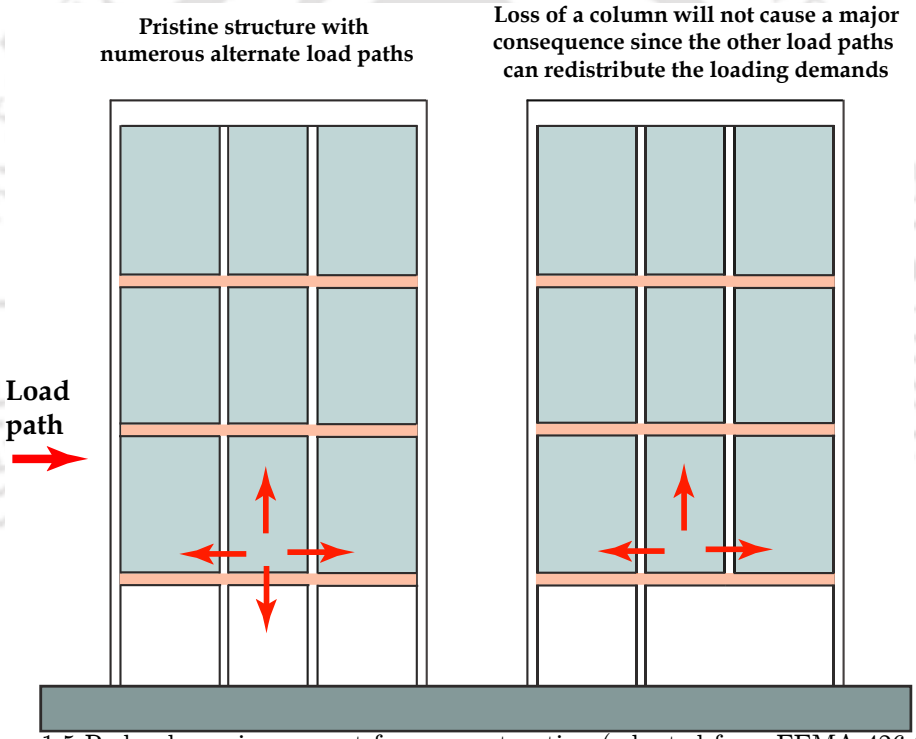

Figure 1.5 Redundancy in moment frame construction (adopted from FEMA-426 2003)

the complete collapse of the structure (Oklahoma City bombing in 1995 and WTC attack in 2001). To avoid catastrophic failures, the structural system should provide continuous path flow for the force for both gravity and lateral loads. For a continuous load path, the connections in the structural system should be superior that should provide sufficient strength for developing the full capacity of the members. The ductile detailing of diaphragm plays a vital role in transmitting inertial force from primary girder to column and thereby to foundations. The redundancy in structure provides alternating and multiple paths for transfer and dissipation of flow of forces. Redundancy plays a vital role in the mitigation of blast effect by preventing progressive

collapse. The schematic diagram of the ductile moment connections with redundancy in the structure can be seen in Figure 1.5.

The philosophy behind redundancy is that it offers multiple paths for the transfer of forces in a situation where a particular load path fails due to blast loading. Redundancy facilitates in the formation of plastic hinges at several locations and reduces the probability of collapse. The redundancy in structure demands effective strengthening of the beam-column connection for proper redistribution of force. Apart from structural strengthening and redundancy, the ductility of the system contributes significantly to mitigate the blast-induced damage. Ductility is defined as a capacity of the system to continue to sustain force for increasing deformation, thereby providing sufficient warning for evacuation. The ductility of the system can be enhanced by confining the concrete core by transversal steel reinforcement and adapting proper structural detailing (refer Figure 1.6).

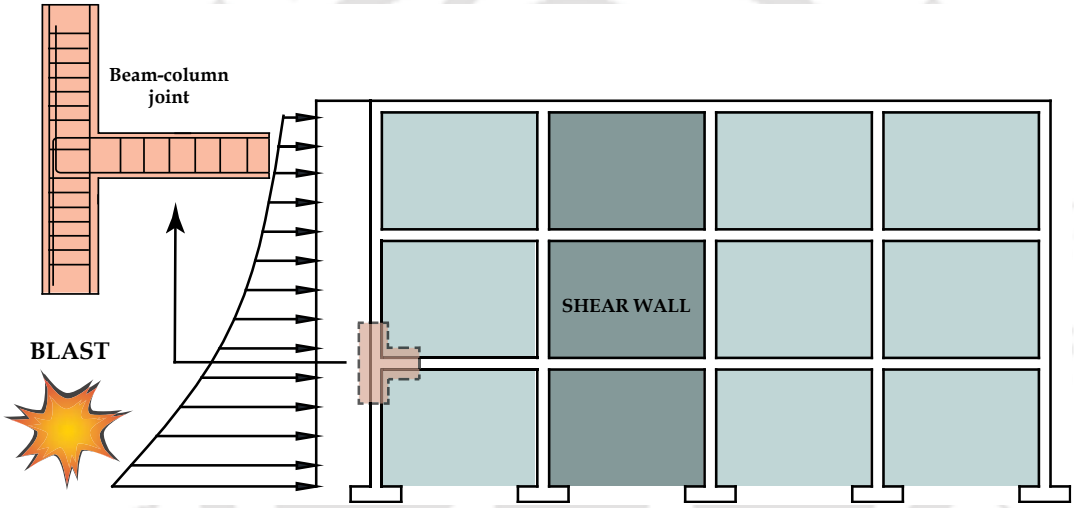

Figure 1.6 Ductile detailing of connection in reinforced concrete structure; note the dense reinforcing in the vicinity of the connection (adopted from FEMA-426 2003)

The positive and negative phase in the blast load profile causes load reversal and uplift of structural members. The structural members, such as slabs that are designed primarily to resist gravity loads experience catastrophic failure due to load reversal and uplift. The connection between slab to floor beams detailed poorly for uplift loads and failure under punching-shear. The details of structural strengthening and ductile detailing in RC structure will be discussed in detail in the literature review.

1.1.4 Sacrificial protective system for blast and impact mitigation

The building is envelops by the structural or non-structural element with the largest surface area that separates the interior of the building from the outdoor. The building envelops must vulnerable to blast, shock, and impact loading due to its direct exposure and transfers it to the load-bearing structure. Therefore, the external façade should be ballistic resistant which can enhance resistance of external spandrel beam, shear wall, and window frame. The blast and impact resistance building envelop to be lightweight,

exhibit ductile and plastic behavior. The protective structure should absorb impact and blast energy by progressive deformation and transmit lower stresses to the primary structure. The sacrificial protective system is designed to arrest the generation of flying debris that increases the risk of injuries.

In practical scenarios, the impactor and fragments gains their high-velocity from the energy driven by shock and blast wave loading (Krehl 2008; Staudhammer et al. 2001). The main mechanics to ameliorate the impact resistance of the structure are: i) energy absorption (Komissarov et al. 2016; Skews et al. 1993; Xia et al. 2016), ii) dissipation (Dharmasena et al. 2008; Wadley et al. 2008), iii) defragmentation and disintegration (Kore et al. 2016; Shelke et al. 2014), iv) impact trapping (Andreopoulos et al. 2007; Igra and Igra 2016; Prasanna Kumar et al. 2018; Xiao et al. 2019), v) reflection/divergence (Yang et al. 2013) and, vi) structural strengthening (Aoude et al. 2015; Ha et al. 2011; Nam et al. 2010; Razaqpur et al. 2009; Tolba 2002; Xu et al. 2016). The impact mitigate strategies included employment of deformable sacrificial protective layer that can dissipate or absorb impact energy and reflect/deflect the impactor. This work focuses on development and implementation of protective sacrificial layered material that mitigate the impact damage by virtue of energy absorption. Impact absorbing devices includes foam based barriers such as metallic, polymeric, polyurethane and aqueous foams (Jourdan et al. 2015; Liverts et al. 2015; Prasanna Kumar et al. 2018). Figure 1.7 shows some innovative sacrificial protective topologies that are effective to resist ballistic loading. Hybrid sandwich composite panel

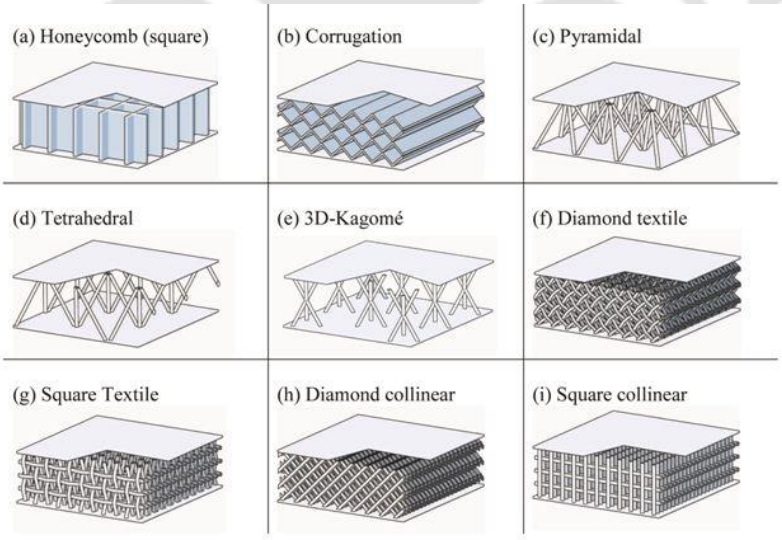

Figure 1.7 Various types of sandwich panel structures made of cellular lattices (Ashby et al. 2000)

embedded with plastically deforming interior core are excellent systems that enhances the impact resistive performance of the civil structures (Angioni et al. 2010; Correia et al. 2012; Uddin 2013). The core attenuates the velocity of the impactor by absorptive and dissipative mechanics through plastic deformation. Distinct topology configuration undergoing plastic deformation that are extensively studied to absorb impact energy

are hierarchal folding of web core (Fang et al. 2017; Gibson and Ashby 1999; He et al. 2018; Hu et al. 2018; Qi et al. 2019), progressively buckling of thin wall honeycomb core (Abrate 2005; Bitzer 2012; Choi 2006; Foo et al. 2008) and globally deforming pyramidal and lattice truss structures (Liu et al. 2015; Yungwirth et al. 2008; Zhang et al. 2013; Zhang et al. 2014). The primary aim of the sacrificial protective cladding is hierarchal plastic deformation to absorb maximum ballistic energy and thereby transmitting residual energy to primary structure.

1.2 Methodology and objectives of the thesis

When designing a structure to safeguard against blast and impact loads, an engineer faces two prominent challenges: Firstly, the quantification and the interaction of the structure due to the blast or shock wave. Secondly, the estimation of the structural response and the subsequent damage prediction is needed.

In order to conduct blast experiments in the academic institutions, it is difficult in terms of security and personals. So, a shock tube setup is developed to conduct the shock and impact experiments in the lab environment with proper safety measures.

The main goal of the thesis is as follows:

1. Development and fabrication of a shock tube facility to perform both shock wave loading and moderately high-velocity impact test.
2. Investigation of the dynamic response of reinforced concrete (RC) external beam-column joint subjected to shock-wave loading. An experimental and analytical investigation is conducted to study the influence of structural deficiencies in the beam-column subassemblies.
3. Development of design aids in the form of simplified shock response spectrum based on a single degree of freedom idealization considering elasto-plastic idealization of RC sub-structure.
4. Development of the sacrificial honeycomb composite system to enhance the impact-resisting performance of the external beam-column subassembly.
5. Formulate an analytical solution to evaluate peak contact force due to low-velocity impact on honeycomb structure considering the material and geometrical uncertainties.
6. Evaluation of enhancement in impact resistance capabilities of honeycomb composite as a protective shield to RC structural members and identification of localized failure modes in protected structure.

1.3 Organization of the thesis

The current chapter describes the background and motivation of the thesis related to the blast and impact studies of RC framed structures and the literature available on the development of sacrificial composite structures to protect the buildings against terrorist activities.

The thesis proposal is organized as follows:

Chapter 2: Background on various studies conducted on the blast and impact loading on the structures as well as beam-column mechanism along with the research plan for the overall thesis.

Chapter 3: Development and characterisation of a shock and impact loading simulator.

Chapter 4: Experimental and analytical investigation of an exterior reinforced beam-column joint subjected to shock loading.

Chapter 5: Mechanical characterisation of the honeycomb structure and its probabilistic contact force model for low-velocity impact.

Chapter 6: Experimental and analytical investigation of honeycomb shielded exterior reinforced beam-column joint subjected to impact loading.

Chapter 7: Conclusions and suggested future work.

The classification of the thesis chapters along with its activities, deliverables, and future work is detailed in Figure 1.8. The glossary of notations and symbols used in the thesis is reported in the nomenclature in Page xxi.

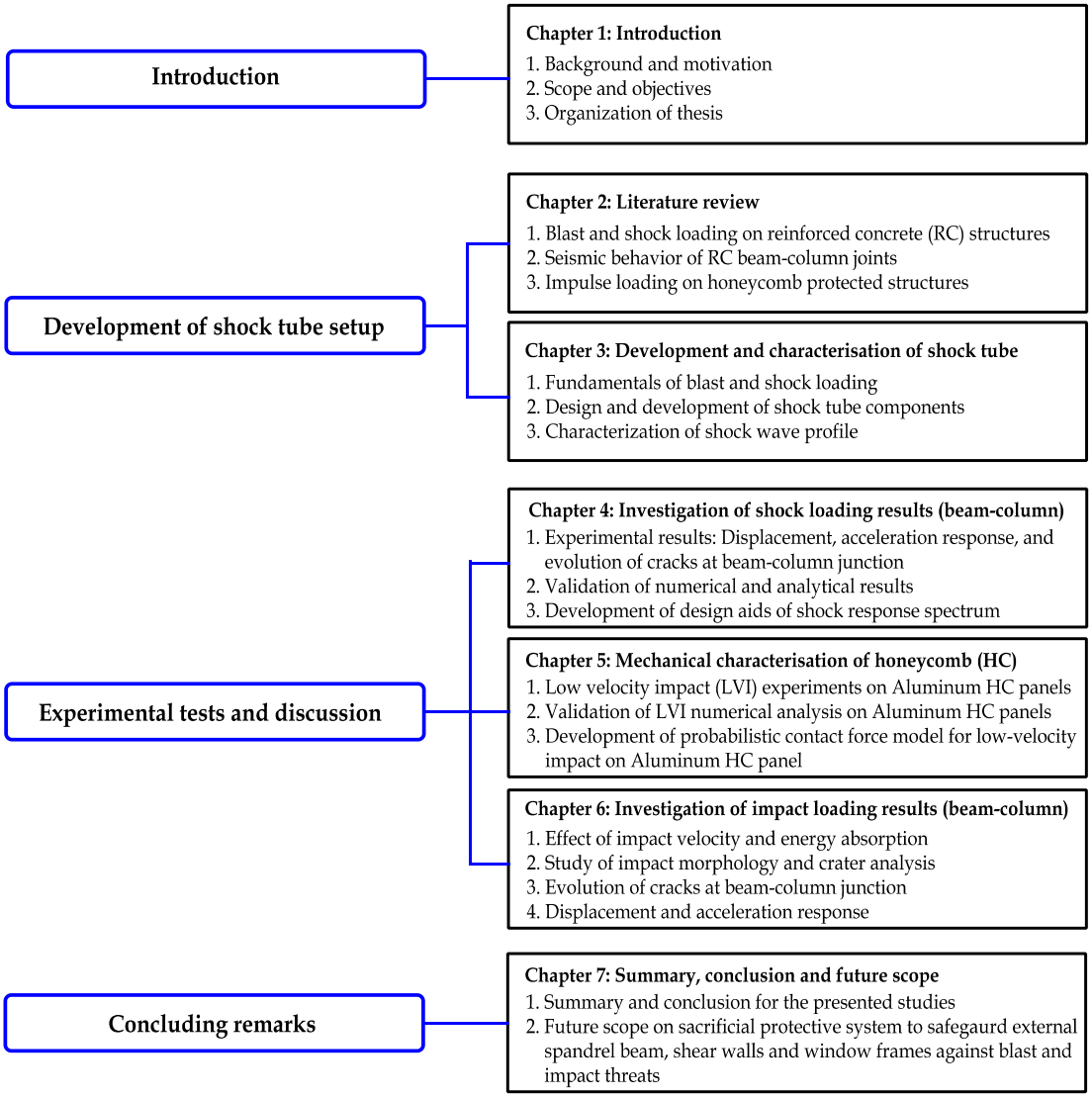

Figure 1.8 Organization of thesis chapters

Chapter 2
Literature review

2.1 Overview

The main objective of the thesis is to develop a protective system comprising of the thin-walled Aluminum composite structure to resist shock and impact loading to safeguard reinforced concrete (RC) structure. In view of the above broad thesis objective, an extensive literature review is conducted on various aspects of behavior of RC structures. This literature review is divided into four major sections. First section deals with the literature on shock and air blast and its interaction with ground surface. Second section deals with the response of RC structural sub-assemblies and members subjected to blast and shock loading. Based on the literature review corresponding to the second section, it was found out that literature on extreme loading was focused on isolated structural elements such as beams, columns, and shear wall. The connections between beams and columns are critical zones in the moment-resisting frames. The performance of such joints dramatically affects the strength and ductility of the overall frame. Under the action of extreme loading, the progressive failure is initiated and propagated due to failure of beam-column joint. Most of the literature focuses on response of beam-column joint subjected to extreme loading that is limited to earthquake and wind loading. Third section summarizes the exhaustive research on beam-column joints subjected to quasi-static and seismic loading at low frequency (< 2 Hz). Based on the literature review corresponding to the third section, it is identified that limited studies are available on extreme loading (blast, shock and impact loading) on beam-column joint that is often the vulnerable component in structure.

The overarching goal of the thesis is to develop a sacrificial protective system to safeguard the vulnerable structural component against threats arising from extreme loading. Composite structures comprising of metallic foams, honeycomb panels and Auxetic structure are widely used to resist extreme events on aerospace structure. Therefore, an extensive literature review is conducted on capabilities of composite structure to resist extreme events that could mitigate the structural damage. The literature review is conducted on the application of composite structure as a sacrificial protective system to resist impact and blast load and thereby safeguard the parent structure. The schematic representation of organization of literature review is shown in Figure 2.1.

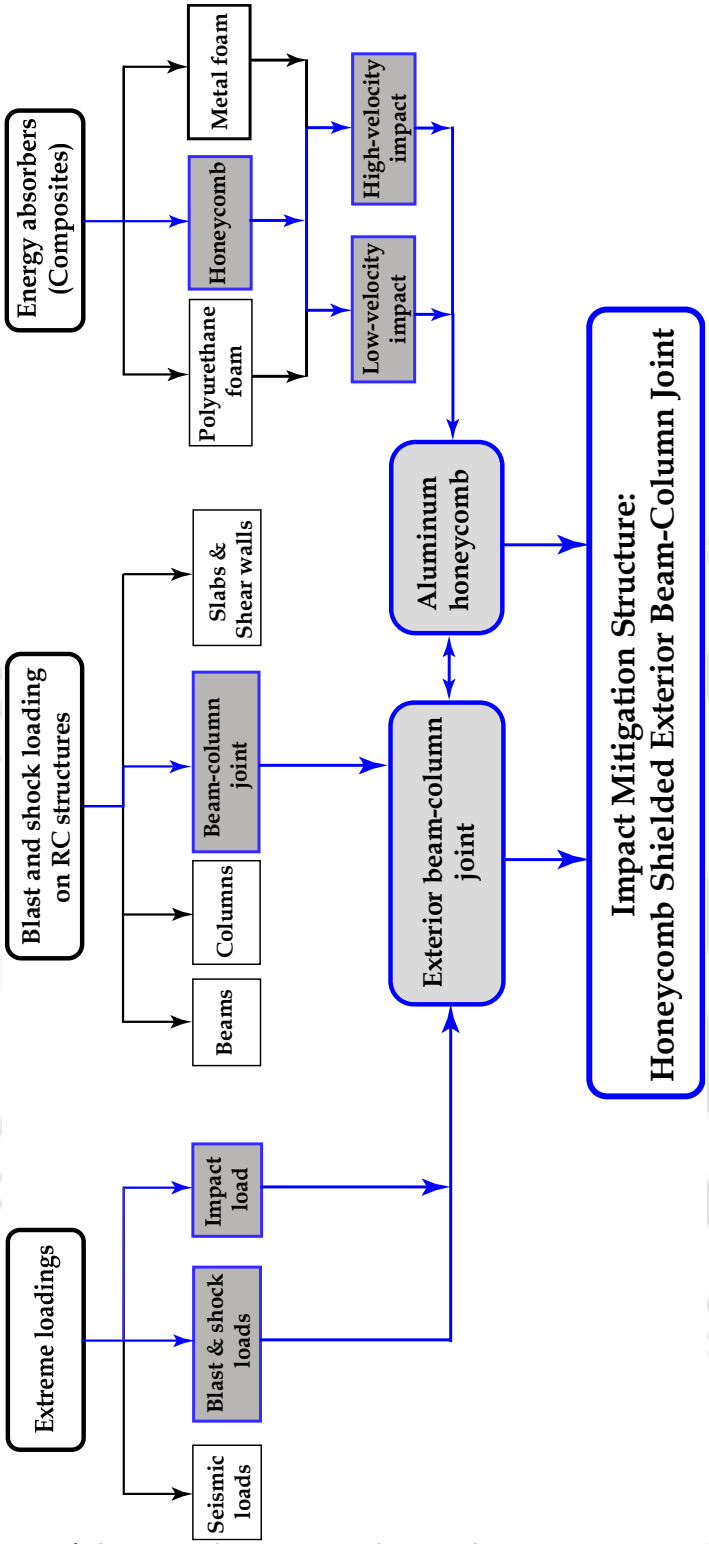

Figure 2.1 Overview of the research on exterior beam-column joint protected with honeycomb sacrificial system under blast and impact loading

2.2 Previous research on blast and shock loading

An explosion is a major hazard that can severely damage the building structures. It is typically categorized as a physical, nuclear, or chemical event based on its origin. Physical explosions are consequences of events such as the eruption of a volcano or catastrophic failure of pressure vessels. A nuclear explosion happens due to the energy

released during the redistribution of protons and neutrons within different interacting atomic nuclei. The chemical explosions occur when the fuel elements of an explosive compound rapidly oxidize, a reaction known as combustion. Most of the practical explosives are solid or liquid in form, also known as condensed explosives. During the reaction process, the hydrogen and carbon atoms comprising the fuel element of the explosive disintegrate violently, releasing heat and high-pressure gas. When the velocity of the high-pressure gas is significantly higher than the speed of sound, the explosive reaction is referred to as detonation and results in a high-intensity shock wave known as a blast wave (Smith and Hetherington 1994). The brief explanation of blast and shock mechanism and its fundamentals are detailed in Chapter 3.

The use of explosives by terrorist groups around the world that target civilian buildings and other structures is a growing problem in modern societies. The terrorist activity of WTC Towers blast and collapse scenario can be seen in Figure 2.2. Structural failures like member collapse and the shattering of glass can increase the fatalities in addition to the immediate effect of the blast wave pressure. Therefore, structural integrity has to be ensured by the engineers under unexpected extreme loading situations.

Figure 2.2 World Trade Center (WTC) Tower with antenna-Blast and collapsed scenario: Tower I (Bangash 2006)

The blast loading is complex to quantify since it depends on the nature of the explosive charge, weight, distance from the target structure, geometry of the building facades, angle of incidence of the shock front, and the level of confinement of the explosion. The wide range of explosives can be represented in terms of the equivalent weight of Trinitrotoluene (TNT). UFC 3–340–02 (2008) gives the various blast load categories and the estimation of the blast parameters of some common explosives.

In the past few decades, considerable research is performed on explosive technique, quantification of blast load on various structures, and design of blast resistant structures. A brief summary of the research investigation on the quantification of blast wave loading upon interaction with various geometries of the target structure is presented below.

Remennikov (2003) studied the methods for predicting blast effects on buildings when a single building is subjected to blast loading produced by the detonation of a high explosive device. An extensive literature is available on various analysis methods to predict the loads and blast pressure from a high explosive blast on buildings. Their research was mainly focused on finding out the ways for protecting structures against bomb attacks. Further, numerical techniques, including Lagrangian, Eulerian, and finite element methods are used for accurate prediction of blast loads on commercial and public buildings.

Remennikov and Rose (2005) studied the different empirical relationships for determining blast loading. These relationships assumed that there is no obstacle between charge and target. In real scenarios, the actual blast load can be reduced due to the adjacent building geometry or can be enhanced due to the presence of other buildings. An approach to determining the enhancement factor was described. Numerical simulation using a computational fluid dynamics (CFD) code Air3D was used for determining blast effects on the building

Naito and Wheaton (2006) presented the methodology for the performance of structural elements under blast loads. They conducted finite element analysis to study the pushover analysis and to calculate the blast resistance of the existing shear wall subjected to an external explosion. Pressure impulse curves were generated to evaluate the blast resistance of the wall relative to various levels of damage. The resulting pressure-impulse curves provide information regarding the damage done by a particular intensity of the blast. This analysis is very useful for the designers to retrofit the structure to withstand the blasts.

Ngo et al. (2007) gave an overview of the explosives and their effects on the structure. Mechanism of the blast wave and nature of explosions was explained. They demonstrated different methods for finding out blast loads and the calculation of structural response. They pronounced that the comprehensive overview of the analysis and design of the structures subjected to blast loads require a detailed understanding of blast phenomena and the characterisation of its parameters. They suggested the design consideration against extreme events like bomb blast is very important and the

design of the building under blast load should be included in the building regulations and design standards.

Koccaz et al. (2008) studied the blast resistant design theories along with the effect of explosives in both architectural and structural design process. Study of explosion and explosives give better understanding to make blast resistant building design. They suggested that cast-in-situ reinforced concrete floor slab are the preferred option for blast resistant buildings, but it may be necessary to consider the use of precast floors in some cases. Lightweight roofs and particularly glass roofs should be avoided and a reinforced concrete or precast concrete slab is preferred. In the case of explosion, columns of reinforced concrete structure are the most important members and should be protected. Wrapping with steel belts and wrapping with carbon fiber-reinforced polymers (CFRP) is provided to protect the columns.

Draganić and Sigmund (2012) studied the method for determining the blast load on structures and explained the method with an example of a structure subjected to a blast load. A comprehensive study was conducted on the blast loading to improve the guidelines provided in the UFC and EUROPEAN code. They modelled a structure in finite element software subjected to three different blast loads with same standoff distance. The main point of the analysis of the structure elements exposed to blast loading was to check their demand ductility. From the results it was evident that non-linear analysis is necessary and simple plastic hinge behavior is satisfactory.

Karlos and Solomos (2013) presented their report in which calculation of the external explosion loads to be considered in the blast protection design of the structure. Empirical formulae for the prediction of the blast loads were proposed for the design of the structure. Several formulae and graphs were included in the report as a design aid. Case studies are presented to understand more efficiently the problem and calculation of blast load.

Mirgal et al. (2014) studied the effect of blast loading on a structure from architectural point of view. Structural form is a parameter that affects the blast loads on the building. Arches and domes are the types of structural forms that reduce the blast effects on the buildings. Single story buildings are more blast resistant compared with multi-story buildings. Internal layout of the building is another parameter from architectural point of view for blast resistant building. Lobby area should be protected with reinforced concrete walls; double doors should be used and the doors should be arranged eccentrically within a corridor to prevent the blast pressure entering the internals of the building.

Hamra (2016) proposed an easy way to examine the type of damage introduced into the building when one compartment is subjected to blast. Initially the whole frame was not studied and individual component of structure like beam, column was studied separately. The materials are assumed elastic - perfectly plastic. For the blast loading, the blast pressure is uniformly distributed along each structural member. For the analysis of simple frame blast loading, two scenarios were involved in the study. The first corresponds to quasi-static blast loading while the others refers to a dynamic blast

loading. The effects of strain rate on the yield strength and the ductility capacity of the structural elements were neglected.

UFC 3–340–02 (2014) Unified Facilities Criteria is a manual titled "Structures to resist the effects of accidental explosions," widely used for analysis and design of structures. UFC manual provides guidelines and standards on the evaluation of (i) Blast, fragment and shock loading, (ii) Types of explosions (iii) Principle of dynamic analysis of blast (iv) Reinforced concrete design (v) Structural steel design, and (vi) Special considerations in explosive facility design. UFC code has proposed a set of design values for given structural steel and reinforced concrete elements based on the dynamic increase factor (DIF). It is defined as the ratio of the dynamic stress to the static stress. Strain rate effect was also considered in the DIF values. However, the DIF values are based on the average strain rate value of the cross-section whereas, the strain rate is time dependent and also varies upon the change in the depth of the cross-section along the length of the beam. These DIF values may also be independent of the blast loading scenario and can be un-conservative in some special cases.

To summarize the section, detailed literatures related to quantification of explosive loads, methods of analysis and structural response to blast loading are presented in Table 2.1.

Table 2.1 Summary of literature review on blast and shock loading

Author	Charge type*	Charge weight (kgs)	Stand-off distance (m)	Duration of event (ms)	Remarks on analysis and approach (Empirical/ Code)
Muszynski and Purcell (2003)	TNT	860	11 - 15	-	Empirical
Muszynski and Purcell (2003)	TNT	830	14.6 - 50.0	-	Empirical
Remennikov (2003)	TNT	100	15	40	-
Luccioni et al. (2004)	TNT	400	2.5	-	Numerical
Remennikov and Rose (2005)	TNT	1000	100	5	Numerical
Pandey et al. (2006)	TNT	10000	100	50 - 250	Code based
Rodriguez-Nikl (2006)	ANFO	558	4.3 - 6.1	10	Numerical and Empirical
Buchan and Chen (2007)	TNT	0 - 860	0 - 24	0 - 100	-
Ngo et al. (2007)	TNT	0 - 6000	30 - 40	0 - 100	-
Schenker et al. (2008)	TNT	1000	20	100	Empirical
Nassr et al. (2011)	ANFO	50 - 250	7.0 - 10.3	40	Empirical
Nassr et al. (2012)	ANFO	50 - 250	7.0 - 10.3	40	Analytical
Nassr et al. (2013)	ANFO	50 - 250	7.0 - 10.3	40	Empirical
Nassr et al. (2013)	ANFO	50 - 250	7.0 - 10.3	40	Empirical and Numerical
Yankelevsky et al. (2013)	-	-	-	-	Empirical
Foglar and Kovar (2013)	TNT	25	15 - 30	120	Analytical and Numerical
Nassr et al. (2017)	ANFO	40 - 250	10 - 30	40	Empirical

* ANFO: Ammonium Nitrate and Fuel Oil, TNT: Trinitrotoluene

2.3 Previous research on blast and shock loading on reinforced concrete (RC) structures

Several terrorist attacks on civil infrastructure and military have raised alertness by revealing the vulnerability of reinforced concrete (RC) structures subjected to shock, blast and impact loading. These deliberate terrorist attacks have resulted in casualties

and caused tremendous damage to the structures (Baker et al. 2012). Some explosions lead to the collapse of the entire structure and surge casualties. According to the Global Terrorism Database of the National Consortium for the Study of Terrorism and Responses to Terrorism (START) at the University of Maryland (USA) (Global Terrorism (Database 2017), and recent publications (Edwards et al. 2016; Shvetsov et al. 2017; Williams et al. 2010) during the period between 2006 and 2019, the total recorded terrorist activities around the world are more than 126,713 with total casualty of more than 216,915. Observing at the trend of recent terrorist attacks in Pentagon and World Trade Center (WTC 2001), Marriott Hotel in Jakarta (2003), Australian Embassy in Indonesia (2004), Night Clubs and Restaurants in Bali (2005, 2002), United States (Boston in 2013), Iraq (2017, 2016, 2014), Afghanistan (2018), and Kenya (2019) it can be seen that predominantly the public buildings, hospitals, theatres, government infrastructure and bridges etc., are targeted. Since, the damage caused during an explosion is a result of extreme loading condition which is normally not accounted in the design procedure. A brief review of past literature was carried out to account on blast and shock events on RC structures.

Ohtsu et al. (2007) conducted experiments to compare the behavior of normal concrete and fiber-reinforced concrete (FRC) slabs subjected to blast loading. The blast experimental setup and damage patterns of slab can be seen in Figure 2.3.

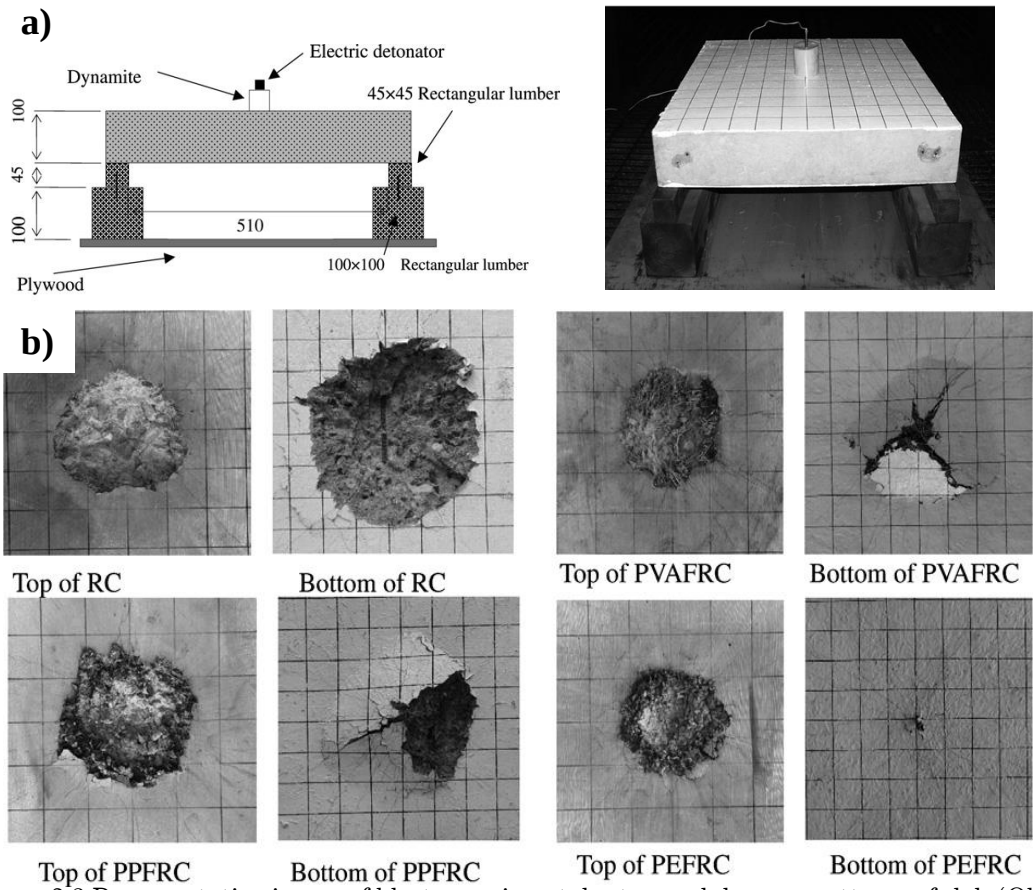

Figure 2.3 Representative image of blast experimental setup and damage patterns of slab (Ohtsu et al. 2007)

Due to the blast load, craters were formed at the top surface and spalling at the bottom surface of the FRC slabs. The diameter of the blast crater was indicative of the amount of damage. It was found that the average diameters of the crater and spalling failure volume significantly decreased with the increase in the flexural toughness of the specimen when FRC was employed.

Wu et al. (2009) conducted a series of experiments to study the blast resistance behavior of reinforced concrete slabs with three variants. It consists of normal reinforced concrete slab (NRC), plain ultra-high performance fibre concrete (UHPFC) and reinforced ultra-high performance fibre concrete (RUHPFC), and the slabs were reinforced with externally bonded (EB) fibre reinforced polymer (FRP) plates. They noticed that the slabs with the addition of EB carbon FRP plates to the compression face of reinforced concrete slab enhanced its ductility and blast resistance. The blast resistance performance of the RUHPFC slab was superior compared to the other two variants.

Fujikura and Bruneau (2010) reported a detailed examination conducted on the blast resistance of bridge piers. Experiments at reduced scales (one-fourth scale) were adopted to investigate the structural behavior of ductile RC columns and non-ductile RC columns retrofitted with steel jacketing. The blast loading test setup and column deformation of bridge piers is shown in Figure 2.4. They noticed that the seismically designed RC and steel jacketed RC columns did not demonstrate well in terms of ductility behavior when subjected to blast loading. They failed due to the shear at the column base instead of flexural yielding. They considered the RC specimens designed for current seismic codes and steel jacketing, which are known to be efficient in seismic performance have shown to be ineffective under blast loading scenario. The experimental results were further validated with analytical results for both types of RC columns. They proposed a moment-direct shear interaction model for the minimization of direct shear resistance on cross sections during the simultaneous application of large moments.

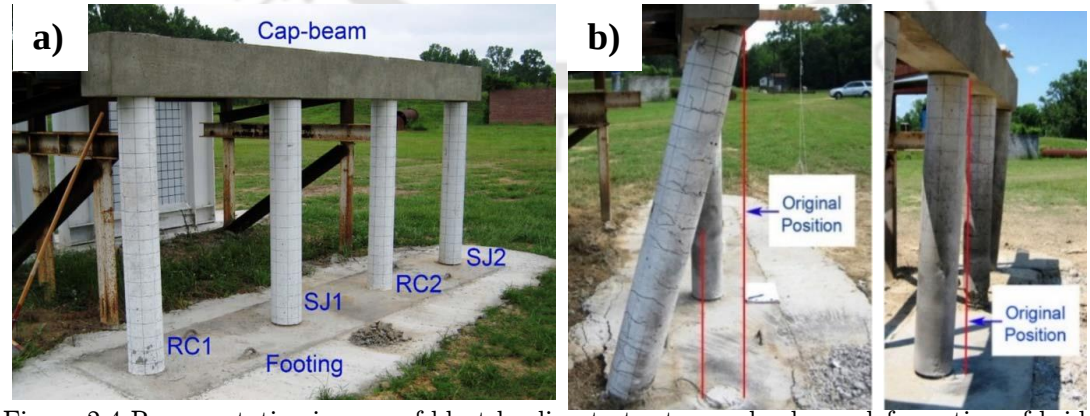

Figure 2.4 Representative images of blast loading test setup and column deformation of bridge piers (Fujikura and Bruneau 2010)

Magnusson et al. (2010) studied the dynamic behavior of the high-strength reinforced concrete beams subjected to air blast loading. They considered two types of

beams i.e., high-strength concrete (HSC) and normal-strength concrete (NSC) that were subjected to air blasts using explosives in a shock tube. Steel fibers were used in the high-strength beams for strengthening it. They tested the beams under in flexure for static loading as well as blast loading tests. They observed the failure mode in the blast loading test varied from the failure mode seen in the static loading tests of respective specimens. In the static tests, the failure mode is noticed as ductile flexure failure whereas in blast loading tests it was a brittle shear failure. The dynamic tests of beams without fiber reinforcement and with a high ratio of the reinforcement demonstrated a shear type of failure. With the increase in the steel fiber volume content, there was an increase in the shear strength and also the ductility of beams. The experimental investigation indicated that the dynamic load capacity of HSC beams was relatively higher compared to other specimens. They suggested that the special attention need to be paid on high-strength concrete beams with high amounts of reinforcement in order to avoid the brittle shear type of failure.

Yusof et al. (2011) demonstrated the comparison of blast test results of plain reinforced concrete and normal strength steel fiber reinforced concrete panels (SFRC). In SFRC panels, three different volume fractions of steel fibers were employed i.e. 0.5%, 1.0%, and 1.5%. Failure modes of all the types of specimens were visually examined for understanding the dynamic behavior under blast scenario. They observed that the panels with 1.5% steel fibers performed well against explosive loading and there was no significant damage found on both the front and back face of the panel. The steel fibers in the panels have been arrested the crack propagation and then transformed the pattern of brittle failure mode to a pseudo-plastic manner. Their study indicates that the SFRC panels containing 1.5% volume fraction have the best performance against blast loading. The obtained experimental results concluded that the increase in the volume of steel fibers enhances the blast resistance of a concrete structure.

Wang et al. (2012) conducted blast experiments on scaled-down one-way slabs. They addressed the scaling of the dynamic response in one-way reinforced concrete slabs under close-range blast loading. They considered a total of six slabs of two groups with different scale-down factors subjected to two scaled distance blasts. In the experimental observations, it shows that the fracture patterns in both groups were almost similar. They characterized the damage levels due to the scaled distance blasts and noticed that the local damage in RC slabs with larger-scale factor is slightly reduced with respect to that of smaller-scale factors. It was found that the larger specimens were having the perforation failure whereas the smaller specimens exhibit the scabbing without any kind of perforation. From the experimental observations, they proposed two empirical equations that can correct the results when a model is scaling up to the prototype.

Foglar and Kovar (2013) performed blast tests on real scale reinforced concrete precast slabs with different fiber content volume. They focused on the blast performance of fiber reinforced concrete slabs and the influence of fiber volume. Due to the application of fibers in the concrete, the specimen failure was transformed from

brittle to ductile and minimized the volume of debris during the blast test. The fibers in the concrete concentrated in the specimen and this accumulation turns into the higher mass in the debris, which it could not fly very far from the blast. They believe that the employing fibers in the concrete will not only increase the ductility but also will decrease the volume of debris ejecting during the blast leading to less number of injuries and fatalities. Minimizing the debris volume by employing fiber content demonstrated a significant enhancement in the overall blast safety of reinforced concrete structures. Further, the experimental results were validated with numerical results. With the addition of fibers to the conventional concrete, it not only increases the compressive strength as well as enhanced the blast performance of the concrete slabs.

Tabatabaei et al. (2013) proposed a method to improve the blast spalling performance of conventional concrete by application of long carbon fibers. They conducted a series of experiments on long carbon fiber reinforced concrete (LCFRC) panels subjected to blast loading. The application of long carbon fibers increased the blast performance significantly and minimized the crack magnitude in the panels. They noticed that the surface damage and debris volume is less in the LCFRC panels than normal RC panels. Furthermore, the experimental results were also compared with the damage level chart provided by UFC 3-340-02 (2014). The Material model 159 (Continuous Surface Cap Model) was used in the numerical analysis (LS-DYNA) for the study of LCFRC panels and it described the accurate response for both tension and shear. To predict the observed damage in the experiment, finite element analysis was carried out and achieved a good agreement. The successful damage prediction by numerical analysis allowed the panels to be studied without any full-scale blast experiments. They performed the parametric study in the numerical investigation for the prediction of the spalling curve in fiber-reinforced concrete panels.

Yankelevsky et al. (2013) explained the response of reinforced concrete residential buildings subjected to full-scale field blasts. They studied the dynamic behavior of both structural and non-structural components that were incorporated in the residential buildings. They addressed the global response of the multi-story buildings under full-scale blast loading and evaluation of their exposure to progressive collapse. A representative schematic arrangement of cubicle specimens blast test arena and arenas of cubicles (before and after) is clearly displayed in Figure 2.5 . They discussed the practical issues during the full-scale field tests to understand the various possibilities to perform the full-scale tests. They focused on providing the insights on full-scale field blast experiments on a five-story reinforced residential building which was instrumented heavily with 200 gauges that include pressure, strain and acceleration sensors. They incorporated the protective shafts to protect the inhabitants of the building as well as to enhance the blast resistance of the buildings. They suggested that the provision of protective shafts and RC staircase shafts in the buildings gives a synergistic effect on multi-story buildings and better resistance against seismic loads.

Figure 2.5 Representative schematic arrangement of cubicle specimens blast test arena and arenas of cubicles [before and after] (Yankelevsky et al. 2013)

Aoude et al. (2015) conducted an experimental investigation on the blast performance of ultra-high performance fiber reinforced concrete (UHPFRC) columns. They considered two variants in the specimen configuration i.e., compact reinforced concrete (CRC) and ultra-high performance fiber reinforced concrete (UHPFRC) columns. The specimens were tested under simulated blast loading with varying blast pressure impulse combinations by employing a shock tube. A representative shock tube setup and comparison showing deformation and fracture patterns of columns (before and after) can be seen in Figure 2.6. A detailed parametric study was conducted on the concrete type, fiber content, fiber properties, transverse reinforcement spacing, and longitudinal reinforcement ratio. They examined the compatibility of using a single degree of freedom (SDOF) analysis to predict the blast response of UHPFRC columns and further studied the insights of blast performance enhancement from the application of UHPFRC in columns. A good agreement in analytical results with the experimental results was observed. The results demonstrated by minimizing maximum and residual displacements, damage tolerance as well as reducing the secondary blast fragments debris volume.

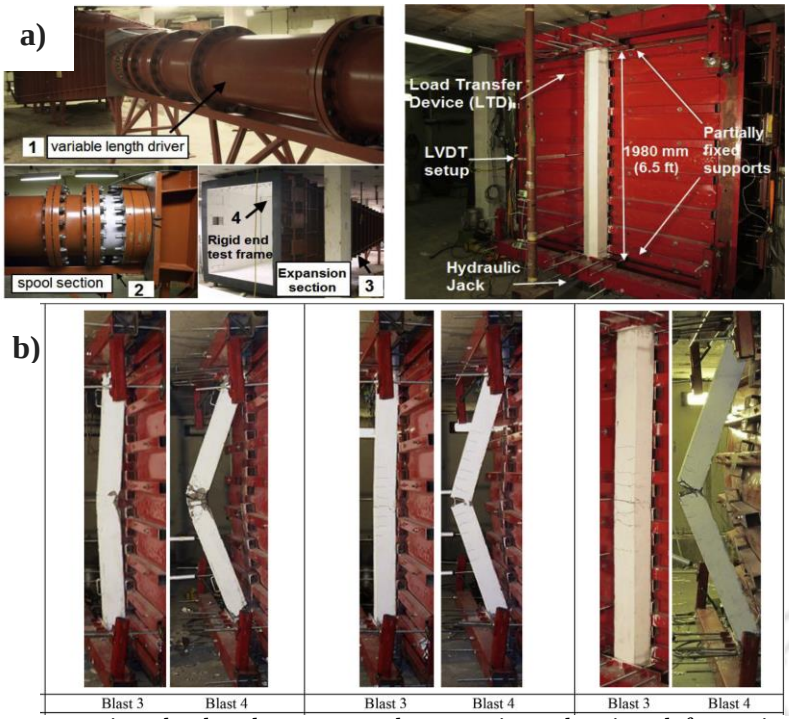

Figure 2.6 Representative shock tube setup and comparison showing deformation and fracture patterns of columns [before and after] (Aoude et al. 2015)

Lee et al. (2018) demonstrated the rate-dependent structural response of reinforced concrete (RC) beams with and without steel fibers and stirrups. They adopted three types of loadings i.e., quasi-static, impact, and blast loading for the testing of RC beams. The experimental results presented that the addition of steel fibers in RC beams enhanced the load carrying capacity, energy absorption and minimizes the maximum and residual displacements. It was found that the application of steel fibers also enhanced the static, impact and blast resistance of the specimens. They observed that the brittle shear failure can be effectively arrested by the incorporation of stirrups. The shear crack inclinations in the RC beams were increased with the increase in the steel fiber amount and strain rate. They stated that the loading rate effect on the load carrying capacity of RC beams was comparatively lesser with a ductile flexural failure mode obtained. The application of steel fibers significantly improved the structural performance under static loading condition when compared with impact and blast tests.

A broad literature review of response of RC structure subjected to blast and shock loading is presented. The review comprises of recent advancements on the extreme loading on structural members such as beams, columns, slabs, and shear walls and is represented in Table 2.2. Limited studies are available on structural behavior of beam-column joint subjected to extreme loading. Therefore, a dedicated effort provided towards the evaluation of the performance of the beam-column sub-assemblies under extreme events which includes seismic and quasi-static loading scenario. A vast literature is available on the aforementioned topic and is summarized in the Section 2.4.

Table 2.2 Summary of literature review on blast and shock on RC structures

Author	Structural element	Material*	Scale/ Dimensions (m)	Blast/ Shock	Charge weight (kg)/Shock wave (kPa)	Remarks on analysis
Ohtsu et al. (2007)	Slabs	RC, PPFRC, PVAFRC, and PEFRC	0.6 x 0.6	B	10	DI
Quintero et al. (2007); Wei et al. (2007)	Slabs	RC	1.22 × 1.22	B	1.16 - 1.71	PI
Fujikura et al. (2008)	Columns	RC and CFST	1 : 4	B	-	PI
Wu et al. (2009)	Slabs	NC, UHPFC, RUHPFC, and EBFRP	1 x 2	B	20	PI
Williams et al. (2010)	Columns	RC	1 : 2	B	-	DI
Fujikura and Bruneau (2010)	Columns	RC and RC+SJ	1 : 4	B	-	PI
Magnusson et al. (2010)	Beams	NSC and HSC	1 : 1	S	1200–3200	DI and PI
Yusof et al. (2011)	Panels	RC and SFRC	0.6 × 0.6	B	1	DI
Fujikura and Bruneau (2011)	Columns	RC and CFST	1 : 4	-	-	PI
Wang et al. (2012)	Slabs	RC	1 : 1, 1 : 1.25 and 1 : 1.67	B	0.19 - 0.94	DI
Foglar and Kovar (2013)	Slabs	RC and FRC	6 × 1.5	B	25	DI
Tabatabaei et al. (2013)	Panels	RC and LCFRC	1.83 × 1.83	B	38.5	DI and PI
Yankelevsky et al. (2013)	Buildings	RC	1 : 1	B	-	DI
Ellis et al. (2014)	Panels	UHPC	1626, 864 and 51	S	-	DI
Stolz et al. (2014)	Slabs	DUCON	2410 × 1140	S	35–250	PI
Aoude et al. (2015)	Columns	UHPFRC (CRC)	1 : 1	S	12.6–108.6	DI and PI
Thiagarajan et al. (2015)	Slabs	HSC-VR, HSC-NR, NSC-VR and NSC-NR	1 : 3	S	350–390	DI and PI
Lee et al. (2018)	Beams	SFRC	125 × 250 × 2438	S	22.78 – 7.81	DI and PI

*RC: reinforced concrete, NC: normal concrete, SFRC: steel fibre-reinforced concrete, PPFRC: polypropylene fibre-reinforced concrete, FRC: fibre-reinforced concrete, CFST: concrete-filled steel tube, RC + SJ: reinforced concrete with steel jacket, NSC: normal strength concrete, UHPC: ultrahigh-performance concrete, PVAFRC: polyvinyl alcoholic fibre-reinforced concrete, PEFRC: polyethylene fibre-reinforced concrete, PPFRC: polypropylene fibre-reinforced concrete, LCFRC: long carbon fibre-reinforced concrete, UHPFC: ultrahigh-performance fibre concrete, RUHPFC: reinforced ultrahigh-performance fibre concrete, EBFRP: externally bonded fibre-reinforced polymer plates, UHPFRC: ultrahigh-performance fibre-reinforced concrete, HSRC: high-strength-reinforced concrete, UHPFRC: ultrahigh-performance fibre-reinforced concrete, CRC: compact reinforced concrete. UHPC: ultrahigh-performance concrete, NSC: normal strength concrete. HSC: high-strength concrete, DUCON: ductile concrete, VR: high-strength low alloy vanadium reinforcement, NR: normal reinforcement, and SFRC: steel fibre-reinforced concrete.
B: Blast, S: Shock.
DI: Damage Index, PI: Performance Index

2.4 Previous research on seismic behavior of beam-column joints

A beam-column joint is defined as the portion of the column within the depth of the deepest beam that frames into the column. Beam-column joints are crucial element in a building as they govern the structural behavior and failure mechanisms under extreme events such as earthquake, blast, and impact. From the past few decades, a significant amount of research has been carried out to study the behavior of RC beam-column sub-assemblies due to gravity as well as seismic loading (Lowes et al. 2003; Park and Paulay 1975; Sarkar et al. 2007; Subramanian 2013; Uma et al. 2006). The functional requirement of a joint, i.e., zone of the junction of beams and columns, is to

facilitate the transfer of stress flow from the primary loading carrying member to the adjacent member. These sub-assemblies should have enough strength and stiffness to withstand the internal force & moment induced by the framing members. A moment-resisting frame can be categorized with three major types of beam-column joints, i.e., interior joint, exterior joint, and corner joint. The further classification of the various beam-column joints with the roof combination is listed in Figure 2.7.

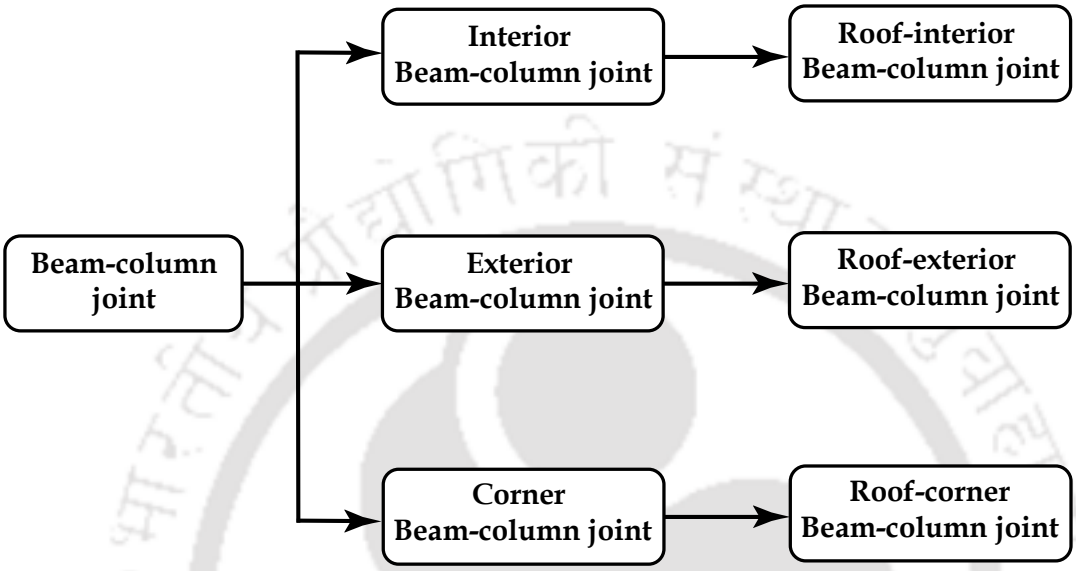

Figure 2.7 Types of Beam-column joint connections

When four beams frames into the vertical faces of a column, the joint is said to be an interior joint. When one beam frames into a vertical face of the column and two other beams frame from perpendicular directions into the joint, then the joint is termed as an exterior joint. When a beam frames to each face of the two adjacent vertical faces of a column, then the joint is called a corner joint (Subramanian 2013). In a roof joint, the columns will not prolong above the joint. When a roof slab is connected with the respective beam-column joint type, then it is said to be roof-interior, roof-exterior, and roof-corner joints, respectively, as shown in Figure 2.8.

Beam-column joints are the principle structural elements as their constituent materials have limited strengths and force-carrying capacity. When these joints are exposed to forces greater than their capacities, during extreme loading conditions, i.e., earthquakes, blast, and wind, these joints are extremely damaged, and repairing such damaged joints is challenging. Therefore, beam-column sub-assemblies must be designed to withstand events like earthquake effects. From past assessments of failed RC buildings due to earthquake events, it is well known that most of the catastrophic failure can be attributed to failure of beam-column joints (Saatcioglu et al. 2001; Sezen et al. 2000).

Under lateral loads, the principle mechanisms of failure of a beam-column joint are: i) shear failure within the joint; ii) anchorage failure of rebars, and iii) bond failure of the beam or column rebars (ACI-ASCE Committee 352: 2010 and, IS 13920:2016).

Structures subjected to earthquake loading undergo large inelastic deformations and require adequate ductility to dissipate energy (MacGregor et al. 1997; Park and Paulay 1975). The ductility of the RC structural member was enhanced by additional detailing and confinement of the concrete with transverse reinforcement (Park and Paulay 1975).

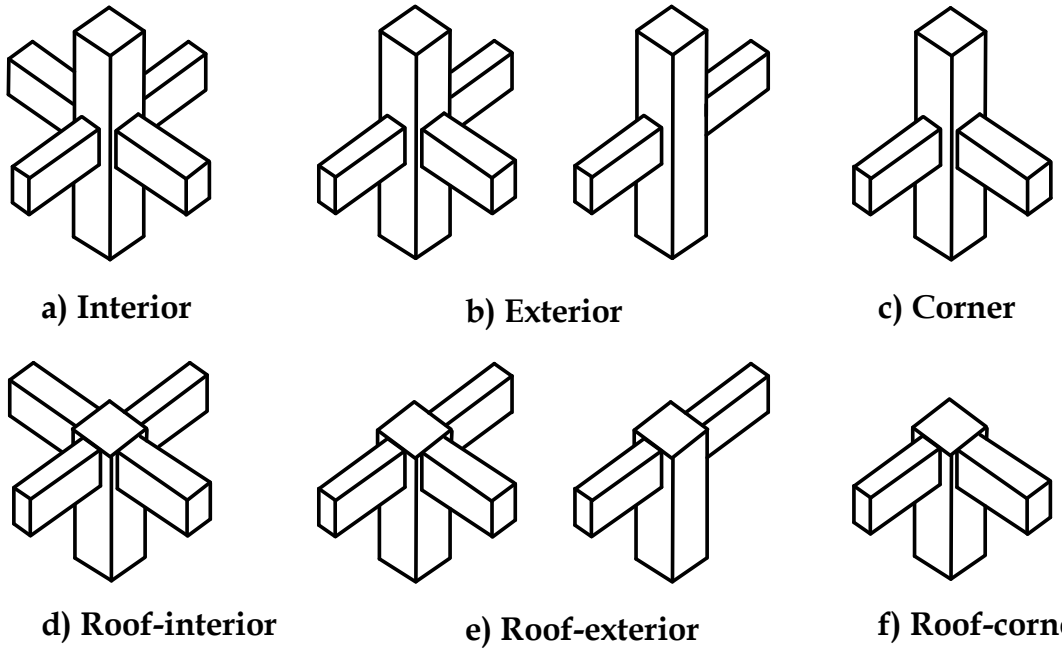

Figure 2.8 Schematic diagram of beam-column joint connections

For the low seismic regions, RC moment-resisting frames (MRF) are primarily designed to resist gravity loads. For RC-MRF under gravity loading, demands for flexure and shear are higher at the internal beam-column connections. As such, the detailing and anchorage of internal beam-column connections must be superior to external connections. Also, internal connections are laterally confined in both directions by their neighbouring joints. On the contrary, the external beam-column joints are laterally confined only with two or three beams and are thereby less efficient in resisting lateral loads. The behavior of an external beam-column joint has been studied under quasi-static lateral loading (0.025 Hz - 2 Hz). Due to inadequate confinement, external beam-column joints are vulnerable to damage under lateral loads, which may arise from an earthquake, impact, shock, and blast. Moreover, existing reinforced concrete buildings are mainly designed for gravity loads and which are typically built in seismic prone countries before the introduction of suitable seismic design provisions and the implementation of capacity design concepts. From the literature studies, it was confirmed that the expected inherent weakness of these systems is observed in the past earthquake events and terrorist attacks.

Pantelides et al. (2002) tested one-way exterior beam-column joint under reversal cyclic loading. They analyzed and computed the beam-column joint response quantities. The typical reinforced frame buildings were designed according to ACI 318-63 (Committee and Standardization 2008), which was developed before the incorporation of seismic guidelines. They built the specimens at a reduced half scale

with an increased reinforcement ratio of the beam to ensure the shear failure of the beam-column assembly. The specimen possesses multiple seismic deficiencies such as poor anchorage of beam longitudinal reinforcement bars in the joint core, lack of transverse reinforcement bars in the joint core, poor column lap slice length and insufficient confining reinforcement in beam and column. The test specimen geometry and reinforcement details were shown in Figure 2.9. The compressive strength and yield strengths of the beam, column, and ties were reported as 46.2 MPa, 454.4, 469.5, and 427.5 MPa respectively.

The experimental setup of the cyclic loading actuator is shown in Figure 2.10. The column was fixed horizontally and roller-support at both the ends. The column was axially loaded equal to $0.1f'_cA_g$ with four threaded DWYDAG bars, and this force was set to the throughout the experiments. The deviations in axial load were measured using strain gauges attached to each rod. The beam end was subjected to the cyclic loading with the help of loading collar, as shown in Figure 2.10. For every load step, three-push and pull cycles were performed.

Initially, the first nine steps were guided through the force control by increasing 22 kN increments until the first yield of reinforcements occurred. Later, the experiment was continued by the displacement control method until the lateral load drops below 50 % of the peak value. The observed failure mode in the joint panel was predominantly a shear failure. The first yield point of longitudinal reinforcement bar occurred at approximately half of the ultimate capacity of the joint. They noticed the hairline cracks in the beam and the joint panel during initial cycles, which lead to severe joint shear cracks and further propagated into the column after reaching the maximum beam end force. Concrete spalling occurred in the joint and the back surface of the column and demonstrated the strength degradation at higher displacement levels.

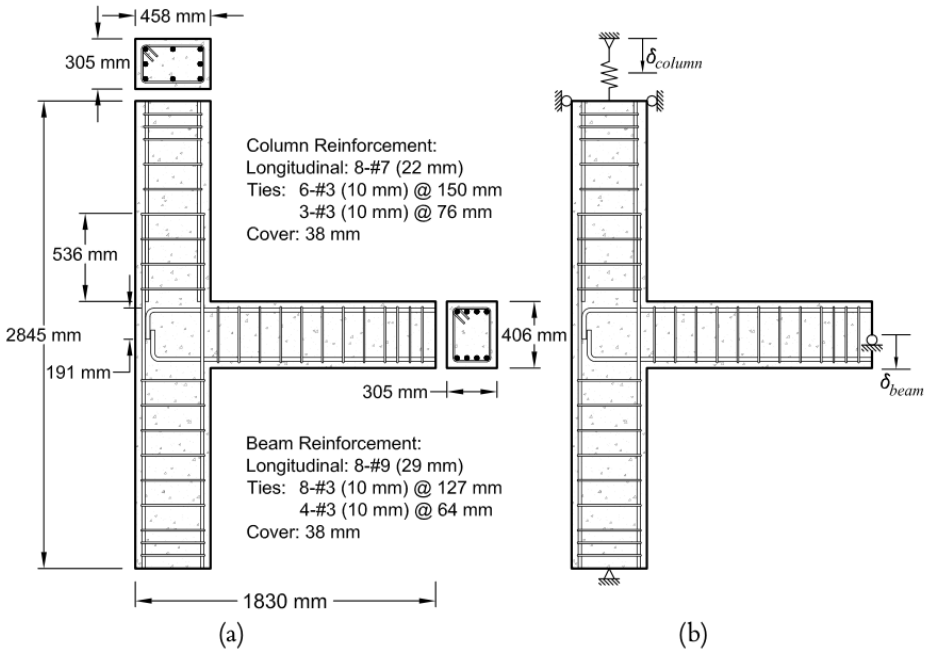

Figure 2.9 Joint Geometry and Idealized Boundary Conditions (Pantelides et al. 2002)

Deaton (2013) conducted numerical analyses of reinforced concrete beam-column joints subjected to cyclic loads, employing a nonlinear finite element analysis software DIANA. They validated the numerical results with the experimental study conducted by Pantelides et al. (2002) and proved that their proto-model reproduced the hysteretic characteristics and failure mechanism with a good agreement. The method of load application and boundary conditions vary among the previous work on beam-column joint experiments. In few cases, the column top was cycled laterally, and the beam end is roller-supported whereas in other cases, the column was laterally supported at top and bottom and the beam was laterally cycled under displacement control. They analyzed both the classifications in their numerical work.

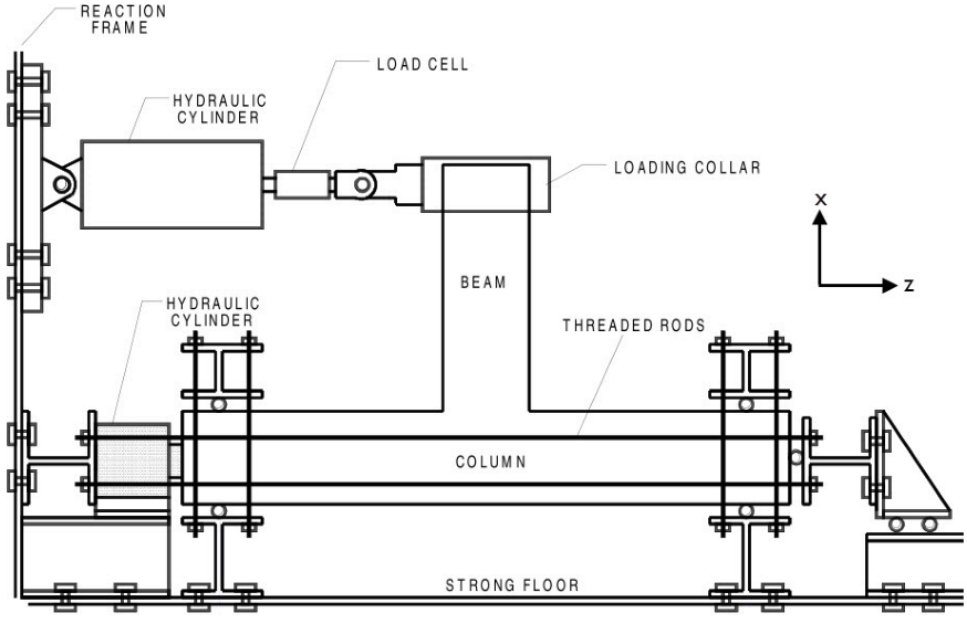

Figure 2.10 Representative schematic of experimental Setup with beam-column joint (Pantelides et al. 2002)

Story drift

When simulating the experiments under lateral, cyclic, and displacement controlled loading was applied to the top of the column, the obtained force-displacement response is represented in terms of story drift, calculated from the ratio of the lateral column tip displacement (δ_{col}) to the unsupported length of the column (l_{col}) as shown in Figure 2.9(a). Likewise, when the loading was applied to the beam end, the force-displacement response is represented in terms of beam displacement ratio, calculated from the ratio of the vertical beam tip displacement (δ_{beam}) to the centerline length of the beam actuator to the centerline of the column (l_{beam}) as shown in Figure 2.9(b).

Stiffness degradation

Stiffness degradation was estimated based on the each-cycle from peak to peak stiffness (K_{pp}). The peak to peak stiffness is defined as the slope of the line connecting the points of maximum and minimum force in the force-displacement history for a given cycle *n*, shown in Figure 2.11 and calculated as

$$K_{pp_n} = \frac{F_{max_n} - F_{min_n}}{XF_{max_n} - XF_{min_n}} \quad (2.1)$$

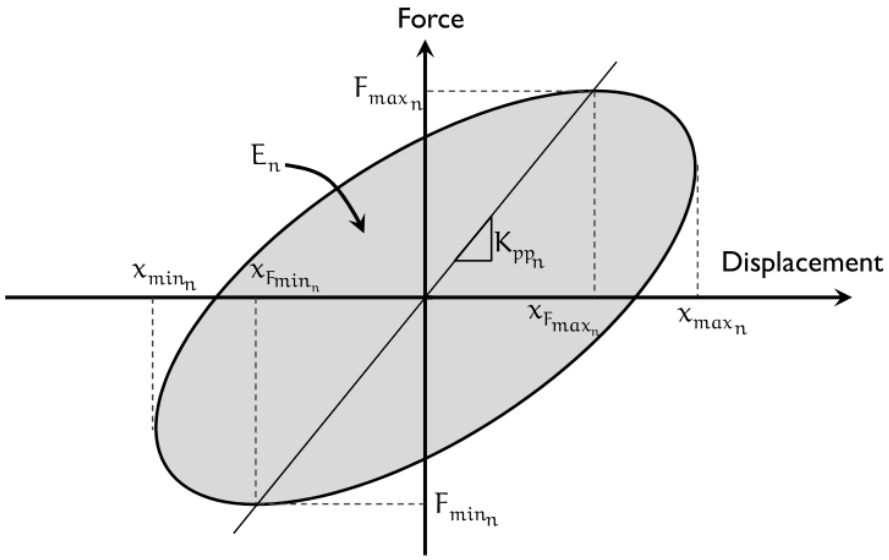

Figure 2.11 Metrics for force-displacement cycle 'n' (Pantelides et al. 2002)

Energy dissipation

The incremental energy dissipation was estimated by calculating the enclosed area by the force-displacement behavior per cycle *n,* represented by E_n and also illustrated in Figure 2.11. The cumulative energy dissipation (E_{cum_n}) was calculated as the integration of E_n overall cycles 1,… *n*, including the contribution of beams in both x and y directions for the beam-column joint specimens. Thus the estimated value of E_{cum_n} corresponding to the final cycle of the analysis characterizes the total dissipated energy during the numerical analysis of the experiment.

Joint shear stress

The average shear stress on a horizontal plane at the mid-height of the joint is termed as joint shear stress. This joint shear failure occurs when the shear stress reaches the maximum level, and it varies with or without adjacent beam yielding conditions. Most of the experimental literature states that the joint shear failure often results from the compressive fracture of the joint core, which occurs due to shear cracking. Based on the obtained external reactions at the column and beam ends, the joint shear can be determined (MacGregor et al. 1997). The equilibrium of the beam-column subassembly and the equilibrium of the joint panel is shown in Figure 2.12.

The beam end force (V_b) induces a moment at the column face equal to $V_b.l_b$, which can be substituted by the statically equivalent force-couple represented by the equal forces C_b and T_b at a distance of j_d, i.e.,

$$C_b = T_b = \frac{V_b.l_b}{j_d} \quad (2.2)$$

In the above equation, the internal moment arm j_d was assumed as with a constant factor 0.875 of the effective depth (d). Therefore, the horizontal shear force at the mid-height of the joint subassembly can be represented as

$$V_{jh} = C_b - V_c \tag{2.3}$$

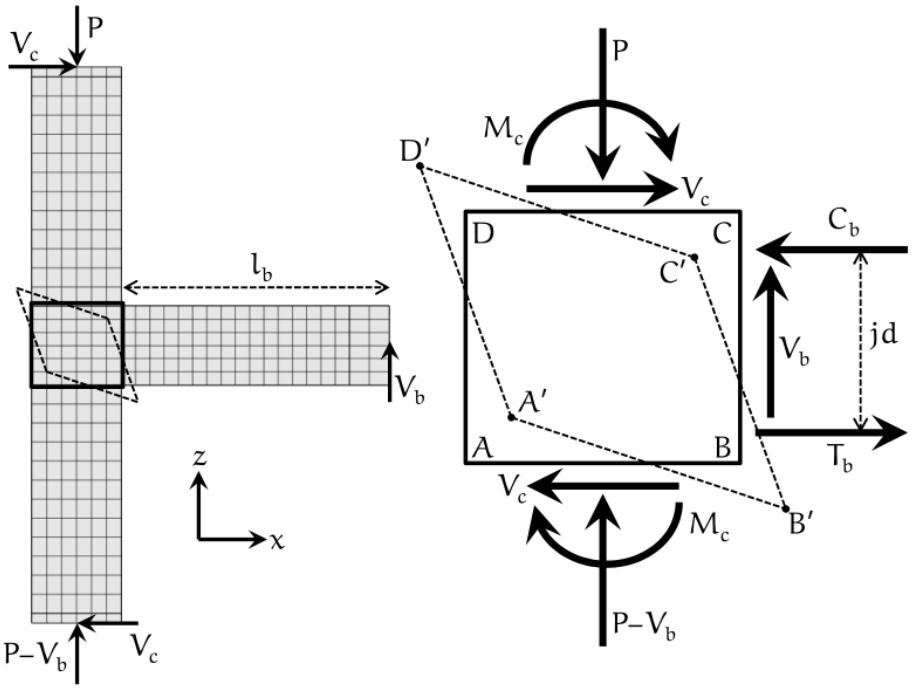

Figure 2.12 Representative schematic of joint panel equilibrium and distortion (Pantelides et al. 2002)

The joint shear stress can be obtained by dividing the joint shear force by the area of the joint mid plane cross-section as

$$\tau_{jh} = \frac{V_{jh}}{h_b . h_c} \tag{2.4}$$

where, h_b = beam height, h_c = column width

The joint shear stress is usually normalized by the square root of the compressive strength of the concrete and represented as

$$\tau'_{jh} = \frac{\tau_{jh}}{\sqrt{f'_c}} \tag{2.5}$$

Joint shear distortion

The joint shear distortion can be estimated from the displacements obtained from the four corners ABCD of the joint panel face, as illustrated in Figure 2.12. The average shear distortion in the deformed configuration ABCD is determined from the average of the change in the angle at each corner, i.e.,

$$\gamma_{ave} = \frac{\Delta\angle ABC - \Delta\angle BCD + \Delta\angle CDA - \Delta\angle DAB}{4} \quad (2.6)$$

The experimental response of the joint shear distortion is highly sensitive depending on the LVDT arrangement which may conflict with the localized spalling or cracking of concrete in the joint region. However, the simulated model may not capture concrete behavior explicitly since the concrete strength was minimized due to the corresponding occurred damage. There will be uncertainties between the experimental and simulated joint shear distortion.

Visualization of crack patterns

The crack strains (ε_{cr}) of the simulated model (DIANA) from the total strain rotating crack model can be estimated at each element integration point as

$$\varepsilon_{cr} = \varepsilon_{nst} - \frac{\sigma}{E} \quad (2.7)$$

where,

ε_{nst} = principal stress in the crack orientation

$\frac{\sigma}{E}$ = elastic strain

The crack patterns in the beam-column joint were visualized using disc plots. From the graphic visualization, small discs were demonstrated parallel to the plane of crack. During the analysis of plane-stress, a disc plot decomposes to a series of the straight lines, but the disc shape will be more visible when the cracks are not uniformly perpendicular to the axis of the reference. The constitutive model depends on the smear representation of cracks; thus, the crack patterns visuals will appear as bands of distributed cracks and localized crack often seen in the experiments.

Hakuto et al. (2000) conducted a detailed experimental study on reinforced concrete one-way interior and exterior beam-column joints under simulated seismic loading tests. They incorporated the substandard reinforcement in the specimens to replicate the typical buildings that were constructed before the 1970s. Currently, the designers are being challenged more in the performance assessment of the existing reinforced concrete structures, and the retrofitting requirement of those structures. They found a vast literature gap dealing with the experimental investigation of the behavior of structures designed with poor reinforcement details, typically designed before the mid-1970s when subjected to extreme seismic actions. They designed the interior beam-column joint test specimens with an inadequate transverse reinforcement, longitudinal bars, and the joint core connection was anchored poorly. Furthermore, the specimens are retrofitted by jacketing and tested with the same loading protocol. They noticed the enhancement of the ductility in the substandard specimens after retrofitting by jacketing. A detailed seismic assessment of interior beam-column joints without transverse reinforcement and exterior beam-column joint with very little transverse

reinforcement has reported. They demonstrated the improvement in the performance of the beam-column joints replicated with the anchorage details which were constructed before the 1970s with the help of retrofitting. They reported the experimental results of interior and exterior beam-column joints of older structures which were constructed without following the requirement of current codal provisions, i.e., lack of anchorage conditions of longitudinal bars and amount of transverse reinforcement. The obtained test results from these substandard specimens are useful for the performance assessment of older structures when subjected to severe earthquakes. They proposed a retrofitting method to increase the section size of the column to limit the joint shear stress.

Murty et al. (2003) also carried out an experimental study of reinforced concrete exterior beam-column subassemblies subjected to cyclic loading. The representative images showing the experimental setup and load-displacement response of exterior beam-column joints are shown in Figure 2.13. These subassemblies include variations in the anchoring details of the longitudinal beam bars, along with the use of transverse reinforcement in the joint region. They reported detailed experimental results on the effectiveness of different types of longitudinal bars of beam anchorage and transverse joint steel reinforcement in enhancing the seismic capacity of reinforced concrete subassemblies. They noticed the specimens showed a poor energy dissipation and low ductility performance with extreme shear cracks in the core portion of the joint. They found that the ACI 352R-02 (2010) standard hook mechanism for the anchorage of longitudinal bars of the beam and hairclip-type transverse joint steel reinforcement gave good results. They proposed this combination of anchorage mechanism and joint steel reinforcement for the moderate ductility demand situations, i.e., low-rise buildings located in low seismic zones.

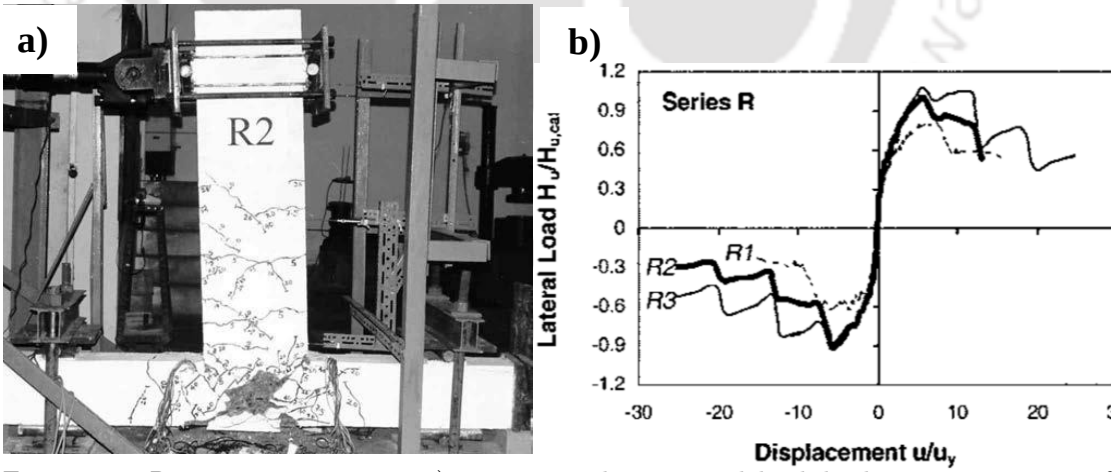

Figure 2.13 Representative image: a) experimental setup, and load-displacement response of exterior beam-column joint (Murty et al. 2003)

Nie et al. (2008) proposed a new configuration in the connection system made with concrete-filled steel tube (CFST) composite column and reinforced concrete beams. In this type of connection system, the steel tube is filled with concrete and is interrupted while the reinforced concrete beams are uninterrupted in the beam-column joint region. To confine the concrete core in the connection zone, they have used multiple lateral

hoops that constitute stiffening rings. They conducted axial compression and reversed cyclic loading experiments on the new beam-column connection system specimens and evaluated load-deflection performance, stress-strain distributions, failure modes, and energy dissipation capacities. The experimental setup and the load-displacement response of interior beam-column joint is shown in Figure 2.14. They investigated the

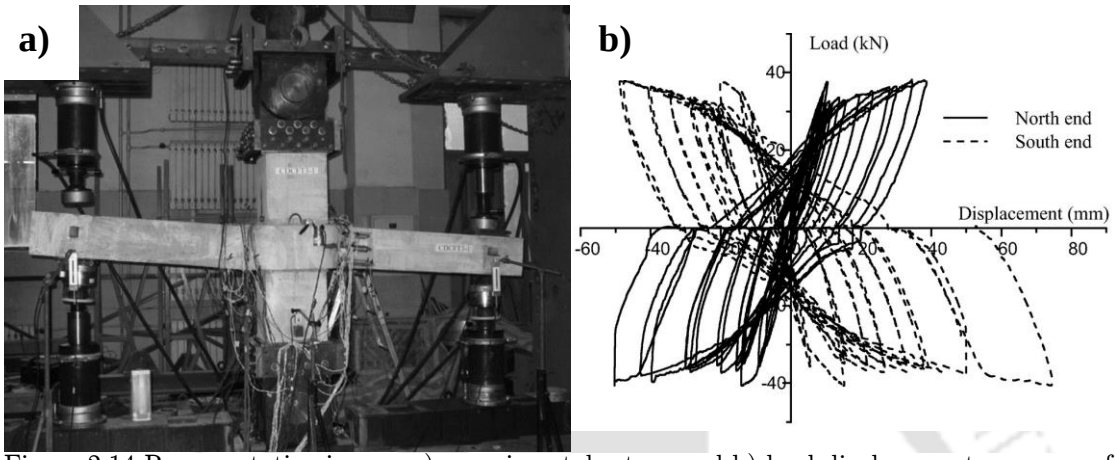

Figure 2.14 Representative image: a) experimental setup, and b) load-displacement response of interior beam-column joint (Nie et al. 2008)

axial load bearing capacity effect due to the variations of the cross-section ratio between the composite CFST column and concrete core confined by the stiffening ring under axial compression loading. The experimental results of the new configuration in the beam-column connection system showed that the provision of effective confinement, i.e., stiffening ring gave a better axial bearing capacity and energy dissipation with superior ductility. They suggested this new connection system for the CFST composite column with reinforced concrete beams as well as for the other types of confined concrete columns.

Sasmal (2009) conducted a detailed experimental and numerical investigation on deficient beam-column joints subjected to cyclic loading. The finite element mesh adopted in the numerical model and load-displacement response of exterior beam-column joint is shown in Figure 2.15. The test program includes retrofitting and

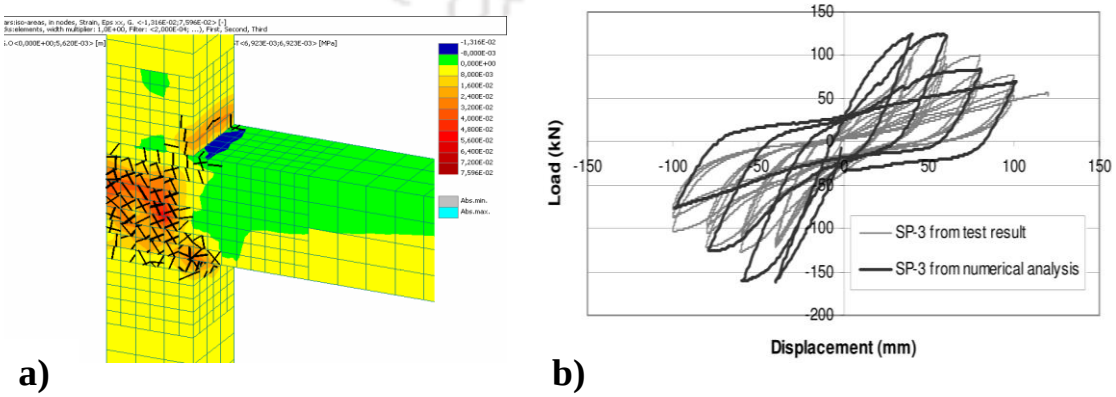

Figure 2.15 Representative image: a) mesh, and b) load-displacement response of exterior beam-column joint (Sasmal 2009)

strengthening of the subassemblies and evaluated for its performance under cyclic loading. The flexural strengthening and retrofitting were carried out by using carbon fiber reinforced plastics (CFRP) fabric and CFRP laminate for the beam-column joints.

They discussed two retrofitting strategies for both non-ductile and ductile structural components. Furthermore, from experimental investigations they evaluated the load-displacement hysteresis, energy dissipation, strength, and stiffness degradation in terms of the performance aspect for both retrofitted and healthy specimens. Using a non-linear finite element analysis ATENA software, the numerical results were validated with experimental values. They presented a comparative study on the energy dissipation values between experimental and numerical studies and were correlated for further practical use. Their studies would provide the aspects of retrofitting and strengthening of deficient structural components and encourages for further research.

Sharma et al. (2011) focused on the seismic performance of various types of beam-column connections in existing non-safety related buildings, i.e., turbine buildings, intake structures, and office buildings. Most of the beam-column joints in the existing constructions had either non-seismic or seismic detailing. With a focus on having a comprehensive overview, they had conducted a series of full-scale experiments on both types, i.e., interior and exterior beam-column joints designed for non-seismic and seismic detailing. They verified the seismic performance of beam-column joints designed for both conforming and non-conforming detailing. The experimental results were compared with the codal recommended values provided by different national standards in terms of strength and ductility aspect. They found that the obtained ductility values are adequate for long period structures, but they are inadequate for short period structures. From the literature studies, it was evident that ductility demand for a particular value of reduction factor considerably increases for a short period structure when compared with long-period structure.

Marthong et al. (2013) worked on the rehabilitation of reinforced concrete exterior beam-column joint using epoxy resin and tested for cyclic loading. The beam-column connections with beam weak in flexure, beam weak in shear, and column weak in shear is quite often scenario in many structures. Therefore, they adopted these all cases of RC beam-column connections subjected to cyclic loading to get comprehensive knowledge about the response of joints. Initially, they conducted the cyclic loading test on all types of beam-column joint, and the damaged joints were rehabilitated using epoxy resin and re-tested for a similar loading to assess the enhanced seismic capacity. They studied the seismic capacity parameters such as stiffness degradation, strength, ductility, and energy dissipation. They found that the rehabilitated connections performed equal or slightly better performance and therefore employing the rehabilitation strategies examined were satisfactory.

Yurdakul and Avsar (2015) conducted experimental studies on the structural repairing of different types of damaged reinforced concrete (RC) beam-column assemblies with carbon fiber reinforced polymer sheets (CFRPs). Based on the damage type and level of damage observed after the earthquake, repairs, and suitable measures

should be adopted for the damaged buildings. Two types of 1:1 scale test specimens designed for Turkish Earthquake Code (TEC 2007) that represent the exterior RC beam-column assemblies taken from inflection points of the frame are considered. The first specimen is well-designed conforming to the Turkish norms, whereas the second specimen characterizes a deficient RC beam-column connection. They incorporated various deficiencies in the form of poor material properties such as low-grade concrete, plain round bars as steel reinforcement and lack of transverse reinforcement in the joint. They tested both types of specimens under cyclic quasi-static loading up to 4% drift ratio and observed the induced level of structural damage. They found that the specimen designed with proper seismic norms exhibits ductile behavior with the concentration of shear and flexural cracks typically in the beam portion. The second specimen was extremely damaged but was almost in their elastic regime. Later these specimens were structurally repaired by wrapping the damaged members with CFRP sheets according to the damage level. They repeated the same experiments on the repaired specimens for the effectiveness of repairing techniques employed for the damaged specimens. They concluded that due to the lack of joint transverse reinforcement in the repaired deficient beam-column joint specimen was exposed to brittle kind of shear failure and affected the seismic performance of the RC structures.

Yurdakul and Avsar (2016) proposed an efficient strengthening method for the substandard reinforced concrete (RC) beam-column joints by external post-tension rods. The substandard RC joints refer to the lack of shear reinforcement in the joint and poor material properties including plain round reinforcement bars, low strength concrete. They tested the joint specimens for cyclic quasi-static loading up to 8% drift ratio for the inspection of various levels of structural damage. Tested specimens were retrofitted by using two post-tension rods that were mounted diagonally at each side of the joint. The healthy specimen exhibits a brittle type of failure behavior along with the shear cracks in the joint regime. Furthermore, a typical joint shear failure was noticed in the retrofitted specimens. They found that the lateral force capacity of the beam-column joints was enhanced up to the codal provision requirements from the proposed retrofitting technique. It provides a feasible solution for on-site construction processes. Based on the truss analogy algorithm, they performed analytical studies and validated the results with experimental values. They suggested that the proposed retrofitting method can be instigated for the exterior, interior subassemblies with floor slab and transverse beams.

De Risi et al. (2016) investigated the seismic performance of unreinforced exterior beam-column joints with deformed bars. They considered two experimental specimens, i.e., unreinforced exterior joints and without transverse beam were tested under cyclic quasi-static loading. These specimens are designed according to the Italy codal provisions (NTC 2008), and design practices followed between the 1970s and 1990s. Their study focuses on the understanding of the experimental assessment of unreinforced exterior joints in the existing reinforced concrete structures. The major contribution is the study the influence of longitudinal reinforcement ratio on the joint

shear strength and the deformability contributions sources to the joint region. The two basic failure modes observed in the experiment are: i) a joint shear failure before the beam yielding (J failure Mode), and ii) a joint shear failure after beam yielding (BJ failure mode). The concerned experimental results were compared with the existing literature on joint shear strength models. The tests presented in work are very valuable in the characterisation of the experimental behavior of unreinforced RC beam-column subassemblies.

Pantelides et al. (2017) presented a study on the seismic performance of reinforced concrete (RC) exterior beam-column joints with substandard details. Majority of the existing buildings have severe structural deficiencies and are substandard as per the current seismic codal provisions. Due to this substandard detailing arises the failure of beam-column joints leadings to the building collapse during strong earthquakes. They conducted a series of experiments on six RC exterior beam-column joints with substandard detailing under quasi-static cyclic loading. They examined the seismic performance in terms of joint shear strength, plastic rotation, residual strength, and strain. Furthermore, they have also studied the bond-slip failure and joint shear failure of substandard specimens. They compared the results of substandard specimens to the current seismic codes: i) lack of transverse reinforcement in the joints categorizes them as non-conforming joints, ii) beam depth to the column reinforcement bar ratio was less than 20, iii) development length of the bottom beam bar was less than the essential length, and iv) column bars exist only on two faces of the joint portion. They found that the joint shear strength of all the test specimens exceeded the performance criteria specified in ASCE 7-05 (2006). However, the joint shear strength was lower than the specified criteria in ACI 352R-02 (2010).

Guan et al. (2018) developed a new precast concrete beam-to-column connection for moment-resisting frames and studied its seismic performance. They conducted cyclic loading experiments on three full-scale beam-column connections. They evaluated the connections seismic performance from the strength, load-displacement hysteresis, ductility, stiffness, hinge formation, and energy dissipation parameters. They observed that there is no combination of anchored reinforcement bars by hook bars that connects the precast members of moment-resisting frames in the existing precast concrete methods. They proposed a new precast concrete beam-column connection system that adopts both longitudinal bars and lap splicing anchoring to attain the beam reinforcement continuity. This continuity or integrity in the beam reinforcement gives a better seismic resistance as well as a monolithic mechanism in the connections. From the experimental results, it was observed that the precast connections has a better seismic performance compared with the monolithic specimen. They proposed the estimation of the plastic hinge length in precast beam-column connections from the models used for monolithic specimens.

Faleschini et al. (2019) conducted the experimental investigation on severely damaged beam-column joints repaired with Fiber Reinforced Polymer (FRP) or Fiber Reinforced Cementitious Matrix (FRCM) composites. Initially, the reinforced concrete

(RC) exterior beam-column joint specimens were tested for significant cyclic loading and resulted in beam-joint failure (B+J), i.e., a shear failure which arose after the longitudinal reinforcement yielding in the beam. Further, the same damaged specimens were repaired using Fiber Reinforced Polymer (FRP) and then tested for a similar cyclic loading history. They studied the experimental behavior for the specimens before repair and after repair in terms of load-displacement hysteresis, shear strength, stiffness deterioration, energy dissipation, ductility, and equivalent viscous damping ratio. The experimental figures of beam-joint (B+J) failure, and the ultrasound pulse velocity contour plot of exterior beam-column joint can be in Figure 2.16. They observed that

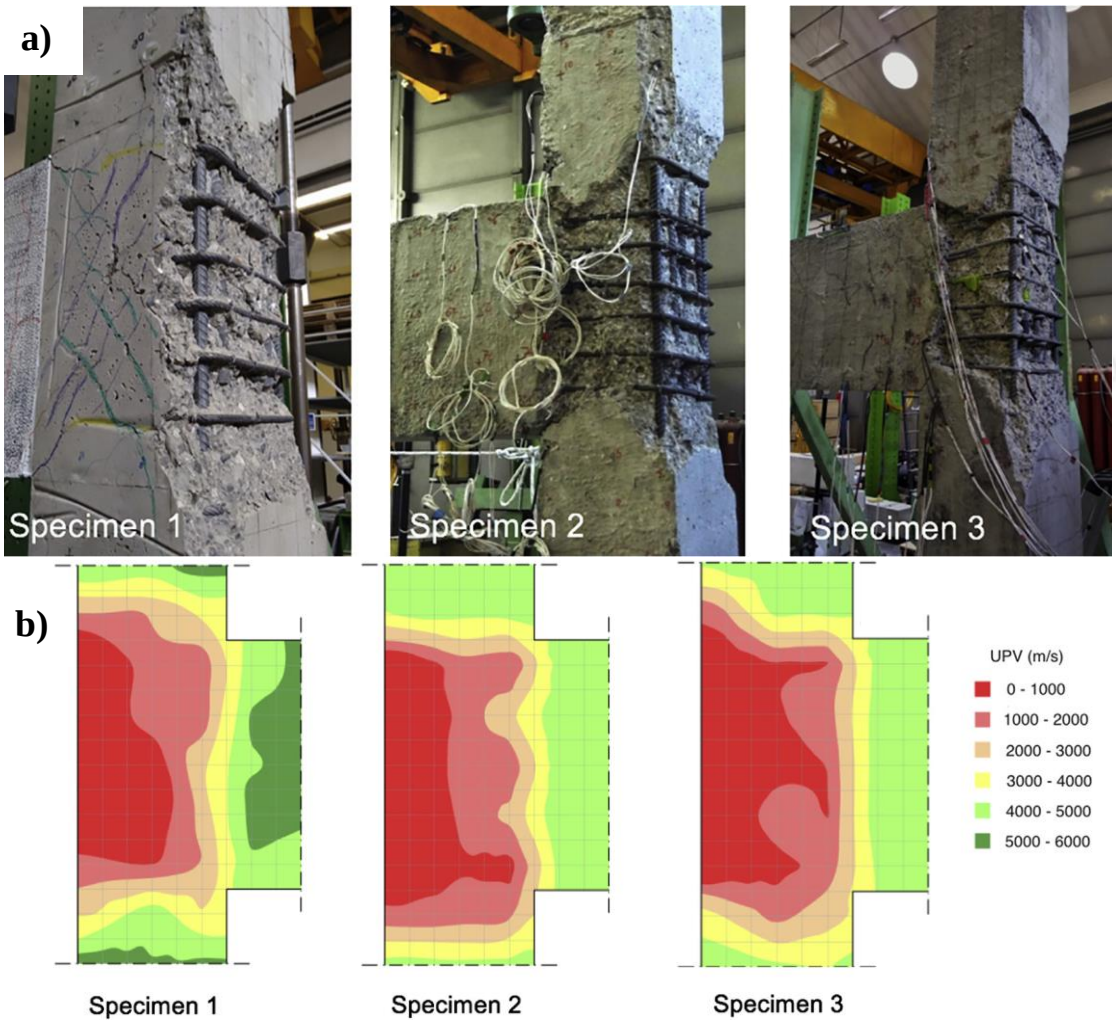

Figure 2.16 Representative image: a) Beam-joint (B+J) failure, and b) ultrasound pulse velocity contour plot of exterior beam-column joint (Faleschini et al. 2019)

the repaired specimens performed a lower initial stiffness compared to the respective original specimens. The load-displacement hysteresis curves of the repaired test specimens were almost similar to that of the original test specimens. Also, the response of the hysteresis curves at the last loading cycles in the repaired specimens was almost close to that of the respective original test specimen. They noticed that the predicted shear strength values by the available models were inconsistent with the experimental

results. They stated that the speculations behind this response are due to the limited experimental database of similar tests that do not include variables such as damage level in the joints and transverse reinforcement ratio. They proposed that further research is much needed to develop and validate the design models for the repaired beam-column joints.

Beam-column joints are critical locations in the building where high plastification occur due to cyclic stress reversal. A comprehensive review of prior efforts on the structural behavior of reinforced beam-column joint has been presented in this section. Since, inelastic response can be seen under the event of seismic load, a brief literatures review has been carried out for beam column joints under seismic loading and summarized in Table 2.3. The review led the identification of research gap on the dynamic response of beam-column joint subjected to blast, shock and impact loading as a critical appraisal from the state of the art.

Table 2.3 Summary of literature review on seismic behavior of beam-column joints

Author	Material	Type of loading	Validation	Remarks
Hakuto et al. (2000)	RC	Seismic	Experimental	Proposed a retrofitting method to increase the section size of the column to limit the joint shear stress.
Pantelides et al. (2002)	RC	Cyclic	Experimental	Observed the various failure mode in the joint panel and further computed the beam-column joint response quantities.
Murty et al. (2003)	RC	Seismic	Experimental	Proposed a typical combination of anchorage mechanism and joint steel reinforcement for the moderate ductility demand situations,
Nie et al. (2008)	CFST	Cyclic	Experimental	Developed a new connection system for the CFST composite column with reinforced concrete beams and confined concrete columns.
Bai et al. (2008)	CFST	Cyclic	Experimental and Analytical	Proposed a theoretical approach to estimate the bearing capacity of confined concrete with multiple transverse hoops.
Sasmal (2009)	RC, CFRP, GFRP	Cyclic	Experimental and Numerical	Provided the aspects of retrofitting and strengthening of deficient structural components.
Sharma et al. (2011)	RC	Cyclic	Experimental	Ductility demand for a particular value of reduction factor considerably increases for a short period structure when compared with long-period structure.

Sasmal et al. (2011)	RC, CFRP, GFRP	Cyclic	Experimental and Numerical	Inadequate wrapping will diminish the energy dissipation and forms plastic hinge in the subassembly.
Deaton (2013)	RC	Cyclic	Numerical	Validated the proto-model with experimental results and reproduced the hysteretic characteristics and failure mechanism.
Ramanjaneyulu et al. (2013)	RC	Cyclic	Experimental	Structures made of gravity load designed (GLD) are susceptible to the medium intensity earthquake.
Marthong et al. (2013)	RC	Cyclic	Experimental	Rehabilitated specimens exhibit lower damage indices when compared to that of the undamaged/healthy specimen.
De Risi et al. (2015)	RC	Cyclic	Experimental	Proposed the capacity models for the seismic assessment of existing ductile and non-ductile RC structures.
Roehm et al. (2015)	NC, SFRC	Seismic	Experimental and Numerical	Proposed a relationship for strength degradation and joint shear deformation for SFRC.
Yurdakul and Avsar (2015)	RC, CFRP	Cyclic	Experimental	Explained the importance of transverse reinforcement for the Structural repairing of different types of damaged reinforced concrete (RC) beam-column assemblies.
Yurdakul and Avsar (2016)	RC	Cyclic	Experimental and Theoretical	Proposed an efficient strengthening method for the substandard reinforced concrete beam-column joints by external post-tension rods.
De Risi et al. (2016)	RC	Seismic	Experimental and Analytical	Proposed the nonlinear models for the seismic assessment of existing non-ductile RC structures.
Ricci et al. (2016)	RC	Seismic	Experimental and Analytical	Seismic performance of unreinforced exterior beam-column joints with plain bars
De Risi et al. (2017)	RC	Seismic	Experimental and Numerical	Proposed a theoretical modeling for nonlinear seismic analysis of RC exterior beam-column joint without transverse reinforcement.
Pantelides et al. (2017)	RC	Seismic	Experimental	Presented a study on the seismic performance of reinforced concrete (RC)

				exterior beam-column joints with substandard details
Guan et al. (2018)	RC	Cyclic	Experimental	Proposed a new precast concrete beam-column connection that adopts both longitudinal bars and lap splicing anchoring to attain the beam reinforcement continuity and achieved better seismic performance.
Faleschini et al. (2019)	RC+ FRP+ FRCM	Cyclic	Experimental	Studied the cyclic loading response of severely damaged beam-column joints repaired with Fiber Reinforced Polymer (FRP).
Saha et al. (2019)	SCC	Seismic	Experimental	Proposed the application of spiral reinforcement stirrups as one of the best alternative technique for the seismic performance.

*RC: reinforced concrete, SCC: self-compacting concrete, CFST: Concrete filled steel tubes, GFRP: glass fiber-reinforced polymer, CFRP: carbon fiber-reinforced polymer, NC: normal concrete, SFRC: steel fibre-reinforced concrete, FRP: fiber-reinforced polymer, FRCM: fiber reinforced cementitious matrix.

2.5 Previous research on impulse loading on honeycomb protected structures

The beam-column joint is the weakest link in the structure and is often strategic location for inducing the maximum damage. Therefore, it is of prime importance to protect the external beam-column joint against threat arising from missiles and windborne debris resulting from tornadoes and hurricanes. In order to protect the structures against impact loadings, a sacrificial protective cladding comprises of hybrid composites are attached on the building façade. Towards this research goal, a detailed literature review of impact dynamics and contact law of projectiles impacting on hybrid composites are reported. These hybrid composites include honeycomb structures, metallic foams, and polyurethane foam. In this section, the fundamental concepts of impact dynamics and contact law are discussed that govern the behavior of structure subjected to impact load. A flowchart showing the different subsections covered in this module is shown in Figure 2.17.

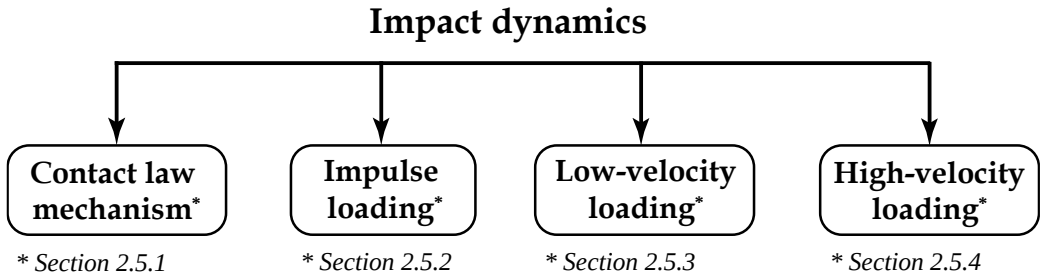

Figure 2.17 Overview of impulse loading literature review of honeycomb structures

2.5.1 Impact dynamics and contact law

When two granular particles are in contact with each other under no external loading, the initial contact established between their surfaces is the point of contact (or likely a line contact). Hertz (1881) published the first article on contact mechanics between solid elastic bodies that describes the local elastic deformation relation between two spherical particles. Hertz's law is widely used in diversified fields of contact mechanics, such as for bearings, metal forming, wheel-rail contact, gasket seals, etc. Hertz (1881) has studied two identical spherical particles of radius 'R' assuming that both particles are topographically smooth on macro and micro scales, such that the elastic wave's motion in the particle can be ignored and the tangential surface interaction between the particles is frictionless.

A schematic view of two particles in contact under compressive force 'F' is shown in Figure 2.18 a. The typical force-displacement curve during interaction of granular chain is shown in Figure 2.18 b. When these particles are compressed against each other towards the contact point 'O', the relative approach between the distant points of two particles is given as $\delta = \delta_1 + \delta_2$, where δ_1, δ_2 represents the displacement of distant point for particles 1 and 2, respectively. Here, $\delta > 0$ for compression and $\delta < 0$ for tension and the particles deform locally at the point of contact 'O' and form a circular contact area. Since the material has a characteristic property to regain its original shape, a resisting force is developed between the two particles. It is assumed that the radii of curvatures of the contacting particles are large as compared to radius of the contact circle, which results in less displacement. The problem is also considered as elasto-static, i.e. the material interaction is linear elastic, and the two particles are in static equilibrium such that the displacement is independent of time.

Based on these assumptions, the generalized interaction force derived by Hertz for two particles is given as (Johnson and Johnson 1987).

$$F = \begin{cases} k\delta^{3/2} & ;\delta \geq 0 \\ 0 & ;\delta \leq 0 \end{cases} \tag{2.8}$$

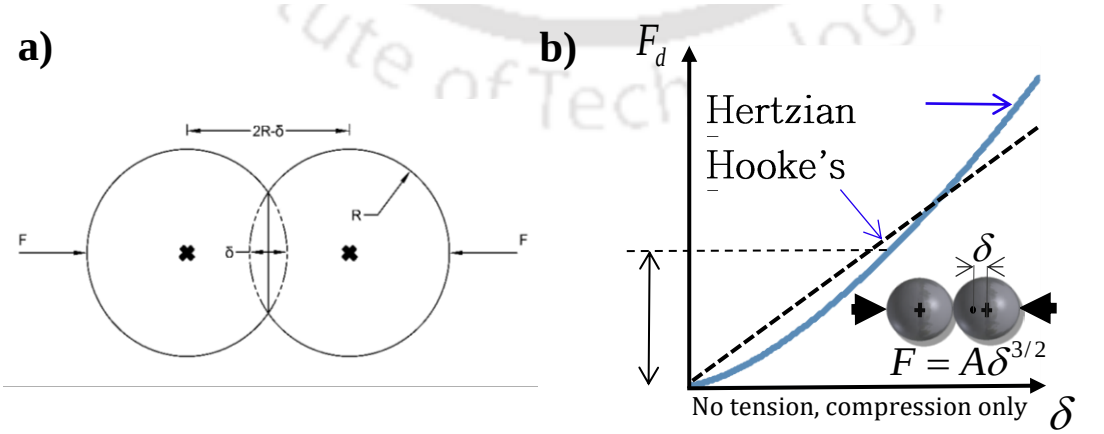

Figure 2.18 Schematic diagram: a) two spherical bodies in contact, and b) force-displacement plot with Hertzian law

The compressive force (F) between the two granular particles is considered zero in tension $(\delta < 0)$ and positive in compression $(\delta > 0)$. During the compression process, the force is initially weak as compared to linear or harmonic spring force for small values of 'δ', and it rises sharply when the 'δ' value is increased as compared to the linear spring force. Therefore, the interaction force in the Hertz model is proportional to the $\delta^{3/2}$, which is a nonlinear contact interaction behavior between two spherical particles that results from the consideration of geometrical effects only. Further, its proportionality relation depends on the two particles contact geometry. Spence (1975) developed a detailed generalization of the Hertz contact law that describes the interaction of two particles of arbitrary axisymmetric contact surface. They calculated the stress distribution and the contact area of overlap between the two particles to determine the interaction force between the particles.

i) For spherical bodies

The Hertzian contact stiffness between two spherical interacting bodies is given as

$$k = \frac{2E\sqrt{r}}{3(1-\mu^2)} \tag{2.9}$$

where, $\mu =$ poisons ratio of spherical striker and r is the equivalent radius.

$$\frac{1}{r} = \frac{1}{r_1} + \frac{1}{r_2} \tag{2.10}$$

ii) For cylindrical bodies in contact

The contact area generated by compressing two cylindrical surfaces against each other depends on the orientation angle (α) between the axes of the two cylinders. For small deformations, this could result in a circular contact area $(\alpha = 90^{o})$.

Let the total displacement of two cylindrical particles under compression is denoted by 'δ'. The relation between the contact force 'F'and the displacement 'δ' is given by Khatri et al. (2012)

$$F = k_{cyl}\delta^{3/2} = \frac{4}{3}\frac{\sqrt{\mathrm{R}_e}E^*}{F_2^{3/2}}\delta^{3/2} \tag{2.11}$$

where,

'R_e' is an equivalent radius

$$\mathrm{R}_e = \frac{\mathrm{R}}{\sin\alpha} \tag{2.12}$$

'E^*' is an effective elastic modulus

$$E^* = \frac{E}{2(1-\mu^2)} \tag{2.13}$$

iii) Spherical striker impacting rigid surface

The interaction behavior of spherical impactor on the rigid plate is similar to the interaction of two spherical impactors with an exception that for one surface, the radius of curvature is infinite.

The effective stiffness (k_o) between the spherical striker and rigid surface is given by Szuladzinski (2009)

$$\frac{1}{k_o} = \frac{3}{2}\left(\frac{1-\vartheta^2}{E}\right)\sqrt{\frac{2}{r_2}} \tag{2.14}$$

The maximum deflection (δ_m) of the spherical striker is a function of mass and velocity of striker and contact stiffness.

$$\delta_m = \left(\frac{5Mv_o^{\ 2}}{2k_0}\right)^{0.4} \tag{2.15}$$

The contact time (t_o) of the impact interaction is given as

$$t_o = \frac{3.214}{(2v_o)^{0.2}}\left(\frac{M}{2k_o}\right)^{0.4} \tag{2.16}$$

The contact radius (a) during interaction of striker with the rigid surface is given as

$$a = \left(\frac{5Mv_o^{\ 2}}{2k_o}\right)^{0.2}\sqrt{r_2} \tag{2.17}$$

a = contact radius in mm

M =mass of the spherical striker in gm

E =modulus of elasticity of spherical striker in MPa

μ = poisons ration of spherical striker

v_0 =velocity of spherical striker m/s

r_2 = radius of spherical striker mm

iv) Spherical striker impacting an elastic surface

Figure 2.19 shows the spherical striker impacting on an elastic surface considered the plane surface as semi-infinite mass. The thickness of plate doesn't affect the interaction between the spherical impactor and plate. When the thick plate was used,

and its thickness reduces below a certain range, it significantly affects the interaction of the impactor and the plate.

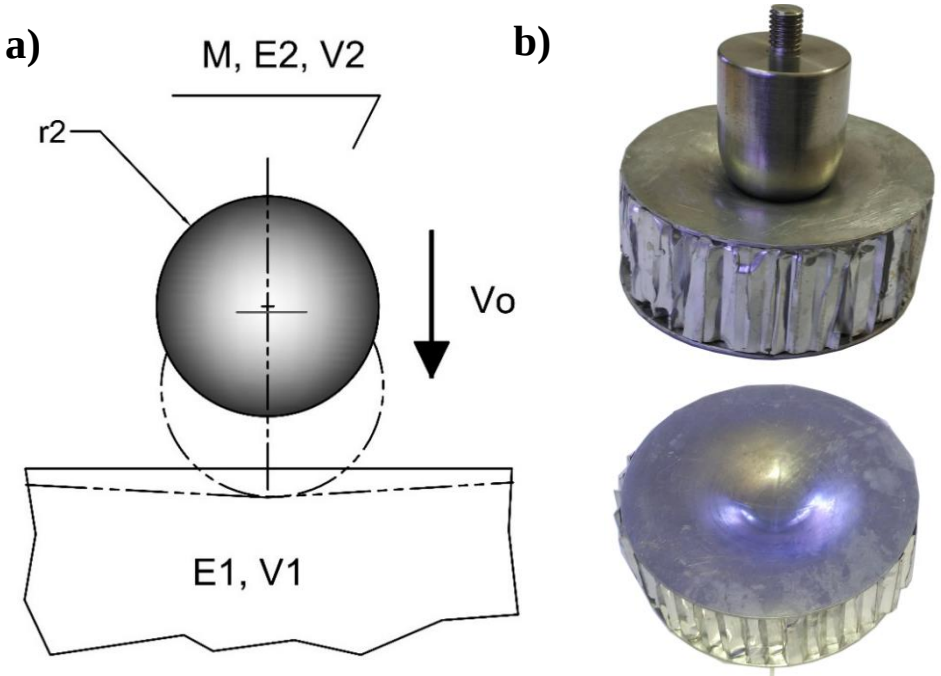

Figure 2.19 a) Spherical ball impacting on elastic surface, and b) Deformed contour of honeycomb panel subjected to spherical ball impact

The contact stiffness (k_o), between the spherical striker and elastic surface is given as

$$\frac{1}{k_o} = \frac{3}{4}\left(\frac{1-\nu^2}{E_1} + \frac{1-\nu^2}{E_2}\right)\frac{1}{\sqrt{r_2}} \tag{2.18}$$

The contact time between interaction of striker and elastic surface is given as

$$t_0 = \frac{3.214}{v_o^{0.2}}\left(\frac{M}{k_o}\right)^{0.4} \tag{2.19}$$

Peak surface contact stress (σ_{cm})

$$\sigma_{cm} = 0.499\frac{M^{0.2}}{r_2}k_o^{0.8}v_o^{0.4} \tag{2.20}$$

Peak surface tension (σ_{tm})

$$\sigma_{tm} = \frac{1-2\nu}{3}\sigma_{cm} \tag{2.21}$$

where, μ_1, μ_2 are the poisons ratio of spherical bodies and elastic surface.

E_1, E_2 are the modulus of elasticity in MPa.

The above fundamental concepts are employed to understand the interaction of impacting body on elastic substrate. Based, on the impact dynamics, literature review of theoretical aspect of low-velocity and high-velocity impact on composite material is conducted.

2.5.2 Impulse response of honeycomb composite

The recent innovations and advancements in the structural materials such as composites and honeycomb sandwich constructions have entirely revolutionized the materials industry. Honeycomb sandwich structures increasingly used in the aerospace industry due to their low weight to high stiffness ratio. The honeycomb core is considerably stiff in out of plane direction compared to in-plane direction. Honeycomb sandwich structure possesses high specific stiffness and can minimize the vibrations, sound, retard fire, besides consisting extremely low-density material. Furthermore, it does not require a large area which lightens stress concentration and thus enhances the fatigue strength. Honeycomb sandwich structures are also used to mitigate the effect of impact and shock loads because of their high energy absorbing capacity. Efforts have been made by researchers to increase the energy absorption capacity of honeycomb sandwich structures by modifying the topology of panels. The objective of this section is to present the comprehensive literature review on the honeycomb composites and to discuss the vital issues validated by the researchers.

Wierzbicki (1983) proposed a theory that describes the crushing behaviour of thin-walled structures using an energy balance approach. It shows that the two-thirds of the plastic energy was dissipated through large deformations in static and dynamic plastic hinge lines. These large deformations are consistent with small sections of shell surface, but they consider the remaining one-third of the dissipated energy.

Klintworth and Stronge (1988) developed a quasi-static model incorporating nonlinear contact interaction. It was based on the energy balance equation to predict the maximum contact force, displacement, and indentation of the sandwich panel. Klintworth and Stronge (1989) presented stress and deformation of the honeycomb structure with a flat punching indentor. After reaching the materials elastic deformation, honeycomb crushes in a thin band in their characteristic directions. Under flat punch, yield strength of honeycomb deformation gets localized in a thin band of crushing cell.

Anderson and Madenci (2000) conducted analytical and experimental research regarding the behavior of graphite/epoxy foam sandwich panels under quasi-static indentation with a rigid spherical indentor. They developed a three-dimensional analytical solution method to evaluate the stress, contact pressure, and displacement fields in sandwich panel arisen by the quasi-static indentation by a rigid sphere. Most of the previous analytical studies were developed by the usual assumption of a Hertzian type contact pressure distribution. The unknown contact area of sphere and pressure distribution due to the indentation attained as a part of the solution by using an iterative solution method which leads to the contact force-indentation. Quantifying the

indentation contact area and pressure distribution in the experiments is challenging as no measuring devices are available to overcome it. They presented an analytical model that provides the three-dimensional stress and displacement along with the contact area and pressure for a composite panel indented by a rigid sphere. For the accuracy verification, a series of quasi-static indentation tests were conducted on graphite/epoxy foam sandwich panels with a different combination of material properties, core, and facesheet. They confirmed the proposed analytical model by comparing the measured force-indentation and predicted values. The validated analytical predictions with experimental indentation results are found to be in remarkable agreement.

Hazizan and Cantwell (2003) conducted the indentation test and shear tests on two Aluminum honeycomb sandwich structures to study strain rate sensitivity. They observed that the flexural modulus of the facesheets and shear modulus of Aluminum honeycomb core failed to exhibit strain rate sensitivity at low-velocity impact. A series of static and dynamic three-point bending tests were conducted on Aluminum foam sandwich panels (Crupi and Montanini 2007). It was found that impact velocity under 1.2 m/s failed to exhibit strain rate sensitivity.

Olsson et al. (2006) derived the delamination threshold load criterion for the transversely isotropic plates subjected to small mass with high-velocity impact. They employed a closed-form approximation for the prediction of peak impact load and delamination threshold velocity. They focused on deriving the delamination threshold load for small mass with high-velocity impact for transversely isotropic plates that were regularly distributed laminates in at least three directions. The quasi-static impact experiments show that the delamination growth in the panel occurs with a rapid decrease in load. They found that the parameters like thickness, contact stiffness play a vital role in predicting the delamination threshold velocity. They considered a hemispherical impactor indenting on a thick isotropic elastic plate having thickness (h) with contact load (F).

A first-order approximation for the approach (α) between the impactor and the plate under small curvature was derived by Suemasu et al. (1994),

$$\alpha = \left(\frac{F}{k_H^*} \right)^{2/3} \tag{2.22}$$

$$\alpha = \left(\frac{F}{k_H^*} \right)^{2/3} \tag{2.23}$$

where,

$$k_H^* = \frac{k_H}{\left(1 - \ln 2F^{1/3} k_H^{2/3} K_0 / h\right)^{3/2}}$$

They validated the theoretical model for a wide range of tests with 3D finite element model simulated using commercial package LS DYNA. They showed the anticipated

delamination threshold loads, and velocities are in excellent agreement with experimental and numerical results.

Zhou and Stronge (2006) proposed an analytical model for lightweight circular sandwich panels subjected to low-velocity impact. They studied the damage mechanism and impact response of Hybrid Stainless Steel Assembly (HSSA) lightweight sandwich panel with simply supported boundary conditions. A representative schematic of spherical ball striking at the center of the sandwich panel and its insight view of indentation is shown in Figure 2.20. They arrived a localized indentation law based on the assumption that the facesheets remain elastic and the core is rigid-perfectly plastic under quasi-static compression. It was evident that the low-velocity impact by a small mass exhibits residual dent without perforation of fibrous core sandwich panel which has thin facesheets. The dent of the facesheet mainly depends on the kinetic energy and the nose shape of the impactor as well as the mass density of the sandwich panel. They conducted a series of impact experiments on fibrous core sandwich panels with varying sizes impacted by the spherical bodies at low velocities. Further, a detailed numerical investigation was conducted using finite element analysis to estimate the impact damage on HSSA lightweight sandwich panels. It was observed that the damage depends on both the structural parameters of the panel and impact variables. They developed a contact relation for the lightweight sandwich panel that incorporates the effect of local membrane stretching of top facesheets. For the cases where the indentation depth on the top facesheet is lesser than that of the core thickness, the force indentation relation varies linearly. Based on the contact relation, they proposed the analytical models for the quasi-static and dynamic behavior of the sandwich panels to evaluate the impact force when subjected to low-velocity impact on sandwich panels.

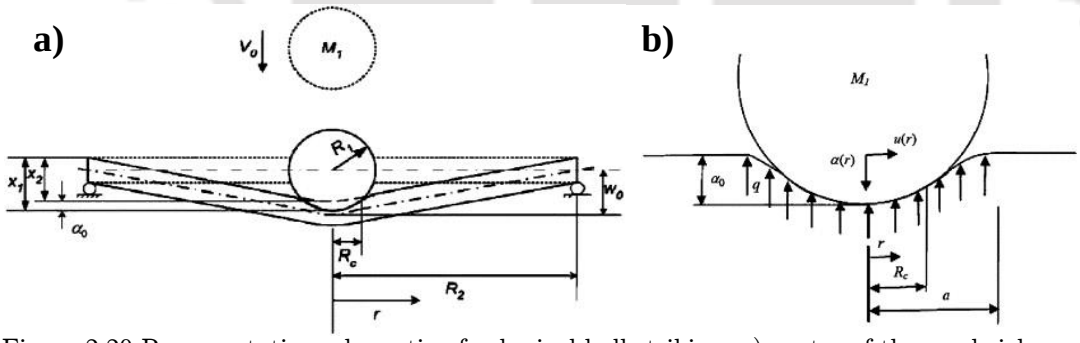

Figure 2.20 Representative schematic of spherical ball striking: a) center of the sandwich panel, and b) insight view of indentation (Zhou and Stronge 2006)

From the Figure 2.20, the profile of the local indentation of the upper facesheet can be characterized by,

$$\alpha(r)=\alpha_0\left(1-\frac{r^2}{a^2}\right)^2 \tag{2.24}$$

where,

'α_0' is the central transverse deflection

'a' is the radius of the local indentation region on the upper facesheet

Thus, the total potential energy can be given as,

$$\Pi = V_1 + V_2 + U_1 + U_2 \tag{2.25}$$

where,

'V_1' is flexible strain bending energy

'V_2' is strain energy due to membrane stretching

'U_1' is the work done by crushing force

'U_2' is the work done by the contact force

In order to obtain the contact force, the total potential energy is minimized with respect to the central deflection, i.e., $\partial\Pi/\partial\alpha_0 = 0$

$$P = \frac{64\pi D_f \alpha_0}{3a^2}\left[1 + \frac{\alpha_0{}^2(7505 + 4250v - 2791v^2)}{17640h_f^2}\right] + \frac{\pi q a^2}{3} \tag{2.26}$$

where,

'D_f' is the diameter of the facesheet

'h_f' is the facesheet thickness

'q' is the yield stress of the core

'P' is the contact force

'v' is Poisson's ratio

Jen and Chang (2008) conducted an experimental study on the four-point bending test of honeycomb sandwich beams with varying core densities. They evaluated the bending fatigue strengths of Aluminum honeycomb sandwich beams. The representative image of debonding failure mode of the specimen under four-point cyclic bending can be seen in Figure 2.21. They considered numerous local and global parameters for the evaluation of fatigue life of sandwich beams under cyclic four-point bending. The primary failure was identified as the debonding of the adhesive between the facesheet and the core. A finite element approach was employed by considering the geometry and dimensions of the adhesive to obtain the local stress and strain. They identified that the predicted locations of debonding initiations using circular-shaped combined interfacial stress parameters were identical with the observed fatigue experiments. Furthermore, there is a lack of systematic research on the fatigue strength of Aluminum honeycomb sandwich beams, and they conducted the experimental study on bending fatigue characteristics of Aluminum honeycomb sandwich beam. They observed that the failure mode of the honeycomb sandwich beam subjected to cyclic bending was debonded between the facesheet and the adhesive. The parameters such as global shear stress and bending stress failed to correlate with the fatigue strength of different types of test specimens due to the global parameter's failure mechanism. They

focused on finding a suitable parameter to correlate with the fatigue strength data of the sandwich beams. The obtained local parameters from the interfacial stress demonstrated a better correlation with the fatigue strength data than the global parameters. They found that the local parameters based on the exhibited failure mechanism predicted the fatigue strength more accurately.

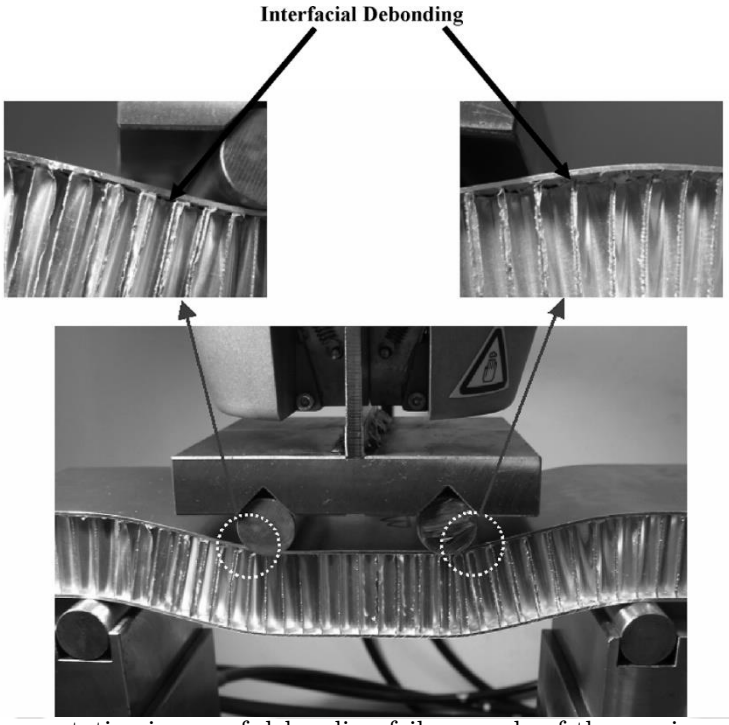

Figure 2.21 Representative image of debonding failure mode of the specimen under four-point cyclic bending (Jen and Chang 2008)

2.5.3 Low-velocity impact studies on sandwich structures

The low-velocity impact refers to velocities leading to a transient response with contact time larger than one-third of the natural period of vibration of the system (Olsson et al. 2006). The representative schematic of response types during impact on plates for the very short impact times, short impact times, and long impact times is illustrated in Figure 2.22. Goldsmith and Sackman (1992) investigated energy-absorbing modes in the honeycomb panels due to core crushing, bending, and membrane stretching of the facesheet. Several analytical studies have been conducted to investigate the dynamic behavior of the elastic plate when subjected to low-velocity impact by a small mass projectile (Olsson et al. 2006). Abrate (2005) has provided an excellent analytical literature review which incorporates nonlinear Hertz contact interaction and Kirchhoff–Love plate theory to model low-velocity impact on honeycomb composite structure. For low mass and velocity impact, wave propagation model based on Hertz contact law is most suitable. Koller (1986) demonstrated that the Hertz contact law is not a suitable contact interaction model to predict the contact force between an impactor and facesheet resting on a plastically deformable honeycomb core. The quasi-static energy balance model is valid for the low-velocity impacts and large impacting mass (M_1) to structural mass (M_2) ratio $(M_1/M_2 = 8)$ (Swanson 1992).

Tan and Sun (1985) employed an empirical Meyer's power contact law to model localized contact stiffness of plastically deformable core. A semi-analytical technique was formulated by idealizing the composite structure with lumped spring and mass model (Choi 2006). Such approaches are material and geometric specific and require detailed material characterisation. For plastically deformable cores, the theoretical models tend to deviate from experimental observations (Bao et al. 2004; Fatt and Park 2001; Koissin et al. 2004; Koissin et al. 2004).

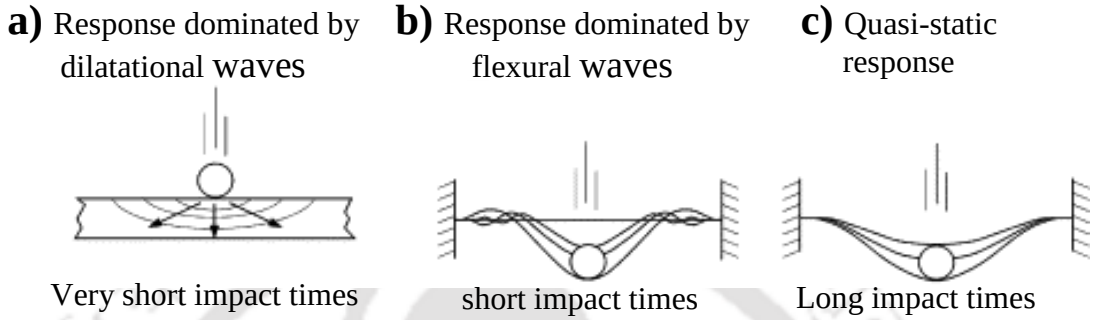

Figure 2.22 Representative schematic of response types during impact on plates: a) very short impact times, b) short impact times, and c) long impact times (Olsson et al. 2006)

Fatt and Park (2001) developed the analytical model for the prediction of transient deformation response of composite sandwich panels subjected to low-velocity impact. To predict the low-velocity impact response, they employed equivalent single and multi-degree of freedom systems. They predicted the impact response for different boundary conditions of sandwich panels, i.e., four-sided clamped, simply supported, two-sided clamped, and rigidly supported. They considered the facesheets as orthotropic and symmetric. The equivalent masses were derived by assuming velocity distributions and computing the kinetic energies in terms of global deflection of sandwich panel and top facesheet indentation. Most of the available literature states that the indentation load at failure and damage characteristic features were acquired from the static indentation tests. However, the recent studies on the impact show that the peak impact force at damage instigation is slightly higher than that of static indentation due to the strain rate sensitivity in the core and facesheet along with the inertia of projectile and sandwich. The key point of their analytical studies is to consider the projectile and sandwich panel inertia along with the strain rate sensitivity of core and facesheet materials in the low-velocity impact response.

The load-indentation behavior can be obtained by using principle of minimum potential energy. Therefore, the total potential energy (Π) is

$$\Pi = U + D - V \tag{2.27}$$

where,

'Π' is the strain energy due to bending,

'D' is the work due to the crushing of core

'U' is the total strain energy

'V' is the work done by the indentation force

Furthermore, the local indentation was assumed due to the bending as follows

$$w(x,y)=\begin{cases}\delta \text{ for } 0\le x^2+y^2\le R^2\\ \delta\left[1-\left(\dfrac{x-R}{\xi-R}\right)^2\right]^2\left[1-\left(\dfrac{y-R}{\xi-R}\right)^2\right]^2\\ \text{for } R^2\le x^2+y^2\le \xi^2,\ \ x\ge 0,\ \ y\ge 0,\end{cases} \tag{2.28}$$

where,

'δ' is the deflection under the indenter,

'ξ' is the lateral extent of the deformation zone,

'R' is the radius of the indenter,

The strain energy due to bending of the orthotropic facesheet is

$$U=\frac{1}{2}\int_s\left\{D_{11}\left(\frac{\partial^2 w}{\partial x^2}\right)^2+D_{22}\left(\frac{\partial^2 w}{\partial y^2}\right)^2+2D_{12}\left(\frac{\partial^2 w}{\partial x^2}\right)\left(\frac{\partial^2 w}{\partial y^2}\right)+4D_{66}\left(\frac{\partial^2 w}{\partial x\partial y}\right)^2\right\}dA \tag{2.29}$$

where,

'D_{ij}' is the laminate bending stiffness matrix,

'$dA=dxdy$', A is the surface area of the deformed facesheet,

Meo et al. (2005) presented the honeycomb sandwich panel behavior under low-velocity impact loading. They conducted the studies on both the experimental and numerical investigation of sandwich panels subjected to impact damage. They employed the test panels from the engine nacelle fan cowl doors of a large commercial aircraft and conducted the low-velocity impact study at five energy levels, ranges from 5 J to 20 J. They studied various parameters such as failure mechanism, damage initiation, and damage propagation of the sandwich panels. They noticed that the conducted energy levels cause barely visible impact damage (BVID) in the top facesheet of the test specimen. They performed numerical simulation using LS-DYNA3D transient finite element analysis for the computation of the contact forces, load distribution, failure analysis, and the impact damage initiation, and delamination. They successfully predicted the impact energy absorption of the sandwich panel and the extent of impact damage. They achieved a good agreement in the validation of numerical results with experimental results. From the experimental results, they suggested that a perfect numerical model can give substantial information for the designer to understand the mechanism of low-velocity impact which help to design a proficient impact resistant aircraft structure.

Yu et al. (2008) performed quasi-static and impact experiments on the Aluminum-foam core. Bending deformation and modes of the impact velocity under 5 m/s follows the similar pattern subjected to quasi-static loading. The representative image showing the impact damage areas after impact and the samples sectioned at impact location for the floor sandwich specimens can be seen in Figure 2.23. A theoretical model was

developed using Gibson's model for the prediction of failure modes and had good

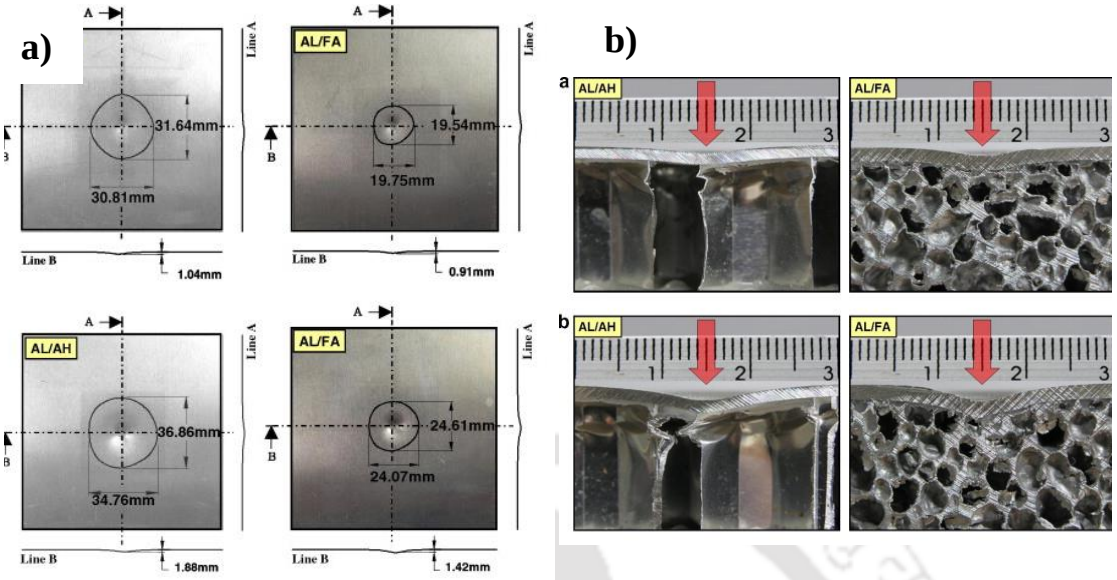

Figure 2.23 Representative image: a) impact damage areas after impact, and b) samples sectioned at impact location for the floor sandwich specimens (Shin et al. 2008)

agreement with the experimental results. Several other researchers also worked on conducted low-velocity impact studies on different sandwich structures which were used in the Korean low floor bus (Shin et al. 2008). Sandwich structures are made of Aluminum and balsa core with woven glass fabric facesheets and Aluminum and balsa core with Aluminum facesheets. Using a three-dimension scanner, the damage location and depth of indentation was quantified. Impact test results show the woven glass fabric sandwich panels have less impact damage compared to Aluminum facesheet panel with Aluminum core. Series of experiments were conducted to evaluate the damage resistance of sandwich panels for the combination of carbon and glass facesheets with Nomex core (Park et al. 2008). The damage was investigated using scanning acoustic microscope (SAM).

Castanié et al. (2008) developed a discrete mass approach for the evaluation of static indentation on core and sandwich panels. It can predict the contact force subjected to low-velocity impact on metal skinned sandwich structures. They considered the interface effect between facesheet and honeycomb core in their model. They suggested that the direct application of their model enabled the contact law when skinned sandwiches were subjected to quasi-statistic load. They found that the model demonstrated highly accurate correlation during indentation tests and three-point bending tests.

2.5.4 High-velocity impact studies on sandwich structures

Usually, the definitions for the low, intermediate, and high-velocity often differ in the available literature (Abrate 2005; Ashby et al. 2000). Few authors compete that the high-velocity refers to the conditions based on the resultant of the full penetration

of the target. However, this kind of phenomenon can be observed in the drop test in which the maximum available velocity is less than 10 m/s. Moreover, this phenomenon of full penetration among the small and large mass impactors with the same velocity. The high-velocity impact is defined as the ratio between the impactor velocity and the transverse compressive wave velocity with a higher maximum failure strain in the wave direction (Abrate 2005). The damage induced due to the high-velocity impact was introduced by the first few compression waves through the thickness when the global moment of the facesheet has not been recognized. Whereas an intermediate velocity impact is considered to be lies between the low and high-velocity ranges. In the intermediate velocity range, there will be excessive deformation due to the projectile mass, especially in the massive projectiles. It may differ from the low-velocity impact concerning the rate of loading and momentum effects.

The available literature survey on the high-velocity impact is as follows:

Deshpande and Fleck (2000) investigated the high strain rate behavior of two cellular Aluminum alloys (Alulight and Duocel) using a split Hopkinson pressure bar and impact tests. They noticed the dynamic behavior of these foams is the same as the quasi-static behavior. The plateau stress and the strain densification are independent of the applied strain rate but vary with the relative density of the foam.

Johnson and Holzapfel (2003) evaluated soft body impact (bird strikes) on fibre reinforced composite structures using finite element analysis. They observed the delamination and ply failures of composite structures subjected to the impact range of 100-200 m/s. A composites failure model to predict the impact damage in shell structures was developed.

Kim et al. (2003) conducted experimental investigations of ice impact (30-200 m/s) on woven carbon/epoxy composite panels to determine the damage resistance of thin-walled composite structures. The representative images of backside view of 42.7 mm simulated hail ice (SHI) impacting 1.22 mm thick panel at 106 m/s is shown in Figure 2.24. They found a linear relationship between the peak force and the projectile kinetic energy.

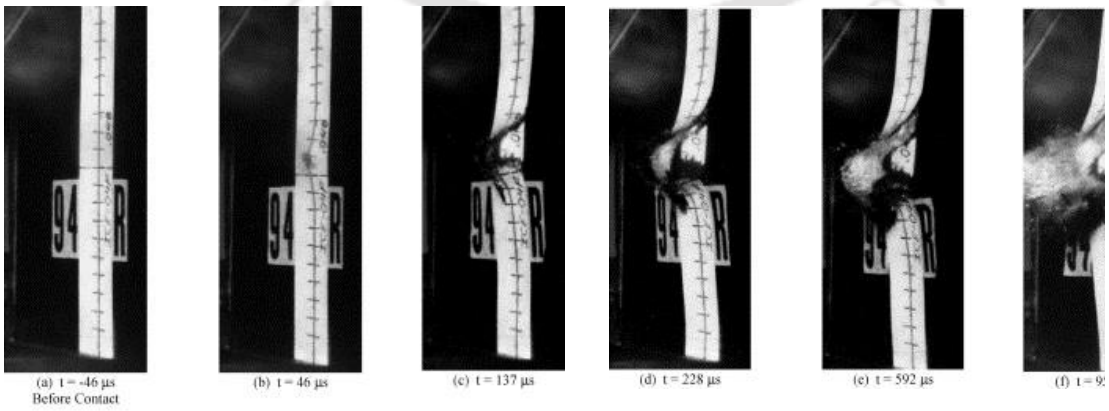

Figure 2.24 Representative images of backside view of 42.7 mm simulated hail ice (SHI) impacting 1.22 mm thick panel at 106 m/s (Kim et al. 2003)

Lopatnikov et al. (2003) conducted Taylor Cylinder-Hopkinson bar impact experiments on a closed-cell Aluminum foam subjected to impact velocities of 26 m/s to 200 m/s. The schematic of impact model of foam materials and the cross-sections collapsed of foam specimens is shown in Figure 2.25. Analytical solutions for dynamic deformation of foam during impact experiment were evaluated. The results obtained from the theory shows a good agreement with the experiment.

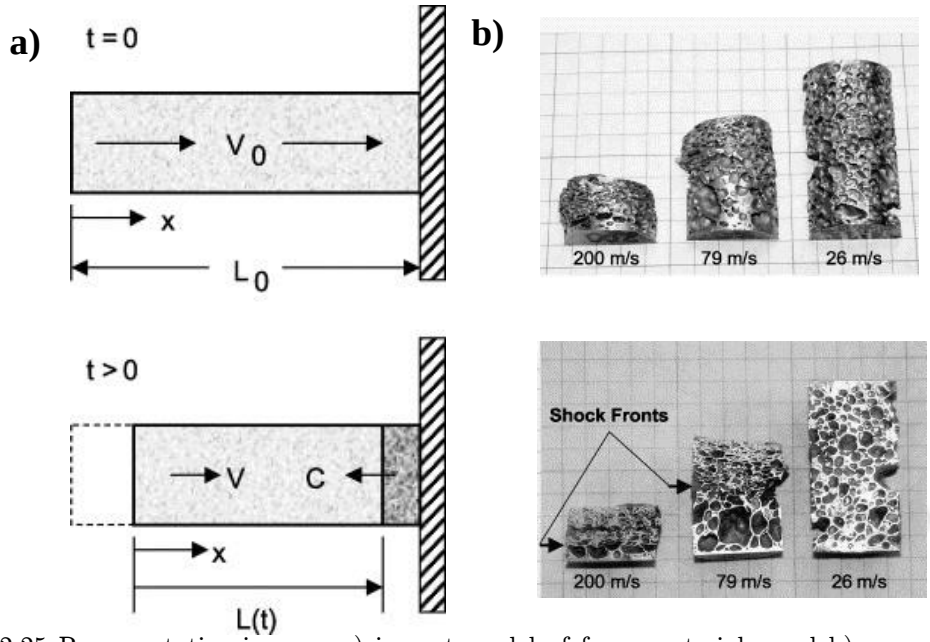

Figure 2.25 Representative images: a) impact model of foam materials, and b) cross-sections collapsed of foam specimens (Lopatnikov et al. 2003)

Bull and Hallstrom (2004) conducted quasi-static and high-velocity impact (1-1000 m/s) on sandwich panels. The impact tested specimens were further tested in in-plane compression with one undamaged specimen for reference. The residual strength of the damaged specimens was analyzed by numerical approach. They observed the damage of the specimens from high-velocity impact is limited, and it can achieve most of the undamaged strength by repair.

Radford et al. (2006) conducted shock wave experiments on sandwich plates having an Aluminum metal foam core. The representative photographs of the dynamically tested specimens can be seen in Figure 2.26. They quantified and observed that shock resistance of sandwich plates is higher than the monolithic plates of equal mass. The sandwich plates demonstrated monolithic plates of equal mass at adequately high values of projectile momentum. They validated the numerical results with experimental results and found to be in excellent agreement.

Radford et al. (2006) investigated dynamic response of sandwich and monolithic beams subjected to metal foam projectiles. These sandwich beams comprise of stainless-steel pyramidal cores, corrugated cores, and Aluminum metal foam. The sandwich beams exhibited a good resistance against shock loading compared to monolithic beams of same mass. They found the metal foam projectiles are convenient tools for conducting shock experiments on structures.

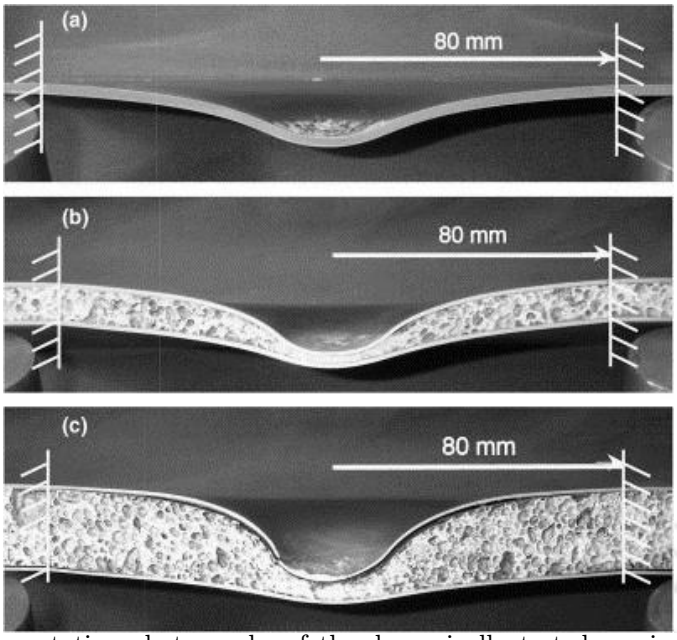

Figure 2.26 Representative photographs of the dynamically tested specimens (Radford et al. 2006)

Zou et al. (2009) analyzed the in-plane dynamic crushing behavior of honeycomb structures under the high-velocity impact (100 m/s) by the finite element approach. They noticed the strain densification increases with the crushing velocity and relative density.

Buitrago et al. (2010) studied the honeycomb sandwich structures subjected to high-velocity impact using a finite element approach. The numerical results of contact time, residual velocity, and ballistic limit were validated with the experimental results. A detailed investigation of energy absorption and failure mechanisms of sandwich panels was carried out.

Feli and Pour (2012) developed an analytical model to predict the perforation of sandwich panels having Aluminum honeycomb core subjected to high-velocity impact. They evaluated the strain, kinetic energy of the facesheets, and energy absorbed by the core. The residual velocity of projectile, energy balance, perforation time, and the velocity of projectile obtained from the numerical simulation were compared with the experimental values. They investigated the effects of composite facesheets and honeycomb core on perforation resistance and ballistic performance of sandwich panels.

Rhymer et al. (2012) likewise performed high-velocity impact tests on carbon composite panels using simulated hail ice spheres. Their study focuses on experimental characterisation of damage resistance for varying panel thicknesses and different diameters of projectiles. A detailed nondestructive investigation was carried out for the characterisation of the delaminated area.

In this section, a detailed literature review is presented focusing on impact dynamics and contact law and its implication on low-velocity and high-velocity impact on hybrid composite. Various modes of failure in a composite structure are identified under the influence of static loading, impact, and blast loading. Various theoretical and numerical models are discussed to evaluate the energy absorption characteristics of thin-wall

composite structures. It is concluded that the composite structure comprising of Aluminum foam and honeycomb material exhibit excellent impact resistive performance. A consolidated summary of impact dynamics that include low-velocity and high-velocity impact is summarized in Table 2.4.

Table 2.4 Summary of literature review on blast and impact response of honeycomb protected structures

Author	Material	Type of loading	Validation	Remarks/Comments
Petras and Sutcliffe (2000)	Nomex honeycombs	Compressive and three-point bending	Experimental and Analytical	Developed a theoretical model using the stress distribution calculation in the core due to the indentation loading.
Anderson and Madenci (2000)	Sandwich panels	Quasi-static loading	Experimental and Analytical	Presented an analytical model that provides the three-dimensional stress and displacement along with the contact area and pressure.
Deshpande and Fleck (2000)	Aluminum alloy foams	High-strain rate	Experimental	The plateau stress and the strain densification are independent of the applied strain rate but vary with the relative density of the foam.
Fatt and Park (2001)	Aluminum Honeycomb	Low-velocity impact	Experimental and Numerical	Developed the analytical model for the prediction of transient deformation response of composite sandwich panels subjected to low-velocity impact.
Hazizan and Cantwell (2003)	Aluminum Honeycomb	Low-velocity impact	Experimental and Analytical	Impact velocity under 1.2m/s failed to exhibit strain rate sensitivity.
Johnson and Holzapfel (2003)	Fibre reinforced composite	High-velocity impact	Experimental and Numerical	Developed a composites failure model to predict the impact damage in shell structures.
Kim et al. (2003)	Carbon/epoxy composite panels	High-velocity ice impact	Experimental	Found a linear relationship between the peak force and the projectile kinetic energy.
Lopatnikov et al. (2003)	Aluminum foam	High-velocity impact	Experimental, Analytical and Numerical	Conducted analytical solutions for dynamic deformation of foam during impact experiment.
Bull and Hallstrom (2004)	Aluminum Sandwich panels	Quasi-static impact and High-velocity impact	Experimental and Numerical	They observed the damage of the specimens from high-velocity impact is limited, and it can achieve most of the undamaged strength by repair.

Sokolinsky et al. (2004)	Soft polymer foam	Free vibration	Experimental, Analytical and Numerical	Predicted natural frequencies and corresponding vibration modes using higher-order theory for sandwich panels.
Koissin et al. (2004)	Honeycomb	Quasi-static loading	Experimental, Analytical and Numerical	Developed the axisymmetric formulations for local indentation.
Meo et al. (2005)	Aluminum Honeycomb	Low-velocity impact	Experimental and Numerical	Predicted the impact energy absorption of the sandwich panel and the extent of impact damage from numerical simulation.
Olsson et al. (2006)	Plate	Quasi-static impact	Experimental, Analytical and Numerical (LS-DYNA)	Derived a delamination threshold load criterion for transversely isotropic plates subjected to small mass with high-velocity impact.
Choi (2006)	Sandwich Plate	Low-velocity impact	Experimental, Analytical and Numerical (NASTRAN)	Proposed a lumped mass model to determine the contact force history of sandwich plates under low-velocity impact.
Zhou and Stronge (2006)	Hybrid Stainless Steel Assembly (HSSA) panels	Low-velocity impact	Experimental, Analytical and Numerical (ABAQUS)	Proposed an analytical model for lightweight circular sandwich panels subjected to low-velocity impact.
Radford et al. (2006)	Aluminum alloy metal foam cores	High-velocity impact	Experimental, Analytical and Numerical (ABAQUS)	The sandwich plates demonstrated monolithic plates of equal mass at adequately high values of projectile momentum.
Jen and Chang (2008)	Aluminum honeycomb beams	Fatigue strength	Experimental, Analytical and Numerical (ANSYS)	The primary failure was identified as the debonding of the adhesive between the facesheet and the core.
Yu et al. (2008)	Closed-cell Aluminum-foam core	Quasi-static and Low-velocity impact	Experimental	A theoretical model was developed using Gibson's model for the prediction of failure modes and had good agreement with the experimental results.
Shin et al. (2008)	Woven glass fabric Composite honeycomb core panel	Low-velocity impact	Experimental	Conducted low-velocity impact studies on different sandwich structures which were used in the Korean low floor bus.

Castanié et al. (2008)	Nomex honeycomb	Low-velocity impact	Experimental and Numerical (SAMCEF)	Developed a discrete mass approach for the evaluation of static indentation on core and sandwich panels.
Zou et al. (2009)	Aluminum honeycomb	Shock	Experimental and Numerical (ABAQUS)	The strain densification increases with the crushing velocity and relative density.
Buitrago et al. (2010)	Carbon Composite honeycomb core panel	High-velocity impact	Experimental and Numerical (ABAQUS)	Conducted a detailed investigation of energy absorption and failure mechanisms of sandwich panels.
Feli and Pour (2012)	Carbon Composite honeycomb core panel	High-velocity impact	Experimental, Analytical and Numerical (ABAQUS)	Developed an analytical model to predict the perforation of sandwich panels having Aluminum honeycomb core subjected to high-velocity impact.
Rhymer et al. (2012)	Carbon/epoxy composite tape laminates	High-velocity ice impact	Experimental	The damage resistance of quasi-isotropic carbon/epoxy composite tape laminates impacted by high-velocity ice

2.6 Summary of literature review

A comprehensive review of prior efforts has presented on the reinforced concrete structures subjected to extreme loadings. In a broad view, the current chapter was more pronounced on the available literature of beam-column joint subjected to extreme events such as earthquake, reversal cyclic, blast, and impact loadings. This review led to the identification of the research gap on reinforced concrete beam-column joints subjected to shock, blast, and impact loading. Based on this review, well-defined examples are available for the reinforced concrete beam-column joints subjected to quasi-static, earthquake, and reversal cyclic loadings. The previous researchers have not adequately established the extension of the research on the extreme events underlining the shock, blast, and impact loadings.

To this end, a research effort to study the response of the reinforced concrete beam-column joints subjected to shock and impact loading was undertaken as the research problem. Furthermore, a protective sacrificial composite system was developed to protect the beam-column joints. The protective sacrificial composite system was tested against the shock and impact loadings, and the same was presented in the subsequent chapters.

Chapter 3

Development and characterisation of shock and impact loading simulator

3.1 Introduction

Over the last few decades, significant attention has been focused on the behavior of engineering structures subjected to blast, shock and impact loading. The application of explosives by terrorists across the world that target the civilian buildings and other public structures is growing as a striking problem in urban areas. Moreover, with technological development, explosive devices have been miniaturized and possess higher explosive energy. Also, it leads to an increase in the mobility of explosive materials with enormous range effects. Most of the casualties during such detonation are not only related to the instant fatalities as a consequence of the immediate release of tremendous energy but also leads to the significant structural failures and could result in great life loss as well as economy.

The emphasis of this chapter is to provide a background understanding of the characteristics of the blast, shock, and impact loading. The current chapter is divided into four sections. i) fundamentals of blast loading, ii) fundamentals of shock loading, iii) design of shock tube components, and iv) characterisation of shock wave. The last two sections discusses the development of the shock and impact testing simulator at IIT Guwahati is then described in detail, highlighting the system's functionality along with the experimental and numerical investigation of the loading relevant to this dissertation.

3.2 Fundamentals of blast loading

3.2.1 Explosions

An explosion is defined as an event occurred in the atmosphere when tremendous energy is released over a small period and in a small volume to generate a pressure that has a finite amplitude moving away from the source. This energy source may have initially stored in diversified forms, i.e., physical, nuclear, chemical, and electrical or pressure energy, which can severely damage building structures.

There are two main types of explosions, i.e., 1) deflagration, and 2) detonation. The deflagration explosion refers to the combustion process of any explosive materials such as dust, gas, oil, and vapor cloud, etc. which travels at a lower rate than the speed of sound in the material and results in propagation of heat of reaction. The detonation is a kind of explosive reaction of solid material such as TNT, RDX, HMX, AFNO, Nitroglycerin, and Semtex, etc. which generates rapidly a high-intensity shock

wavefront that releases an enormous magnitude of pressure and temperature gradients. The detonation reaction rate lies in a range of 1500 to 9000 m/s, which is appreciably faster than the propagation by the thermal processes observed in deflagration (Mays et al. 1995). A typical blast event showing the shock wave and its fireball (heat) and schematic of the blast wave propagation are shown in Figure 3.1.

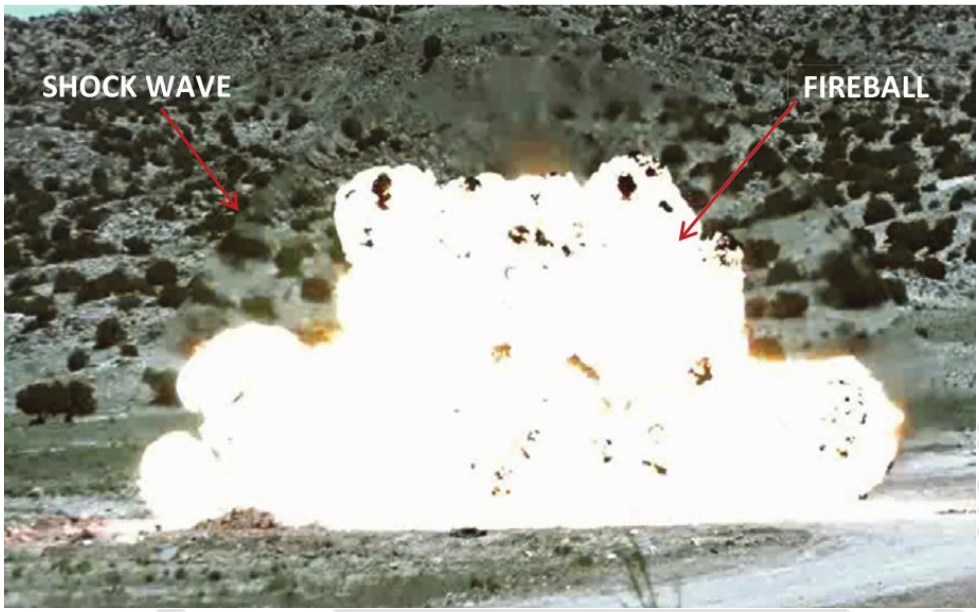

Figure 3.1 Shock wave and fireball created during an explosion (Huson 2012)

3.2.2 Blast-loading categories

Based on the UFC 3–340–02 (2008) design manual, explosions are characterized as unconfined and confined explosions. When the expansion occurs freely without any obstacles or rigid boundaries, it is referred as unconfined explosions. When any blast or explosion occurs in a closed location i.e. containment structures, nuclear towers that amplifies the blast wave due to the wall or boundary interaction, it is said to be a confined explosion. The different types of unconfined blast loads: i) Free air burst; ii) Air burst, and iii) Surface burst.

i) Free-air bursts: The explosive charge is detonated in the air, the blast waves propagate spherically outwards and strike directly onto the structure without prior interaction with other obstacles or the ground.
ii) Air bursts: The explosive charge is detonated in the air, the blast waves propagate spherically outwards and strike onto the structure after having interacted first with the ground thereby creating a Mach wavefront.
iii) Surface bursts: The explosive charge is detonated near the ground surface, the blast waves immediately interact locally with the ground, and thereby skims on the surface and evolved outwards to impinge onto the structure.

The various types of unconfined blast loads illustrating the blast wave propagation towards the target along with its interaction and amplification due to the reflections are shown in Figure 3.2. The various categories of blast loading along with the pressure loads is presented in Table 3.1.

Free Air Burst

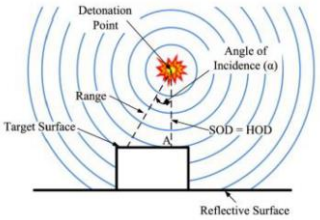

Blast wave propagates to target without prior disruption or amplification due to reflection.

Air Burst

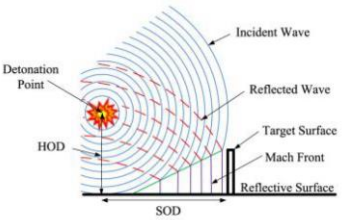

Detonation is at a distance from and above the target surface.
Reflection of the incident wave occurs before impacting target
surface

Surface Burst

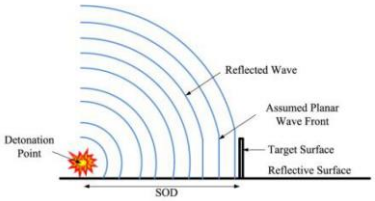

Charge is detonated on or close to a reflective surface.
The incident wave is reflected and amplified at the point of detonation.

Figure 3.2 Schematics illustrating different types of unconfined blast loads: a) Free air burst; b) Air burst, and c) Surface burst (Geretto et al. 2015)

Table 3.1 Blast loading categories, UFC 3–340–02 (2014)

Charge confinement	Category	Pressure loads	Protective structure
Unconfined Explosions	1. Free air burst 2. Air burst 3. Surface burst	a. Unreflected b. Reflected b. Reflected	Shelter
	4. Fully vented	c. Internal shock d. Leakage	Cubicle
Confined Explosions	5. Partially confined	c. Internal shock e. Internal gas d. Leakage	Partial containment cell or Suppressive shield
	6. Fully confined	c. Internal shock e. Internal gas	Full containment cell

3.2.3 Explosion phenomenology

An explosion that occurs outside the building usually generates four types of loads i.e., i) Impact of primary fragments, ii) Impact of secondary fragments, iii) Overpressure, and iv) Reflective pressure as shown in as shown in the Figure 3.3 (a). The primary fragments during an explosion are fragmentation of the casing shells of the bomb. Secondary fragments consist of the parts that are struck up and protruded as the blast flashes. It includes the equipment or other objects which were not firmly attached to the ground, bricks from the walls, or other cladding works of the structure. During the blast or explosion, both the primary and secondary fragments are associated with substantial casualties, but in most of the cases, they don't contribute to the major damage in the structure. When the blast wave with peak overpressure approaches an

object perpendicular to its path, the wave is reflected by forming an elevated pressure. The magnitude of the reflected pressure is dependent on the shape of the target object and its orientation concerning the blast wave (Naito et al. 2006).

A distributed reflected pressure is generated when the blast waves are directly imparted on the structural element which results in immediate rise time to a peak positive pressure that consequently disperses to atmospheric pressure within milliseconds [refer Figure 3.3 (b)]. The positive phase pressure is followed with a decay known as negative pressure phase which has low magnitude but for a long duration. However in few instances, the negative pressure region exhibits a little effect on the structural behavior and can be ignored. By equating the area under the exponential curve with the area under the triangular curve [refer Figure 3.3 (c)], the impulsive energy can be retained, resulting in a reasonable estimation of the blast demand.

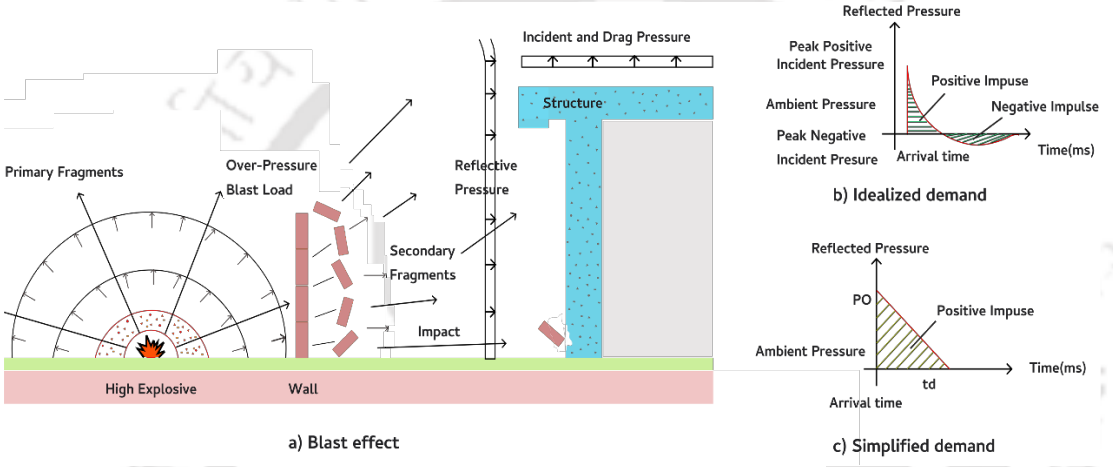

Figure 3.3 Blast load demands with its effects

To design the blast-resistant building, primarily the charge weight and standoff distance of an explosive need to be defined. To estimate the blast parameters of these wide varieties of explosives, researchers have adopted a universal quantity as TNT (Trinitrotoluene) as its blast characteristics resemble the most of solid type explosives. A list of conventional explosives used in the commercial as well as military applications with the mass-specific energy values and its TNT equivalent factor is presented in Table 3.2.

TNT equivalence is defined as the ratio of the explosives specific energy (Q_e) to that of TNT and is denoted as '$W_{TNT_{eq}}$'. An equivalent TNT weight is computed from the following Eq.(3.1) (Mays et al. 1995):

$$W_{TNT_{eq}} = \frac{Q_e}{Q_{TNT}} W_e \tag{3.1}$$

3.2.4 Blast parameters

i) Scaled distance (Z)

The scaled distance is defined based on the standoff distance and equivalent amount of TNT (trinitrotoluene) used in the detonation. The application of TNT (trinitrotoluene) is commonly considered as a reference. When a high explosive other than TNT was used, then the equivalent energy is acquired by using the charge factor (CF). The charge factor is the ratio of the actual mass of the charge to the mass of the TNT equivalent. The various charge factors for different explosives based on the specific energy ratio is presented in Table 3.2.

Therefore, the scaled distance, 'Z' is defined as

$$Z = \frac{R}{\sqrt[3]{W}} \tag{3.2}$$

where, 'R' is the standoff distance from the detonation source to the target point in metre, and 'W' is the weight of the TNT equivalent charge of explosive in kilogram.

All the blast parameters are fundamentally dependent on the amount of energy released by an explosion which generates the blast wave and the distance from the blast. The effect of the distance on various blast parameters is thus described using scaled distance. According to Hopkinson-Cranz law, during the explosion of two charges with the similar geometry but have different charge weight are situated at the same scaled distance from the target produces similar blast waves as long as they are under the same atmospheric conditions.

ii) Peak overpressure (P_{so})

During a blast scenario, the shock wavefront reaches a point, and the pressure rises instantaneously to a maximum magnitude above the ambient pressure. This peak pressure is also referred to be side-on peak overpressure (P_{so}). The magnitude of the peak overpressure and the velocity of propagated shock wave decreases with the increase in the distance from the detonation point. After reaching a peak magnitude, the pressure decreases exponentially until it reaches the ambient pressure. This entire duration is referred as positive phase duration. Further, the pressure decays and becomes smaller than the ambient value called as negative pressure, which is longer than the positive phase, and the minimum pressure value is denoted as P_{so}^{-}. During this negative phase, the structures will be experienced to the suction forces. This suction pressure can leads to the development of glass fragments and removal of building cladding and facades. The positive phase induces much more damage to any structure when compared to the negative phase of the explosion due to its higher magnitude. Therefore, the negative phase is often not considered during the design process as they don't create much impact on the structural integrity of buildings under blast loads. The positive phase duration is indicated by t_d and the negative phase

duration by t_d^-. Researchers have proposed various equations to estimate the peak incident pressure for the different blast situations like spherical or air and hemispherical or surface blasts (Brode 1955). The peak overpressure due to the spherical blast is given as below.

$$\begin{aligned} P_{so} &= \frac{6.7}{Z^3} + 1 && \text{for } P_{so} > 10 \text{ bar} \\ P_{so} &= \frac{0.975}{Z} + \frac{1.455}{Z^2} + \frac{5.85}{Z^3} - 0.019 && \text{for } 0.1 < P_{so} < 10 \text{ bar} \end{aligned} \tag{3.3}$$

Table 3.2 Explosives and charge factors (CF) (Bangash 2006; Hetherington and Smith 2014)

Explosives	Mass specific energy Q_e(kJ/kg)	TNT Equivalent (CF) (Q_e/Q_{TNT})
TNT	4520	1.00
GDN (glycol dinitrate)	7232	7232/4250 = 1.6
Pyroxilene	4746	1.05
Pentrinite	6689.6	1.48
Dynamite	5876	1.30
Schneiderite	3164	0.70
Dinitrotoluene (DNT)	3164	0.70
Compound B [0.6RDX + 0.4TNT]	5190	1.148
RDX (Cyclonite)	5360	1.185
HMX	5680	1.256
Nitroglycerin (liquid)	6700	1.481
Blasting gelatin	4520	1.000
60% Nitroglycerin dynamite	2710	0.600
ANFO	3930	0.870
Semtex	5660	1.250

Newmark and Hansen (1961) introduced a relationship to estimate the maximum blast overpressure (P_{so}), for a high explosive charge detonates at the ground surfaces as,

$$P_{so} = 6784\frac{W}{R^3} + 93\sqrt{\frac{W}{R^3}} \tag{3.4}$$

where,

'W' is the charge weight in metric tons of TNT,

'R' is the distance of the surface from the center of the spherical explosion in m,

Kinney and Graham (2013) proposed the following formula for the incident overpressure (P_{so}) in kPa, and the positive phase duration $'t_d'$ in ms,

$$\frac{P_{so}}{P_{atm}} = \frac{808(1+(Z/4.5)^2}{\sqrt{1+(Z/0.048)^2}\sqrt{1+(Z/0.32)^2}\sqrt{1+(Z/1.35)^2}} \tag{3.5}$$

and

$$\frac{t_d}{W^{1/3}} = \frac{980\left(1+(Z/0.54)^{10}\right)}{\left(1+(Z/0.02)^3\right)\left(1+(Z/0.74)^6\right)\sqrt{1+(Z/6.9)^2}} \tag{3.6}$$

where, P_{atm} = 103.25 kPa is the atmospheric pressure.

The most widely accepted method to estimate the peak overpressure is by using the Kingery and Bulmash (1984). These are the standard curves that were employed in the UFC 3–340–01 (2002) for the reference manual of blast resistant design of structures. The manual provides various formulations for the calculation of blast parameters in both spherical (free air bursts) and hemispherical pressure waves (surface bursts). They also provide the values of the incident and reflected pressures as well as of all other blast parameters. Their proposed blast parameters are valid for the stand-off distances from 0.05 m to 40 m.

iii) Idealized blast wave equation

The pressure wave variation with time can be characterized by the Friedlander's blast wave shown in Figure 3.4 and the equation as follows:

$$P_s(t) = P_{so}\left(1-\frac{t}{t_d}\right)e^{-b\frac{t}{t_d}} \tag{3.7}$$

where (P_{so}) is the peak overpressure, '*b*' is a decay coefficient of the waveform, t_d is the positive phase duration, and '*t*' is the time elapsed, measured from the instant of blast arrival. The decay coefficient '*b*' can be calculated through a non-linear fitting of an experimental pressure time curve over its positive phase, $'P_o'$ is the ambient pressure and $'t_a'$ is the time of arrival of the shock front. Impulse is an important blast parameter of the blast wave pulse. It is the total force applied on a structure due to the blast per unit area. It is defined as the area under the overpressure-time curve of Figure 3.4. The impulse is classified into positive (i_s) and negative (i_s^-), based on the relevant phase of the blast wave time history. During the blast analysis for the structural collapse as failure criteria, it was considered the positive phase impulse is more prominent than its negative counterpart.

$$i_s = \int_{t_A}^{t_A+t_a} P_s(t)dt \tag{3.8}$$

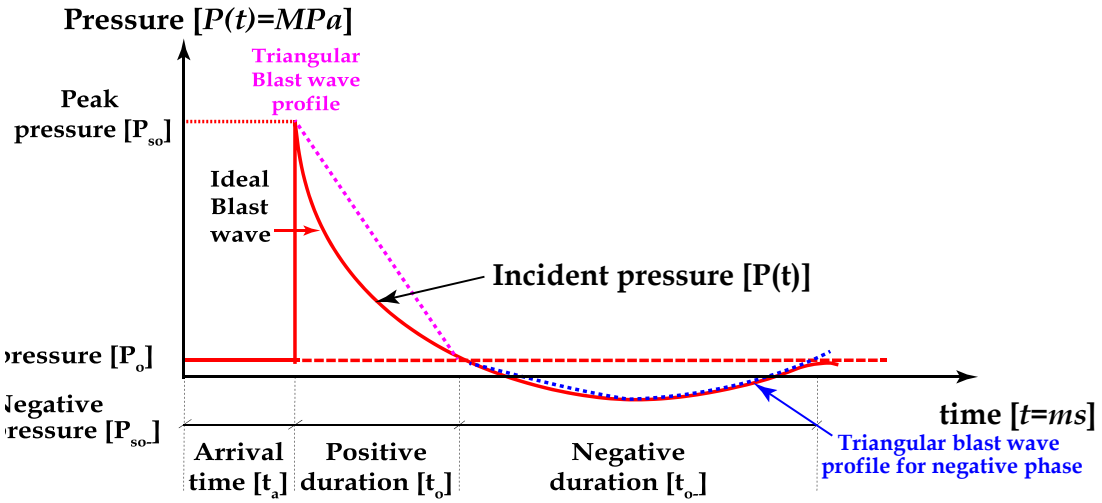

Figure 3.4 Ideal blast wave pressure-time history

iv) Reflected pressure (P_r)

When a blast wave interacts with the target, the generated pressure pattern will be different than the idealized time history shown in Figure 3.4. As the blast wave moves through space, there will be decay in the peak pressure and decrease in the speed which surrounds every object/structure that lies within the blast range. Further, the blast wave comes in contact with a rigid surface, and the pressure reflected has a larger magnitude than that of incident peak pressure$\left(P_{so}\right)$, can be seen in Figure 3.4. The reason behind the rise in the reflected wave is due to the nature of the propagation of blast through the air. The blast wave travels along with the air particles and collides with the surface upon the arrival. In an ideal linear-elastic case, the particles may bounce back freely that leads to a reflected pressure equal to the incident pressure, and thus the surface would experience a magnification of the acting pressure. For a strong intensity blast wave, a non-linear phenomenon case, the reflection of these particles is prevented by subsequent air particles that are transferred and results in higher magnitude and intensity in the reflected pressure.

The acting pressure acting on the contact surface of the target structure experiences higher incident pressure, and this pressure should be considered while designing the blast-resistant structure. The reflected pressure decreases with the increase in the angle of incidence 'α', can be seen in Figure 3.5. The minimum value of reflected pressure is equal to the incident pressure, which was induced on the target surface perpendicular to the shock front when 'α' is equal to 90°. A peak incident pressure is also termed as peak side-on overpressure as it is equal to the reflected pressure on the target surface that is parallel to the direction of the blast wave.

The maximum reflected pressure acts on a target surface (building) when the angle of incidence 'α' becomes zero. A schematic showing the angle of incidence and reflected

pressure can be seen in Figure 3.5. Therefore the value of maximum reflected pressure is given by Kingery and Bulmash (1984),

$$P_r = 2P_{so}\left(\frac{4P_{so}+7P_o}{P_{so}+7P_o}\right) \tag{3.9}$$

where, (P_{so}) is the incident peak overpressure and (P_o) is the ambient pressure.

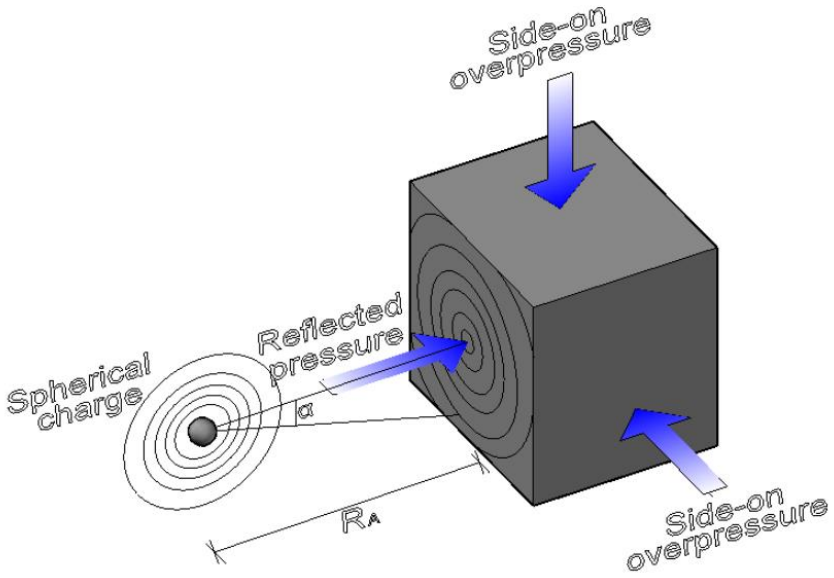

Figure 3.5 Angle of incidence and reflected pressure (Karlos and Solomos 2013)

v) Dynamic pressure (q)

The blast wave generated through the air travels with a speed more significant than the speed of sound and decreases continuously due to the propagation. The air behind the shock front of the blast wave travels in the same direction of the wind with a smaller velocity. The generated winds from the blast wave are responsible for loading on the target surface for the whole positive phase duration. The produced pressure is referred as dynamic or drag pressure $q(t)$. It has an initial peak value q_o, which is lesser than the incident or reflected pressures for both small and medium overpressures which attenuates eventually. Both the incident and reflected pressures last for a very short duration, usually less than one second, whereas the dynamic pressure may last for longer periods up to 2-3 seconds (Karlos and Solomos 2013). This dynamic pressure depends on the density of the air and the wind velocity released from the shock front of the blast wave, which is influenced by the peak incident overpressure. Its effectiveness depends on the drag coefficient and the orientation of the target surface with respect to the propagation of blast wind direction. Due to security issues in conducting the blast experiments in an academic institution, a shock tube testing facility is developed as a part of research work at Indian Institute of Technology Guwahati. A shock tube is a good research tool which can produce a substantial magnitude of pressure waves that can mitigate the blast pressure magnitude. The shock

tube testing facility is employed in the current dissertation to conduct the shock and impact testing experiments. The fundamentals of the shock wave is discussed in the succeeding sections. Furthermore, the calibration of the shock tube and its characterisation is emphasized in the subsequent sections.

3.3 Fundamentals of shock loading

A shock wave is defined as the propagating disturbance, which can move faster than the speed of sound in the medium. A shock wave carries enormous energy that can propagate through the medium, but it is described by an abrupt, irregular, change in pressure, temperature, and density of the medium (Anderson Jr 2010; Grady 2017). Shock waves primarily exist in nature as characteristics for energy dissipation. Shock waves are the events that are observed mainly in the supersonic regime of flow (Davison 2008). Over several decades, researchers had worked on the shock waves, but the comprehensive intricate physics behind its mechanics is however not fully understood. Most of the research groups across the world focused on the fundamental physics associated with the generation of the shock wave and its propagation. Based on the Mach number achieved from the shock wave, the flow regimes are classified into four types, i) Subsonic, ii) Transonic, iii) Supersonic, and iv) Hypersonic. The typical range of the Mach number of the flow regimes are listed in Table 3.3. It involves learning the mechanisms with regards to shock thickness, thermal and chemical non-equilibrium of gas behind strong shock waves, shock attenuation, and shock movement over uneven surfaces, etc. The shock wave propagation and its movement through the solids and liquids are even not widely known phenomena (Kumar et al. 2014). Researchers had pursued the study of the response of a shock wave generated in gas then propagated onto a liquid or solid. Their efforts help in providing better insight on the blast-resistant materials to safeguard against the blast and shock loading.

Table 3.3 Different regimes of flow

Mach number range	Flow regime
$M < 1$	Subsonic
$0.8 < M < 1.2$	Transonic
$M > 1$	Supersonic
$M > 5$	Hypersonic

3.3.1 Generation of shock wave

The generation of the shock wave in the shock tube is very similar to the accelerating piston in the tube. The schematic diagram of the shock tube section before the rupture of diaphragm is shown in Figure 3.6 (a). The driver section labelled with region 4 with pressure referred to as P4 and the driven section is region 1 that have atmospheric pressure P1. These two sections have gases that have predetermined pressure ratios which demonstrates the initial condition of the shock tube.

These are the initial condition of the shock tube. The initial temperature of both the section is the same. The driver gas is filled continuously into the driver section until the diaphragm gets sudden rupture at a certain pressure P4. When the diaphragm ruptures, the gas stored in the driver section releases with high pressure through the driven section from driver to driven section. It will start increasing the pressure at the driven section, and region 1 starts converting into pressure region 2, as shown in the Figure 3.6 (b).

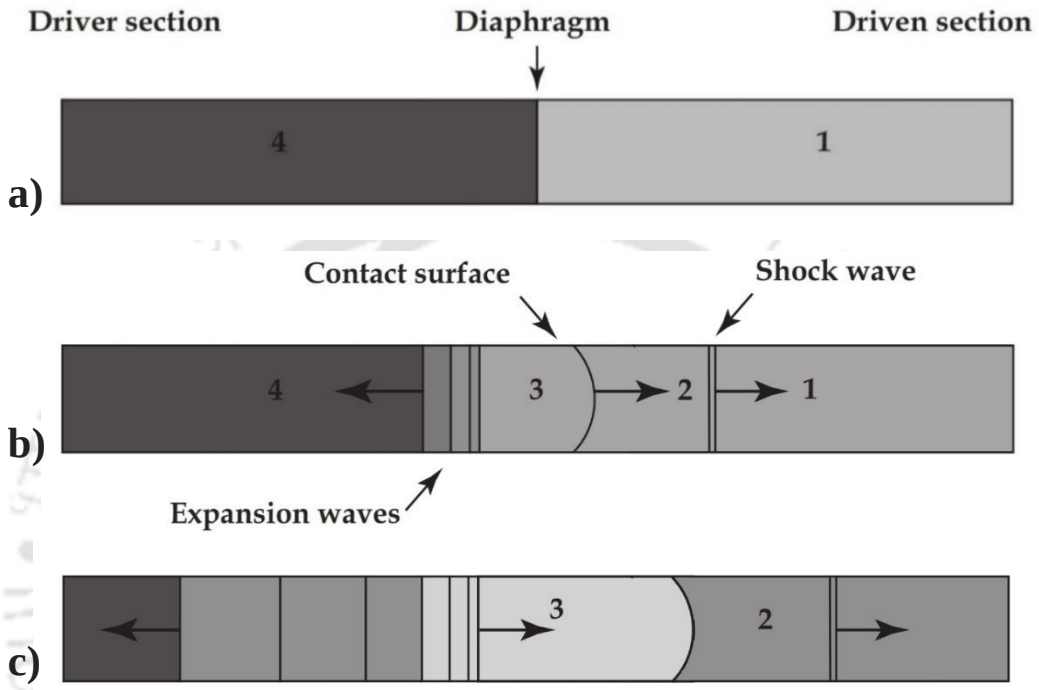

Figure 3.6 a) Initial pressure condition of the shock tube, b) Pressure variation when primary shock formed after diaphragm ruptur, and c) Shock moves forward into the driven gas

The generation of expansion wave will arise, which moves opposite to the direction of the shock wave from right to left. These expansion waves and shock waves will be separated with the help of the contact surface, as shown in the Figure 3.6 (b). Near the contact surface, the temperature, pressure, and the density remain the same for both shock and expansion waves. This expansion wave depreciates the pressure of the driver section to the lower pressure. The pressure variations in the shock tube before and after burst can be seen in Figure 3.7.

Subsequently, the driven section will become region 2, where the shock wave has reached up to the end of the section. When the driven section is filled with P2 to maintain the pressure from the atmospheric pressure, it again starts decreasing and is shown in Figure 3.6 (c). The pressure variations along the length of the shock tube can be seen in Figure 3.7. It shows the pressure difference in the driver and driven section. In general, a shock tube can produce normal shock waves, in which wave is perpendicular to the orientation of flow. When the flow traverse across a normal shock wave, the velocity drops to the subsonic value. The flow regime depends on the Mach

number of the flow. Mach number is the ratio of velocity gas particle to the velocity of sound. Different type of flow regime has been shown in Table 3.3.

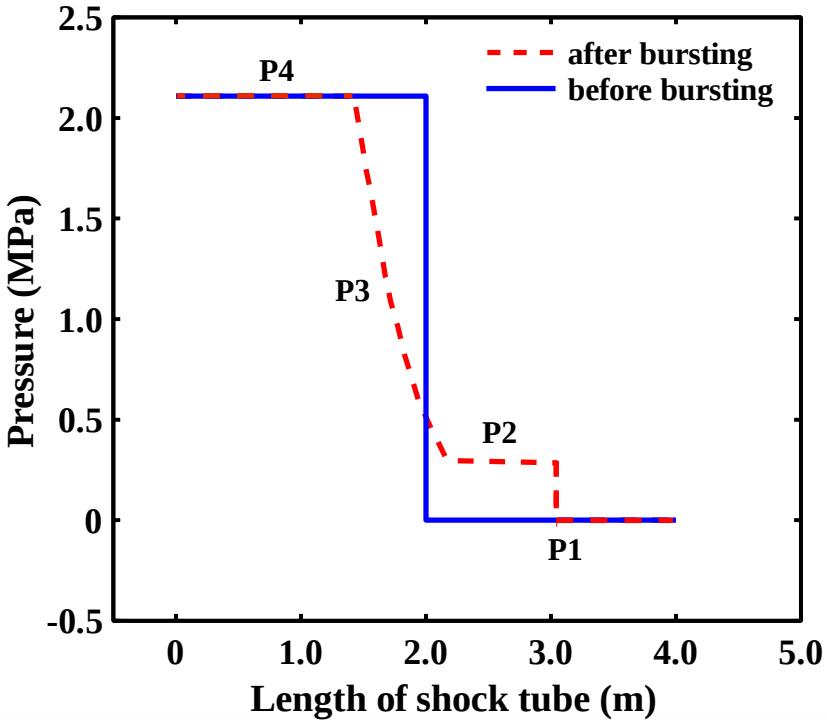

Figure 3.7 Pressure variation along the length of the shock tube for both before and after bursting

$$M = \frac{U}{a};\ a = \sqrt{\gamma RT} \tag{3.10}$$

where,

$\gamma_1 = \gamma_4$ = Ratio of specific heat = 1.4

a = velocity of sound (m/s)

M = Mach number

R = gas constant = 287 J/ Kg k

T = temperature of gas

U = velocity of gas particle in medium (m/s)

From the past literature, it was found that the gas with lighter molecular weight gives a high-pressure shock wave with a high value of speed. The developed shock tube in the current research has employed with both Nitrogen and Helium gas for the initial calibration and validated with simulation results. The chemical properties of the Nitrogen and Helium are shown in in Table 3.4 at atmospheric temperature.

Table 3.4 Properties of different driver gas

Gas	Specific heat ratio (γ)	Sound velocity a (m/s)	Molecular weight (g/mole)
Nitrogen	1.40	349	14
Helium	1.67	1007	4

3.4 Design and development of shock tube components

The shock tube test setup is fabricated to generate localized near-field shockwave loading on the experimental specimen. The conceptual figure of the shock tube and various stages of experimental setup is shown in Figure 3.8. The four main components of the shock tube are the driver, diaphragm, driven sections, and the protection chamber. The driver section is filled with pressurized gas, known as a high-pressure region that is separated from the driven section by diaphragm section which contains several membranes of Mylar. The sudden membrane rupture in the diaphragm section due to high pressure generates a shock wave in the driver section and travels towards the end-wall of the shock tube.

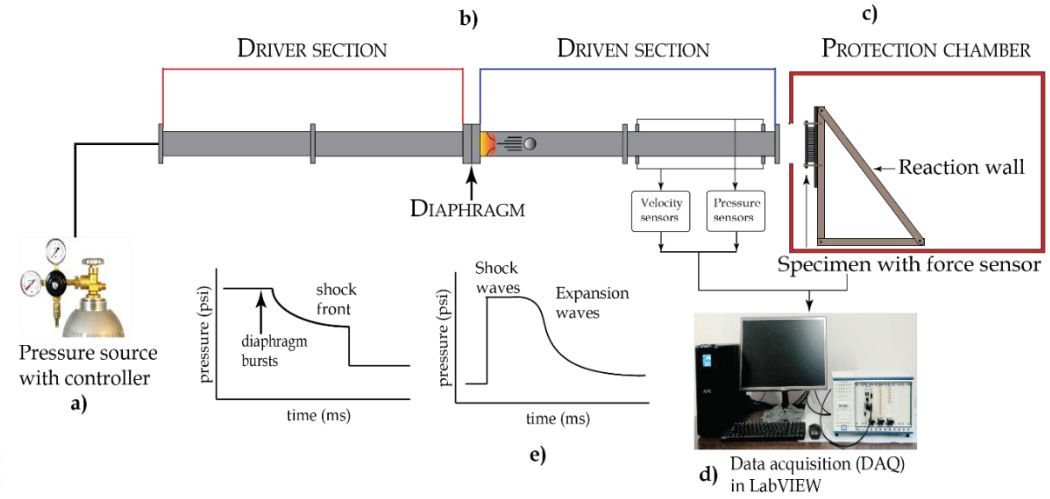

Figure 3.8 Conceptual figure of the shock tube setup; a) high-pressure cylinder, b) shock tube section, c) protection chamber with reaction wall, d) data acquisition, and e) shock wave profile

The schematic diagram and the experimental setup of the shock tube is shown in Figure 3.9 and Figure 3.10 respectively.

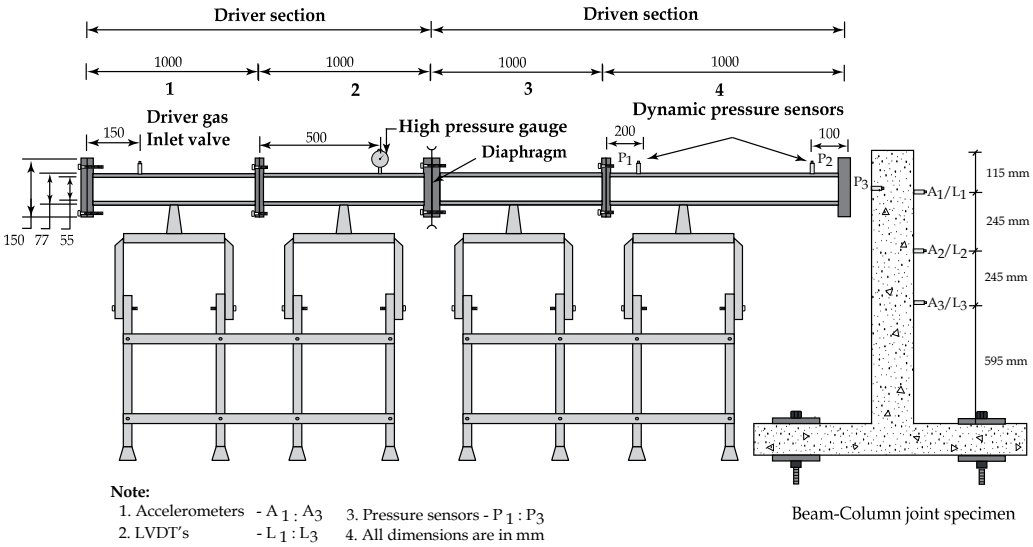

Figure 3.9 Schematic diagram of the shock tube and details of the specimen

The desired shock wave intensity depends on the thickness and material of the diaphragm. Finally, the shock wave exits from the end-wall of the shock tube and

imparts on the specimen mounted in the protection chamber. The detailed information of the components is given in the subsequent sections.

3.4.1 Driver section

The driver section of the shock tube accumulates the low molecular gases like Helium, Hydrogen, and high molecular (Nitrogen) to generate high pressure that propagates the shock wave in the driver, referred to as a high-pressure region. The three extensively used methods for generating high-pressure in the driver section are rupture membranes, fast opening valves (solenoid) and combustion technique. Considering the safety measures as a primary aspect and combustion technique is not used in the IITG shock tube facility. Therefore, the rupture membrane method has been employed using Nitrogen gas as driver gas to drive the shock tube. Driver section is regulated with a high-pressure regulator and monitored with analog and digital pressure gauge.

The flanges used in the diaphragm section is termed as breech flanges. It is fabricated with stainless steel (SS) that was welded using multiple pass groove welds with a fine finish. The back end of the driver section is closed with SS flange and the other end is connected to a male breech flange with a 4-mm sealing O-ring. The male flange will be connected to the female breech flange of the driven section as shown in Figure 3.10. A 9.5 mm (3/8") dia. flexible gas pipe of high-strength (18 MPa) is connected to the inlet nozzle of the driver section. To acquire the burst pressure of the Mylar membrane, an analogue pressure gauge of 6.9 MPa (1000 psi) is connected at a distance of 1500 mm from the back end of the driver. The maximum shock pressure attained from the Mylar membranes was 2 MPa.

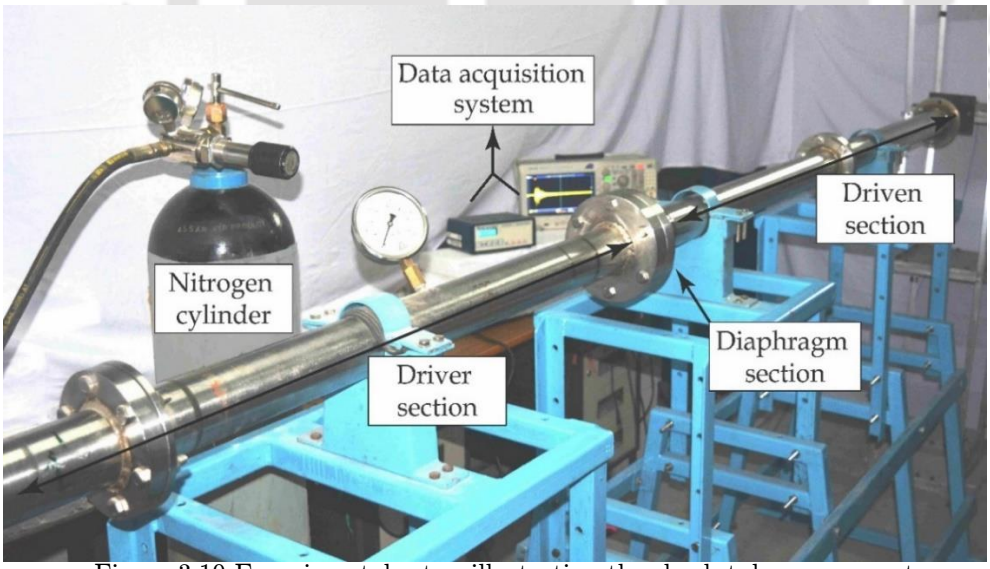

Figure 3.10 Experimental setup illustrating the shock tube components

3.4.2 Diaphragm section

The conventional materials used for the rupture membranes for a shock tube are Matt, Mylar or ductile metal membranes such as Aluminum or stainless steel. The main disadvantage of using the metallic membranes has the probability to destroy the

sensors as well as experiments due to the propulsion of high-density fragments. As the fabrication of metallic membranes is high-priced, Mylar membranes are adapted for their low cost, consistent, and easy to use.

Figure 3.11 shows the membrane clamping mechanism i.e. the diaphragm section. One clamping surface i.e. breech flange is directly machined to the driver section which comprises of female O-ring with an inner diameter of 105 mm. It will be mated with the breech flange machined to the driven section which has a male O-ring with an inner diameter of 100 mm. This sealing O-ring holds and presses the membranes such that it prevents from slipping. Further, both the flanges were tightened with clamping bolts of total 6 number of 10 mm diameter with 120 mm length. After the installation of membranes, clamping bolts should be tightened in a star pattern to ensure proper sealing. This will prevent the driver gas from the leakages. Likewise, the bolts should be loosened gradually in the same star pattern to avoid the load concentrations on single bolts.

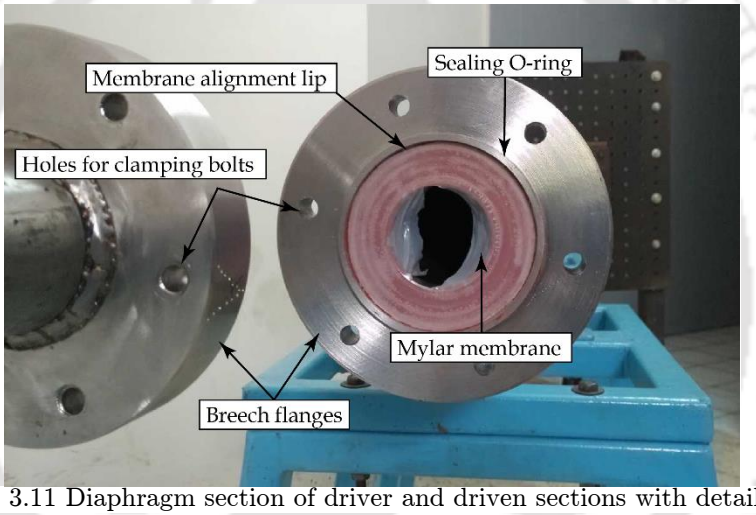

Figure 3.11 Diaphragm section of driver and driven sections with detailed view

3.4.3 Driven section

The driven section was maintained at atmospheric pressure and temperature, referred to as a low-pressure region. One end of the driven section is machined with the breech flange which is a mating part of the diaphragm and the other end i.e. end-wall of the shock tube is machined with a normal flange. Due to the pressure variation between the two sections, sudden rupture of membranes results in the formation of the compression waves. It combines to form a strong shockwave front in the driver section that propagates towards the driven section and leads to the end of the shock tube. Two dynamic pressure transducers are employed to measure the shock wave pressure which was separated by a distance of 700 mm. This transient pressure profile is used to measure shock wave velocity.

3.4.4 Driver and driven section support

Both the driver and driven sections are resting on the U-shape clamps which are bolted to the tubular framework structure. The driver section resting on the U-shape

clamp is allowed to slide back for the membrane loading. The driven section resting on the U-shape clamp is bolted tightly against sliding. There are four adjustable U-clamps mounted on their respective stands along with the shock tube segments as shown in Figure 3.12.

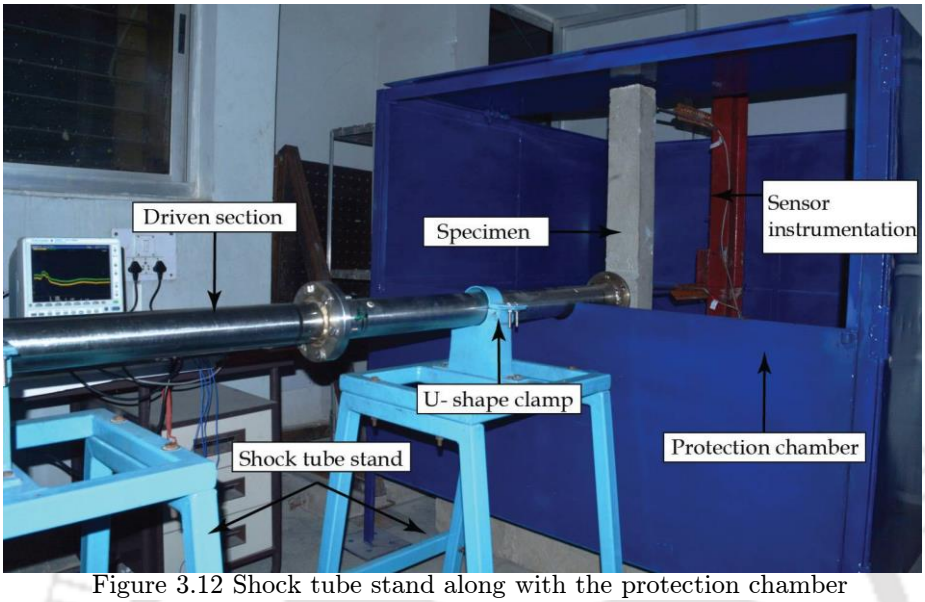

Figure 3.12 Shock tube stand along with the protection chamber

3.4.5 Protection chamber

The protection chamber is made of mild steel frame work of 1.8 m x 1.8m square chamber used for placing the experimental specimen and the data acquisition as shown in Figure 3.12. It has a circular opening on the front face to insert the shock tube end-wall into the protection chamber. It has one large access location throughout the wall that will open up completely like a window for mounting the specimens, viewing them during shock and impact loading. All the faces of the walls are configured with welded and bolted connection to one another. The accessing window is provided with a hinge mechanism to open it and hoist for easy access. The entire framework of the protection chamber is made with ISA 50 x 50 x 4 angles sections welded on the edges of 10 mm thick mild steel plate.

3.5 Characterisation of shock wave profile

The current section briefs the shock tube configurations used for generating the shock waves with focusing towards the characterisation of shock wave. The effects of thickness of diaphragm in terms of number of membranes, type of membranes are described in this section. Adapting these parameters generates different shockwave profiles with varying burst pressure, impulse and the duration of shock decay. To generate a higher peak overpressures, using Helium as driver gas which has low molecular weight is preferable than Nitrogen with high molecular weight. In this case, the negative portion of a Helium-driven shock wave and pulse duration is less prominent and significantly shorter than from a Nitrogen driven shock wave. The bursting of diaphragm from the high-pressure Helium driven gas did not exhibit any

substantial negative pressure in the shockwave profile. It was observed that the increase in the thickness of the diaphragm membrane increases the burst pressure and peak over pressure of shock wave linearly.

3.5.1 Membrane burst characteristics

As discussed in the preceding section, there are different types of burst membranes that can be used in the shock tube application. The ruptured membranes of Matt, Mylar and Aluminum during the shockwave experiment are shown in Figure 3.13, Figure 3.14, and Figure 3.15 respectively. In the current research, Mylar membranes of 1 mm thickness are used in the diaphragm section. The diameter of the Mylar membrane was 100 mm. To increase the burst pressure and shock wave velocity, stacking of multiple membranes was employed. It was observed that the burst pressure of Mylar membranes creates a linear increase pattern with an average value of 0.71 MPa which is nearly three-fourths of the 0.91 MPa burst pressure measured for a 101 mm breech (Holmberg 2010).

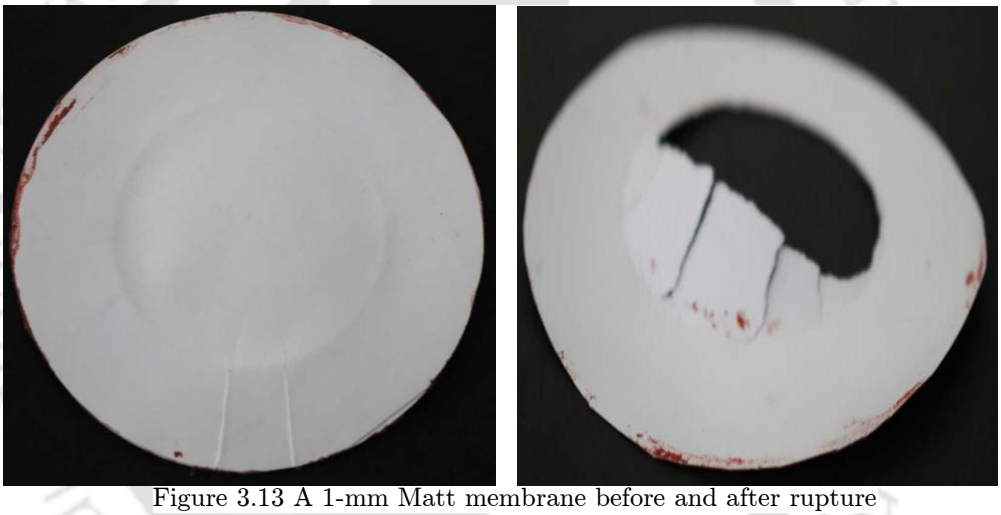

Figure 3.13 A 1-mm Matt membrane before and after rupture

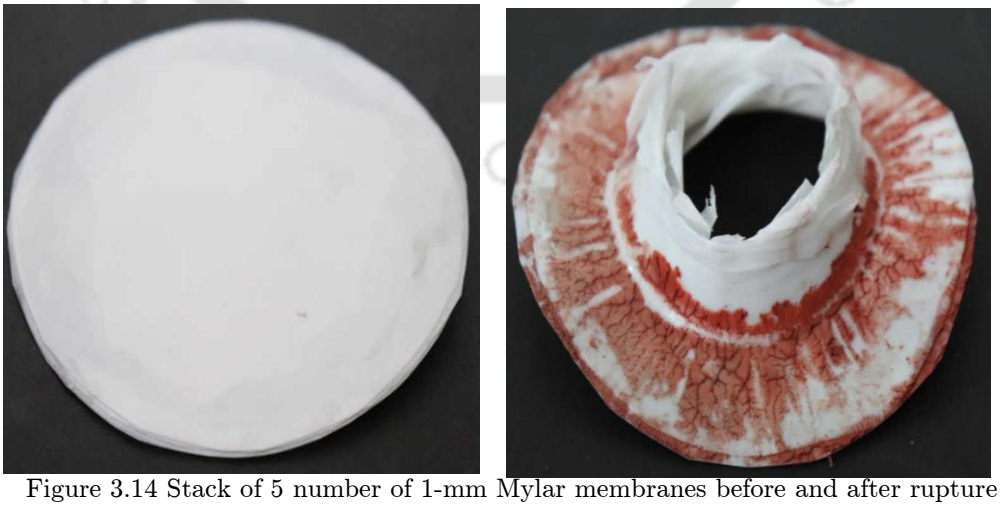

Figure 3.14 Stack of 5 number of 1-mm Mylar membranes before and after rupture

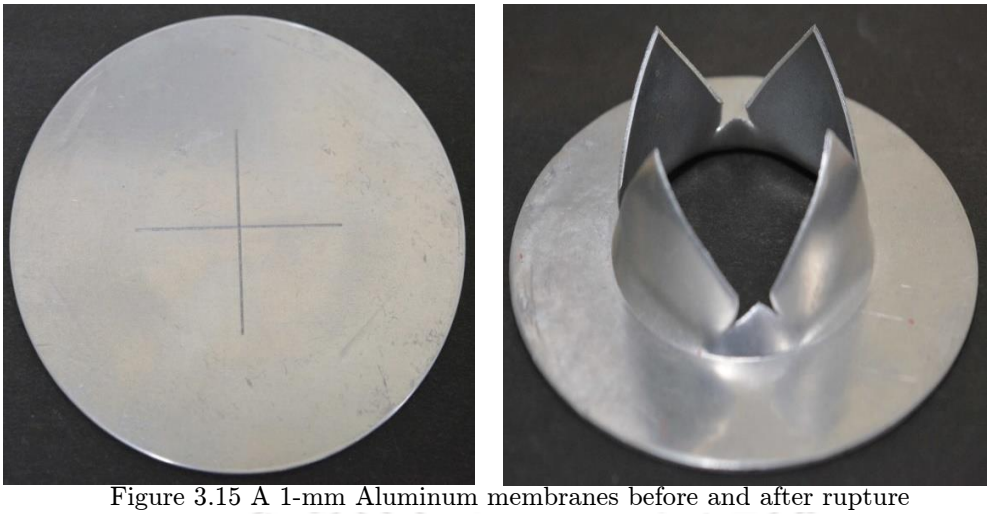

Figure 3.15 A 1-mm Aluminum membranes before and after rupture

Figure 3.16 shows the variation of burst pressure with the number of Mylar membranes. It was observed that the burst pressure increases linearly with the increase in the thickness. The variations in the burst pressure are due to the membrane inconsistencies, different driver gas filling rates, and the pressure transducer sensitivity. It should be considered that any kind of defect on a single membrane layer becomes less significant as the number of membrane layers increases.

3.5.2 Shock wave characterisation

The shock tube was characterized using Nitrogen gas for varying thicknesses of Mylar membranes. The generated shock wave profiles for the thickness of Mylar membranes of one number to five number are shown in Figure 3.17 to Figure 3.19. From the shock wave profile, P1 and P2 refer to the pressure exerted inside the shock tube and P3 refers to the normal pressure imparted directly on the reaction wall.

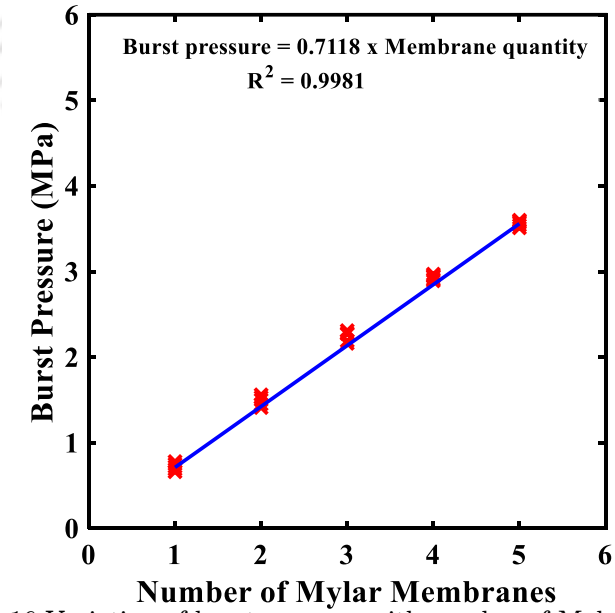

Figure 3.16 Variation of burst pressure with number of Mylar membranes

The burst pressure in the driver section was measured using an analogue pressure gauge. The shockwave pressure profile is measured using dynamic pressure transducers were placed in the driven section that is separated by a distance of 700 mm. The shock arrival of the first local peak will be considered as peak overpressure. The typical rise time of shock wave is about 5 microseconds.

3.5.3 Experimental results and discussion

The calibration of the shock tube was carried out by mounting a dynamic pressure transducer on the reaction wall, and the shock wave was imparted on it. For the characterisation of the shock tube, a total of 15 trails with three repetitions for each set of 1, 2, 3, 4, and 5 Mylar membranes was carried out to ensure reproducibility of the results. The shockwave pressure is measured using two dynamic pressure transducers were placed in the driven section that is separated by a distance of 700 mm. Another pressure transducer is placed normal to the direction of shock wave mounted on the test specimen. Due to the pressure difference in the driver section (P_4) and the driven section (P_1), the diaphragm ruptures resulting in the formation of a shockwave. The parameters controlling the Mach number of the shockwave is the ratio of the pressure (P_4/P_1) and speed of sound (a_4/a_1) of the gases in the driver and driven sections (Gaydon and Hurle 1963). The shock Mach number (M_s) is expressed by Eq.(3.11).

$$\frac{P_4}{P_1}=\left[1+\frac{2\gamma_1}{\gamma_1+1}\left(M_s^2-1\right)\right]\left[1-\frac{\left(\gamma_4-1\right)\left(\sqrt{\frac{a_1}{a_4}}\right)\left(\left\{1+\frac{2\gamma_1}{\gamma_1+1}\left(M_s^2-1\right)\right\}-1\right)}{\sqrt{2\gamma_1}\left(\sqrt{2\gamma_1+\left(\gamma_1+1\right)\left(\left\{1+\frac{2\gamma_1}{\gamma_1+1}\left(M_s^2-1\right)\right\}-1\right)}\right)}\right]^{\frac{-2\gamma_4}{\gamma_4-1}} \tag{3.11}$$

Here, γ_4 (=1.4) and $\gamma_1$are the specific heat ratios for the driver (Nitrogen) and driven (air) gas, respectively. The speed of sound in the gases is given by $a=\sqrt{\gamma RT}$. Here, R_4,T_4 and R_1,T_1 are the characteristic gas constant and initial static temperature for the driver and driven gas, respectively. For the calibration of the shock tube setup, numerous experiments were carried out with different Mylar membranes. The shock wave pressure profile acquired by the pressure transducers from bursting of 1, 2, 3, and 4 Mylar membranes are shown in Figure 3.17 (a and b), and Figure 3.18 (a and b) respectively. The summary of the burst pressure, peak pressure, shock rise, and maximum impulse are detailed in Table 3.5.

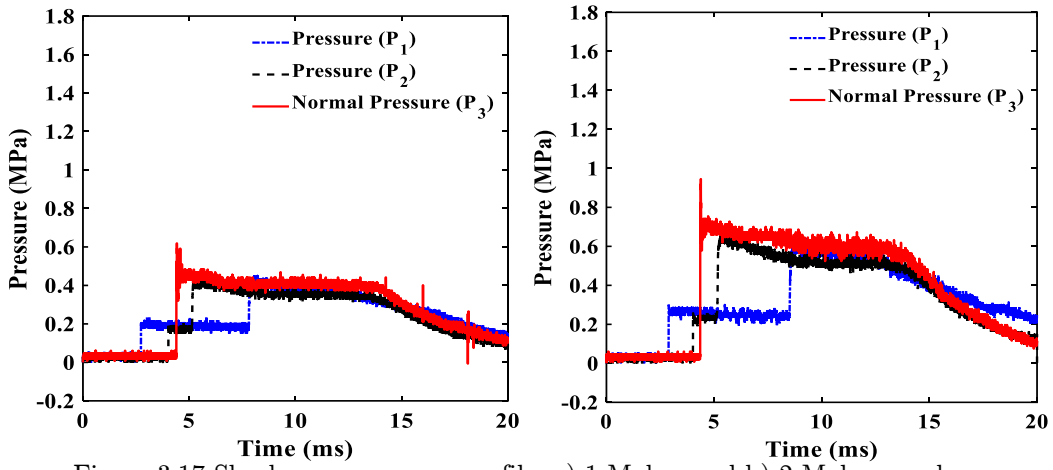

Figure 3.17 Shock wave pressure profile: a) 1-Mylar, and b) 2-Mylar membranes

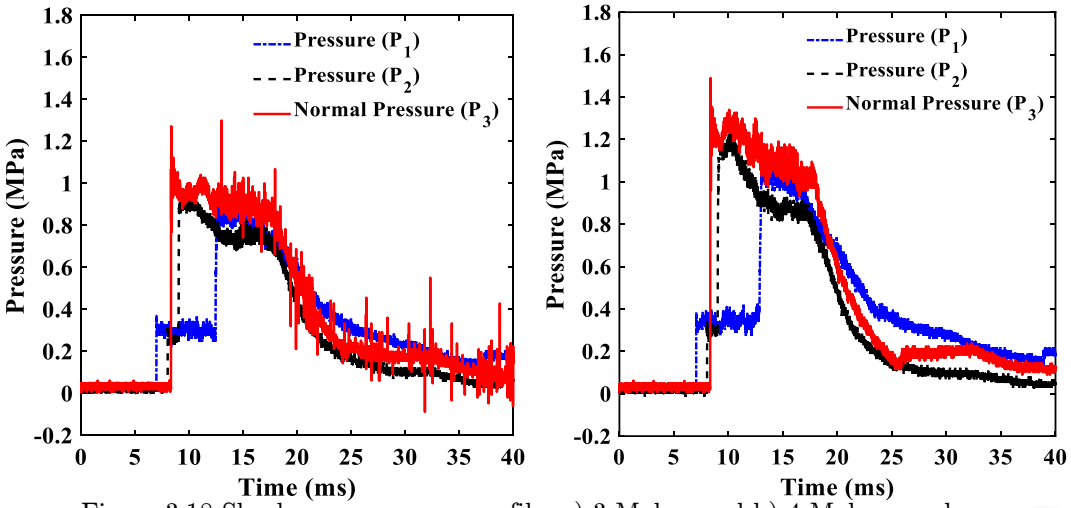

Figure 3.18 Shock wave pressure profile: a) 3-Mylar, and b) 4-Mylar membranes

For the current experimental investigation (results presented in Chapter 4, Section 4.2.2), the diaphragm comprises of 5 Mylar membranes. The Mylar paper ruptures when the pressure in the driver section reaches a bursting pressure of 3.59 MPa at a temperature of 300 K. This results in the generation of a shock wave at the open end of driven section, which travels at a supersonic velocity. The reflected pressure of the generated shock wave is measured to be 1.67 MPa. The shock wave pressure profile for 5 Mylar membrane is shown in Figure 3.19. The average pressure ratio $\left(P_4/P_1\right)$ for rupturing the diaphragm is 24.5. The rise time for the propagation of the shockwave is 10 μs (0.01ms). Based on the experimental time difference in arrival, the average shock wave velocity $\left(V_s\right)$ is calculated as 707 m/s.

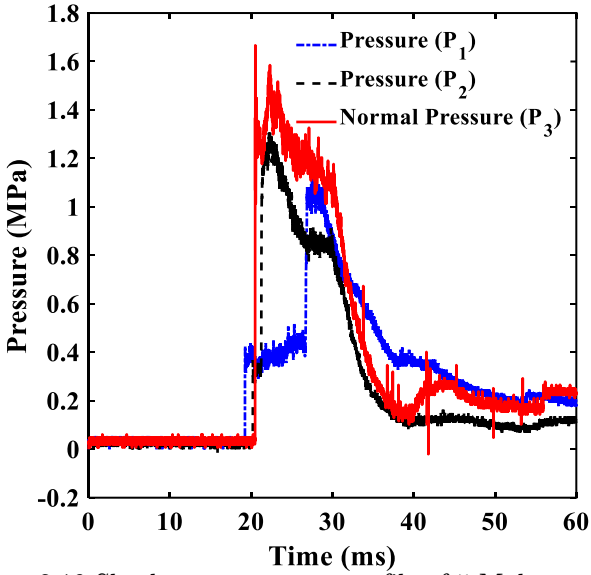

Figure 3.19 Shock wave pressure profile of 5-Mylar membrane

Table 3.5 Summary of burst pressure, peak pressure, shock rise, maximum impulse, and shockwave velocity of the shock wave

Membrane quantity	Burst pressure (MPa)	Peak pressure (MPa)	Shock rise time (ms)	Maximum Impulse (MPa-ms)	Shock wave velocity (m/s)
	0.66	0.39	0.029	5.021	533.7
1	0.72	0.42	0.034	5.053	542.6
	0.78	0.46	0.036	5.142	558.3
	1.41	0.59	0.027	7.163	615.8
2	1.45	0.64	0.032	7.480	618.4
	1.56	0.70	0.033	7.780	623.4
	2.18	0.89	0.025	13.206	640.5
3	2.27	0.91	0.028	13.548	670.5
	2.30	0.96	0.030	13.620	689.4
	2.77	1.03	0.031	15.232	696.4
4	2.89	1.15	0.032	15.545	702.8
	2.97	1.21	0.036	15.757	706.9
	3.47	1.18	0.027	29.071	718.3
5	3.59	1.22	0.030	29.267	721.6
	3.66	1.27	0.035	29.571	734.7

3.5.4 Numerical analysis of shock tube

Finite element analysis is carried out to simulate the inviscid flow of complete shock tube using commercial CFD solver (ANSYS Fluent 13.0). It provides a clear visualization of the flow inside the shock tube as well as the vital information about the pressure and flow magnitude to be acquired for a better insight. The governing Euler's equations of continuity, momentum, and energy are discretized in time and space domain using finite volume approach. The influence of different driver and driven gas regions is incorporated by solving the species transport equations herein. Performing finite element simulation in 3-D approach is computationally expensive and to minimize it axisymmetric 2-D approach has been used which can also give an accurate visualization of the real flow configuration. The computational domain of the shock tube is modeled as an axisymmetric body and the associated initial boundary conditions are illustrated in Figure 3.20.

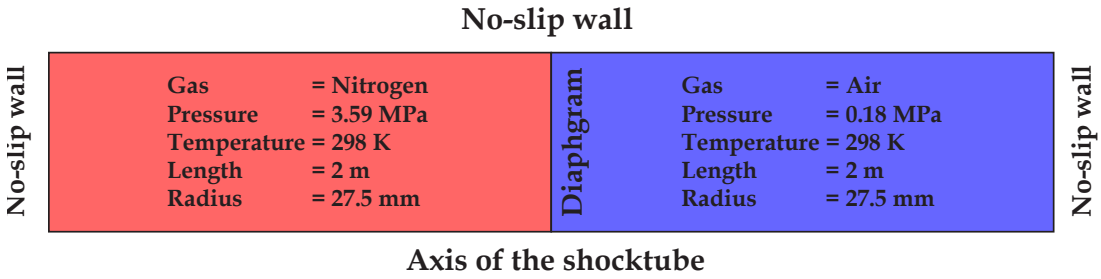

Figure 3.20 Boundary conditions and the computational domain of shock tube

To recreate the experimental conditions, certain boundary conditions are applied in the simulation setup. In the high-pressure region, nitrogen gas is defined at a pressure of 0.72 MPa (Burst pressure for 1 Mylar membrane), and in the low-pressure region, air with atmospheric pressure is defined, having a value of 0.101 MPa. At the beginning of the simulation, the diaphragm was treated as a wall boundary condition. The rupturing of this diaphragm was indicated by changing this wall instantaneously to the interior of the shock tube. No-slip wall condition was used for all the walls except axis of the axis-symmetry. The walls were considered adiabatic with a constant temperature. For the current numerical simulation, the advection upstream splitting method (AUSM) flux vector splitting scheme has been adopted to compute the convective fluxes by using the spatial discretization by Green-Gauss node based 2nd order upwind scheme (De and Thangadurai 2011; Desai et al. 2016; Liou and Steffen Jr 1993; Nanda et al. 2017; Wada and Liou 1997).

A well-structured fine mesh is assigned for the computational domain of the shock tube. In the current simulation, a density-based implicit solver with the Runge-Kutta scheme fourth-order scheme has been employed. To compute the convective fluxes, "Advection Upstream Splitting Method (AUSM)" flux vector splitting scheme is considered. AUSM retains the simplicity and efficiency of a Flux-vector splitting (FVS) scheme, but achieves the high level of accuracy attributed only to Flux-difference splitting (FDS) methods (Liou and Steffen Jr 1993). It has proven that far to be a robust formulation as a variety of Euler and Navier-Stokes calculations will bear out.

The first step is to recognize that the inviscid flux vector, $F_{interface\ 1/2}$ consists of two physically distinct parts, i.e., convective and pressure terms as shown in Eq.(3.12):

$$F_{interface\ 1/2} = \begin{pmatrix} \rho u \\ \rho u^2 \\ \rho H u \end{pmatrix} + \begin{pmatrix} 0 \\ p \\ 0 \end{pmatrix} = F^{(c)}_{interface\ 1/2} + \begin{pmatrix} 0 \\ p \\ 0 \end{pmatrix} \tag{3.12}$$

$$F_{interface\ 1/2} = \frac{1}{2}\left[(\rho u)_{interface\ 1/2} (\psi_L + \psi_R) - \left| (\rho u)_{interface\ 1/2} \right| (\psi_L + \psi_R) \right] + p_{interface\ 1/2}$$

where,

$$\psi = (1, u, H)^t = \frac{\varphi}{\rho}, \quad \varphi = (\rho, \rho u, \rho H)^t$$

where,

$\psi_L, \psi_R = L, R$ properties of corresponding left and right elements

Liou and Steffen Jr (1993) developed an analytical expression for AUSM (M-splitting) as

$$(\rho u)_{interface} = \frac{1}{2}\left[M_{interface} (\rho_L c_L + \rho_R c_R) - \left| M_{interface} \right| (\rho_R c_R - \rho_L c_L) \right] \tag{3.13}$$

where,

$$M_{interface} = u_L / c_L + u_R / c_R, \left| M_{interface} \right| = abs\left(M_{interface} \right)$$

It is noted that the mass flux of the M-splitting AUSM vanishes at a stationary discontinuity, making the AUSM a less dissipative scheme among the above schemes from Eq.(3.14).

$$p_{interface} = p_L + p_R \tag{3.14}$$

where,

$$p_{L,R} = p u_R \begin{cases} \frac{1}{c}\left(\pm 2 - \frac{u}{c} \right) & if\ |u| \le c, \\ \frac{1}{u} & otherwise. \end{cases}$$

For the initialization of the computational domain into two different sections viz. driver and driven sections, a User defined function (UDF) has been adapted (Appendi A). The diaphragm is assumed to ruptured instantly at time t = 0, with an initial condition as shown in the Figure 3.20 which describes the details of simulation configuration. Mesh optimization is performed along with the varying time steps to converge the result. The final mesh and time step used in the simulation to get the results which are independent of the mesh size and time step with adequate resolution of the flow field. The total nodes in the adapted mesh is 320000. Pressure contours

after 4 ms of the rupture of the diaphragm are shown in Figure 3.21. A clear view of incident wave moving from right and an expansion fan from left can be seen in the Figure 3.21. The incident shockwave hits the end wall and reflects back creating high temperature and pressure zone behind it, which can be seen in the Figure 3.21.

As both primary and reflected shocks are the crucial factors during experiments, so jump across these shocks is the critical information acquired as an outcome of simulation and has been compared with the theoretical values in the Table 3.6 and Table 3.7. From Table 3.6 , it was observed that the Mach number (M) of Matt diaphragm for the experimental, analytical, and numerical results are in good agreement with a close match. From Table 3.7, it was found that the Mach number (M) of Mylar diaphragm for the experimental results are having a slight deviation with the analytical, and numerical results. For the given initial conditions, pressure behind the primary shock is calculated from the CFD simulation and formulated in the mentioned tables. A good agreement between the experimental and numerical values strengthens the numerical ability to capture the flow phenomena inside the shock tube. The same numerical model can be used further to estimate the force coefficients on any test model under certain flow conditions by changing the input variables according to the driver gas.

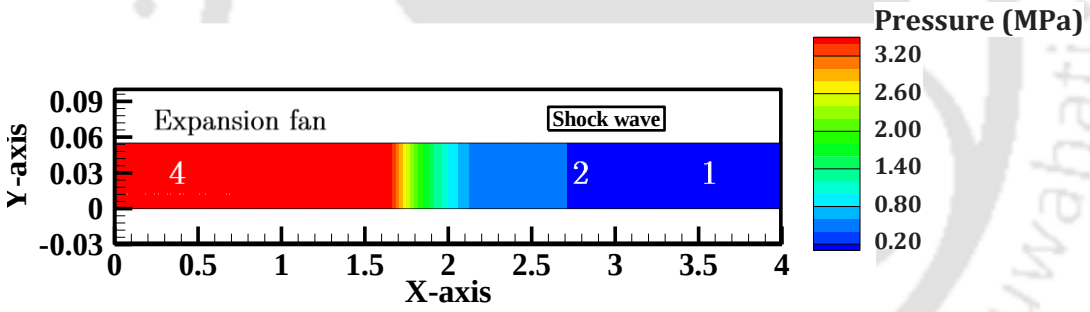

Figure 3.21 Pressure distribution after diagram rupture

Table 3.6 Comparison of experiment, analytical and numerical results of shock tube for Matt diaphragm

No. of Matt Membranes	Burst pressure (P_4)		P_4/P_1	Experimental results			Analytical results			Numerical results		
	Psi	MPa		Output pressure P_2 (MPa)	Mach number (M)	P_2/P_1	Output pressure P_2 (MPa)	Mach number (M)	P_2/P_1	Output pressur P_2 (MPa)	Mach number (M)	P_2/P_1
1	24	0.17	1.64	0.061	1.23	0.61	0.06	1.23	0.61	0.06	1.22	0.59
2	39	0.27	2.67	0.085	1.317	0.84	0.09	1.32	0.86	0.09	1.32	0.85
3	54	0.38	3.72	0.111	1.386	1.1	0.11	1.38	1.08	0.12	1.4	1.18
4	70	0.49	4.82	0.132	1.446	1.3	0.13	1.27	1.27	0.14	1.5	1.36

Note: P1- 1 atm (0.101 MPa)

Table 3.7 Comparison of experiment, analytical and numerical results of shock tube for Mylar diaphragm

No. of Mylar Membranes	Burst pressure (P_4)		P_4/P_1	Experimental results			Analytical results			Numerical results		
	Psi	MPa		Output pressure P_2 (MPa)	Mach number (M)	P_2/P_1	Output pressure P_2 (MPa)	Mach number (M)	P_2/P_1	Output pressur P_2 (MPa)	Mach number (M)	P_2/P_1
1	103	0.72	7.11	0.2	1.55	2.01	0.26	1.55	2.57	0.25	1.2	2.47
2	207	1.45	14.31	0.24	1.78	2.41	0.36	1.78	3.55	0.34	1.64	3.33
3	324	2.27	22.4	0.3	1.94	2.95	0.42	1.94	4.15	0.39	1.69	3.89
4	413	2.89	28.52	0.37	2.03	3.64	0.46	2.03	4.54	0.43	1.86	4.24
5	513	3.59	35.43	0.42	2.04	4.18	0.47	2.04	4.64	0.46	2.03	4.57

Note: P1- 1 atm (0.101 MPa)

Chapter 4

Experimental and analytical investigation of an exterior reinforced concrete beam-column joint subjected to shock loading

4.1 Introduction

Several terrorist attacks on military and civil infrastructure have raised alarms by exposing the vulnerability of reinforced concrete (RC) structures subjected to shock, blast and impact loading. These deliberate events have resulted in casualties and caused catastrophic damage to structures (Baker et al. 2012). The blast shockwave travels at a supersonic velocity and transmits an enormous amount of energy by compressing the air domain. The duration of the shock wave profile is typically in the range of 2 ms to 20 ms (Baker et al. 2012; UFC 3–340–01 (2002); UFC 3–340–02 (2014); UFC 4-010-01 (2013); Meyer et al. 2011). Based on the standoff distance from the source of the explosion, a shock wave can impart both local and global damage to the structure. Global failure is associated with large structural deformation, which is attributed to the excitation of vibration modes (Baker et al. 2012). For a near-field blast, the stress wave propagation through the medium governs the transient response of the structure. The large amplitude stress wave induces nonlinear effects and causes excessive localized material failure (Meyer et al. 2011).

Due to security issues, limited information is available in the open domain on the response of structures subjected to blast loading. The majority of investigations related to blast and shock resistant design are confined to critical infrastructure such as nuclear power plants and other defense installations (ASCE manual 42 (1985), UFC 3-340-01 (2002), UFC 3-340-02 (2014)). Due to high threat level but low return period, limited investigations have been performed on the shock and blast resistant behavior of low-rise buildings. Recently, the frequent use of small-scale explosives has highlighted the importance of considering shock wave effects in the design of residential buildings. Residential buildings majorly constitute RC moment resisting frames (MRF), which are typically designed to resist gravity, wind and earthquake loadings.

From past assessments of failed RC buildings due to earthquake events, it is well known that most of the catastrophic failure can be attributed to the beam-column joints (Saatcioglu et al. 2001; Sezen et al. 2000). These joints are critical and play a vital role in transferring forces and moments between the beam and column (Sezen et al. 2000). The performance and the safety of framed type structures not only depend on the individual structural elements but also on the integrity of the joints. Under lateral loads, the principal mechanisms of failure of a beam-column joint are: i) shear

failure within the joint; ii) anchorage failure of rebars and; iii) bond failure of the beam or column rebars (ACI guidelines and, IS 13920:2016). Structures subjected to earthquake loading undergo large inelastic deformations and require adequate ductility to dissipate energy (MacGregor et al. 1997; Park and Paulay 1975). The ductility of the RC structural member is enhanced by additional detailing and confinement of the concrete with transverse reinforcement (Park and Paulay 1975).

For the low seismic regions, RC moment resisting (MRF) frames are primarily designed to resist gravity loads. For RC-MRF under gravity loading, demands for flexure and shear are higher at the internal beam-column connections. As such, the detailing and anchorage of internal beam-column connections must be superior to external connections. Also, internal connections are laterally confined in both directions by their neighboring joints. On the contrary, the external beam-column joints are laterally confined only with two or three beams, and are thereby less efficient in resisting lateral loads. The behavior of an external beam-column joint has been studied under quasi-static lateral loading (0.025 Hz - 2 Hz) (De Risi et al. 2015; De Risi et al. ; De Risi et al. 2016; De Risi et al. 2017; De Risi and Verderame 2017; Murty et al. 2003; Nie et al. 2008; Pantelides et al. 2017; Ramanjaneyulu et al. 2013; Ricci et al. 2016; Roehm et al. 2015; Sasmal 2009; Sasmal et al. 2011; Sharma et al. 2011; Verderame et al. 2018; Yurdakul and Avsar 2016; Yurdakul and Avsar 2015). Due to inadequate confinement, external beam-column joints are vulnerable to damage under lateral loads, which may arise from an earthquake, impact, shock and blast (Ngo et al. 2007; Parisi and Augenti 2012; Sezen et al. 2000). Moreover, existing reinforced concrete buildings are mainly designed for gravity loads and which are typically built in seismic prone countries before the introduction of suitable seismic design provisions and the implementation of capacity design concepts. From the literature studies, it is confirmed that the expected inherent weakness of these systems is observed in the past earthquake events and terrorist attacks (Agbabian et al. 1994; Dhakal et al. 2005; Hakuto et al. 2000; Marthong et al. 2013; Schofield et al. 2006) . Furthermore, the current chapter is emphasized in the study of the dynamic response of the external beam-column assemblies with typical structural weaknesses/deficiencies involved in the pre-1990s' buildings. However, limited studies have been conducted on the effect of the loading rate on performance of beam-column joints whilst considering various deficiencies such as weak beams in flexure, weak beams in shear and weak columns in shear (Agbabian et al. 1994; Dhakal et al. 2005; Hakuto et al. 2000; Marthong et al. 2013; Schofield et al. 2006). The external beam-column joint, being the weakest link in the structure, requires a comprehensive study for localized shock loads.

Studies have been conducted to evaluate the performance of RC structural members such as beams, columns and slabs subjected to blast and impact loads (Adhikary et al. 2017; Aoude et al. 2015; Cui et al. 2017; Gombeda et al. 2018; Kong et al. 2016; Krauthammer 2017; Lee et al. 2018; Li et al. 2017; Luccioni et al. 2018; Luccioni et al. 2004; Masi et al. 2018; Nystrom and Gylltoft 2011; Peng et al. 2016; Shi et al. 2008;

Thomas et al. 2018; Xu et al. 2016; Yuan et al. 2017). Fujikake et al. (2009) incorporated the high strain rate effect to estimate the flexural capacity of a RC beam subjected to impact. Carta and Stochino (2013) modified their model to develop a theoretical moment-curvature relation for a RC beam under blast loading. Saatcioglu and Baingo (1999) observed that the structures designed and detailed for seismic loading also perform satisfactorily in terms of ductility and drift demands when subjected to blast loading. Lim et al. (2016) conducted finite element analysis to investigate the influence of the shear and diagonal reinforcement detailing on the blast resistance of beam-column joints.

Aoude et al. (2015) conducted a simulated blast loading test on a steel fiber reinforced column (SFRC) and demonstrated its superior blast resistant characteristics. Due to restrictions on the use of explosives, blast simulators such as shock tubes and hydraulic blast actuators are used to characterize the response of a structure subjected to blast loading (Stewart and Durant 2016; Subramaniam et al. 2009; Vivek and Sitharam 2018). Magnusson and Hallgren (2003) conducted an air blast loading test on a RC beam and studied the influence of the steel fibers and strength of concrete on its performance under blast loading. The air blast test was conducted with the TNT explosive charge detonated inside a shock tube. It was observed that the inclusion of fibers enhances the ductility of the member. It was also observed that the beam with a high steel reinforcement ratio fails under shear while beam with low a reinforcement ratio fails in flexure. Li et al. (2012) conducted a series of blast simulator tests on columns designed with seismic considerations. They observed that such columns showed blast resistant characteristics in terms of high ductility and enhanced damage tolerance.

Krauthammer (Krauthammer 2008) studied the influence of blast overpressures on the ductility of a RC structural member. The magnitude of damage in the structure is quantified using a performance indicator based on the support rotation and ductility. ASCE manual 42 and UFC 3-340-01 consider the damage to be severe when the member rotation exceeds 4° for a doubly reinforced beam and column. However, Krauthammer (2017), argued that the member level ductility and maximum support rotation are not sufficient to evaluate the level of damage, and overall stress and strain behavior in the member should be investigated. Krauthammer (2017) and Abedini et al. (2018) have proposed simplified design charts such as shock response spectra and pressure inpulse (P-I) diagrams for predicting the structural behaviour and quantifying the damage level of RC structures subjected to blast loading. These popular design charts are derived from a single degree of freedom (SDOF) approximation using an elastic-perfectly plastic resistance function UFC 3–340–02 (2014).

Based on the literature review, most of the investigations are focused on far-field shock loading (Adhikary et al. 2017; Kyei and Braimah 2017; Ngo et al. 2007; Parisi and Augenti 2012). There is lack of systematic research on the structural response of members subjected to near-field shock loading. Also, limited investigations have been conducted on the performance of beam-column joints under blast loading, which are

most vulnerable to such threats (Lim et al. 2016; Parisi and Augenti 2012; Remennikov et al. 2017; Syed et al. 2018). The key motivation of the current research is to study the behavior of a beam-column sub assemblage subjected to shockwave loading. The aim of this chapter is to study the dynamic response of an external beam-column joint under shock loading using experimental and numerical investigations. Most of the earlier investigations have focused on shock, blast and impact loading on individual structural members i.e., beam, column and slab elements (Abedini et al. 2018; Aoude et al. 2015; Kyei and Braimah 2017; Li et al. 2012; Lim et al. 2016; Magnusson and Hallgren 2003; Ngo et al. 2015; Syed et al. 2018; Zhang et al. 2013). Conducting full-scale blast tests in the field is expensive, and also requires experience and licensing in handling explosives. Experiments at reduced scales are adopted to investigate the structural behavior and dynamic response. In this investigation, the dynamic response of the external beam-column joints with deficiencies such as weak beams in flexure, weak beams in shear, and weak columns in shear, are studied in detail. The beam column sub-assemble is idealized as a single degree of freedom system and its dynamic response is evaluated. The peak dynamic response for a bilinear resistance system is evaluated for different amplitudes and durations of shock loading to generate a design aid using the shock response spectrum.

4.2 Experimental program

A far-field blast is a typical unconfined explosion that occurs above the ground level. Figure 4.1 shows the propagation of blast wave on building along with deflected shape of the frame. As the shock wave propagates and continues outwards along the ground surface, a wave front known as Mach stem is formed by the interaction of the reflected wave and initial wave (Geretto et al. 2015). The intermediate amplification of the wave caused by ground reflections arises prior to the arrival of the initial blast

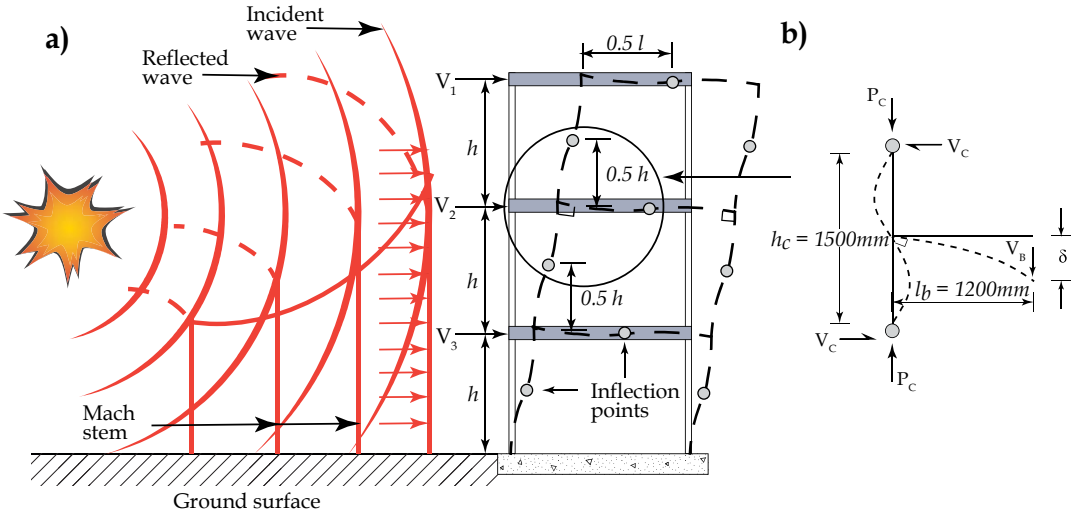

Figure 4.1 a) Propagation of blast wave on building along with deflected shape of the frame showing the points of contra-flexure under lateral loading, and b) isolated external beam-column joint sub-assembly

wave near the building. For a typical far-field blast, due to enough standoff distance from the explosive location, this Mach stem when approaches the building gets converted into a distributed lateral pressure along the building height as shown in the Figure 4.1 (a). Full scale experimental testing of moment frames is infeasible and therefore we idealized the experiments to simulate the loading conditions under a far field explosion.

4.2.1 Materials and specimen fabrication

The design of the beam-column sub-assembly is conducted according to IS 456: 2016 and IS 13920: 2016. The specimens are classified into three categories: i) Beam weak in shear (BS); ii) Beam weak in flexure (BF), and iii) Column weak in shear (CS). The first two configurations are designed based on the concept of a strong column-weak beam design philosophy for efficient energy dissipation (Park and Paulay 1975). However, the third specimen is considered for studying the dynamic behavior of the weak column in shear. Under each category, two test specimens are considered, which are: i) designed for gravity loads without any seismic detailing; and ii) designed with seismic detailing. For all the three categories of the specimens, the joint core is designed as unreinforced for both seismic and non-seismic specimens. A total of six half-scale beam-column joints are tested under localized shock loading. The description and notation used for the test specimens are listed in Table 4.1. Material tests are conducted to estimate the strength properties of the concrete and reinforcing steel. The mean characteristic compressive strength (f_{cr}) and mean split tensile strength (f_{tr}) of the concrete at 28 days of curing is 35.7 N/mm^2 and 4.0 N/mm^2, respectively. The yield strength (f_y), ultimate strength (f_t) and hardening ratio of the 12 mm longitudinal reinforcing steel bar is 566 MPa, 688 MPa and 1.21, respectively. The experimental investigation is conducted to study the evolution of cracks at the beam-column joint due to localized shock loading. Dynamic response quantities such as displacement and acceleration are measured at distinct locations along the length of the beam.

Table 4.1 Notation for the frame configuration used for the test specimens

Frame configuration	Gravity load design (IS 456: 2016)	Gravity load design with seismic detailing (IS 456: 2016 & IS 13920: 2016)
Beam weak in shear	BSNS	BSS
Beam weak in flexure	BFNS	BFS
Column weak in shear	CSNS	CSS

The typical full-scale structure is considered to have an inter-story height of 3.0 m and a beam length of 4.8 m. In the present study, the half-scale model is used to study the behavior of the isolated external beam-column subassembly as shown in Figure 4.1 (a) & (b). Under lateral loading, the typical deflected shape of the moment resisting frame is as shown in Figure 4.1 (a).

For typical moment resisting frames, the point of contra-flexure is assumed to be at the mid-height of the column and mid-length of the beam. At the inflection points, the shear force and axial load in the column are represented by V_C and P_C, respectively, and the shear force in the beam is represented by V_B. This test configuration is widely adopted by the earthquake engineering community and used to assess the seismic performance of the beam-column joint, and here it is extended to assess performance under shock/blast loads (Lim et al. 2016; Park and Paulay 1975). The reinforcement details of the beam-column joint specimens are listed in Table 4.2. A schematic of the reinforcement detailing in the external beam-column joint is illustrated in Figure 4.2.

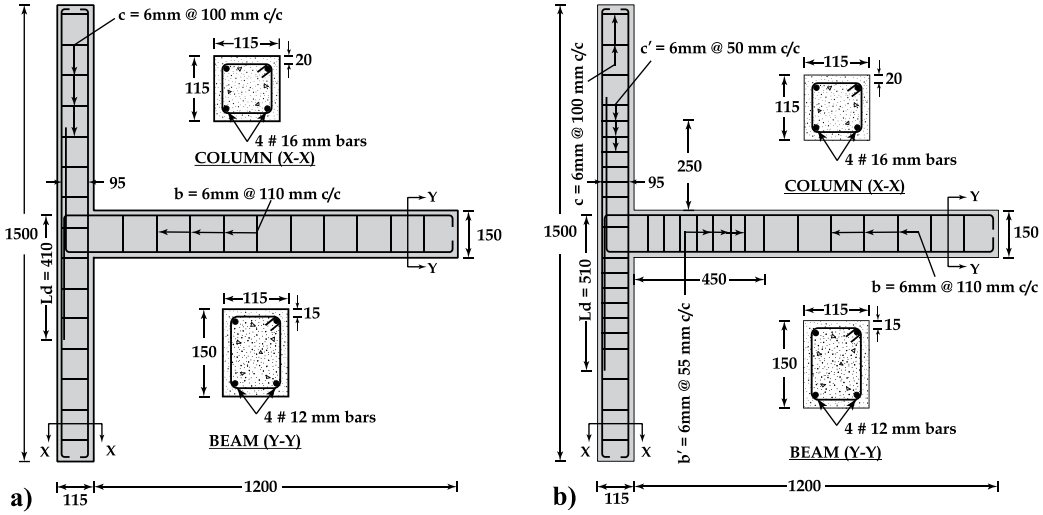

Figure 4.2 Beam-column joint geometry and reinforcement detailing of: a) BSNS; and b) BSS specimens at half-scale

Table 4.2 Reinforcement details of the beam-column joint

Specimen Notation	Beam reinforcement			Column reinforcement		
	Main bars	Vertical stirrups spacing of 6 mm bars		Longitudinal bars	Lateral ties spacing of 6 mm bars	
BSNS	4 – 12mm ø	b = 180 mm c/c		4 – 16mm ø	c = 100 mm c/c	
BFNS	4 – 10mm ø	b = 110 mm c/c		4 – 16mm ø	c = 100 mm c/c	
CSNS	4 – 12mm ø	b = 110 mm c/c		4 – 12mm ø	c = 250 mm c/c	
BSS	4 – 12mm ø	b = 180 mm c/c	b' = 90 mm c/c	4 – 16mm ø	c = 100 mm c/c	c' = 50 mm c/c
BFS	4 – 10mm ø	b = 110 mm c/c	b' = 55 mm c/c	4 – 16mm ø	c = 100 mm c/c	c' = 50 mm c/c
CSS	4 – 12mm ø	b = 110 mm c/c	b' = 55 mm c/c	4 – 12mm ø	c = 250 mm c/c	c' = 125 mm c/c

4.2.2 Experimental setup and instrumentation

The detailed presentation of experimental setup and loading is discussed in Chapter 3 (Section 3.5.3). In this study, the pressure profile achieved from the bursting of 5 Mylar membranes is used to conduct experimental investigations. The shock wave profile employed in the present study is represented in Figure 3.19. The shockwave pressure profile is measured using dynamic pressure transducers (ICP pressure probe, PCB Piezotronics Model #113B22) with a sampling rate of 100 kS/s recorded for 100 ms that are separated by a distance of 700 mm. The propagated shockwave is directly imparted on the RC beam. The beam-column sub-assembly is subjected to shock loading; respective accelerations and displacements are measured along the beam's length at a distance 115 mm, 360 mm, 605 mm, and 850 mm, from the tip of the beam. The acceleration in the beam was measured using accelerometers (ICP Shock accelerometer, PCB Piezotronics Model #350C04) and processed using signal conditioner (4-Channel ICP Signal conditioner, PCB Piezotronics Model #482C24) with a sampling rate of 250 kS/s recorded for 40 ms. The deflection of the beam was measured using three linear variable differential transducers (Inductive Displacement Measurement with Loose plunger, HBM Model #WA-L) with a sampling rate of 10 kS/s recorded for 100 ms. The dynamic response is acquired with the help of oscilloscope (Tektronix Mixed Domain- MDO-3024) having a bandwidth of 200 MHz and a maximum sampling rate of 2.5 GS/s. The shock tube setup along with the experimental specimen instrumented with sensors is shown in Figure 4.3.

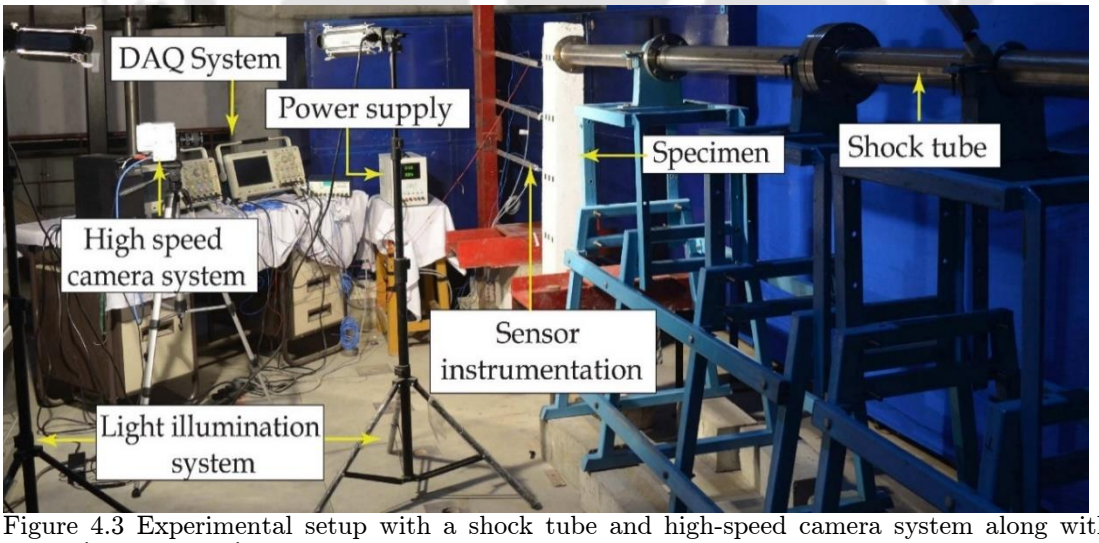

Figure 4.3 Experimental setup with a shock tube and high-speed camera system along with sensor instrumentation

A high-speed video camera (Phantom VEO 640L) was employed to record the dynamic response of the beam-column sub-assemblies. The imaging is recorded at 7,300 frames per second (FPS) with a pixel resolution of 512 x 1024 to maintain a proper visualization of the shock phenomena on the specimen. To facilitate a good illumination during the imaging process a pair of non-flickering high wattage halogen lights were

installed. The exposure time of each photograph is 135.25 μs with an inter-frame time of 15ms. The speckles (black square markers) attached along the length of the beam are used to track the transverse displacement using image correlation. Triggering of the camera is facilitated by a piezoceramic (PZT) sensor attached on the rear side of the tip of the beam as shown in Figure 4.3.

4.3 Numerical investigation

Finite element analysis is conducted to simulate the dynamic response of the RC beam-column joint subjected to shock loading using commercial FEM software Abaqus 6.8. The constitutive behavior of concrete is modelled using the concrete damage plasticity (CDP) model (Lubliner et al. 1989). The damage induced in the material is quantified using two scalar damage variables in compression and tension as d_c and d_t, respectively. Birtel and Mark (2006) has proposed empirical equations for the damage parameters, which are used in current investigation. These damage parameters are functions of inelastic strain.

4.3.1 Constitutive relationship for confined concrete with strain rate effect

Mander et al. (1988) proposed a unified stress-strain relationship of confined concrete under compression and is employed in the present study and shown in Figure 4.4 (a). The influence of the confinement by transversal reinforcement is incorporated in the material model. The details of the stress-strain relationship for confined concrete can be found at Mander et al. (1988). The influence of strain rate on the stress-strain behavior of confined concrete is incorporated based on the model proposed by Fujikake et al. (2009). Under dynamic loading, the effects of high strain rates and transverse confinement increases the concrete capacity due to strain hardening effects. The static material properties are no longer valid and the dynamic effects should be accounted. For any given strain rate $\dot{\varepsilon}$, the modified values of f_c, ε_c, E_o are given by Eqs. (4.1), (4.2) and (4.3), respectively (Fujikake et al. 2009). Here $\dot{\varepsilon}_{sc}$ is representative of the strain rate for concrete under compression and is given as $\dot{\varepsilon}_{sc} = 1.2\times10^{-5}\left(s^{-1}\right)$.

$$f_{cd} = f_c\left(\frac{\dot{\varepsilon}}{\dot{\varepsilon}_{sc}}\right)^{0.006\left[\log\left(\frac{\dot{\varepsilon}}{\dot{\varepsilon}_{sc}}\right)\right]^{1.05}} \tag{4.1}$$

$$\varepsilon_{cd} = \varepsilon_c\left(\frac{\dot{\varepsilon}}{\dot{\varepsilon}_{sc}}\right)^{-0.036+.01\left[\log\left(\frac{\dot{\varepsilon}}{\dot{\varepsilon}_{sc}}\right)\right]} \tag{4.2}$$

$$E_{od} = E_o\left(\frac{\dot{\varepsilon}}{\dot{\varepsilon}_{sc}}\right)^{0.002\left[\log\left(\frac{\dot{\varepsilon}}{\dot{\varepsilon}_{sc}}\right)\right]^{1.12}} \tag{4.3}$$

In the above equations, the subscript 'cd' refers to the values in compression under dynamic loading. Similar to compression, the modified tensile properties of concrete due to strain rate effects are given by Eqs. (4.4) and (4.5), respectively. $\dot{\varepsilon}_{st}$ is the reference strain rate of concrete in tension $\left(1\text{x}10^{-7}(\text{s}^{-1})\right)$. The ultimate tensile strain in concrete is limited to $\varepsilon_{tu} = 4\times10^{-4}$. The tensile strength under static loading is related to the peak compressive strength of concrete (Fujikake et al. 2009). The flexural strength and ductility of the concrete section are significantly increased due to lateral confinement. Mander et al. (1988) have developed a unified constitutive model for confined concrete and proposed a strength amplification factor.

$$f_{td} = f_t\left[\exp\left(0.00126\left(\log_{10}\left(\frac{\dot{\varepsilon}}{\dot{\varepsilon}_{st}}\right)^{3.373}\right)\right)\right] \tag{4.4}$$

$$f_t = 0.23 f_c^{2/3} \tag{4.5}$$

4.3.2 Constitutive material model for reinforcing steel

An elastic-plastic constitutive relationship with strain hardening is assumed for the reinforcing steel and is shown in Figure 4.4(b). Based on the experimental investigation, it was assumed that the elastic modulus E_s and the strain hardening modulus E_{sp} are independent of loading rates (Ammann et al. 1982; Limberger et al. 1982). The influence of rate of loading on the yield strength is considered in the present study. The relationship of dynamic yield strength $\left(f_{syd}\right)$ on the strain rate is adapted from Japan Society of Civil Engineers (JSCE) 1993 and given by Eqs. (4.6) - (4.8):

$$f_{syd} = f_{sys}(1.202 + 0.040\text{x}\log_{10}\dot{\varepsilon}) \geq f_{sys} \tag{4.6}$$

where, f_{syd} = dynamic yield strength at any stain rate $\dot{\varepsilon}$ and f_{sys} = static yield strength. Finally, the stress-strain relationship for reinforcing steel is given as

$$\sigma = E_s\varepsilon \quad \text{for} \quad \varepsilon \leq \varepsilon_{syd} \tag{4.7}$$

$$\sigma = f_{syd} + E_{sp}(\varepsilon - \varepsilon_{syd}) \quad \text{for} \quad \varepsilon > \varepsilon_{syd} \tag{4.8}$$

in which ε_{syd} = strain corresponding to the dynamic yield strength: $\varepsilon_{syd} = f_{syd} / E_s$ and E_{sp} = strain hardening modulus. The slope of loading and unloading is assumed to be same and equal to E_s.

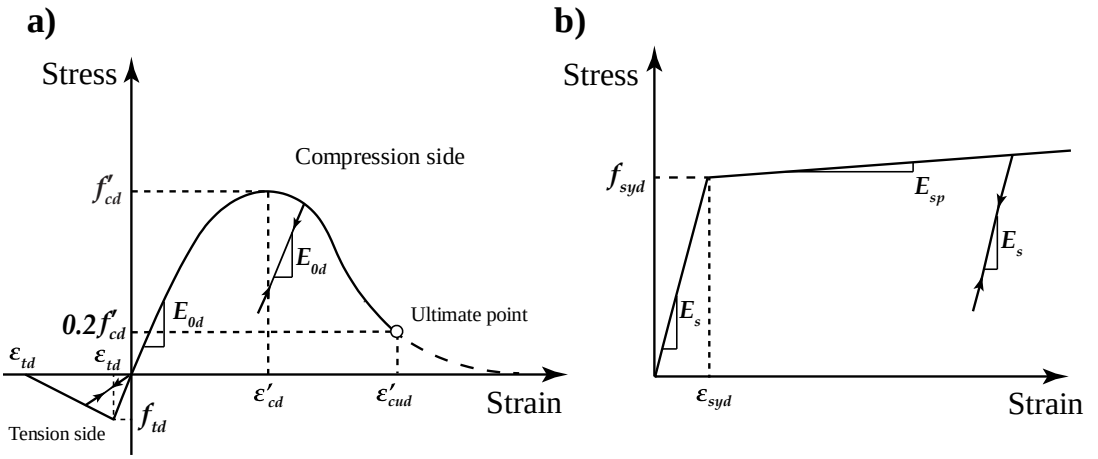

Figure 4.4 Stress strain relationship: a) confined concrete, and b) reinforcing steel with strain rate effect

4.3.3 Geometric and model parameters

The geometric and reinforcement detailing of the experimental specimens are presented in Section 4.2.1. The concrete section is modelled using continuum three-dimensional eight noded hexagonal element with reduced integration (C3D8R). A finer mesh is generated near the beam-column joint to accurately capture the dynamic response. The longitudinal and transverse reinforcement bars are discretized as T3D2 truss elements. An embedded region constraint is used to simulate the bond between the reinforcement bars and the surrounding concrete. The reinforcement detailing and the finite element mesh of the beam-column subassembly are shown in Figure 4.5.

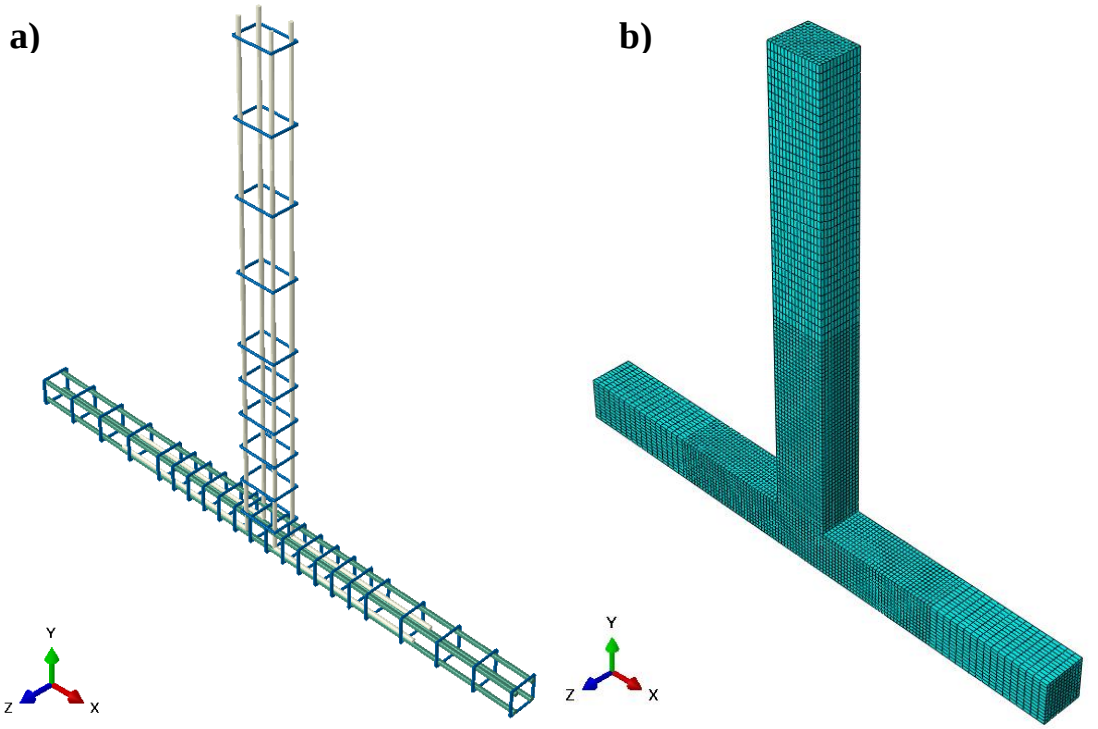

Figure 4.5 a) Reinforcement detailing, and b) Finite element mesh of the beam-column sub-assembly

A relatively fine mesh is needed for numerical convergence. Hence, the specimen is discretized into a total of 32,500 elements. The Young's modulus and Poisson's ratio of steel reinforcement are 200 GPa and 0.3, respectively. The density of steel and concrete is assumed to be 7850 kg/m^3 and 2400 kg/m^3, respectively. The Poisson's ratio of concrete is taken as 0.2. The points of contra-flexure in the column are provided with a pin-joint restraint. The shock pressure is recorded during the experiments using pressure sensors. This time, variant pressure is applied over an area equal to the cross-sectional area of the shock tube. The displacement time histories are calculated at the nodes where LVDT's are located. The finite element response is compared with the experimental results and the results are reported in Figure 4.19 and Table 4.5.

4.4 Analytical investigation

4.4.1 Moment-curvature relationship

The flexural capacity and the ductility of the RC section is estimated using the moment-curvature $(M-\varphi)$ relationship. In this study, a simplified bilinear approximation is adapted to idealize the nonlinear $M-\varphi$ relationship. Under-reinforced sections are always preferred in the design of RC structures because they ensure a ductile mode of failure. Over-reinforced RC sections show a brittle mode of failure with little or no warning prior to failure. The moment and curvature are determined at yield and ultimate states by imposing translational and rotational equilibrium (Carta and Stochino 2013). Curvature ductility of the section is defined as the ratio of the ultimate curvature to the yield curvature. For a doubly reinforced concrete section, the variation of stress and strain along the section depth is shown in Figure 4.6. For under-reinforced sections, when the tensile steel reinforcement yields, the strain in the extreme compression fiber is less than the limiting strain in concrete $\varepsilon_{c,\lim}$. The effect of dynamic strain rate and lateral confinement are considered, and the amplified strength parameters are used in the equilibrium equation. Assuming the tensile force of concrete to be zero, translational equilibrium of the concrete section under compression and tension gives:

$$b\int_0^{X_y}\frac{f_{cc}^{'}\left(\frac{\varepsilon}{\varepsilon_{cc}^{'}}\right)r}{r-1+\left(\frac{\varepsilon}{\varepsilon_{cc}^{'}}\right)^r}d_y+\sigma_{ss}A_{sc}=\sigma_{sy}A_{st} \tag{4.9}$$

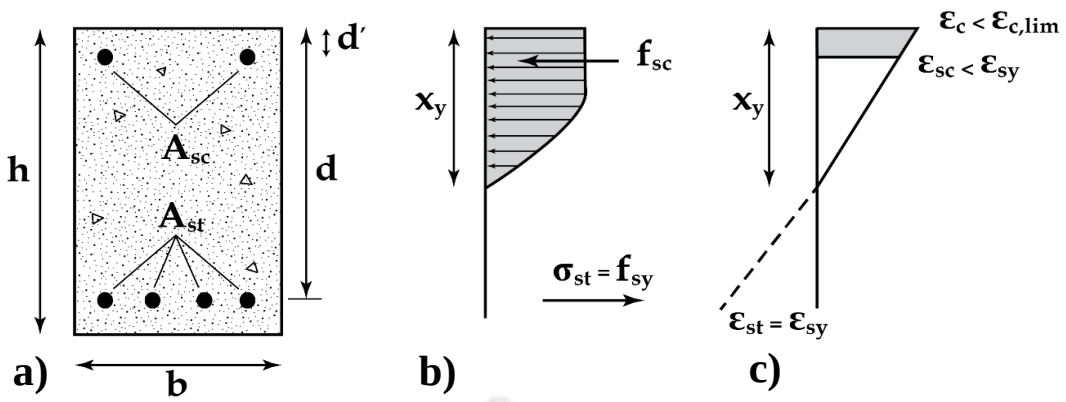

Figure 4.6 a) Cross section of a doubly reinforced concrete beam, b) stress diagram at the yield state, and c) strain diagram at the yield state

Here, X_y represents the depth of the neutral axis. The strain $'\varepsilon'$ at any depth $'y'$ from the top compression fiber is written as, $\varepsilon = \varepsilon_{sy}\dfrac{X_y - y}{d - X_y}$ from the property of similar triangles (Figure 4.6). Replacing the $'\varepsilon'$ and $'\varepsilon_{ss}'$ in Eq.(4.9), we obtain:

$$b\int_0^{X_y}\frac{f_{cc}^{'}\left(\dfrac{\varepsilon_{sy}}{\varepsilon_{cc}^{'}}\dfrac{X_y - y}{d - X_y}\right)r}{\left(r - 1 + \left(\dfrac{\varepsilon_{sy}}{\varepsilon_{cc}^{'}}\dfrac{X_y - y}{d - X_y}\right)^r\right)}d_y + E_s\varepsilon_{sy}\left(\frac{X_y - d'}{d - X_y}\right)A_{sc} = \sigma_{sy}A_{st} \qquad (4.10)$$

The solution of Eq.(4.10) provides the depth of the neutral axis. The resisting bending moment (M_y) of the section at yield is obtained by imposing rotational equilibrium as follows:

$$M_y = b\int_0^{X_y}\frac{f_{cc}^{'}\left(\dfrac{\varepsilon_{sy}}{\varepsilon_{cc}^{'}}\dfrac{X_y - y}{d - X_y}\right)r}{r - 1 + \left(\dfrac{\varepsilon_{sy}}{\varepsilon_{cc}^{'}}\dfrac{X_y - y}{d - X_y}\right)^r}(d - y)d_y + E_s\varepsilon_{sy}\left(\frac{X_y - d'}{d - X_y}\right)(d - d')A_{sc} \qquad (4.11)$$

Once the tensile reinforcement has yielded, further application of the continuous moment will cause the concrete to attain its ultimate limit strain $(\varepsilon_{c,\lim})$.At this stage, one of two scenarios is likely to occur i.e. the compressive reinforcement is i) elastic; or ii) yields. Assuming that the compressive steel is elastic, the strain $'\varepsilon'$ at any depth $'y'$ from the top compression fiber is given by $\varepsilon = \dfrac{\varepsilon_{c,\lim}}{\varepsilon_{cc}^{'}}\dfrac{X_u - y}{X_u}$. Using a similar analogy to that discussed above, the ultimate moment M_u is determined. The yield curvature (φ_y)

and ultimate curvature (φ_u) is derived from the strain-distribution diagram using Eqs. (4.12) and (4.13), respectively.

$$\varphi_y = \frac{\varepsilon_{sy}}{d - X_y} \tag{4.12}$$

$$\varphi_u = \frac{\varepsilon_{c,\lim}}{X_u} \tag{4.13}$$

The representative moment curvature relationship for the specimen of type 'BSNS' is shown in Figure 4.7.

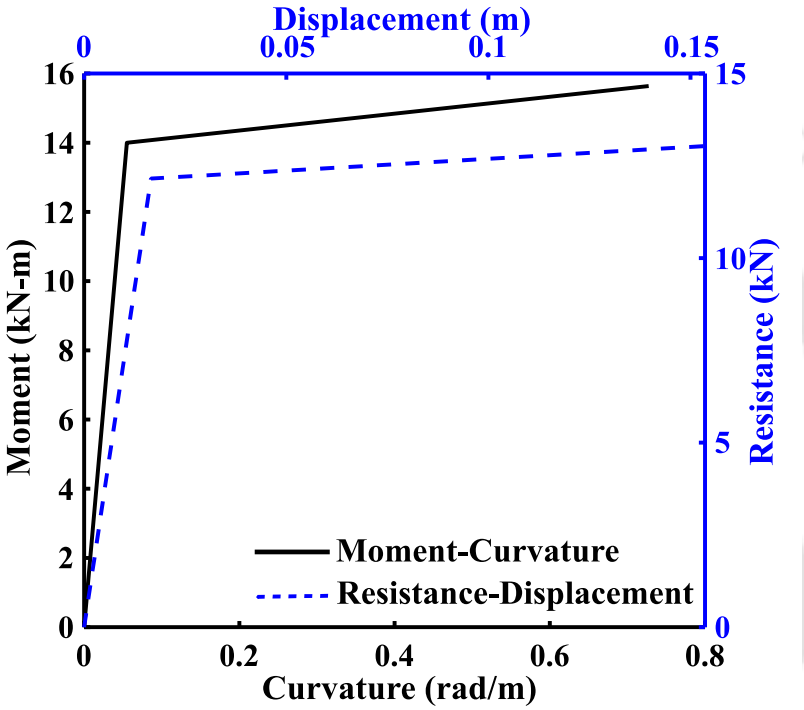

Figure 4.7 Moment-curvature and resistance-displacement relation of an RC section

4.4.2 Resistance-deflection relationship

The resistance–displacement $(r-\delta)$ curve is derived using moment-curvature relationship. For the loading condition under consideration, the system is idealized as a cantilever. The yield load and ultimate load is evaluated as follows:

$$r_y = P_y = \frac{M_y}{l} \tag{4.14}$$

$$r_u = P_u = \frac{M_u}{l} \tag{4.15}$$

The rotation between ends A and B can be obtained by integrating the curvature (φ) over the length AB (refer Figure 4.8). The total deflection (δ) at the point of interest is calculated by taking the moment of area under the curvature diagram.

$$\theta_{AB} = \int_{A}^{B} \phi(dx) \tag{4.16}$$

$$\delta_{AB} = \int_{A}^{B} \phi x(dx) \tag{4.17}$$

A concentrated plastic hinge is assumed to form at the fixed end. Figure 4.8 shows the bending moment diagram and curvature diagram along the length of the beam for the assumed load conditions. The total rotation at the free end is calculated using the area under the curvature diagram. The length of the plastic hinge l_p is assumed as $l_p = d_{eff} + 0.05l$ (Mattock 1967).

$$\theta = \theta_{el} + \theta_{pl} \tag{4.18}$$

$$\theta = \frac{1}{2}\varphi_y l + \left(\varphi_u - \varphi_y\right) l_p \tag{4.19}$$

Similarly, total plastic deflection at the free end is expressed as a sum of the elastic and plastic deflection as follows:

$$\delta_u = \delta_y + \delta_{pl} \tag{4.20}$$

$$\delta_u = \frac{\varphi_y l^2}{3} + \left[\left(\varphi_u - \varphi_y\right) l_p \times \left(l - \frac{l_p}{2}\right)\right] \tag{4.21}$$

After calculating δ_y and δ_u, the equivalent elastic stiffness K_{el} and plastic stiffness K_{pl} is calculated as:

$$K_{el} = \frac{P_y}{\delta_y} \tag{4.22}$$

$$K_{pl} = \frac{P_u - P_y}{\delta_u - \delta_y} \tag{4.23}$$

4.4.3 Single degree of freedom (SDOF) idealization

The dynamic response of the RC beam-column joint is evaluated using a SDOF idealization. The governing equation of motion of a SDOF system with a bilinear resistance function under an external excitation $P(t)$ is given as:

$$M_{el}\frac{d^2y(t)}{dt^2}+K_{el}y(t)=P(t) \text{ for } 0\le y\le \delta_y \tag{4.24}$$

$$M_{pl}\frac{d^2y(t)}{dt^2}+K_{pl}y(t)+\left(K_{el}-K_{pl}\right)\delta_y=P(t) \text{ for } \delta_y< y\le \delta_u \tag{4.25}$$

M_{el} and M_{pl} are the equivalent masses in the elastic and plastic regime, and are calculated using load mass factors K_{LM}. The load mass factor is defined as ratio of load factor K_L over mass factor K_M. The mass factor K_M is the ratio of mass of the equivalent system M_E to total mass of the actual system M.

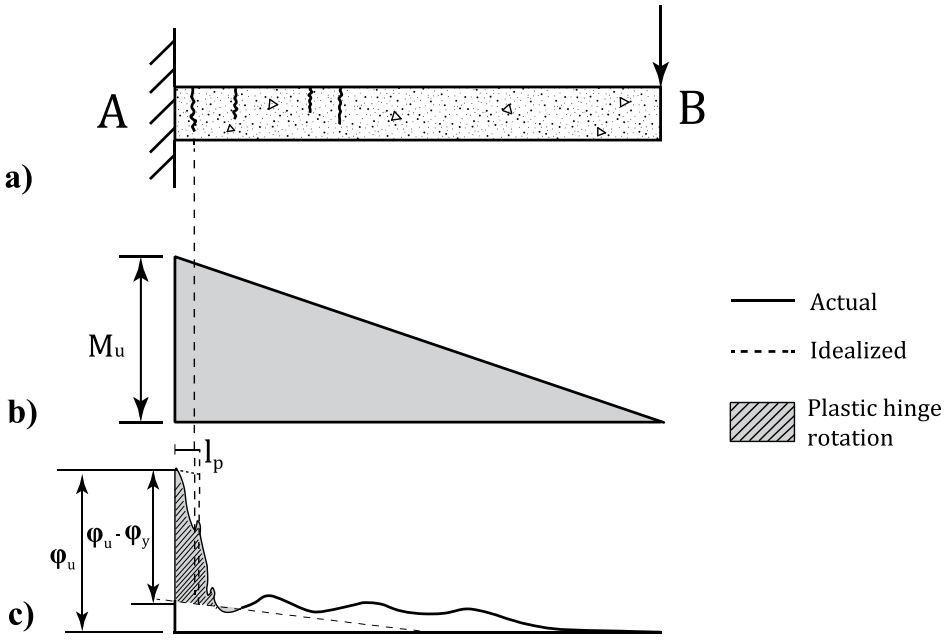

Figure 4.8 a) Cantilever beam with a load at free end, b) Bending moment diagram, and c) Curvature along the length of beam

$$M_{el}=K_{LM,el}\times M \tag{4.26}$$

$$M_{pl}=K_{LM,pl}\times M \tag{4.27}$$

The load mass factors in the elastic case $K_{LM,el}$ and plastic case $K_{LM,pl}$ are 0.24 and 0.33, respectively (UFC 3–340–02 (2014)).

4.5 Results and discussion

4.5.1 Experimental results

i) Transient displacement response

High-speed imaging is used to measure the dynamic response of the beam-column sub-assemblies. The results for specimen types BSNS and BSS subjected to shockwave loading are shown in Figure 4.9 (a) and Figure 4.9 (b), respectively. The imaging is performed at 7,300 frames per second (FPS) with a pixel resolution of 512 × 1024 and a time step of 130 `s. The speckles (black square markers) attached along the length of the beam are used to track the transverse displacement using image correlation.

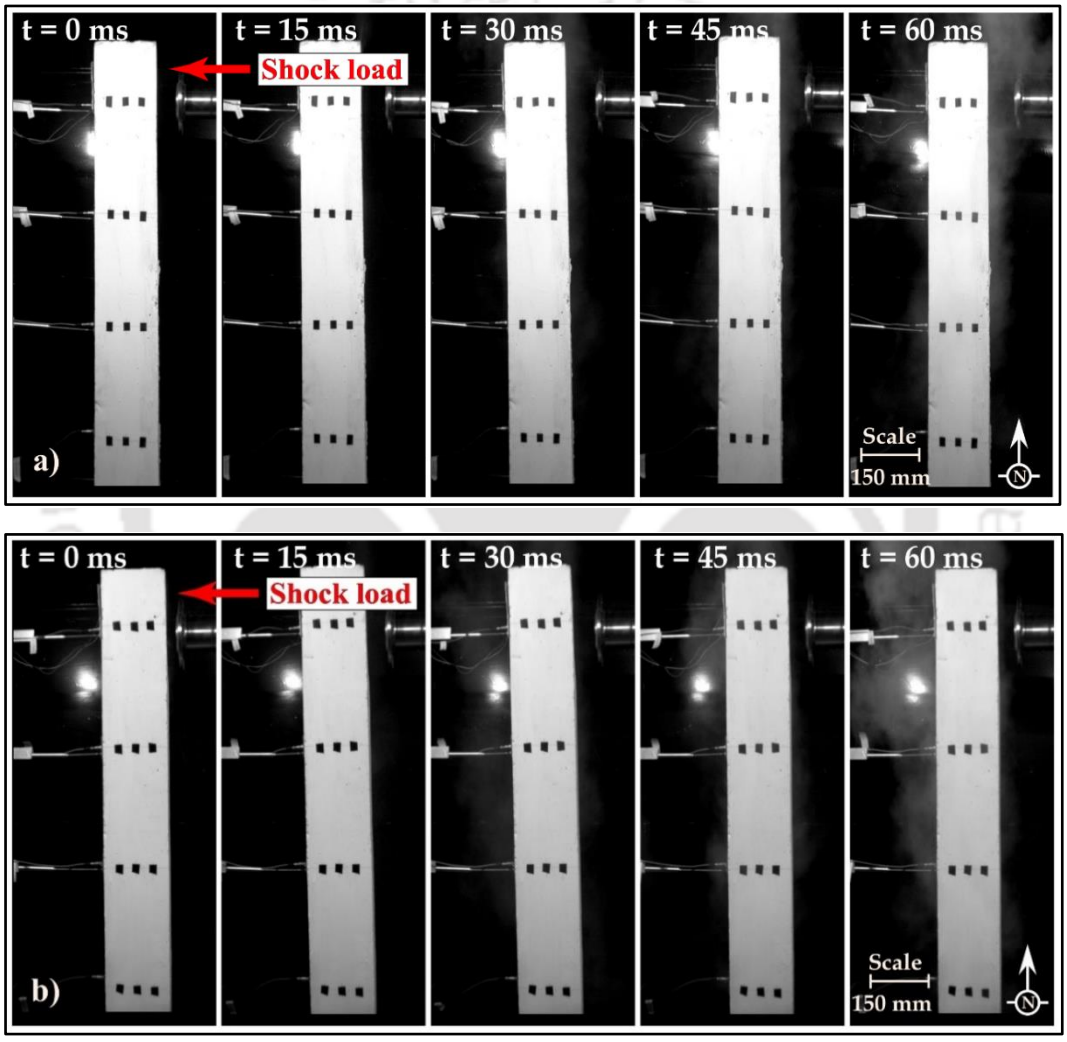

Figure 4.9 High-speed imaging showing the blast fragments for specimens: a) BSNS, and b) BSS at an acquisition rate of 7,300 FPS

The displacement time histories are recorded for a total duration of 175 ms and plotted in Figure 4.10 to Figure 4.12. The response of the structural member is categorized into three phases: i) impulsive, ii) dynamic and iii) quasi-static, that are governing by the ratio of the load duration to the natural period. In the current study, the duration of the shock pulse is approximately 35 ms. The natural period of the

specimens is in the range of 45-50 ms. Therefore, the t_d/T_N ratio is around 0.72 and the loading is thereby considered impulsive. For impulsive loading, the peak maximum response is observed in the forced vibration phase as shown in Figure 4.10 to Figure 4.12. The maximum transverse displacement for the specimens with seismic detailing is smaller than that of their non-seismic counterparts. The maximum displacements are presented in Table 4.3. For specimen type BS (beam weak in shear), the peak displacement is reduced by 35% because of seismic detailing. Similar behavior is observed for specimens CS (column weak in shear) and BF (beam weak in flexure). Thus, seismic detailing of the beam-column joint enhances its resistance to shock loads.

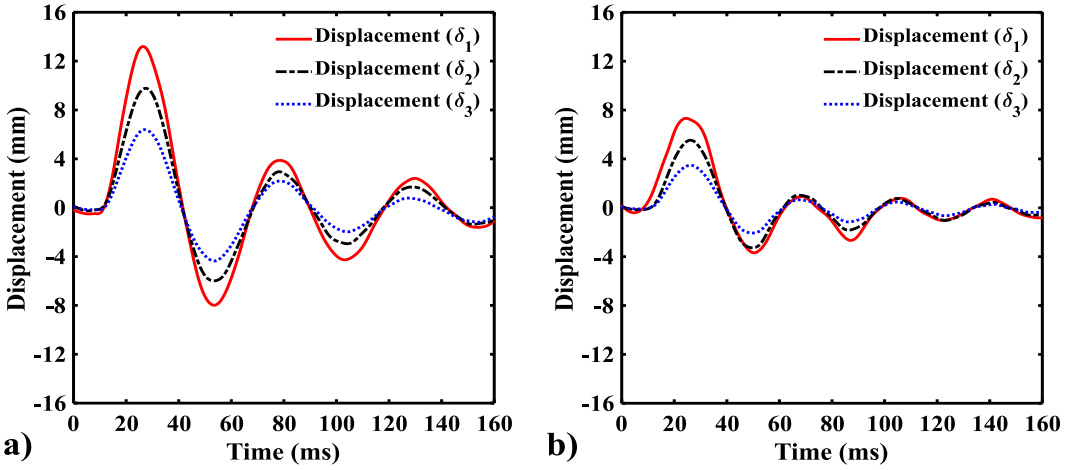

Figure 4.10 Transient displacement profile for specimens: a) BSNS, and b) BSS under shock loading

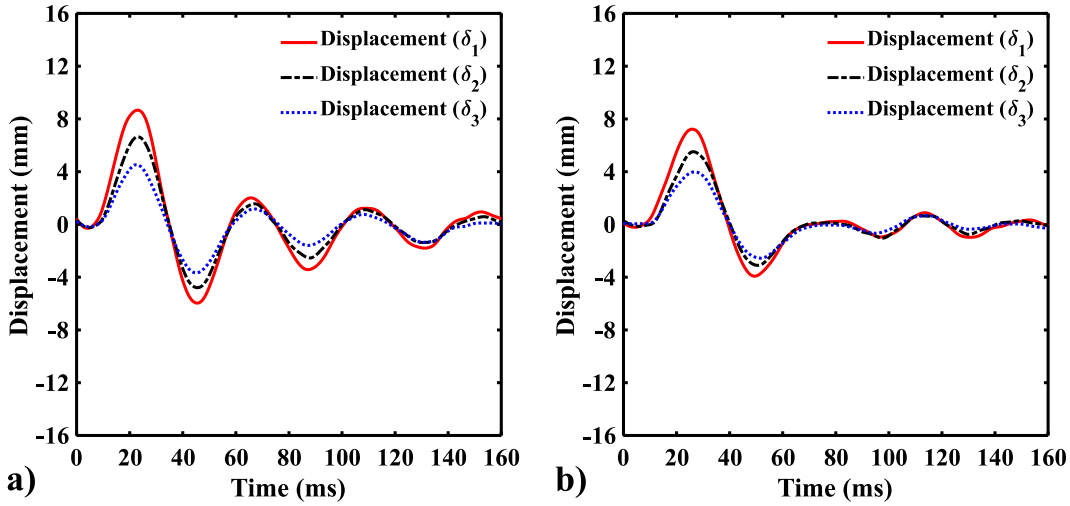

Figure 4.11 Transient displacement profile for specimens: a) BFNS, and b) BFS under shock loading

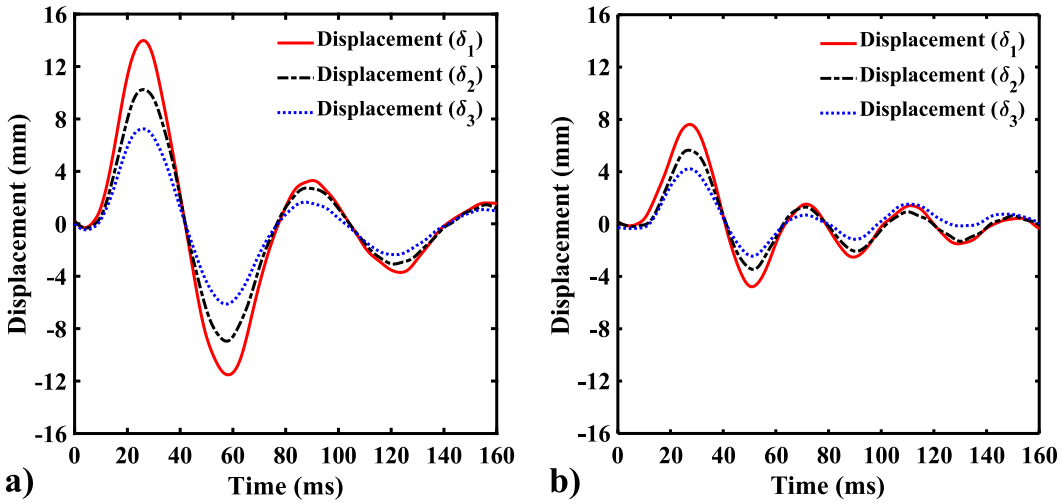

Figure 4.12 Transient displacement profile for specimens: a) CSNS, and b) CSS under shock loading

Table 4.3 Maximum displacements recorded in the beam-column joint tests

Specimen type	Non-Seismic			Seismic		
	BSNS	BFNS	CSNS	BSS	BFS	CSS
δ_1 (mm)	13.20	8.66	13.98	7.32	7.23	7.62
δ_2 (mm)	9.77	6.65	10.24	5.53	5.52	5.65
δ_3 (mm)	6.39	4.54	7.24	3.48	3.99	4.23

ii) Acceleration response

The acceleration time histories are acquired using shock accelerometers that are installed at three distinct locations along the length of the beam. The location of the three accelerometers is shown in Figure 3.9. The first accelerometer is located exactly at the rear face of the region of shock loading. The acceleration time histories near the inflection point of the beam for the specimens designed for gravity and seismic loading are shown in Figure 4.13 to Figure 4.15, respectively. The peak shock accelerations acquired from the recordings are presented in Table 4.4.

Table 4.4 Peak shock accelerations recorded in the beam-column joint tests

Specimen type	Non-Seismic			Seismic		
	BSNS	BFNS	CSNS	BSS	BFS	CSS
A_1 (m/s^2)	1411.2	823.2	1097.6	1960.0	1607.2	1646.4

The seismic specimens behave stiffer compared to their non-seismic counterparts due to ductile reinforcement detailing and thereby experience higher accelerations. Correspondingly, the peak displacement of the seismic specimens is lower compared to

that of their non-seismic counterparts. However, the specimen types CSNS and CSS are designed for the column that is weak in shear. These trends are observed from the peak values presented in Table 4.4.

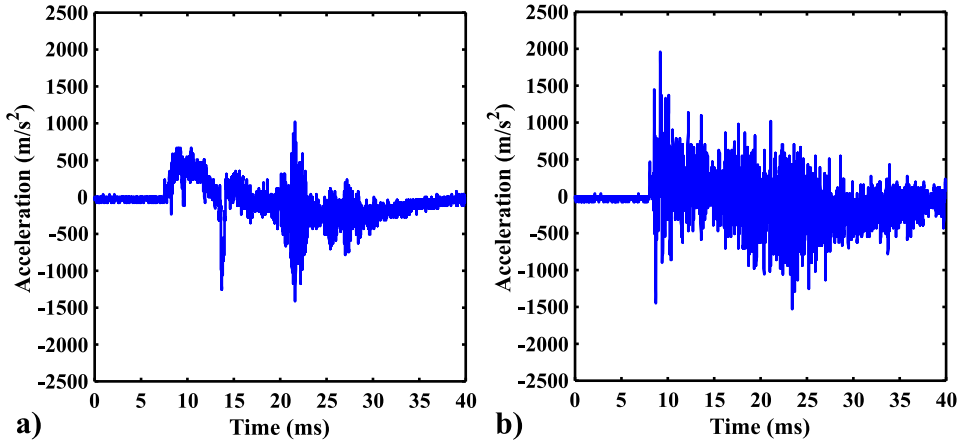

Figure 4.13 Acceleration–time histories for specimens: a) BSNS, and b) BSS under shock loading

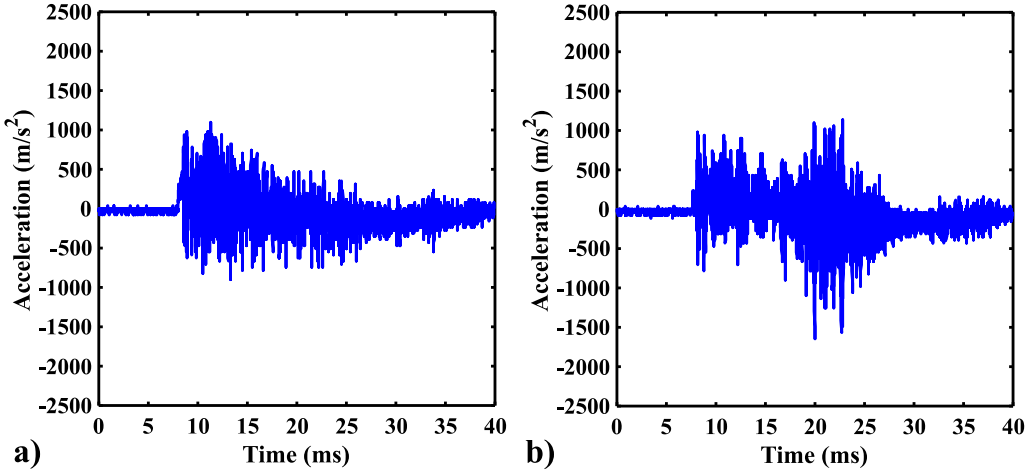

Figure 4.14 Acceleration–time histories for specimens: a) BFNS, and b) BFS under shock loading

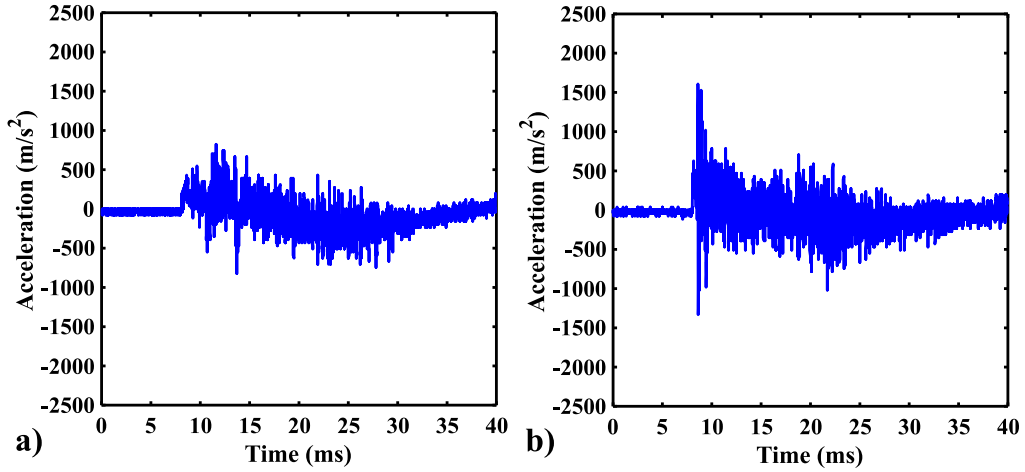

Figure 4.15 Acceleration–time histories for specimens: a) CSNS, and b) CSS under shock loading

iii) Evolution of cracks near beam-column joint

A visual inspection is conducted to examine the evolution of cracks in the test specimen. The crack patterns are carefully studied to qualitatively evaluate the behavior of the beam-column joint. The crack patterns at the beam column junction for all the six specimens are marked and discussed below.

a) Specimen BSNS and BSS

For specimens BSNS and BSS, the crack pattern at the beam-column joint is presented in Figure 4.16. The specimens are designed with weak shear reinforcement (BS). As a result, the shear cracks in the D-region are severe for both specimens. The shear cracks extend all over the beam-column joint. Due to the provision of additional shear reinforcement for the BSS specimen, the development of shear cracks in this specimen is relatively smaller compared to its non-seismic counterpart (BSNS). Additional horizontal cracks are observed in the BSNS specimen at a distance of 260 mm from the beam-column joint due to larger transverse reinforcement spacing.

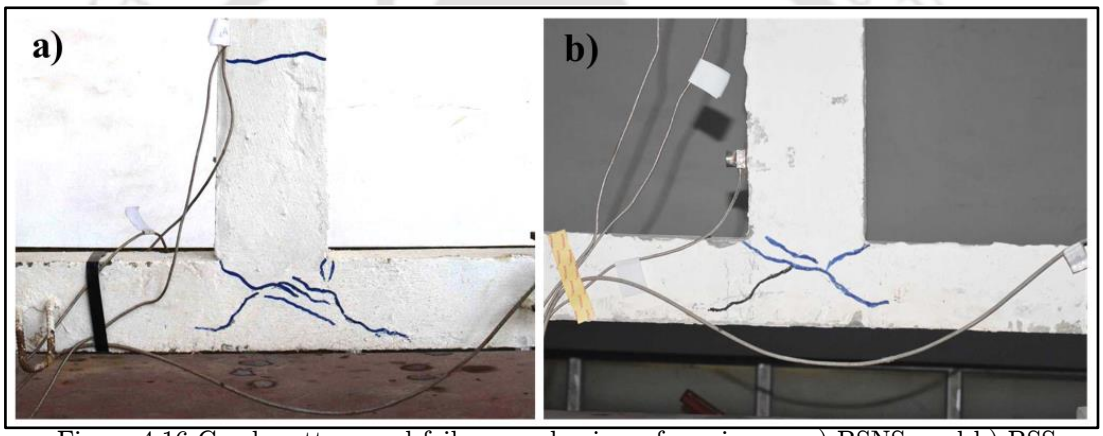

Figure 4.16 Crack pattern and failure mechanism of specimens: a) BSNS, and b) BSS

b) Specimen BFNS and BFS

The crack pattern for BFNS and BFS specimens is presented in Figure 4.17. The specimen designed with non-seismic detailing (BFNS) has a larger shear crack in the D-region compared to that of the specimen designed with seismic detailing (BFS). The shear cracks in the D-region of BFNS started propagating from the beam junction and ended at the column exterior face. On the other hand, the specimen BFS shows significantly less cracking. This implies that the seismic reinforcement detailing has contributed in resisting the shock loads by arresting the shear cracks. The transverse reinforcement spacing for BSNS and BFNS specimens is 180 mm and 110 mm, respectively. The larger reinforcement spacing for the BSNS specimen resulted in severe shear cracks in the beam-column joint compared to the BFNS specimen, which can be observed in Figure 4.16 and Figure 4.17. Similar behavior is observed for the specimens with seismic detailing (BSS and BFS).

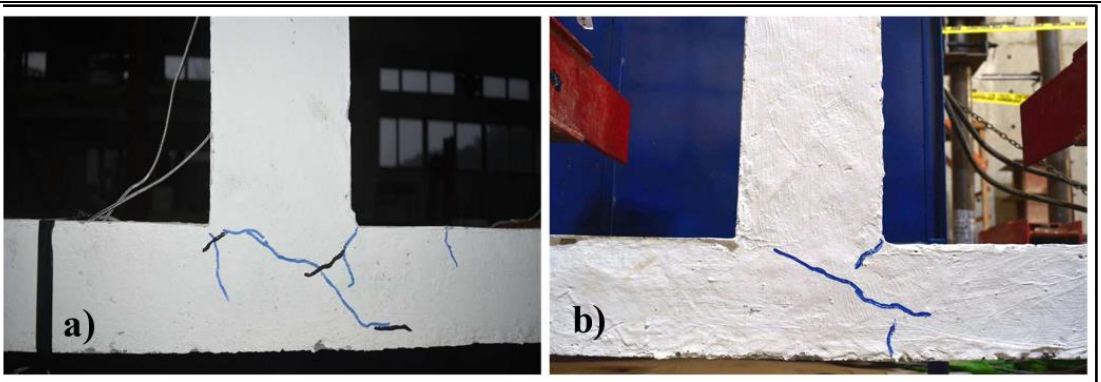

Figure 4.17 Crack pattern at the beam-column joint for specimens: a) BFNS, and b) BFS

c) Specimen CSNS and CSS

The crack pattern for the CSNS and CSS specimens is presented in the Figure 4.18. It is observed that the cracks formed in the D-region are not confined to the beam-column junction for the CSNS specimen. The cracks initiate diagonally in the beam-column junction and further propagate along the height of the column. The longitudinal crack propagation in the column is due to relatively larger tie spacing. However, the specimen with seismic detailing (CSS) has confined the cracks to the beam-column junction by restricting further propagation. Therefore, it is inferred that the specimens with seismic detailing are more effective in resisting shock loads.

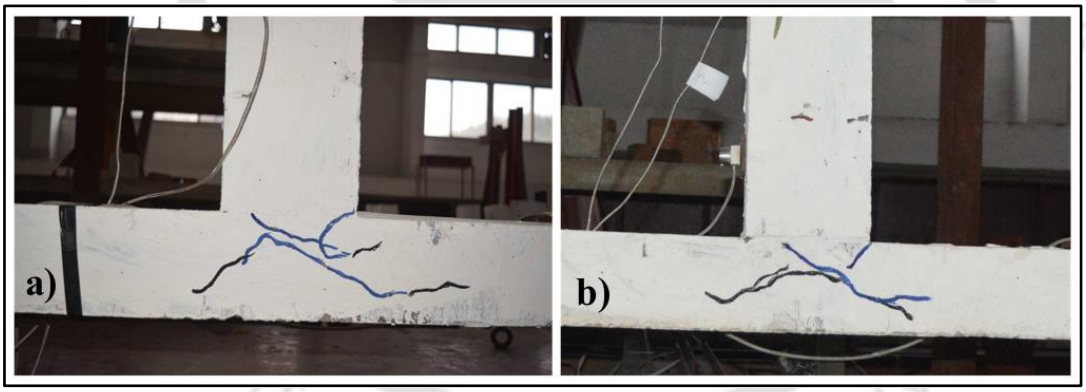

Figure 4.18 Crack pattern and failure mechanism of specimens: a) CSNS, and b) CSS

4.5.2 Numerical results

In this section, the numerical results are compared with the experimental results. The nodal displacements in the transverse direction of the beam are obtained at three distinct locations (115mm, 260mm and 500mm from the tip of the beam). For the impulsive loading regime, the peak response parameters such as peak displacement and acceleration are of paramount importance in the design of structural members. It is observed from the experimental results that the maximum displacement occurs within the duration of shock wave loading. Hence, to minimize the computational effort, the finite element simulation is terminated at the end of the shock loading duration. For brevity, a representative comparison is shown only for BSNS and BSS specimens, and similar results are obtained for the BFNS-BFS and CSNS-CSS specimens. Figure 4.19

shows a comparison between the experimental and finite element results for specimens BSNS and BSS at three distinct locations. The experimental and numerical results are in close agreement and the corresponding errors are tabulated in Table 4.5.

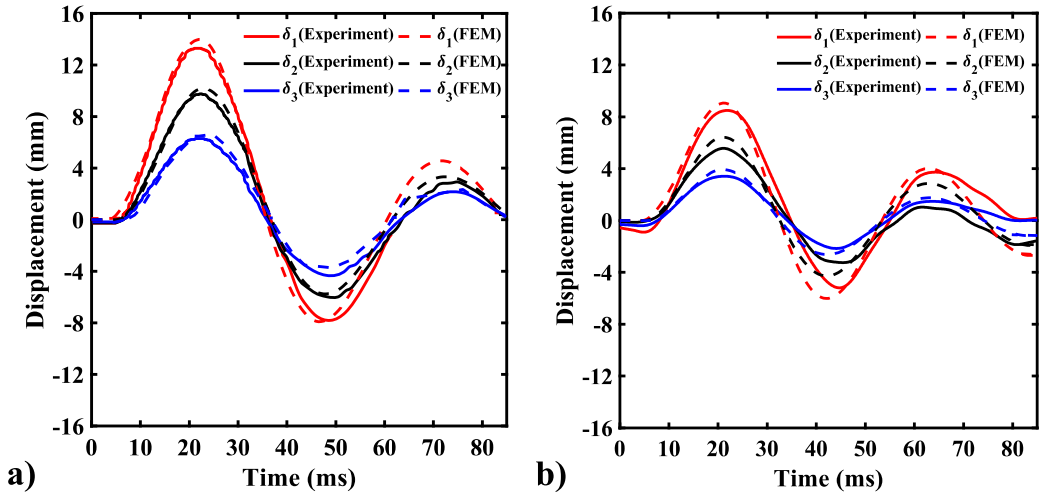

Figure 4.19 Comparison of the displacement profile between the experiment and finite element simulations: a) BSNS, and b) BSS

Table 4.5 Maximum transverse displacements recorded in the beam-column joint tests

	Non-Seismic specimens				Seismic specimens		
	Experiment (mm)	FEM (mm)	Error		Experiment (mm)	FEM (mm)	Error
BSNS	13.20	14.27	8.1 %	BSS	7.32	8.23	11.8 %
BFNS	8.66	9.98	15.2 %	BFS	7.23	8.10	12.0 %
CSNS	13.98	15.25	9.1 %	CSS	7.62	7.91	3.8 %

The peak displacement contour in the beam-column joint for the BSNS and BSS specimens is shown in Figure 4.20. Due to the constraints of the experimental setup, the shock wave amplitude could not be increased further. As the loading becomes severe, the structure will experience substantial inelastic deformations. Due to laboratory safety regulations, experimental investigations at a severe shock wave intensity are not feasible. In the current study, the finite element results are within an error of 16 %. The nonlinear material behavior is explicitly incorporated in the finite element model to account for large inelastic deformations. Therefore, for severe shock wave loadings, finite element simulations are preferred over experimental investigations and is beyond the scope of this work.

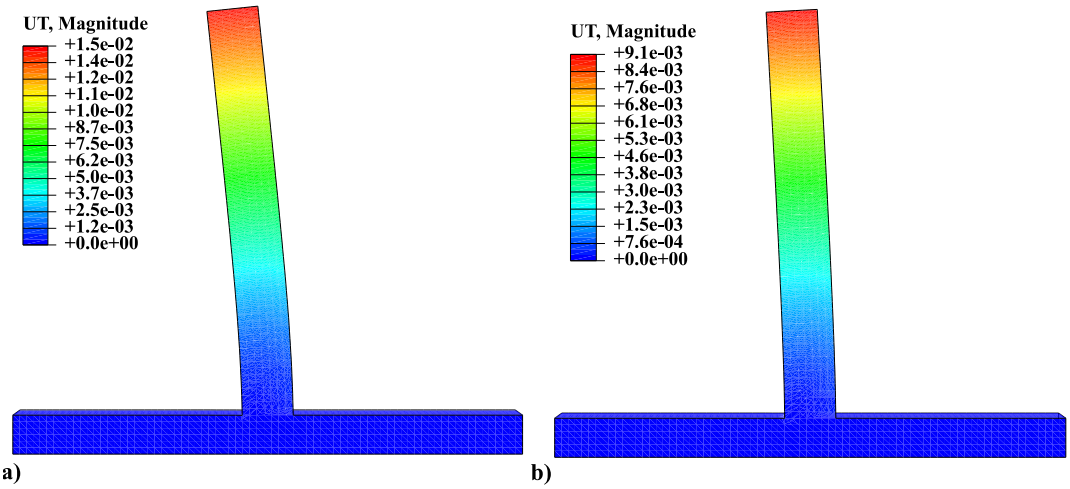

Figure 4.20 Transient displacement contour profile for specimens: a) BSNS, and b) BSS

4.5.3 Analytical results

As discussed in Section 4.4, an analytical model with a bilinear resistance curve has been proposed for the beam-column sub-assembly. As an illustration, a comparison between the transient displacements of the BSS specimen obtained from experimental, numerical and theoretical investigations are shown in Figure 4.21. It is observed that the analytical model slightly under-predicts the time period of the specimens designed with seismic considerations. This is because the analytical model is a lumped mass

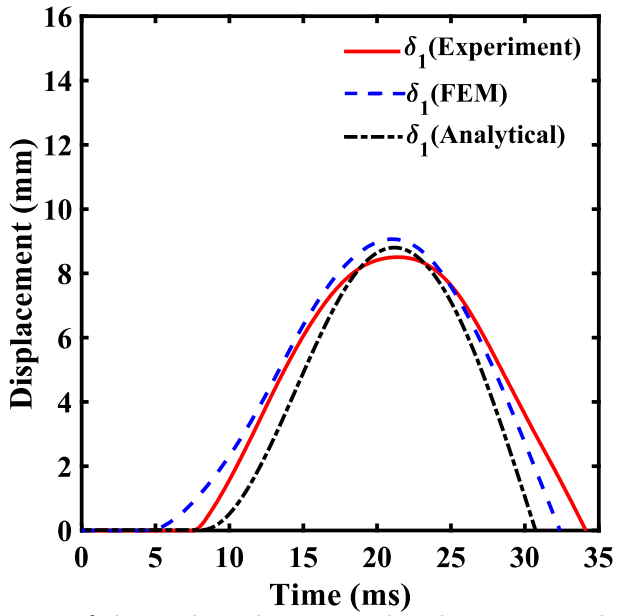

Figure 4.21 Comparison of the analytical, numerical and experimental transient displacement profiles for the BSS specimen

approximation of the beam-column sub assembly and cannot capture the variation in the reinforcement spacing. Also, the formulation proposed in Section 4.4.3 is idealized for a cantilever beam and cannot simulate the actual beam-column joint behavior. The analytical peak displacement values are reasonably in close agreement with the experimental and numerical results. However, the finite element results are more

accurate, but extensive and computationally expensive simulations are needed to develop design charts. Therefore, the results obtained from simplified theoretical model are suitably adapted to derive the shock response spectra. The summary of the experimental results are presented in Table 4.6.

Table 4.6 Summary of experimental results for all specimen configuration

S.No	Specimen configuration	Joint shear (kN)	Shear strength of joint (kN)	Peak displacement (mm)	Peak acceleration (m/s^2)	Evolution of cracks at beam-column junction
1	BSNS	123.8	168.5	13.2	1411.2	
2	BFNS	119.1	168.5	8.7	823.2	
3	CSNS	123.8	168.5	14.0	1097.6	
4	BSS	123.8	168.5	7.3	1960.0	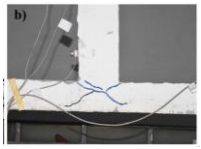
5	BFS	119.1	168.5	7.2	1607.2	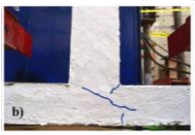
6	CFS	123.8	168.5	7.6	1646.4	

4.5.4 Response spectra

The maximum deflection at the critical location is an important design parameter for structures subjected to extreme loads such as blast, shock and impact. Performing a complete time history analysis requires computationally expensive finite element simulations for various geometries, materials and load combinations. An alternative approach is adopted by the US Department of the Army, TM5-1300 (1990) to predict the maximum response of the structure with respect to the amplitude and time duration of the shock load. In this approach, a shock spectrum is generated by idealizing the structure as a SDOF system and its stiffness is modeled by an equivalent elasto-plastic spring (Abedini et al. 2018; Biggs 1964; Krauthammer 2008; Krauthammer et al. 2008). The maximum displacement is obtained from the equation of motion for the SDOF system subjected to shock loading using a time step integration technique, namely the Newmark-Beta algorithm. Using the maximum dynamic response, a shockwave spectrum is generated as a design tool for various combinations of load and duration.

A shock response spectrum is used to predict the maximum response of an elasto-plastic SDOF system subjected to shockwave loading. A typical shock response spectrum for the system with a bilinear resistance curve, which is excited with a triangular shock load in time, is shown in Figure 4.22. In generating the response spectrum, the shock impulse was assumed to be triangular with a peak amplitude (P) and duration (t_d) as obtained from the shock tube experiment. The response spectrum consists of plots of the maximum deflection normalized with the elastic deflection $\left(\frac{x_{\max}}{x_{el}}\right)$ vs the duration of loading normalized with the natural period of vibration of the system $\left(\frac{t_d}{T_N}\right)$ for various combinations of resistance to the applied loading $\left(\frac{r_u}{P}\right)$. In the developed shock spectrum, the time ratio $\left(\frac{t_d}{T_N}\right)$ varies from 0.1 (impulsive loading) to 20 (Quasi-static loading). The resistance ratio $\left(\frac{r_u}{P}\right)$ varies from 0.3 (highly vulnerable) to 4 (moderately safe).

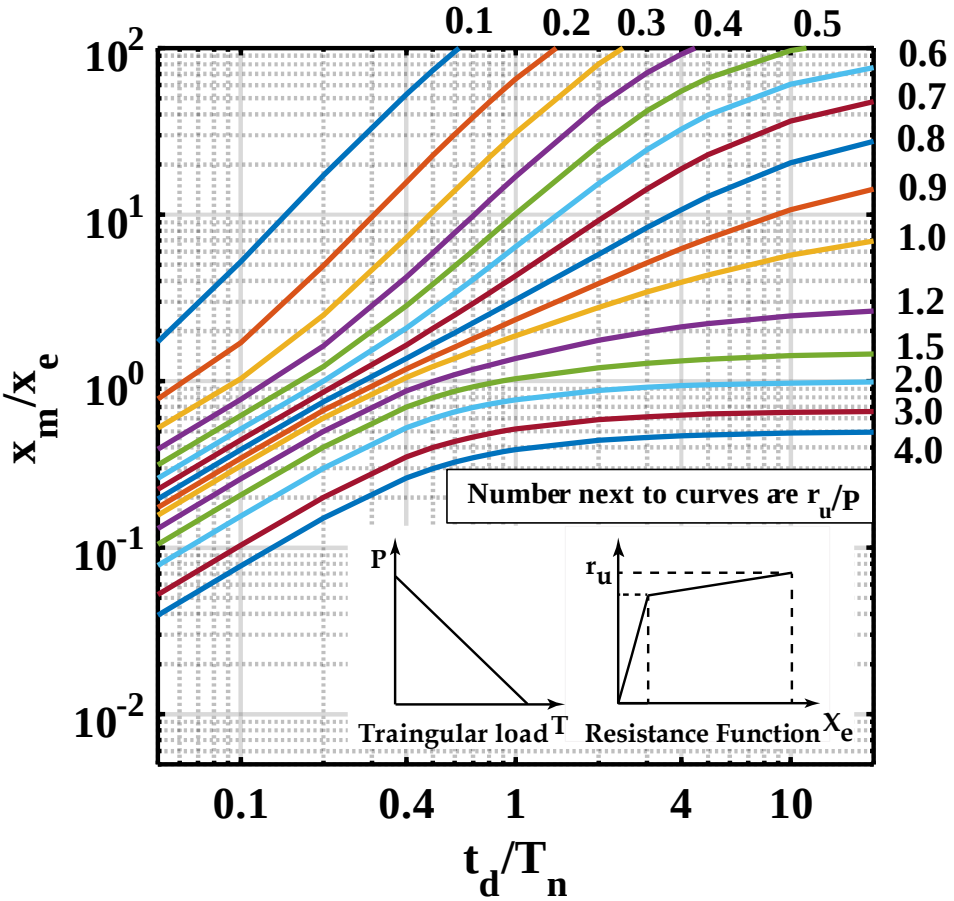

Figure 4.22 Response spectrum of an SDOF system with a bilinear resistance function

The shock spectrum has several limitations i.e. it cannot account for various failure modes in complex geometry and is ill-suited for irregular blast impulse shapes that may arise from a localized detonation. In order to account for the aforementioned limitations and material uncertainties, the ultimate resistance is reduced by a factor of 0.9 to remain on the conservative side. As the experimental and numerical simulations are time-consuming, the approximate but conservative shock spectrum is still preferred. However, the importance and need for experimental investigations and detailed finite element simulations will always be superior to the simplified analytical approach.

4.6 Concluding remarks

In this chapter, experimental investigations are conducted to evaluate the effect of localized shock loading on exterior beam-column joint assemblies having following deficiencies: i) Beam weak in shear (BS); ii) Beam weak in flexure (BF); and iii) Column weak in shear (CS). The influence of high strain rate loading on the flexural capacity of the specimens designed using gravity and seismic considerations is studied. The enhancement of the reinforcement at the beam-column joint improves the ductility of the subassembly. Under high strain rate loading, the ductile subassembly exhibits high stiffness and ultimate strength.

It is observed that the specimens designed using seismic considerations undergo smaller displacements compared to their counterparts designed for gravity loading. For instance, the maximum dynamic displacement of the BSS is approximately 44% smaller than BSNS. The specimens designed with ductile design considerations experience a higher magnitude of acceleration due to the higher flexural and shear strength of the subassembly. The acceleration of the BSS specimen is 38% greater than that of the BSNS specimen.

A post-mortem inspection is conducted to study the evolution of failure modes and crack patterns in the beam-column sub-assembly due to shock loading. The failure and crack pattern indicate that the beam-column joint mechanism is affected by the amount of longitudinal and transverse steel reinforcement in the D-region. The BSNS and BSS specimens designed with a weak beam in shear experiences a higher displacement magnitude. In these specimens, the shear cracks propagate throughout the beam-column junction due to the lack of confining shear reinforcement in the beam. The test specimen CSNS designed with a weak column in shear shows severe cracks in the D-region compared to CSS. The ductile reinforcement is critical in the D-region to safeguard against blast and shock loadings. The reinforcement in the beam-column junctions offers enhanced resistance by increasing the shear strength, which thereby results in the arrest of shear cracks. The key finding of this study based on detailed experimental and numerical investigation is that the structures designed with seismic criteria demonstrate better resistance to deformation and damage against to shock loading.

Chapter 5

Applicability of honeycomb as a sacrificial composite to resist low-velocity impact: Mechanical characterisation

5.1 Introduction

Honeycomb sandwich structures are increasingly used in the aerospace industry due to their low weight to high stiffness ratio. The honeycomb core is considerably stiffer in the out of plane direction compared to in-plane direction (Abrate 2005; Sharma et al. 2006). However, they are vulnerable to damages such as local indentation, core buckling, matrix cracking, shearing, rupture, collapse of core, and delamination. Such damages could arise from extreme loading scenarios such as impact, shock and blast. Several researchers have conducted detailed experimental and numerical study to quantify damage/failure in honeycomb sandwich structures (Crupi et al. 2012; Feng and Aymerich 2013; Feng and Aymerich 2014; Jen and Chang 2008; Petras and Sutcliffe 1999). Zhu and Chai (2013) presented critical loads for different failure modes of honeycomb sandwich structures under impact loads. Sun et al. (2017) conducted three-point bending test and in-plane compression tests to understand the crushing behavior of sandwich panels. It was observed that collapse modes of honeycomb specimen were greatly influenced by several structural parameters. It is challenging to understand the dynamic failure mechanism of honeycomb structure because of complex collapse or failure modes (Meo et al. 2005).

Honeycomb sandwich structures are also used to mitigate the effect of impact and shock loads because of their high energy absorbing capacity. Efforts have been made by researchers to increase the energy absorption capacity of honeycomb sandwich structures by modifying the topology of panels. Sun et al. (2016) have proposed a novel technique by introducing structural hierarchy in the honeycomb specimens. Crushing characteristics of hierarchical honeycomb structures have shown higher energy absorption capacity when compared to regular honeycombs (Fang et al. 2017). Moreover, these hierarchical honeycomb specimens allow minimum transmission of momentum to the superstructure. It is because of this high stiffness to weight ratio and high energy absorption capacity; honeycomb sandwich panels are widely used in industry. Therefore, it is of paramount interest to quantify the contact force and indentation experienced by honeycomb sandwich structures when subjected to impacts.

The current chapter is focused on the performance evaluation of honeycomb composite panels subjected to low-velocity impact. The low-velocity impact refers to velocities leading to a transient response with the contact time larger than one third of the natural period of vibration of the system (Goldsmith and Sackman 1992; Harding

and Sneddon 1945; Olsson 1992; Olsson et al. 2006; Zener 1941). Two widely accepted analytical model used to evaluate the impact response of composite structure are i) Spring mass model and, ii) Energy balance model. Several researchers have idealized the composite structure as a lumped spring and mass model (Abrate 2005; Anderson and Madenci 2000; Choi 2006; Lal 1983; Shivakumar et al. 1985). These idealized models tend to deviate from experimental observations due to an inappropriate assumption of Hertz contact law for plastic deformation (Bao et al. 2004; Fatt and Park 2001; Koissin et al. 2004; Olsson and McManus 1996). Vaidya et al. (2008), has studied multi-functional 3-D sandwich composites with hollow core and polyurethane foam filled core. Series of low-velocity impact experiments conducted on both sandwich composites and found foam filled specimens have supported the core piles and enhanced the strength of the laminated composite. It was also observed that the delamination mode of failure was absent in the foam filled composites when compared to the traditional sandwich structures.

Zhou and Stronge (2006), have proposed a quasi-static energy balance model with modified nonlinear contact interaction to predict contact force, indentation, and global deflection in sandwich structure. However, this model assumes the honeycomb sandwich structure to behave as an elastic-perfectly plastic material. In reality, no material confines to such simplistic assumptions. To account for this error, several researchers have conducted computationally exhaustive finite element analysis. They incorporated nonlinear material behavior and progressive failure criteria of the honeycomb core (Hou et al. 2000; Kelly and Hallström 2005; Lee and Huang 2003). Petras and Sutcliffe (2000) conducted a comprehensive study on failure of honeycomb sandwich beams under indentation loading.

It is practically impossible to manufacture the honeycomb core to exact specified dimensions and grade because of complex geometry. This results in high uncertainties in both geometrical and material parameters. Based on the literature review, it is observed that none of the existing models are able to incorporate the uncertainties associated with material and geometrical properties. All these models are deterministic in nature and derived from simplified assumptions and idealizations. Often, the applicability of the deterministic models is valid for a narrow range of input variables. With evolution of the performance based design, it is essential to incorporate the uncertainties governing the impact behavior of the honeycomb composites (Choe et al. 2008; Gardoni et al. 2002; Gardoni et al. 2007; Huang et al. 2010; Ramamoorthy et al. 2006; Sharma et al. 2014; Sharma et al. 2015; Zhong et al. 2008). The uncertainties could arise from measurement errors and unavailability of the experimental data.

Therefore, a probabilistic model is proposed to predict the unbiased estimate of the contact force in honeycomb sandwich structure during impact. The accuracy of the probabilistic model depends on the availability of experimental data over a wide range of input parameters. It is practically impossible to obtain specimens having all possible combinations of geometrical and material properties. Due to unavailability of such a

wide range of experimental data, we resort to multiple deterministic Finite Element (FE) simulations. The numerical analysis has an added advantage of specifying exact values of the dimensions and material properties of the specimen without leading to uncertainties. In the initial phase of study, material and geometrical parameters that highly influence the structural response are identified. The range for each input variable is selected based on actual honeycomb sandwich structures used for aerospace application. Within the range of input variables selective design points are generated based on a D-optimal algorithm and is elaborated in section 5.5. Detailed finite element simulations are conducted at these design points to generate representative data over the range of input variables. The FE results are then used for calibrating the probabilistic model. The probabilistic model can be formulated based only on experimental data without any mechanistic justification. Even if such probabilistic models perform satisfactorily, they lack credibility from the analytical perspective.

Therefore, a probabilistic model is formulated by correcting the inherent bias in the analytical model. The theoretical model also helps in proposing the explanatory input functions which largely influence the dynamic structural response. The analytical model in conjunction with virtual experimental data is used to formulate the probabilistic model to predict contact force due to impact. An equivalent framework could be used, to predict other physical quantities of interest, such as local indentation. The probabilistic model developed in this study intends to estimate the load demand for given input variables. The proposed framework is demand based probabilistic study and results in the development of an accurate predictive model that enhances our understanding on behavior of composite structures. However, the model quantifies the load demand and cannot predict the failure in the structure.

5.2 Experimental investigation

Experimental investigations are conducted to study the response of the honeycomb sandwich structure under the static and dynamic loading. A rectangular shaped honeycomb is used for conducting quasi static test and a circularly shaped honeycomb specimen as shown in Figure 5.1 (a) is used for dynamic low-velocity impact tests.

5.2.1 Quasi-static compression test

Crushing of core is one of the predominant failure modes of honeycomb composite structures. Energy absorption capacity of honeycomb sandwich structure depends on the static core crushing strength. A dynamic universal testing machine (INSTRON) is employed to conduct quasi-static compression test on honeycomb core. These honeycomb cores are manufactured from the Aluminum alloy Al 3003. The experimental and schematic representation of honeycomb and its unit cell is shown in Figure 5.1.

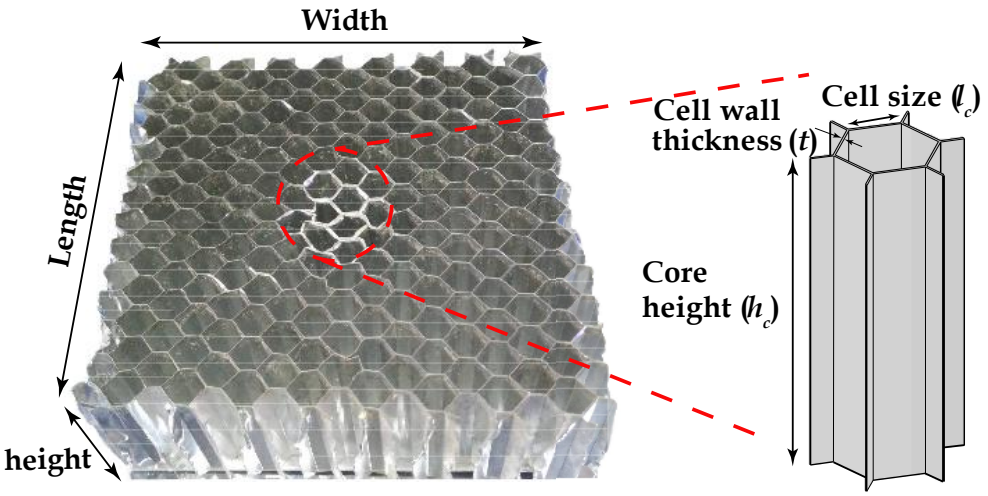

Figure 5.1 Aluminum honeycomb core with a schematic view of the unit cell (HC 50)

The quasi-static compression tests are carried out on rectangular shaped Aluminum honeycomb core of dimensions 80mm x 40mm x 36.5 mm. The specimen has a cell wall thickness of 70 μ and a cell size of 6.5 mm. The honeycomb core is sandwiched between rigid plates for uniform stress distribution during the compressive loading. A displacement-controlled loading is applied at a strain rate of 10mm/min. Ten samples are tested in a controlled environment, to ensure reproducibility. The density of honeycomb core is approximately determined to be 63 kg/m^3 using Eq. (5.1) (Gibson et al. 1989; Guo and Gibson 1999)

$$\frac{\rho_c}{\rho_{alu}} = \frac{8}{3}\left(\frac{t}{c}\right) \tag{5.1}$$

Figure 5.2 shows the force displacement plot of the quasi-static compression test conducted on a honeycomb core having dimensions as mentioned above. The inset shows the deformation of the specimen at yield and plateau stress condition.

Upon compressive loading in out of plane direction, the hexagonal honeycomb will elastically buckle (symmetric breaking bifurcation) at limit load (point A, Figure 5.2) and subsequently yield producing an undulated stress plateau. In the post buckling phase, these undulations are result of contact between crushed cell wall layers. At very large strains, the specimen will densify but we confine our analysis to regime before initiation of densification. This unique mechanism is leveraged for the design of efficient impact energy absorbing device by maximizing the area under the constant stress curve (Wu and Jiang 1997). The static compression test result shows that honeycomb specimen behaves similarly to an elastic perfectly plastic material. However, this represents the global behavior of the specimen i.e. at the structural level.

Wierzbicki and Abramowicz (1983), developed an analytical expression relating the mean core crushing strength to flow stress, geometrical configuration of the cell as

$$\frac{q}{\sigma_c} = 6.6\left(\frac{t\sqrt{3}}{c}\right)^{5/3} \tag{5.2}$$

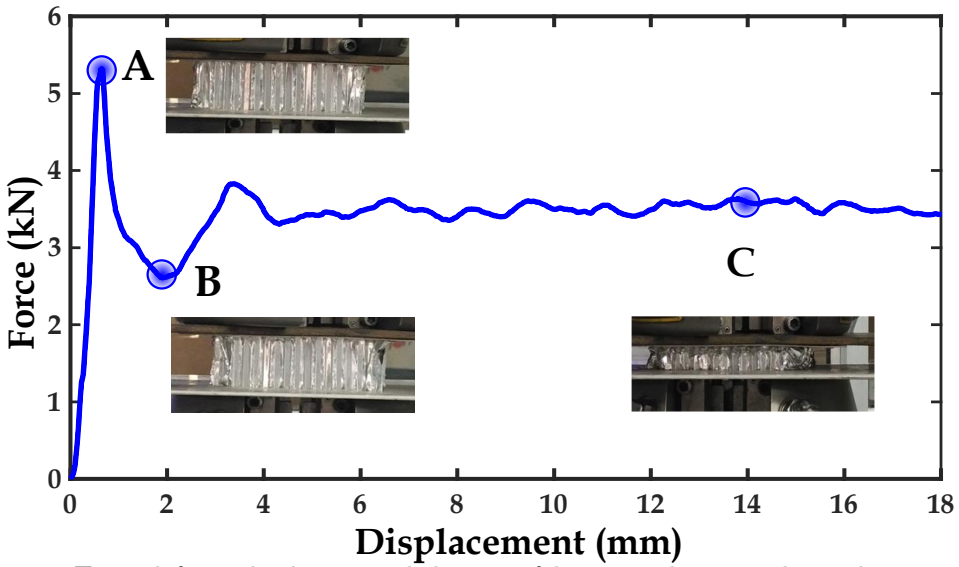

Figure 5.2 Typical force displacement behavior of honeycomb core subjected to quasi-static compression, inset shows deformation of honeycomb structure at indicated displacements

The peak yield stress and plateau stress of the honeycomb core has been found to be 1.65 MPa (point A) and 1.08MPa (point C), respectively. The objective of static compression test was to determine the overall behavior of specimen under quasi-static loading.

5.2.2 Dynamic impact drop test

As mentioned in section Chapter 5, the study aims to develop a demand based probabilistic model which is calibrated using numerical simulations. It is required to validate the numerical results using low-velocity experiments. Therefore, impact drop tests are conducted for a honeycomb sandwich specimen with varying impact energies. Figure 5.3 shows the experimental setup of the impact-testing instrument. The dynamic drop test is performed on a circular shaped Aluminum honeycomb of diameter 100 mm. A one mm thick circular facesheet made of Aluminum alloy 3003, are laminated to the core with glue. It is made sure that the facesheet and core are laminated to each other to avoid any delamination during the impact. Both facesheet and honeycomb core are made of an Aluminum alloy Al 3003 with a yield strength of 220 MPa.

A blunt hemispherical indentor of mass 3.386 kg (including overhanging weight) is used to conduct drop weight test. The sandwich specimen is placed on the rigid base and the indentor is guided along the centerline. The impactor is released to strike the top facesheet using an electromagnetic switch. This triggers the data acquisition system and acquires the transient response of contact force. A series of impact tests are conducted for drop heights varying from 0.1 m to 0.5 m. This results in minimum impact energy of 2.95 J to a maximum energy of 16.38 J. The range of impact energy considered in the present study conforms to the category of low-velocity impacts. To resist higher impacts, specimens are to be manufactured from higher grade Aluminum alloy that could avoid excessive deformation. The experimental observations and their comparison with theoretical and numerical results will be discussed in Section 5.4.

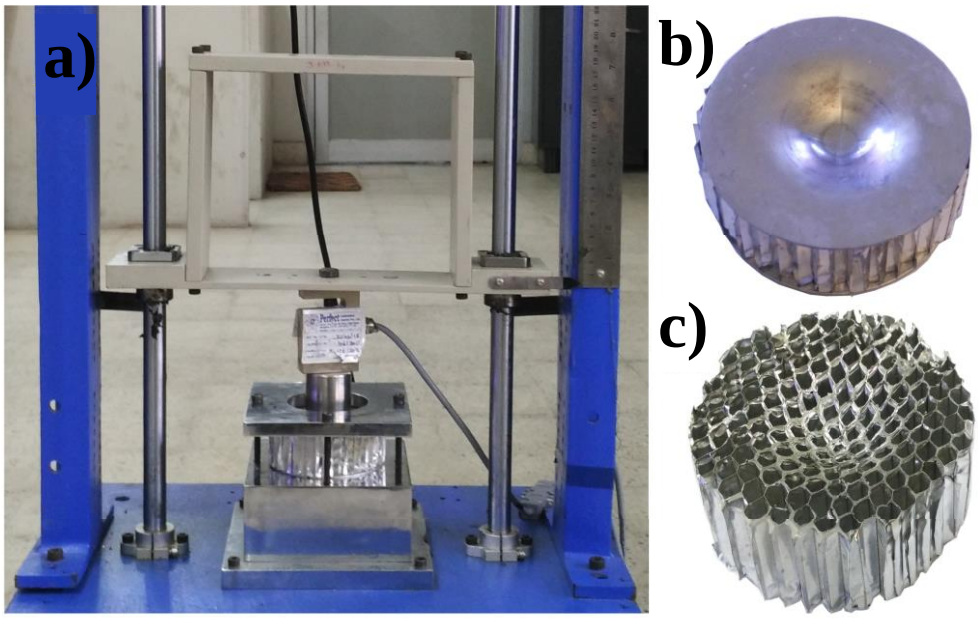

Figure 5.3 (a) Low-velocity impact testing instrument, (b) Deformed sandwich panel, and (c) Deformed honeycomb core

5.3 Analytical model

5.3.1 Contact force formulation

A theoretical model is adapted to quantify the contact force and indentation due to low-velocity impact on the honeycomb sandwich panel (Zhou and Stronge 2006). Consider a circular honeycomb core of radius (R_f) and thickness (h_c) impacted by a spherical impactor. The honeycomb panel is sandwiched between Aluminum facesheet of thickness (h_f). A spherical impactor of diameter and mass (M_1) is strikes the top facesheet at velocity (V_o) normal to the plane of the panel. The maximum local indentation due to impact is denoted by (α_o). The core is assumed as elastic-perfectly plastic material. The top and bottom facesheet are laminated to the honeycomb core restricting the delamination of facesheet. The top circular plate is assumed to be clamped along the periphery (Koissin et al. 2004). The honeycomb sandwich panel is assumed to rest on the rigid base, which induces local indentation and negligible global deflection. Considering the lowest mode of vibration of a circular plate, the local indentation profile in the honeycomb structure due to spherical impactor is assumed as given in Eq.(5.3).

$$.\alpha(r) = \alpha_o\left(1-\left(\frac{r}{a}\right)^2\right)^2. \tag{5.3}$$

where, α_o and a are the transversal local indentation and contact radius respectively.

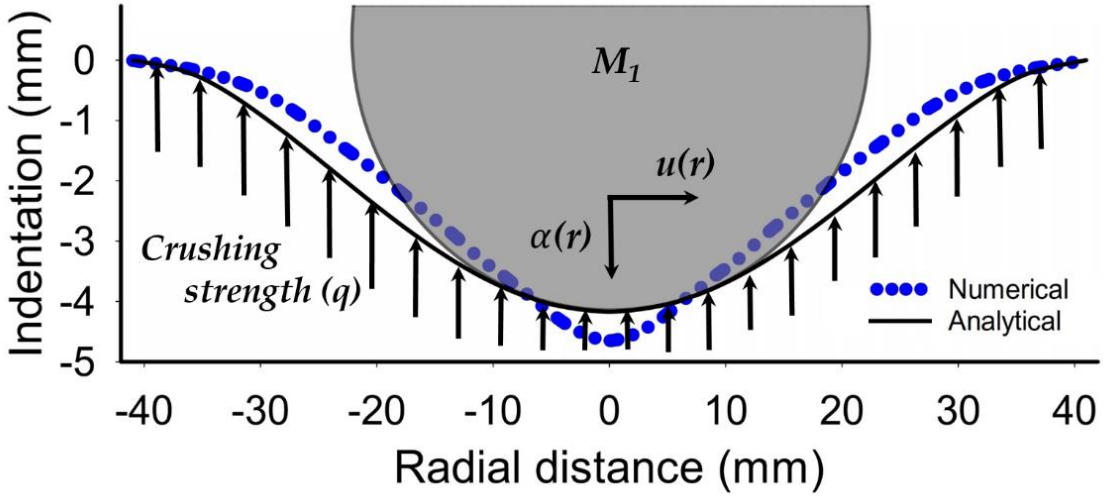

Figure 5.4 Overlay of theoretical and numerical indentation profile due to impact

The accuracy of the analytical model depends on an appropriate indentation profile, as this forms the basis in formulating the analytical model. The displacement profile obtained from FE simulation substantiate the assumed deflected shape given by Eq.(5.3). An overlay of both analytical and numerical indentation profile is shown in Figure 5.4. The indentation on the honeycomb composite is resisted by crushing strength of the core as indicated in Figure 5.4. Principal of the minimization of potential energy is used to quantify the load displacement relationship (Timoshenko and Woinowsky-Krieger 1959). The potential energy of the system is sum total of bending and membrane energy stored in top facesheet, work done by contact force, and work done due to core crushing as given by Eq. (5.4) (Zhou and Stronge 2006)

$$\prod = V_B + V_M + U_1 + U_2 \tag{5.4}$$

The detailed expressions for all the terms are presented in Table 5.1. Minimizing the potential energy with respect to the indentation α_o, i.e. $\frac{\partial \prod}{\partial \alpha_o} = 0$ results in a contact force as expressed below.

$$P = \frac{64\pi D_f \alpha_o}{3a^2}\left[1 + \frac{\alpha_o^2(7505 + 4250\nu - 2791\nu^2}{17640h_f^2}\right] + \frac{\pi q a^2}{3} \tag{5.5}$$

Further, minimizing the contact force 'P' with respect to contact radius 'a' i.e., $\frac{\partial P}{\partial a} = 0$, yields a force-indentation relationship as

$$P = \frac{16\pi}{3}\sqrt{D_f q \alpha_o\left[1 + \frac{(7505 + 4250\nu - 2791\nu^2)\alpha_o^2}{17640h_f^2}\right]} \tag{5.6}$$

Table 5.1 Formulas for various influencing parameters (Zhou and Stronge 2006)

Parameters	Expression
Mass of honeycomb panel	$M_2 = \pi R_f^{\,2}(2\rho_f h_f + \rho_c h_c)$
Radial strain	$\varepsilon_r = \frac{du}{dr} + \frac{1}{2}\left(\frac{d\alpha}{dr}\right)^2$
Tangential strain	$\varepsilon_\theta = \frac{u}{r}$
Bending energy	$V_B = \frac{D_f}{2}\int_0^{2\pi}\int_0^{a}\left[\left(\frac{\partial^2\alpha}{\partial r^2}\right) + \frac{1}{r^2}\left(\frac{\partial\alpha}{\partial r}\right)^2 + \frac{2\nu}{r}\frac{\partial\alpha}{\partial r}\frac{\partial^2\alpha}{\partial r^2}\right] r dr d\theta$
Flexural rigidity	$D_f = \frac{E_f h_f^{\,3}}{12(1-\nu^2)}$
Membrane rigidity	$D_m = \frac{E_f h_f}{(1-\nu^2)}$
Assumed radial displacement profile	$u(r) = r(a-r)(A+Br)$
Membrane stretching energy stored	$V_M = \frac{\pi E h_f}{(1-\nu^2)}\int_0^{a}\left(\varepsilon_r^2 + \varepsilon_\theta^2 + 2\nu\varepsilon_r\varepsilon_\theta\right) r dr$
Work done by crushing of core	$U_1 = 2\pi\int_0^{a} q\alpha r dr$
Work done by the contact force	$U_2 = -\int_0^{\alpha_o} P(d\alpha_o)$
Shear stiffness	$K_s = \frac{4\pi G_c (h_f + h_c)^2}{h_c(1 + 2\ln R_f / R_c)}$
Bending stiffness	$K_b = \frac{16\pi D}{(1-\nu)(3+\nu)R_f^{\,2}}$
Bending stiffness of sandwich panel	$D = \frac{E_f (h_f + h_c)^2 h_f}{2} + \frac{E_f h_f^3}{6}$
Membrane stiffness	$K_m = \frac{2\pi E_f h_f}{(3+\nu)^4 R_f^{\,2}}\left[\frac{191}{648}(1+\nu)^4 + \frac{41}{27}(1+\nu)^3 + \frac{32}{9}(1+\nu)^2 + \frac{40}{9}(1-\nu) + \frac{8}{3}\right]$
Bending energy	$E_b = \frac{K_s}{K_b + K_s} E_{bs}$

Shear energy	$E_s = \frac{K_b}{K_b + K_s} E_{bs}$
Membrane energy	$E_m = \frac{1}{4} K_m w_o^4$

5.3.2 Static equivalent contact force model

The energy balance concept is used to predict the equivalent static contact force and indentation in the sandwich panel. The kinetic energy of the impactor is balanced by strain energy induced due to bending-shear, and membrane effect and work done by the contact force (Eq.(5.7)).

$$\frac{1}{2} M_1 V_o^2 = E_{bs} + E_i + E_m \tag{5.7}$$

The work done by the contact force P is given as follows

$$E_i = \int_o^{\alpha_{om}} P d\alpha \tag{5.8}$$

The contact force is nonlinearly dependent on the global displacement (Abrate 2005) as given below.

Substituting contributing energy terms in Eq. (5.7) yields

$$\frac{1}{2} M_1 V_o^2 = \frac{1}{2} K_{bs} w_o^2 + \frac{1}{4} K_m w_o^4 + \int_0^{\alpha_{om}} P d\alpha \tag{5.9}$$

Here, the global deflection (w_o) and indentation (α) are unknowns in the energy balance equation. Combining Eq.(5.6) and Eq. (5.9), gives a nonlinear relationship between global deflection and indentation.

$$\frac{16\pi}{3} \sqrt{D_f q \alpha_o \left[1 + \frac{(7505 + 4250\nu - 2791\nu^2)\alpha_o^2}{17640 h_f^2} \right]} = K_{bs} w_o + K_m w_o^3 \tag{5.10}$$

Global deflection (w_o) and indentation (α) are evaluated by solving coupled nonlinear equations using numerical methods like Newton-Rapson (Eqs. (5.9) and (5.10)). Subsequently, Eq. (5.6) is used to quantify the contact force due to impact on the honeycomb structure.

5.4 Numerical simulations

Low-velocity impact tests cannot be conducted over the entire range of input variables as they are time consuming and expensive. Also, finding a set of specimens with desirable geometrical and material combination is practically impossible. Due to unavailability of the experimental data over the wide range of input parameters extensive finite element (FE) simulations are conducted to develop the probabilistic model. In this study, FE simulations are conducted at selective design points generated using D-optimal design of experiments. The numerical results are validated by

conducting low-velocity impact experiments on honeycomb sandwich specimen. Once validated, the FE simulation results are treated as virtual experiment data and used for calibrating the probabilistic model. The reason to resort to FE results as virtual experiments is the practical limitation to perform repetitive experiments with all possible combination of input variables. Gardoni et al. (2002); Sharma et al. (2014), adapted a similar approach to propose a probabilistic demand and capacity modeling for impact problems. A Similar approach has been implemented in the current study to formulate the probabilistic model. Once the probabilistic model is developed, it circumvents any further dependency of conducting expensive FE simulations and predict the contact force using an explicit equation. Numerical analysis is conducted using commercial finite element software Abaqus 6.8. The mean geometrical and material parameters considered for the representative FE model are shown in Table 5.2 (a) and (b), respectively.

Table 5.2 a) Mean geometrical properties of representative honeycomb sandwich structure

Description	Geometrical property	Symbol	Value
Facesheet	Thickness of facesheet (mm)	h_f	1
	Radius of facesheet (mm)	R_f	62.5
Honeycomb core	Height of core (mm)	h_c	27
	Cell wall thickness (μ)	t	70
	Cell size (mm)	c	6.5
Impactor	Diameter of impactor (mm)	ϕ	20
	Lumped mass (kg)	M	2
	Drop height (m)	h	0.5

Table 5.2 b) Mean material properties of representative honeycomb sandwich structure

Material property	Facesheet	Honeycomb core	Impactor
Young's modulus (GPa)	70	70	200
Density (kg/m^3)	2700	2700	7850
Poisson's ratio	0.3	0.3	0.3
Yield strength of core (MPa)	250	250	-

The impactor is modeled as a solid deformable hemisphere and meshed using four-node linear tetrahedral continuum elements. These elements are stiff and are easily adaptable to the curved geometry. To simulate the experimental conditions, a nonstructural lumped mass of two kg is added to the impactor. The impactor is made of steel and is stiffer when compared to thin walled honeycomb core. For low impact energies, the impactor is assumed to undergo small deformations in the linear elastic range and hence is defined as an elastic material. A predefined velocity is imparted to the indentor resting on the deformable facesheet. The facesheet is modelled as solid

deformable body and is discretized using eight node hexahedral continuum elements (C3D8R). During the impact, the facesheet experiences high stress concentration within the contact region. Hence, a fine mesh is adapted in the contact region to accurately capture the response. To resemble the boundary conditions of the experiment, the bottom facesheet is restrained in all the three directions and the top facesheet is clamped along the periphery. Mesh optimization study is conducted to achieve convergence and reduce the rigid body modes of the deformation. Thin facesheet undergoes excessive bending and membrane stretching which results in induces enormous stress in the contact region. Therefore, the facesheet is divided into five elemental layers along the thickness to incorporate shear deformation and control excessive distortion at the contact area.

In the current study, FE simulation results are used to generate data for probabilistic model. The credibility of the probabilistic model depends on the numerical results and therefore a suitable material model is to be adopted for achieving accurate results. Honeycomb core shows similar behavior to elastic perfectly plastic material from the quasi static compression test. However, this represents the global behavior of specimen at the structural level and may differ from the actual stress-strain behavior of the material. Foo et al. (2008) extensively investigated the response of honeycomb sandwich structures for different material models like elastic perfectly plastic, bilinear, Ramberg-Osgood. Though nonlinear strain hardening models like Ramberg-Osgood provide enhanced accuracy, the computational demand is very high. Consideration of material non-linearity into model, significantly increases the simulation runtime. In addition to the time taken for each simulation, it also increases the number of input variables and design points, which makes it very cumbersome for probabilistic study. FE simulations are conducted for different material models to determine the influence on contact force and indentation. The elastic perfectly plastic assumption is also in accordance with existing literature on honeycomb sandwich specimen for low-velocity impacts (Foo et al. 2008; Jen and Chang 2008; Sun et al. 2017; Zhou and Stronge 2006). Therefore, in the current study, the honeycomb sandwich specimen is assumed to behave as an elastic-perfectly plastic material.

The circularly shaped honeycomb core is modelled using four-node shell element with reduced integration (S4R) because of their capability to capture large deformations. To capture core-crushing behavior, the honeycomb core is finely meshed with total number of 2,00,000 elements. The finer mesh controls excessive distortion of elements within the contact region. Surface-to-surface contact pair is applied between the colliding surfaces. In addition, general contact algorithm is also employed to account for any possible interactions between the cell walls during the crushing of honeycomb core. The compatibility of displacement between facesheet and honeycomb core is ensured through surface based tie constraint (Foo et al. 2008). The facesheet acting as master surface governs the displacement of slave nodes on core surface and prevents delamination during deformation.

As the probabilistic model is calibrated using numerical results it is essential to validate these FE results with benchmark experiments. Figure 5.5 shows the validation of the numerical and experimental contact force at an impact energy of 13.28 J for the specimen having dimensions as shown in section 5.2. The overall dynamic response is in good agreement with each other. This behavior is in accordance with the previous investigation on low-velocity impact on honeycomb structures (Foo et al. 2008). Figure 5.6 shows the comparison of the experimental and numerical deformation pattern of the honeycomb composite at an impact energy of 13.28 J. Numerical results are compared with experimental observations for impact energies mentioned in section 5.2. It is observed from Figure 5.7 that the analytical predictions deviate from both experimental and numerical results significantly. The divergence in the results predicted by deterministic model makes it a compulsion for development of the probabilistic model which could correct the biased results.

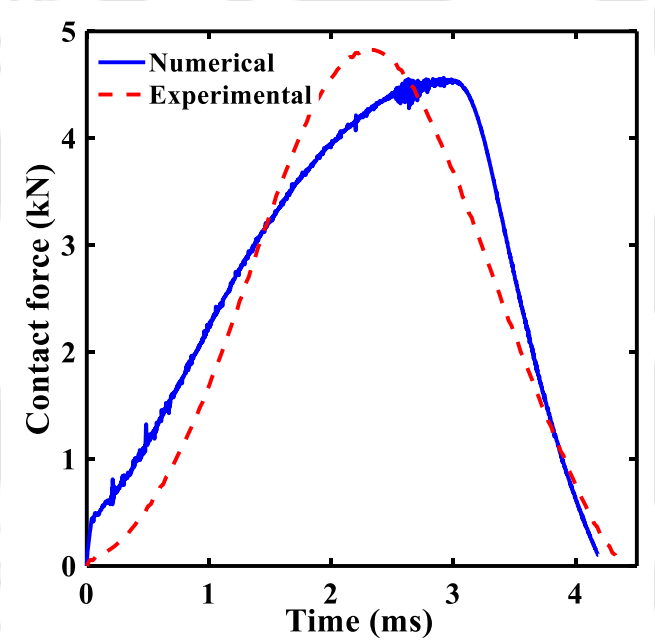

Figure 5.5 Force-time history of experimental and FE simulation for an impact energy of 13.28J

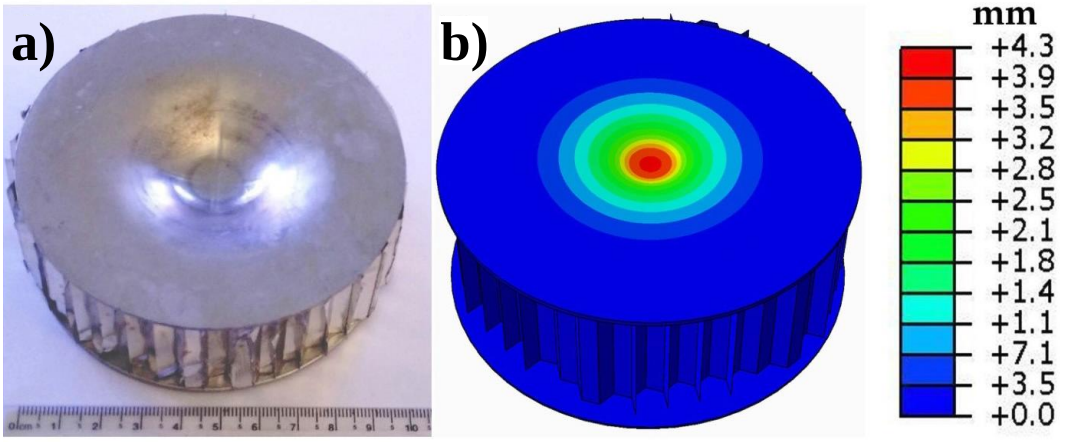

Figure 5.6 Deformation contour of honeycomb sandwich specimen subjected to impact energy of 13.28J (a) Experiment specimen, and (b) FE model

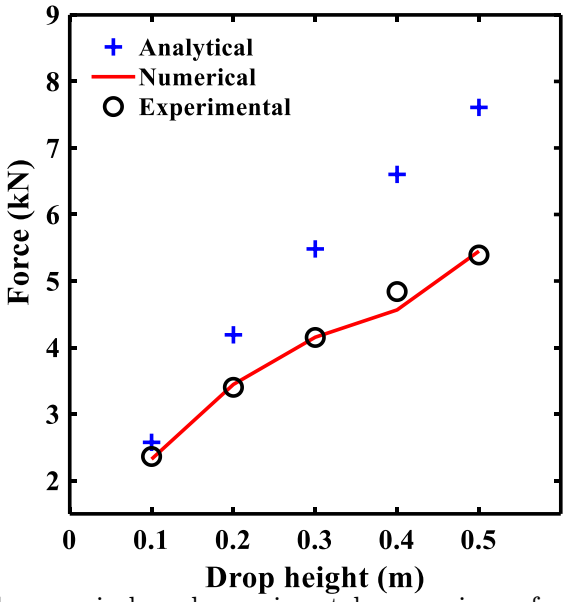

Figure 5.7 Analytical, numerical, and experimental comparison of contact force for different drop height

5.5 Probabilistic contact force model

The material constitutive behavior is quite complex and difficult to implement in the analytical model. It is essential to propose an accurate idealization of the problem resembling the physical observations. Therefore, a probabilistic model is developed by training the virtual experimental observations with respect to deterministic results using multiple linear regression approach. For the aforementioned univariate problem, multiple inputs are the nonlinear functions of geometrical and material parameters. Figure 5.8 demonstrates a methodical approach adopted in developing a probabilistic framework to predict the contact force on honeycomb composite structure when subjected to a low-velocity impact. The probabilistic model unifies analytical solution and experimental/numerical observation to predict the contact force for honeycomb structures.

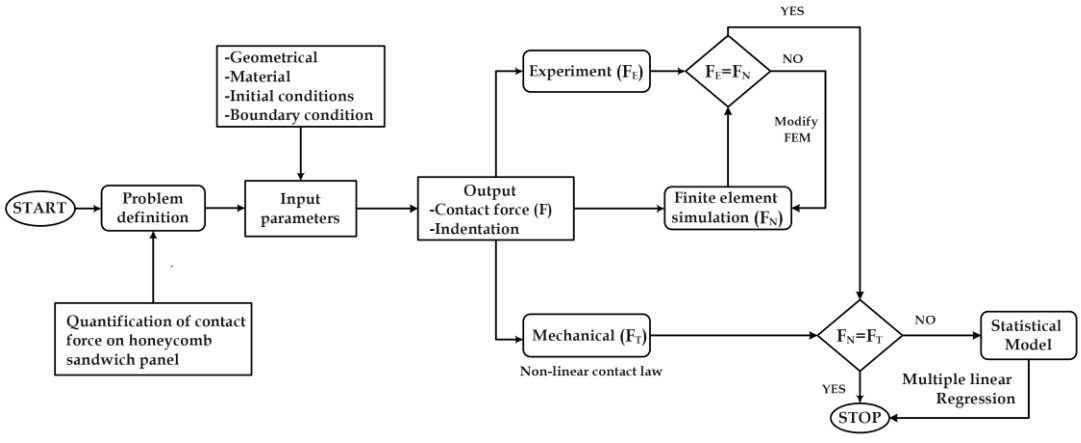

Figure 5.8 Proposed methodology for development of probabilistic contact force on honeycomb sandwich structure due to impact

5.5.1 Design of experiments

The proposed probabilistic model will be used to quantify the contact force for the uncertain input parameters within the limits of design variables. Outside the design limits, the applicability of model relies on extrapolation, which needs to be applied judiciously. The peak dynamic contact force experienced by honeycomb sandwich structures is dependent on several material and geometrical parameters. Sun et al. (2018) conducted a parametric study to determine the influencing structural parameters. They extensively investigated the influence of geometrical parameters on indentation, energy absorption and failure modes in the sandwich specimen under quasi static loads. In the initial phase, material and geometrical parameters that influence the peak dynamic contact force experienced by honeycomb sandwich specimen are identified. The range for each independent variable is optimally selected so that they represent more realistic and extreme scenario. Bitzer (2012) provides insight in defining the range for several geometrical parameters and material parameters. Table 5.3 list the extremum and mean value of geometrical and material parameters that influence the contact force response. Once the input variables and their range are defined, the probabilistic model is calibrated using data generated through multiple deterministic finite element simulations at selective design points.

The material and geometrical parameters are greatly influenced by raw material and manufacturing process that gives rise to statistical uncertainties. Honeycomb specimens are highly complexed thin walled structures and it is practically impossible to manufacture them to exact specified dimensions. This leads to uncertainties in terms of several geometrical parameters like cell wall length, foil thickness, height of core etc. The strength and material properties of a particular grade alloy vary from individual specimen leading to material uncertainties. As the input variable comprising initial conditions, material and geometrical parameters are uncertain, the influence is propagated and reflected in the contact force. The probabilistic model requires very large data over the range of input variables for removing the statistical uncertainty in structural configuration. Monte-Carlo simulations that incorporate statistical uncertainty of parameters demands rigorous FE simulations that are computationally expensive. Therefore, an efficient algorithm D-optimal design is employed and detailed FE analysis is conducted at optimally selective points (Montgomery 2017). These design points give a representative data over the entire range of input variables and is used for calibrating the probabilistic model. It is to be noted that the probabilistic model yields accurate results when applied within the range of input variables. Outside the design limits, the applicability of model relies on extrapolation. In the current study, the experimental design points comprise of 100 unique combinations of input variables.

Table 5.3 Extremum and representative values of material and geometrical parameters considered for the experimental design

Variable	Symbol	Range	Representative value
Young's modulus of facesheet (GPa)	E_f	60 – 80	70
Poisson's ratio	μ	0.28– 0.32	0.3
Yield strength of core (MPa)	σ_c	100 – 400	250
Thickness of facesheet (mm)	h_f	0.5 – 1.5	1.0
Radius of facesheet (mm)	R_f	50 – 75	62.5
Height of core (mm)	h_c	18 – 36	27
Cell wall thickness (`m)	t	40 – 100	70
Cell size (mm)	c	5 – 8	6.5
Diameter of impactor (mm)	ϕ	10 – 40	20
Lumped mass (kg)	M	0.5 – 3.0	2.0
Drop height (m)	h	0.1 – 1.0	0.5

5.5.2 Multiple linear regression model

Gardoni et al. (2002), has proposed a probabilistic framework which is adapted in the present study to predict the peak contact force. The normalized contact force is formulated as

$$\ln[\hat{F}_P(X,\Theta)] = \ln[\hat{F}_T(X)] + \gamma_D(X,\beta) + \sigma_D\varepsilon_D \tag{5.11}$$

where, $\hat{F}_P = \frac{F_p}{F_H}$ and $\hat{F}_T = \frac{F_T}{F_H}$ are predicted (F_P) and theoretical (F_T) contact force, respectively Eq. (5.6).

The peak contact force is normalized with Hertz contact force (F_H) given by $F_H = \left(\frac{5}{4}MV_o^2\right)^{0.6} K_o^{0.4}$.

where, $K_o = \frac{4}{3\pi}\sqrt{R}E^*$ and $\frac{1}{E^*} = \frac{1-\nu_1^2}{E_1} + \frac{1-\nu_2^2}{E_f}$.

The set of unknown model parameters are given by $\Theta(\beta,\sigma)$. The correction term for the mechanical model is given by $\gamma_D(X,\beta)$, where $\gamma_D(X,\beta) = \beta_o + \beta_1X_1 + \beta_2X_2 \ldots\ldots \beta_nX_n$. Here, β_i is model coefficient and X_i are the model explanatory functions. The predictive model error is given by $\sigma_D\varepsilon_D$, where σ_D is standard deviation of the model error and ε_D is random variable with zero mean and unit variance. The probabilistic model is stabilized with natural logarithmic

function to satisfy the homoscedasticity (σ_D is independent of X_i) and normality assumption (i.e. ε_D is normally distributed).

5.5.3 Explanatory terms and parameter estimation

Formulation of uncorrelated and independent set of covariates is a crucial aspect of performing regression analysis. Largely, deterministic model provides an insight on the functions that may govern the physical responses. In the first step, all the possible explanatory functions were considered, which may influence the dependent variable and are tabulated in Table 5.4. .All the explanatory terms are dimensionless and normalized to the same order. Term 'X_o' captures any inherent bias in the model, 'X_1' accounts for the impact velocity ratio. Terms 'X_2' and 'X_3' elucidates the dependency of contact force on slenderness and strength ratio of the honeycomb composite structure, respectively. Term 'X_4' accounts for the stiffness ratio of core, 'X_5' indicates the mass ratio of impact system whereas 'X_6' includes the expression for contact time and resonance. With 'n' observations and 'p' explanatory functions, the model is expressed as follows (Montgomery and Runger 2010)

$$\{Y\}_{n\times 1} = [X]_{n\times p}\{\beta\}_{p\times 1} + \{\in\}_{n\times 1} \tag{5.12}$$

Based on multiple linear regression, the least square estimates of model parameters are determined using Eq.(5.13).

$$\hat{\beta} = (\mathrm{X'X})^{-1}X'Y \tag{5.13}$$

The unbiased estimator of residual mean square error is evaluated as

$$\hat{\sigma}_D{}^2 = \frac{e'e}{n-p} \tag{5.14}$$

Here, e represents the residual of predicted and experimental values. The covariance matrix of estimated regression coefficients $(\hat{\beta})$ is defined as

$$\mathrm{C}(\hat{\beta}) = \sigma^2{}_{\mathrm{D}}(X'X)^{-1} \tag{5.15}$$

The square root of the diagonal terms of $C(\hat{\beta})$ are defined as estimated standard error

$$\text{se}(\hat{\beta}_i) = \sqrt{\left[C(\hat{\beta})\right]_{ii}} \tag{5.16}$$

5.5.4 Model assessment

However, it is evident that not all the candidate variables substantially upsurge the model accuracy. A probabilistic model needs to be parsimonious comprising minimum set of regressors. The insensitive regressors are deleted using step-wise element deletion technique to reduce the model complexity (Gardoni et al. 2002). Model parameters having coefficient of variation (c.o.v) significantly greater than standard deviation (σ_D) of the model error does not contribute to its accuracy. Hence, these independent variables can be conveniently deleted for the model simplicity. For the first trial, the model is assessed considering all the assumed variables as listed in Table 5.4. The largest c.o.v (β_3) is found to be 0.69 while the standard deviation of the model error is 0.19. The model is stepwise reassessed by deleting the parameters have c.o.v greater than the standard deviation of model. The parameter deletion step is terminated when there is significant increase in σ_D. Figure 5.9 tracks the changes in c.o.v and σ_D during the stepwise deletion process. In step 5, the model parameter with largest c.o.v is 0.25, which is approximately equal to the σ_D (0.21). The final regression model includes X_1, X_2, X_3, and, X_4 terms, as any further parameter deletion increases σ_D considerably. The least square estimates of the model parameter $\left(\hat{\beta}\right)$ and their standard deviation are summarized in Table 5.5.

.

Table 5.4 Tabulation of explanatory regressor functions

Regressor	Variable	Expressions	Nomenclature
Constant bias	X_o	1	
Velocity ratio	X_1	$X_1 = \frac{V_c}{V_s}$ $V_s = \frac{M_1}{M_1 + M_2} V_o$; $V_c = \frac{q}{c_0 \rho_c}$; $c_o = \sqrt{\frac{E_f}{\rho_{alu}}}$	V_s-Velocity of composite structure V_c-Deformation speed of the core c_0 - Speed of sound wave
Slenderness ratio	X_2	$X_2 = \frac{c}{h_c}$	c - cell size h_c - height of core
Strength ratio	X_3	$X_3 = \frac{q}{\sigma_c}$	q - crushing strength σ_c - yield strength
Stiffness ratio	X_4	$X_4 = \frac{K_b}{D_m}$	K_b-bending stiffness D_m-membrane rigidity
Mass ratio	X_5	$X_5 = \frac{M_1 + M_2}{M_2}$	M_1- mass of the impactor M_2-mass of the panel
Resonance-Time ratio	X_6	$X_6 = \omega T_c \; X_4$ $\omega = \sqrt{\frac{s(M_1 + M_2)}{M_1 M_2}}$; $T_c = 2.87 \left(\frac{M_1^{\,2}}{\mathrm{R_e} E^{*2} V_o} \right)^{1/5}$ $s = \frac{\partial P}{\partial \delta}$; $P = K_{sp} \delta_z^{3/2}$	ω-contact resonance (s^{-1}) T_c-contact time(s) s - effective stiffness

Table 5.5 Estimates of Model Parameters

Variable	Mean	Standard error
β_1	0.0590	0.0075
β_2	-0.8017	0.1090
β_4	-0.0388	0.0099
σ_D	0.2114	0.0216

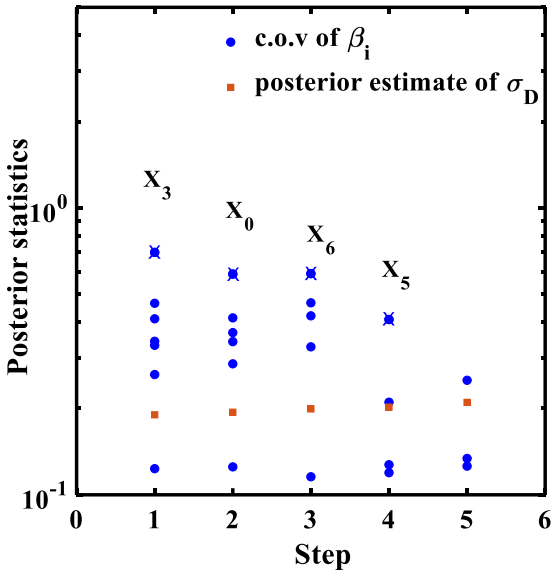

Figure 5.9 Step-wise element deletion of regressors

The correlation coefficient matrix of the standardized explanatory functions is shown in Table 5.6. The diagonal terms of inverse of correlation coefficient matrix are defined as variance inflation factors (VIF). The VIF for the model lies between 1 and 1.8 indicating no significant multi- collinearity.

Table 5.6 Correlation coefficient matrix of the explanatory functions

	β_1	β_2	β_4	σ_D
β_1	1.000	-	-	-
β_2	-0.0863	1.000	-	-
β_4	0.0018	-0.646	1.000	-
σ_D	0.000	0.000	0.000	1.000

The probabilistic model for the prediction of the peak contact force on the honeycomb composite structure due to low-velocity impact is given as

$$\hat{F}_P = \hat{F}_T \exp\left\{0.059\frac{V_c}{V_s} - 0.802\frac{c}{h_c} - 0.039\frac{K_b}{D_m}\right\} \tag{5.17}$$

The residual of the model is normally distributed with mean zero. Several residual plots are examined to determine the usefulness of the individual candidate variables. In all the cases, the standardize residue is randomly scattered with respect to explanatory function in the given bounds. Validation of the predicted results is indispensable for determining the accuracy of the probabilistic model. The comparison between deterministic responses and design of experiments data set is shown in Figure 5.10 (a). The analytical results are compared against the numerical model of design of experiments data set. The results depicted in Figure 5.5 is also a data point in the

Figure 5.10 (a). As expected, due to the uncertainties involved, the response variables are highly dispersed in the vicinity of 1:1 line. This figure lays the strong justification to incorporate of the uncertainties in geometrical and material parameter in analytical models. For an idealistic well behaving system, the analytical and experimental results will lie exactly on an 1:1 line. To prove the strength of the proposed technique, the results predicted from the probabilistic model is plotted against design of experiments data set. Figure 5.10 (b) shows the prediction capability of the probabilistic model as evaluated from Eq. (5.17). In Figure 5.10 (b), few points are the validation data points which are obtained from the experiments. Here, the validation data points are established by comparing experimental results with finite element simulation as discussed in section 5.4 (Figure 5.5). Later they are compared with proposed probabilistic model which does incorporate the uncertainty. The dotted lines indicate the confidence bound interval of the probabilistic model in form of $1{:}1 \pm \sigma_D$. The proposed model enhanced the accuracy of the prediction in low force regime. However, it is observed that the model tends to deviate for extreme combinations of material, geometric, and high impact energies. In such extreme scenarios, the honeycomb composite is excessively damaged due to perforation and it no longer remains a case of low-velocity impact.

For the input parameters within the acceptable range as established in Table 5.3, the probabilistic model predicts accurate results. The proposed model was validated by conducting experiments for set of input variables outside the training data set. This step ensures that the proposed model is not restricted to be applied only for the training data set. Also, the upper bound of the applicability of the model is evaluated through the experimental validation in upper bound data set. These experimental data points are overlaid on the Figure 5.10 (b) and lies in vicinity of 1:1 line. As seen in Figure 5.10 (b) the validation points lie within the confidence bounds and ensure applicability of the model. The proposed model performs satisfactorily for the considered range of input parameters but need to be judiciously applied for other cases.

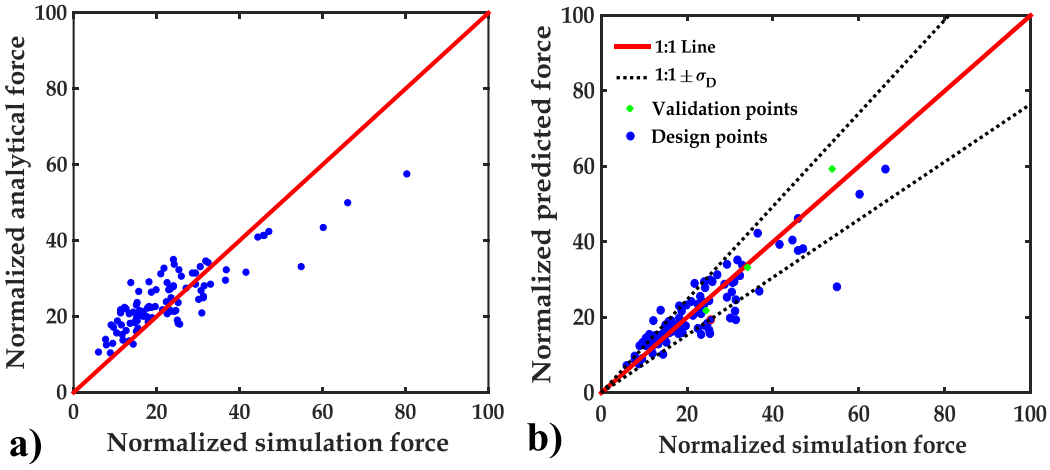

Figure 5.10 Comparison between normalized contact force: (a) Analytical and FE simulation, and (b) Probabilistic and FE simulation

5.6 Concluding remarks

In this chapter, a probabilistic model is proposed to predict the peak contact force induced in the honeycomb sandwich structure subjected to low-velocity impact. The theoretical prediction of the physical responses is always ambiguous due to the uncertainties involved in the estimation of geometrical and material parameters. Therefore, conducting experimental and numerical simulations is always preferred for analyzing such uncertain systems. However, these approaches being uneconomical and time consuming, are least preferred for routine applications. The existing theoretical model based on energy balance principle is unable to accurately predict the contact force. The influencing parameters which are not given due consideration in the theoretical model are identified through extensive numerical investigations. Impactor mass and velocity are found to be the highly influencing parameters. It is also observed that the theoretical model does not accurately account for the core crushing strength and core density. In addition, the slenderness ratio also significantly contributes to the model response. The excessive deformation of facesheet is predominant and accounted by stiffness ratio. The knowledge of mechanics provides an insight to develop the explanatory functions incorporating the aforementioned contributing factors. These parameters correct the inherent model error using multiple linear regression stabilized in natural logarithm domain.

The present research proposes a simplified and accurate model based on knowledge gained from experimental, theoretical, and numerical investigations. Through the probabilistic equation, it is inferred that the deterministic model has undermined the contribution of velocity ratios and overemphasized the contribution from stiffness and slenderness ratios. The probabilistic model expresses the response in a simplified explicit equation, which is an alternative for experimental and numerical simulations. The evaluated response from the proposed model could be incorporated in the design of smart, efficient, and safe aerospace composites.

The current research is the first step under the framework of the performance based probabilistic study. The demand based probabilistic model accounts for the uncertainties in the structure and quantifies the peak dynamic load. Once the demand model is developed the approach can be extended towards the development of the capacity model. The subsequent study of probabilistic framework is to develop capacity based probabilistic model which can quantify the damage induced in the structure and is beyond the scope of the current study.

Chapter 6

Experimental and analytical investigation of honeycomb shielded exterior reinforced beam-column joint subjected to impact loading

6.1 Introduction

Some explosions may lead to the collapse of the entire structure and surge the casualties. It's not only limited to defense-related structures but as well as civilian structures. Therefore, it is predominant to protect the building structures from extreme events such as explosions and terrorist attacks. A lot of effort has been taken in this area to enhance the strength and ductility of the structures to withstand against such extreme loading events (Bangash 2006; Uddin 2013). In this chapter, the development and implementation of protective sacrificial layered material is carried out to mitigate the impact damage by virtue of energy absorption. Impact absorbing devices includes foam based barriers such as metallic, polymeric, polyurethane and aqueous foams (Jourdan et al. 2015; Liverts et al. 2015; Prasanna Kumar et al. 2018). Few researchers have worked on the ballistic response of composite pyramidal lattice truss structures. These lattice composite structures showed better results in mitigating the blast effects during explosions (Wadley et al. 2008; Yungwirth et al. 2008). Shukla et al. (2010) developed a metallic corrugated core sandwich panel filled with polymeric foam and conducted shock loading experiments. They observed the influence of foam infill and corrugations improved the shock performance, buckling and bending rigidity of core. Research efforts have also been devoted to the protective barriers made of woven wire mesh to protect the buildings and their occupants against blast and vehicle impact (Xiao et al. 2019). Xia et al. (2016) conducted experimental investigations on RC slab when protected with Aluminum foam composites of different graded densities under blast loading. It is observed that the linear density gradient offers a better stress-strain curve than uniform density foams. The test results demonstrate that the Aluminum foam composites are capable of mitigating the blast impact effects during their application on the RC slabs. Furthermore, the gradient densities have shown a significant effect during the blast. In contrast, the ascending density can increase the effectiveness of the foam when subjected to blast. When a structure is wrapped or strengthened with composite materials, its ductility behavior gets enhanced and will exhibit a better resistance to the extreme loadings (Mohotti et al. 2013; Mohotti et al. 2015). From the literature, it was acknowledged that Aluminum foam and honeycomb composites have shown promising results in resisting blast and impact loads (Ebrahimi et al. 2016; Hou et al. 2010; Lopatnikov et al. 2004; Schenker et al. 2008; Wu et al.

2010; Wu and Sheikh 2013; Zhu and Lu 2007; Zhu et al. 2008; Zhu et al. 2009). Several experimental studies on impact found that the application of Aluminum foam panels increases the energy absorption and impulse transfer to the protected structure (Lopatnikov et al. 2004; Schenker et al. 2005; Wu et al. 2010; Wu and Sheikh 2013).

Several numerical and analytical studies noticed that the energy absorption efficiency of Aluminum foam composites depends on its peak stress and its initial density. Likewise, in Aluminum honeycombs, it depends on the ratio of the cell size to its cell wall thickness. The performance assessment of impact mitigating devices can be computed using two extensively conventional analytical models based on *i)* Lumped spring mass model, and *ii)* Energy balance model. There are numerous studies available on the impact behavior based on lumped spring mass model approach by idealizing the composite structure (Abrate 2005; Gibson and Ashby 1999). They have proposed a probabilistic quasi-static energy balance model with modified nonlinear contact interaction to predict contact force, indentation, and global deflection in a sandwich structure. It is evident that extensive numerical and analytical investigations are essential to optimize the design of protective devices for improving the effectiveness of the dissipative protective device.

It is worthy to mention that significant progress has been made to understand the behavior of isolated composite sandwich panel to resist shock and blast loading. However, limited research literature is available on the performance of beam-column joints subjected to impact loading, which is most vulnerable to such threats (Birtel and Mark 2006; De Risi et al. 2016; Grimsmo et al. 2016; Kim and LaFave 2009; Lim et al. 2016; Parisi and Augenti 2012; Zhao et al. 2017). Furthermore, there is a lack of systematic research on the beam-column joints protected using composite shielding material to resist impact loading. The current research aims to study the endurance and sustainability of gravity design (IS 456:2016) and seismic design criteria (IS 1893:2016, IS 13920:2016) of exterior reinforced concrete beam-column joint subjected to impact loadings. The goal of the research work is to evaluate the impact resistance performance of the external beam-column assembly protected by honeycomb sacrificial composite system. Experiments at reduced scales are adopted to investigate the structural behavior and dynamic response of beam-column joint. Impact studies are conducted on half-scale models of exterior reinforced concrete beam-column joint shielded with and without honeycomb sandwich panel. In the present study, a series of impact tests were conducted to investigate the efficacy of using the Aluminum honeycomb composite to protect beam-column joints against impact loading. A comparative study has been conducted on the results obtained from Aluminum honeycomb sandwich panel with pristine specimens. In addition, honeycombs with different areal densities and beam-column joint specimens that were designed for seismic and non-seismic were also investigated. The results obtained from the impact test demonstrated the efficacy of utilizing the honeycomb composite as sacrificial shielding material that absorb the impact energy by progressive plasticization of core.

6.2 Experimental program

6.2.1 Materials and specimen fabrication

i) Aluminum honeycomb core

In the current investigation, two variants of hexagonal Aluminum honeycombs manufactured from the Aluminum alloy ACG-3003 grade were employed as cores. These honeycombs are varied in terms of their cell size and cell wall thicknesses. The Aluminum honeycombs are represented based on the configurations of Density - Cell size - Cell wall thickness and all other dimensions are expressed in SI units. For example, 56-9-70 designates an Aluminum honeycomb with a density of 56 kg/m^3, the cell size of 9 mm and the cell wall thickness of 70 micron. The height of the cell core for this group is 30 mm. A rectangular shaped honeycomb is used for conducting static compressive test is shown in Figure 5.1. The geometrical properties of the Aluminum honeycombs is shown in Table 6.1. To determine the mechanical properties of Aluminum honeycomb cores (HC 30 and HC 50), quasi-static uniaxial compressive tests were conducted at a loading rate of 10 mm/min by using an INSTRON compression testing machine as shown in Figure 6.1. The dimensions of the test samples were 100 mm x 100 mm x 30 (HC 30) and 100 mm x 100 mm x 50 (HC 50) respectively. Total of three samples was tested in a controlled environment to ensure the repeatability of the results. The honeycomb samples were sandwiched between two rigid steel plates for the uniform stress distribution during the test.

Table 6.1 Geometrical properties of Aluminum honeycombs

Group	Specification [*density - cell size- cell wall thickness*] (kg/m^3- mm - μ m)	Notation	Density ρ_c (kg/m^3)	Core height h_c (mm)	Cell size l_c (mm)	Cell wall thickness t (mm)	t/l_c
I	56-9-70	HC30	56	30	9	0.07	0.008
II	84-6-70	HC50	84	50	6	0.07	0.012

All the test samples were compressed up to densification zones at 0.001 s^{-1} strain rate. For the quasi-static compressive tests, specimens without face sheets were considered. The mechanical properties of the Aluminum honeycombs are shown in Table 6.2.

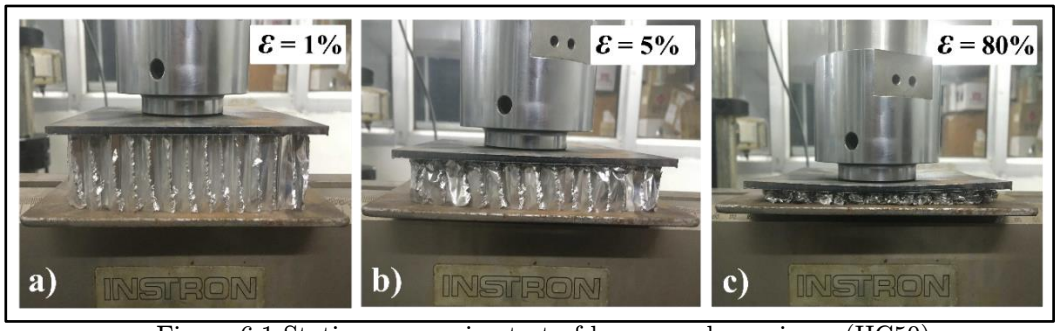

Figure 6.1 Static compressive test of honeycomb specimen (HC50)

Table 6.2 Mechanical properties of Aluminum honeycombs in the out-of-plane direction

Group	Specification [*density - cell size- cell wall thickness*] (kg/m³ - mm - μm)	Notation	Yield stress, σ_y (MPa)	Plateau stress, σ_0 (MPa)	Densification strain, ε_D	Modulus, E_c (GPa)
I	56-9-70	HC30	2.53	1.93	0.87	0.84
II	84-6-70	HC50	2.46	1.36	0.90	1.25

The density and modulus of elasticity of the honeycomb core are determined by using Eq. (6.1) and Eq. (6.2) from Gibson and Ashby (1999).

$$\frac{\rho_c}{\rho_{alu}} = \frac{8}{3}\left(\frac{t}{l_c}\right) \tag{6.1}$$

$$\frac{E_c}{E_{alu}} = \frac{2}{\cos\alpha(1+\sin\alpha)}\frac{t}{l_c} \tag{6.2}$$

The stress-strain relationship of the Aluminum honeycomb specimens is presented in Figure 6.2. Aluminum honeycombs are well known for their energy dissipating characteristic and their resistance to the external loads. The energy absorption capacity of the sacrificial Aluminum honeycomb is evaluated by the area under the stress-strain curve as shown in Figure 6.2.

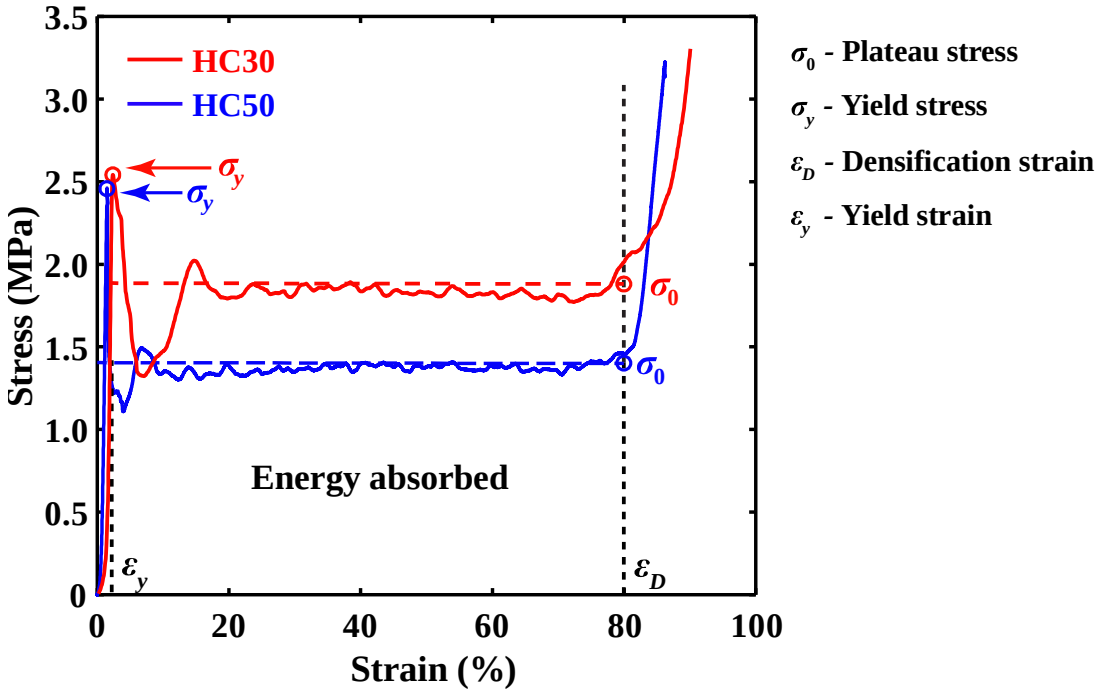

Figure 6.2 Typical stress–strain behavior of honeycomb core subjected to out-of-plane compression for HC 30 and HC 50

Thus, the absorption capacity of honeycomb is mainly governed by the magnitude of the plateau stress and the area enclose within it. From the Figure 6.2, it is evident that the plateau stress increases with the core density. Each honeycomb specimen possess yield stress (σ_y) following with its plateau stress (σ_0) region before reaching its densification strain (ε_D). In this current study, the upper yield stress point (peak value) is considered as the yield stress (σ_y) shown in Figure 6.2. The strain densification is determined from efficiency-strain curve according to the energy absorption efficiency by using Eq. (6.3) from Li et al. (2006)

$$\eta(\varepsilon) = \frac{1}{\sigma(\varepsilon)} \int_{\varepsilon_y}^{\varepsilon} \sigma(\varepsilon) d\varepsilon \tag{6.3}$$

where, 'η' is energy absorption efficiency and 'ε_y' is yield strain at the beginning of the plateau region. The strain densification is the point where the energy absorption reaches the maximum efficiency-strain curve as shown in Figure 6.2.

ii) Aluminum face sheets

The face sheets in the honeycomb panels were made of Aluminum alloy AL-5052H32. The thickness of the facesheet adopted for all the specimens was 1.5 mm. To determine the mechanical properties of these Aluminum face sheets, quasi-static tensile tests were conducted at a strain rate of 1 mm/min by using an INSTRON machine. The dimensions of the test samples following the tensile testing of metallic material standard (ASTM E8/E8M: 2016) is shown in Figure 6.3 (a). To ensure the

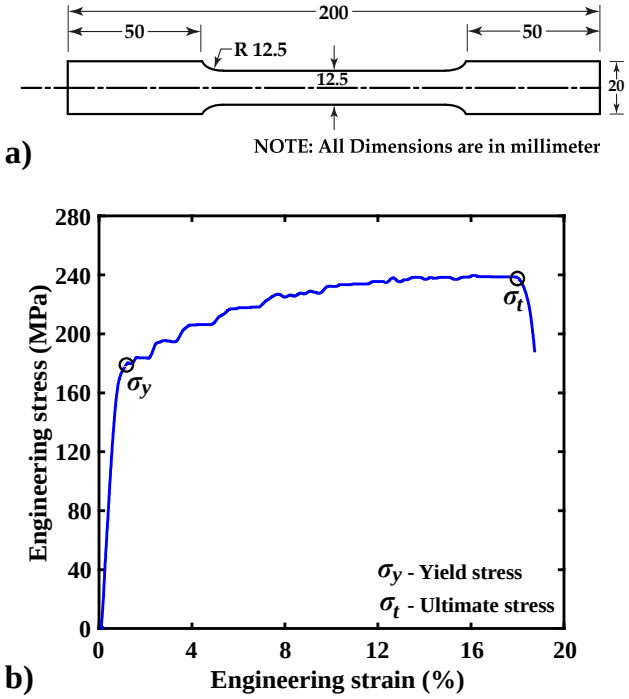

Figure 6.3 Quasi-static testing of Aluminum alloy AL 5052 H32: a) sketch of sample dimension as per ASTM E8/E8M:2016, and b) typical stress-strain curve

reproducibility, three samples were tested in a controlled environment. From the obtained force-displacement data, engineering stress-strain were calculated and plotted in Figure 6.3 (b). The average mechanical properties of three Aluminum sheet samples are as follows: Young's modulus (E) = 71 GPa, tensile yield strength = 178 MPa and ultimate tensile strength = 234 MPa.

iii) Honeycomb sandwich beam preparation

In the current investigation, there are two variants in honeycomb sandwich beam were manufactured by laying honeycomb core between two 1.5 mm thick Aluminum face sheets. For a better bonding between the face sheets and honeycomb core, rough surface was prepared on the face sheets by sanding it. Prior to bonding the face sheets with the core, both the facesheets were dried and cleaned with acetone to remove leftover surface oil. These face sheets are bonded using an epoxy adhesive. The laminated sandwich panels were left to cure for 24 hrs at room temperature at 23°C. A weight was placed on the top of the panels to give a uniform pressure that helps in the curing process. The sandwich beams were grouped as Group-I and Group-II as per the configuration of the honeycomb core. Each group consists of three samples, as shown in Table 6.2. The geometrical parameters and the configuration of honeycomb sandwich beams are shown in Table 6.3.

Table 6.3 Geometric parameters for honeycomb sacrificial composite

Description	Geometrical property	Symbol	Value
Al Facesheet (AL-5052H32)	Thickness of facesheet (mm)	d_f	1.50
	Length of facesheet (mm)	L_f	1200
	Breath of facesheet (mm)	B_f	115
Al Honeycomb core (ACG-3003)	Core height (mm)	h_c	30 50
	Core cell size (mm)	L_c	9 6
	Cell wall thickness (mm)	d_c	0.07

iv) Beam-column assembly idealization for shock driven impacts

A far-field blast is a conventional unconfined explosion that happens above the ground surface level. During this process, a shock wave propagates and progresses outwards along the ground surface, a wave front experienced as Mach stem is developed due to the interaction of the reflected wave and incident wave (Geretto et al. 2015). The intermediate amplification of the wave caused by the ground reflections rises prior to the return of the initial blast wave near the building. The propagation of the blast wave on building and its deflected shape is illustrated in Figure 6.4. For a conventional far-field blast, due to adequate standoff distance from the explosive vicinity, this Mach

stem when progress near the building gets converted into a distributed lateral pressure along the building height as shown in the Figure 6.4 (a).

Conducting full-scale moment frames is infeasible and therefore we idealized the experiments to simulate the loading conditions under a far-field explosion. A typical full-scale structure is considered to have an inter-story height of 3.0 m and the beam length of 4.8 m. In the current research, a half-scale model is employed to study the behavior of isolated external beam-column subassembly is illustrated in Figure 6.4 (a) & (b). The typical deflected shape of the moment resisting frame under the lateral loading is shown in Figure 6.4 (a). The point of contra-flexure for a typical moment resisting frame is assumed at mid-height of column and mid-length of the beam. At inflection points, shear force and axial load in the column are represented by 'V_C' and 'P_C' respectively and the shear force in the beam is represented by 'V_B'.

During a blast scenario of any explosive, the temperature and pressure inside the bomb will increase rapidly and the casing shell will expand until it breaks up in fragments. One of the maximum threats during a blast is fragmentation of the casing shells with a larger imparting velocity. Thereby, the structure can be exposed to at least three types of loading effects. They are a) impulse load from blast wave, b) impulse load from striking fragments, and c) impact load from striking fragments. An impulse is considered to give a global response whereas impact is said to be a local response caused by the penetration of fragments (Baker et al. 2012; Baker et al. 1981; Krauthammer 2008). In the current research an attempt is made to replicate the impact load from striking fragments i.e. a projectile driving with a shock wave. A shock tube has been successfully used to generate impact loading through a projectile (Li et al. 2007; Shukla et al. 2010; Yahaya et al. 2015). To achieve a controlled loading and simulate the impact scenario, we have designed and fabricated a shock tube test facility which provides a range of loading configurations that can be studied with a quantifiable assessment. The test facility has the ability to produce the impulsive loading of a wide range of intensities. In the current experimental program, a hemispherical nosed projectile with a mean velocity of 33.2 m/s, standard deviation of 0.5 was achieved during the impact experiments. The schematic illustration of the shock tube and the experimental test setup is shown in Figure 6.13 and Figure 6.14. The detailed experimental methodology is explained in the subsequent section.

v) Beam-column joint design

The beam-column sub-assembly was designed with respect to IS 456: 2016 and IS 13920: 2016. The specimens are classified into two categories i.e. *i)* Non-Seismic (NS), designed for gravity loads without any seismic detailing, and *ii)* Seismic (S), designed with seismic detailing. Both of the categories are designed and satisfied with the concept of strong column-weak beam design philosophy for efficient energy dissipation (Park and Paulay 1975). The material tests are conducted for the assessment of the strength properties of concrete and reinforcing steel. The mean characteristic

compressive strength $\left(f_{cr}\right)$ and mean split tensile strength $\left(f_{tr}\right)$ of concrete at 28 days curing was 35.7 MPa and 4.0 MPa. The yield strength $\left(f_y\right)$, ultimate strength $\left(f_t\right)$ and hardening ratio of the 12 mm longitudinal reinforcing steel bar was 566 MPa, 688 MPa and 1.21 respectively. The schematic view of the reinforcement detailing in the external beam-column joint is illustrated in Figure 6.5. The reinforcement details of the beam-column joint specimens are listed in Table 6.4. The beam-column joint specimens were shielded with Group-I and Group-II Aluminum honeycomb sandwich panel; and beam-column joint without Aluminum honeycomb sandwich panel is compared with the respective category of design. The detailed configurations of the Aluminum honeycomb beams are shown in Table 6.2 and Table 6.3. This Aluminum honeycomb beam was attached to the impact face of the beam using Z-clamp (mild steel) as shown in Figure 6.14. A total of eighteen half-scale beam-column joints is tested under impact loading. Under each category, three specimens are tested. The detailed description and notation used for Table 6.5. The experimental investigation is conducted to study the dynamic response of beam-column joints shielded by Aluminum honeycomb sandwich panel and were subjected to impact loading. The dynamic response quantities include evaluation of target damage, target morphology, displacement, and acceleration are measured at a distinct location along the length of the beam.

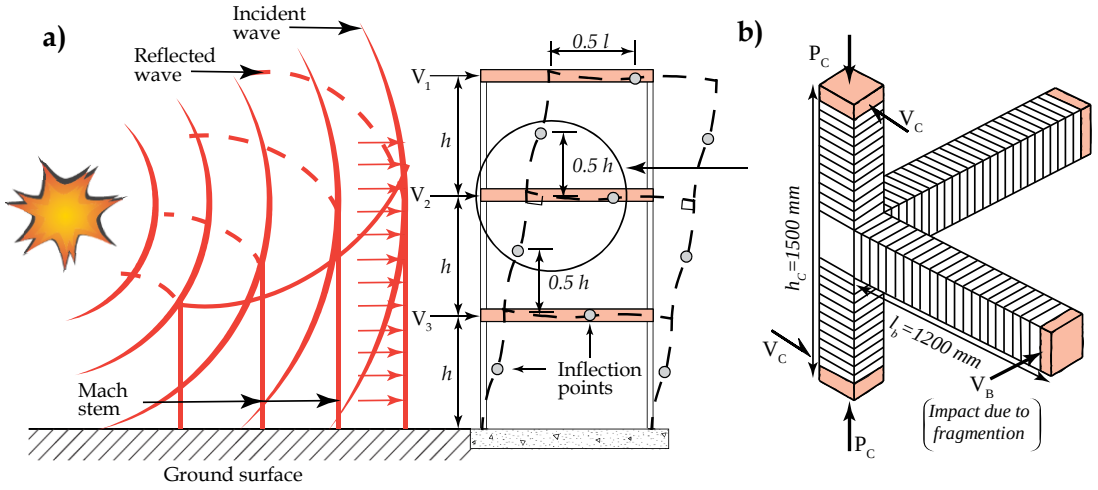

Figure 6.4 Propagation of blast wave on building along with deflected shape of the frame showing the points of contra-flexure under lateral loading, and b) isolated external beam-column joint sub-assembly with fragmentation loading

The beam-column joint specimens were shielded with Group-I and Group-II Aluminum honeycomb sacrificial composite. The impact endurance of beam-column joint without Aluminum honeycomb is compared with the protective system. The detailed configurations of the Aluminum honeycomb composite system are shown in Table 6.2 and Table 6.3. A total of eighteen half-scale beam-column joints were tested under impact loading. Under each category, three specimens are tested. The detailed description and notation used for test specimens are shown in Table 6.5.

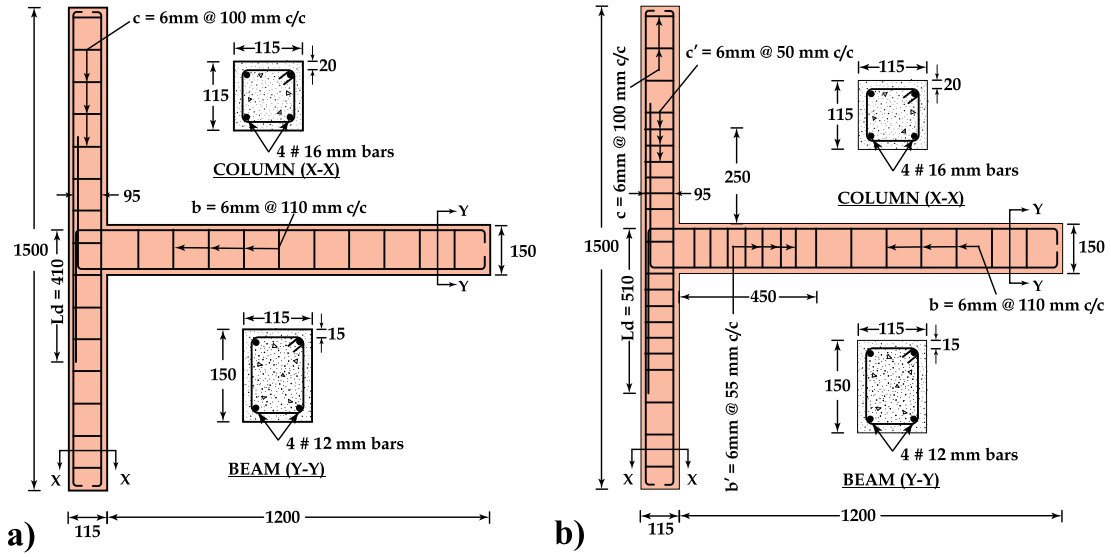

Figure 6.5 Beam-column joint geometry and reinforcement detailing: a) Non-seismic (NS), and b) Seismic (S) specimen at half-scale

Table 6.4 Reinforcement details of the specimen

Specimen Notation	Beam reinforcement		Column reinforcement	
	Main bars	Vertical stirrups spacing of 6mm bars (mm c/c)	Longitudinal bars	Lateral ties spacing of 6mm bars (mm c/c)
NS	$4-12$ mm ϕ	$b=110$	$4-16$ mm ϕ	$c=100$
S	$4-12$ mm ϕ	$b=110, b'=55$	$4-16$ mm ϕ	$c=100, c'=55$

Table 6.5 Notation for frame configuration used for the specimens

Gravity load design (IS 456: 2016)			Gravity load design with seismic detailing (IS 456: 2016, IS 13920: 2016)		
Without honeycomb	With honeycomb		Without honeycomb	With honeycomb	
NS-A	NSHC-30A	NSHC-50A	S-A	SHC-30A	SHC-50A
NS-B	NSHC-30B	NSHC-50B	S-B	SHC-30B	SHC-50B
NS-C	NSHC-30C	NSHC-50C	S-C	SHC-30C	SHC-50C

6.2.2 Experimental setup and loading protocol

i) Quasi-static cyclic loading

A schematic of the test setup and loading actuator employed in the current study is shown in Figure 6.6. The loading actuator, strong floor, strong wall, and the other clamping frames was facilitated and available in the dynamic structural testing facility at Indian Institute of Technology Guwahati. The loading setup was made of servo-hydraulic dynamic actuators (Model: MTS, USA) having a capacity of 100 kN with a displacement range of ± 120 mm. The beam-column joint specimen was erected on the strong floor with support beneath it and was clamped with MS flat strips, as shown in

Figure 6.7. The column of the subassembly was mounted horizontally with restrained supports at both ends, and the beam was placed in the vertical position in the test frame. The specimen was constrained to the strong floor through clamping system was helpful in the experimental investigation of the beam-column joints.

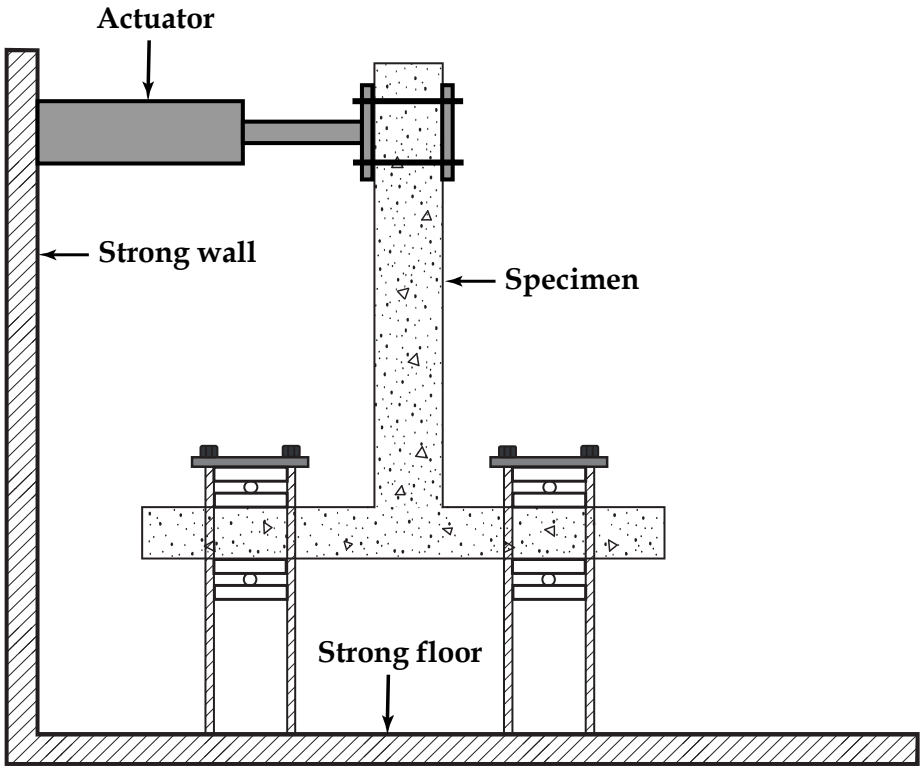

Figure 6.6 Schematic diagram of cyclic loading set up (MTS actuator) with beam-column joint specimen

Initially, the beam was attached to the actuator head and fixed it firmly for the application of load. Further, an axial load of 10% of the gross capacity of the column (horizontal member) was applied to the column to characterize the gravity load as recommended by Priestley et al. (1994). To ensure a conservative result, the applied axial load is lower than that of the load acting on the columns in the buildings. The column ends were rested and hanged at the height of 500 mm to simulate the support conditions at both ends of the column; the test setup with the complete arrangement is shown in Figure 6.7. A dynamic hydraulic actuator (Model: MTS, USA) with displacement control was applied the lateral load at the end of the beam through a loading collar mechanism. It was well-equipped with an inbuilt load cell as well as linear-variable differential transformer (LVDT) between the actuator and loading collar measures the quasi-static cyclic load applied on the beam and displacement respectively. Two additional Linear Variable Displacement Transducers (LVDTs) located along the beam axis, were used in all the experiments in order to have a more reliable measure of beam displacement, as shown in Figure 6.6. The sampling data frequency was set to a maximum acquiring data acquisition rate of 100 Hz during the test with a higher rate of loading.

Figure 6.7 Experimental setup of the actuator along with sensor instrumentation

Loading pattern and characteristics

Seismic loading is one of the extreme loadings which can devastate the entire infrastructure from the roots depends on the earthquake intensity. Much effort has been taken in this area to study the structural response under earthquake loadings as well as to enhance the strength and ductility of the structures (Uddin 2013). Most of the critical structures are likely to be situated in the highly seismic prone areas, and their design was governed by respective country seismic codes (ACI 318-14, ASCE 7-10, EC 8, NZS 1170-2004). Furthermore, such important structures identified in the seismic prone area were designed based on the current seismic codes provided by the Indian Standard (IS 1893:2016, IS 13920:2016). An exterior Beam-Column joint plays a vital role in the RC framed buildings and are probably the most exposed structural components during the earthquakes. The shear failure, anchorage, and bond failure within these vital beam-column assemblies may lead to the progressive collapse of the entire structure, which ends with the massive loss of causalities and property (Choi and Kim 2011; Yu and Tan 2013).

Many researchers adopted the quasi-static cyclic tests for testing of RC beam-column subassemblies. In the current research, the seismic loading is applied to the beam-column joint using an MTS hydraulic dynamic actuator to evaluate the structural performance. A total of two types of specimens were considered in the present study, i.e., seismic and non-seismic designed beam-column joints. All the specimens were subjected to the cyclic displacements with a gradual increase in the amplitudes applied at a loading frequency of 0.025 Hz. Initially, for every test, the lateral load was applied on the beam cyclically, in a quasi-static way at the end of the beam. The amplitude of the displacement histories considered in the current study can be seen in Figure 6.8. A drift angle is defined as the ratio of the beam tip displacement

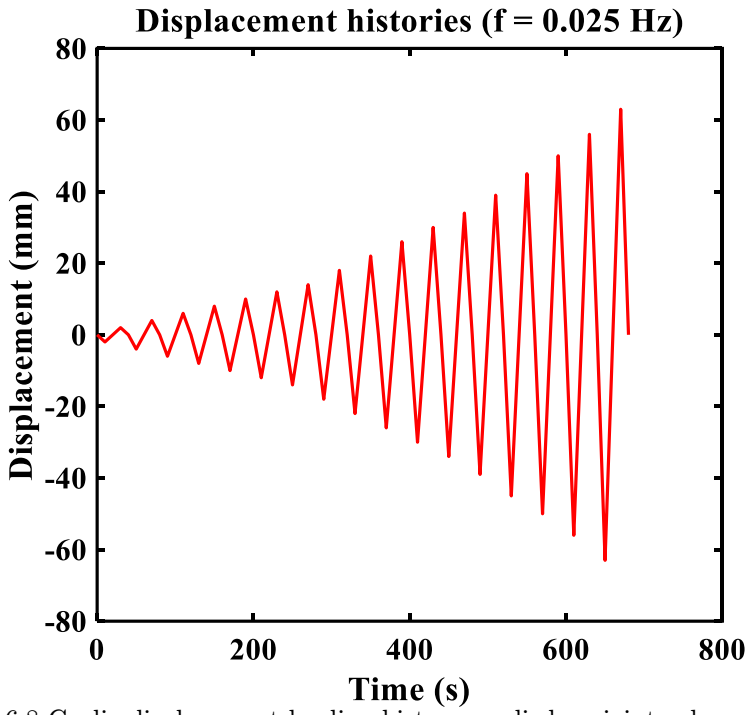

Figure 6.8 Cyclic displacement loading history applied on joint subassemblages

to the length of the beam. The loading procedure was based on the displacement-controlled steps started with the first amplitude of ±2 mm followed by steps of ±4 mm, ±6 mm, ±8 mm, ±10 mm, and after that displacement amplitude increment of ffi2mm was considered for all the experimental specimens. Each drift step consisted of 2 cycles of push and pull. During the pilot study, experiments were conducted with high frequency (0.5 Hz, 1 Hz, and 2 Hz) and found to be excited higher modes for which the responses of the test specimen are relatively lesser, and the profile of the energy dissipation was not smooth. Thus, the lower frequency (0.025 Hz) was found to be justifiable. Tests were aborted when there is a degradation in the load-carrying capacity lies in a range of 50 to 60 %. Furthermore, the damage failure pattern and mechanism in the beam-column junction zone was also monitored, and the test was aborted when the damage in the junction region was severe enough from the view of safety of the testing equipment.

Experimental results

In the current section, the experimental results obtained from the lateral load-displacement response of tested specimens were analyzed, and the evolution of crack pattern in the beam-column junction was described. After every experiment, a detailed visual inspection was carried out to examine the evolution of cracks and its propagation in the beam-column junction zone of all the specimens. The crack patterns were studied to evaluate the performance of the beam-column joint for both seismic and non-seismic design specimens. The discussion of the evolved crack pattern at the beam-column joints is as follows.

Hysteresis curves

Seismic specimen

The cyclic loading results of the beam is represented with lateral force versus displacement related to the *seismic* specimen, as shown in Figure 6.9 with insight view of crack propagation at beam-column junction. The response of the beam looks quite symmetric under push-pull cycles. The initial uncracked stiffness is equal to 1.5 kN/mm. Slowly the load was increased till the displacement reaches to 44.9 mm, and

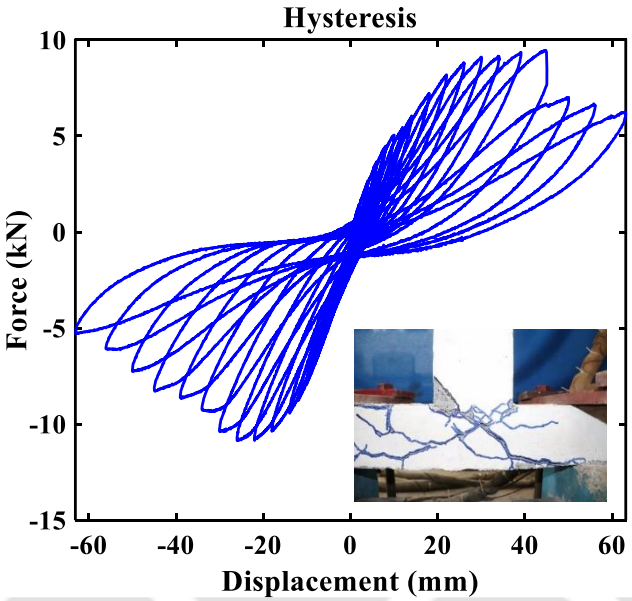

Figure 6.9 Hysteretic response of Seismic specimen (S)

later there was a sudden drop in the lateral force with the increase in the displacement. Significant crack propagation was instigated at a displacement of 5 mm to 7 mm. The peak values of lateral force in the beam were 9.5 kN and -10.8 kN respectively for positive and negative loading direction. The peak lateral force was reached for a displacement equal to 63.1 mm for positive loading direction and -63.1 mm for negative loading direction. In the current *seismic* specimen designed with ductility reinforcement, the joint shear failure occurred before yielding of the beam, i.e., at 9.3 kN, which is said to be J-failure (ACI-ASCE Committee 352). After the yielding of the beam followed up with the joint failure, the post-peak phase was characterized by gradual degradation of the stiffness of the member, i.e., stiffness softening can be observed from Figure 6.9.

Non-seismic specimen

The cyclic loading results of the beam is represented with lateral force versus displacement related to the *non-seismic* specimen, as shown in Figure 6.10 with insight view of crack propagation at beam-column junction. The response of the beam looks quite symmetric under push-pull cycles. The initial uncracked stiffness is equal to 1.0 kN/mm. Slowly the load was increased till the displacement reaches to 42.1 mm, and

later there was a sudden drop in the lateral force with the increase in the displacement. Significant crack propagation was instigated at a displacement of 3 mm to 5 mm. The peak values of lateral force in the beam were 7.9 kN and -9.1 kN respectively for positive and negative loading direction. The peak lateral force was reached for a displacement equal to 60.1 mm for positive loading direction and -60.1 mm for negative loading direction. In the current *non-seismic* specimen designed only for gravity loading, experienced with the initiation of cracks in the beam-column junction interface which further propagated into the column (associated with a localized strength reduction) reaches a maximum yielding point at 7.8 kN, which is said to be BJ-failure (ACI-ASCE Committee 352). After the yielding of the beam followed up with the joint failure, the post-peak phase was characterized by gradual degradation of the stiffness of the member, i.e., stiffness softening can be observed from Figure 6.10.

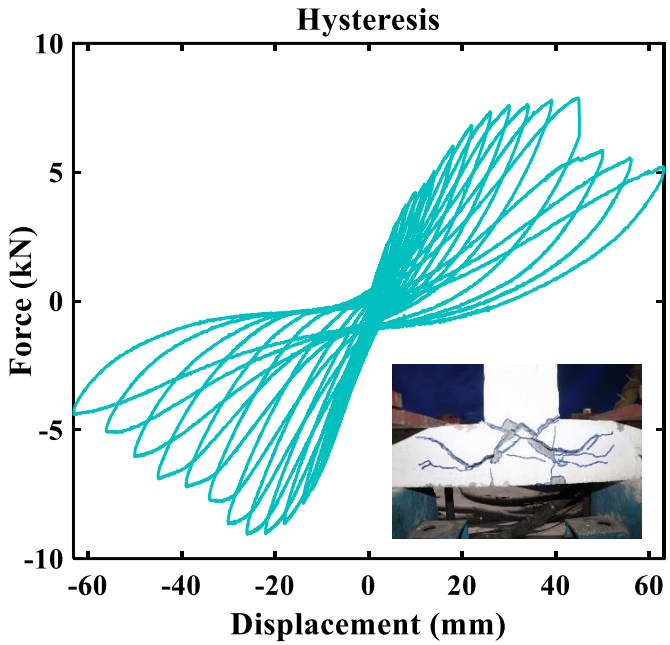

Figure 6.10 Hysteretic response of Non-Seismic specimen (NS)

Local response

Seismic specimen

Further, the evolution of damage and its crack patterns are detailed explained and shown in Figure 6.11 and Table 6.6.

a) Displacement at 5 mm

b) Displacement at 10 mm

c) Displacement at 20 mm

d) Displacement at 30 mm

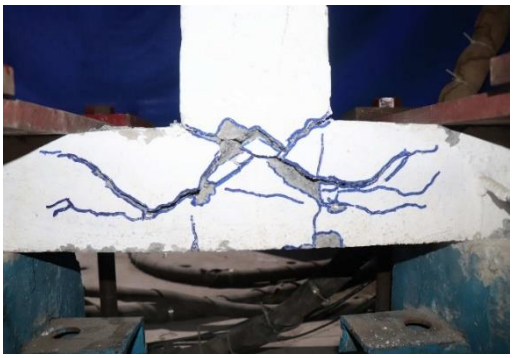

e) Displacement at 40 mm

Figure 6.11 Evolution of damage in Seismic specimen (S)

Table 6.6 Description of the evolution of damage for Seismic specimen

Description of the evolution of damage for seismic specimen			
Displacement (mm)	Damage description		
	Beam	Joint	Column
5.0	Minor hairline crack at beam-junction interface along the width of the beam	No damage	No damage
10.0	Crack opening at beam-junction interface along the width of the beam	Initiation of diagonal cracks at beam corner	–
20.0	Length of the crack opening is increasing with the load	Propagation of diagonal cracks in the beam-column junction from the initial crack	Development of joint crack into the column surface
30.0	–	Formation of new diagonal cracks	–
40.0	–	Formation of new diagonal cracks	–
50.0	Spalling of concrete from the crack opening due to the severe extension of crack	Spalling of concrete cover on the interface along the diagonal cracks	Lengthening of existing diagonal crack from joint-interface

Non-seismic specimen

Further, the evolution of damage and its crack patterns are detailed explained and shown in Figure 6.12 and Table 6.7 .

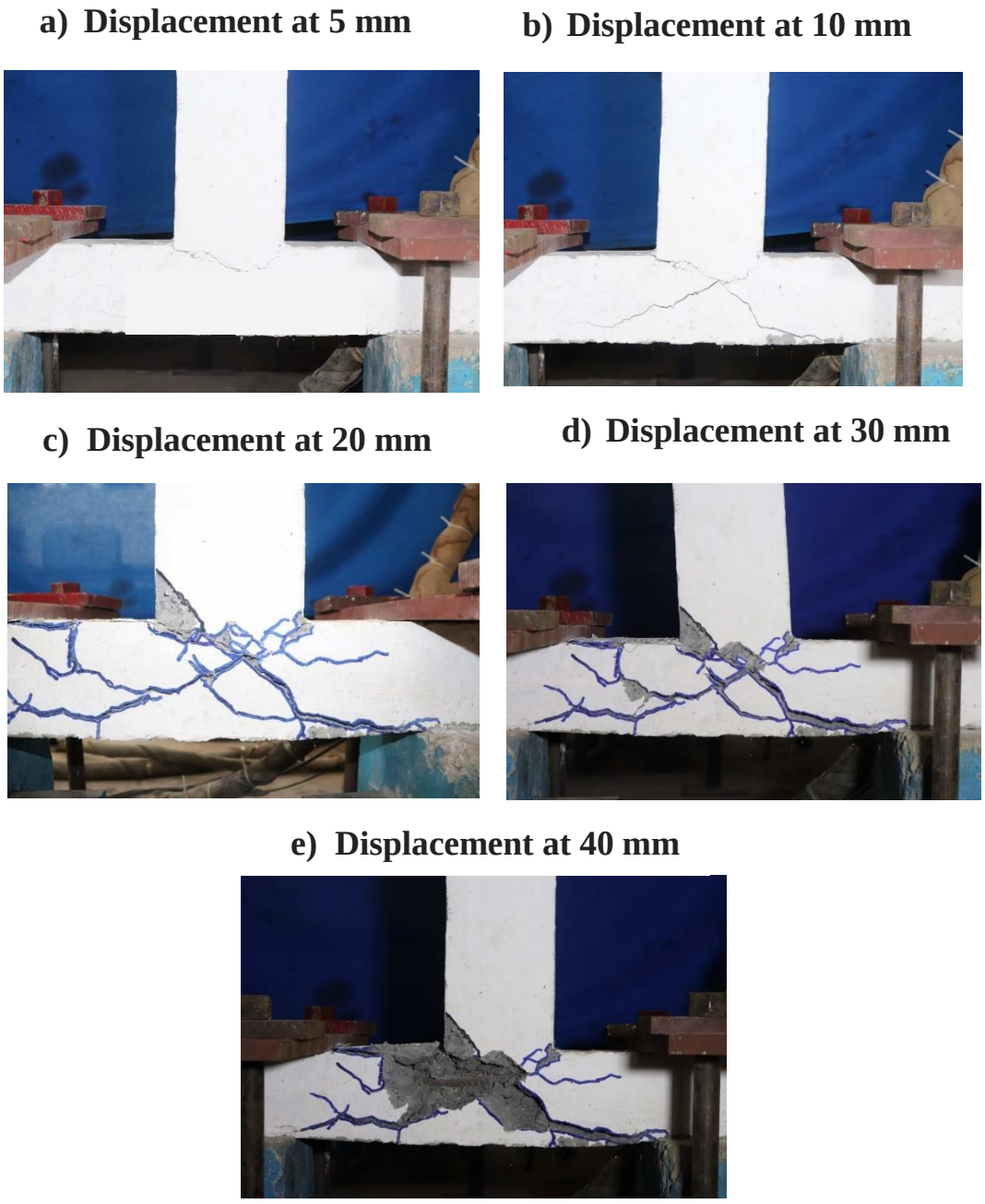

Figure 6.12 Evolution of damage in Non-Seismic specimen (NS)

Table 6.7 Description of the evolution of damage for Non-Seismic specimen

Description of the evolution of damage for non-seismic specimen			
Displacement (mm)	Damage description		
	Beam	Joint	Column
5.0	Hairline crack at beam-junction interface along the width of the beam	Initiation of diagonal cracks at beam corner	No damage
10.0	Crack opening with concrete spalling at beam-junction interface along the width of the beam	Propagation of diagonal cracks in the beam-column junction from the initial crack	Development of joint crack into the column surface
20.0	Length of the crack opening is increasing with the load	Formation of new diagonal cracks	Development of joint crack into the column surface
30.0	–	Formation of new diagonal cracks	–
40.0	–	Spalling of concrete cover on the interface along the diagonal cracks	Lengthening of existing diagonal crack from joint-interface
50.0	Spalling of concrete from the crack opening due to the severe extension of crack	Significant lengthening of existing diagonal cracks along the interface of spalled concrete	Exposure of longitudinal reinforcement in the column due to spalling extension from joint

ii) Impact loading

The shock tube test setup is used to generate impact loading on the beam-column joint. The schematic diagram and experimental setup of the shock tube is shown in Figure 6.13. The experimental investigation is conducted to study the dynamic response of beam-column joints protected using Aluminum honeycombs as a shielding material and were subjected to impact loading. The Aluminum honeycomb shielding was attached to the beam-column assembly using Z clamp (mild steel) as shown in Figure 6.14.

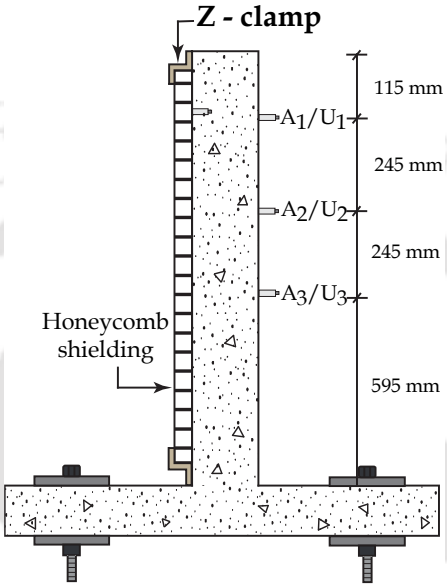

Figure 6.13 Schematic diagram of beam-column specimen with honeycomb protective system

The dynamic response quantities includes evaluation of target damage, impactor morphology, displacement, and acceleration that are measured at a distinct location along the length of the beam. In the current research work, 1 Mylar sheet (0.5mm thick) is used for all the set of experiments. Since the pressure difference in the driver and driven section reaches the extreme value and ruptures the Mylar sheet generates the shock wave and drives the projectile in the driven section towards the specimen face. The beam-column sub-assembly is subjected to impact loading and the accelerations and displacements are measured along the length of the beam at a distance 115 mm, 360 mm, 605 mm and 850 mm, from tip of the beam. The acceleration in the beam was measured using accelerometers (ICP Shock accelerometer, PCB Piezotronics Model #350C04) and processed using signal conditioner (4-Channel ICP Signal conditioner, PCB Piezotronics Model #482C24). The deflection of the beam was measured using three linear variable differential transducers (Inductive Displacement Measurement with Loose plunger, HBM Model #WA-L). The dynamic response is acquired with help of oscilloscope (Tektronix Mixed Domain- MDO-3024) having a bandwidth of 200 MHz and maximum sampling rate of 2.5 GS/s.

The experimental setup with the high speed camera system along with sensor instrumentation is shown in Figure 6.14. The internal pressure profile recorded during in the shock tube experiment is detailed in the Table 6.8. In the current research work,

a speckled hemispherical nosed projectile is used in the low-pressure regime at a distance of 600 mm away from the mouth of the shock tube for conducting the impact

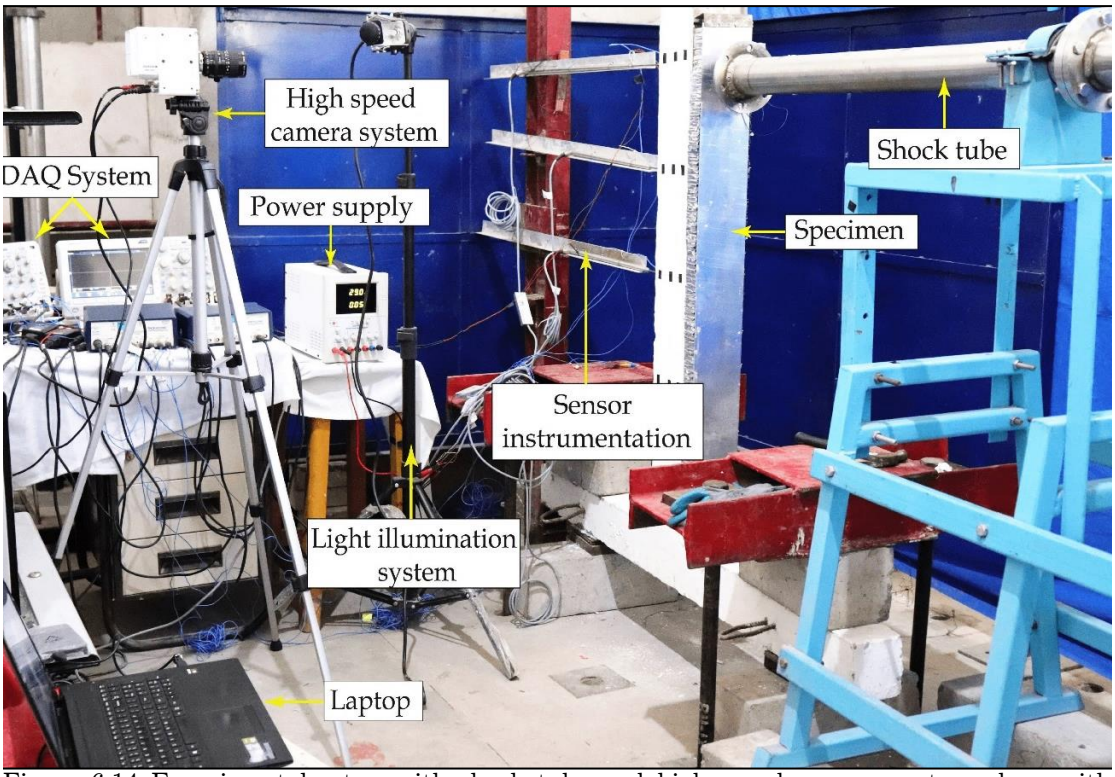

Figure 6.14 Experimental setup with shock tube and high speed camera system along with sensor instrumentation

experiment on the beam-column joint. The projectile is made up of high strength stainless steel SS 304 series. It is fabricated as a hemispherical nosed (diameter = 40 mm) with a mass of 430 g attached to a nylon shaft (diameter = 50 mm, length = 200 mm) having a mass of 370 g, thus the projectile is with a total mass of 800 g as shown in Figure 6.15.

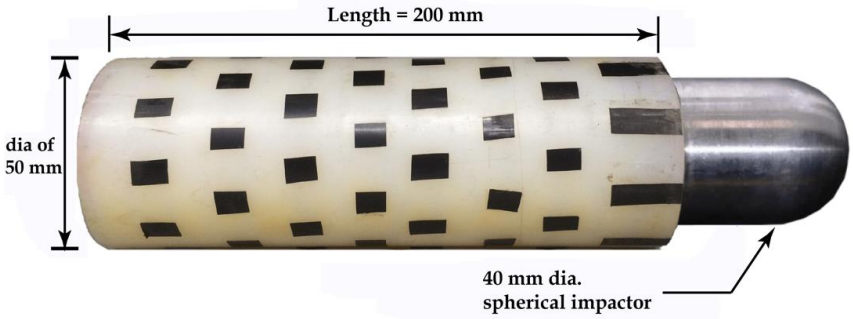

Figure 6.15 Hemispherical nosed projectile details used in experimental test

All impact tests were performed under the same test conditions, and the achieved mean velocity of the projectile was 33.2 m/s with a standard deviation of 0.5. Before conducting the proper impact tests, several trails on pre-specimens were carried out for optimal conditions and the repeatability of tests. Similar failure modes, damage

patterns and displacements were observed for the same type of test specimens. High-speed imaging of the test specimen is executed using Phantom Model #VEO 640L high-speed camera. The camera is set to record the images with 512 x 1024 pixel resolution at 7300 frames per second with an exposure time of 130 `s. Triggering of the camera is facilitated by a PZT sensor attached on the rear side of the tip of the beam.

Table 6.8 Impact experiment properties

Test	Bursting pressure (Driver section) kPa	Reflected Pressure (P_r) kPa	Avg. positive phase duration (t_d) ms
1 Mylar impact	690	619	15.62

6.3 Experimental observations

High-Speed imaging is employed to capture the perforation process during the impact along with the dynamic response of the beam-column joint. A high-speed video camera (Phantom VEO 640L) was employed to record the impact phenomenon and also to measure the projectile's normal incidence and residual velocities. The imaging is recorded at 7,300 frames per second (FPS) with a pixel resolution of 512 x 1024 to maintain a proper visualization of the perforation process. To facilitate a good illumination during the imaging process a pair of non-flickering high wattage halogen lights were installed. The exposure time of each photograph is 130 `s with an inter-frame time of 15 ms. The speckles (black square markers) attached along the length of the beam and projectile are used to track the transverse displacement, projectile velocity and residual velocity using the image correlation process. The sequence of images reveals the penetration of impactor into the specimen. The front face of the honeycomb and the beam exhibits a circular crater without a global deformation. Since the diameter of the projectile is confined to 40mm it created a localized tunnel kind of indentation and penetration in the specimens shielded with 30 mm and 50 mm honeycomb cores respectively.

The typical photographic sequence of specimen type NS-A and NSHC-30A are shown in Figure 6.16. It can be noticed that the projectile has been striking the specimen NS-A shown in Figure 6.16 (a) and the perforation was initiated at the time t = 5 ms and results with a peak displacement of 12.8 mm. The specimen NSHC-30A shown in Figure 6.16 (b), at the time t = 5 ms, the projectile was perforated in the honeycomb protective composite and minimized the damage of the specimen that results with a peak displacement of 11.6 mm. In the specimen cladded with honeycomb, initially the delamination of the facesheet occurs and led to the formation of fracture and further crushes through the honeycomb core. The various failure modes are briefly explained in Section 6.4.3.

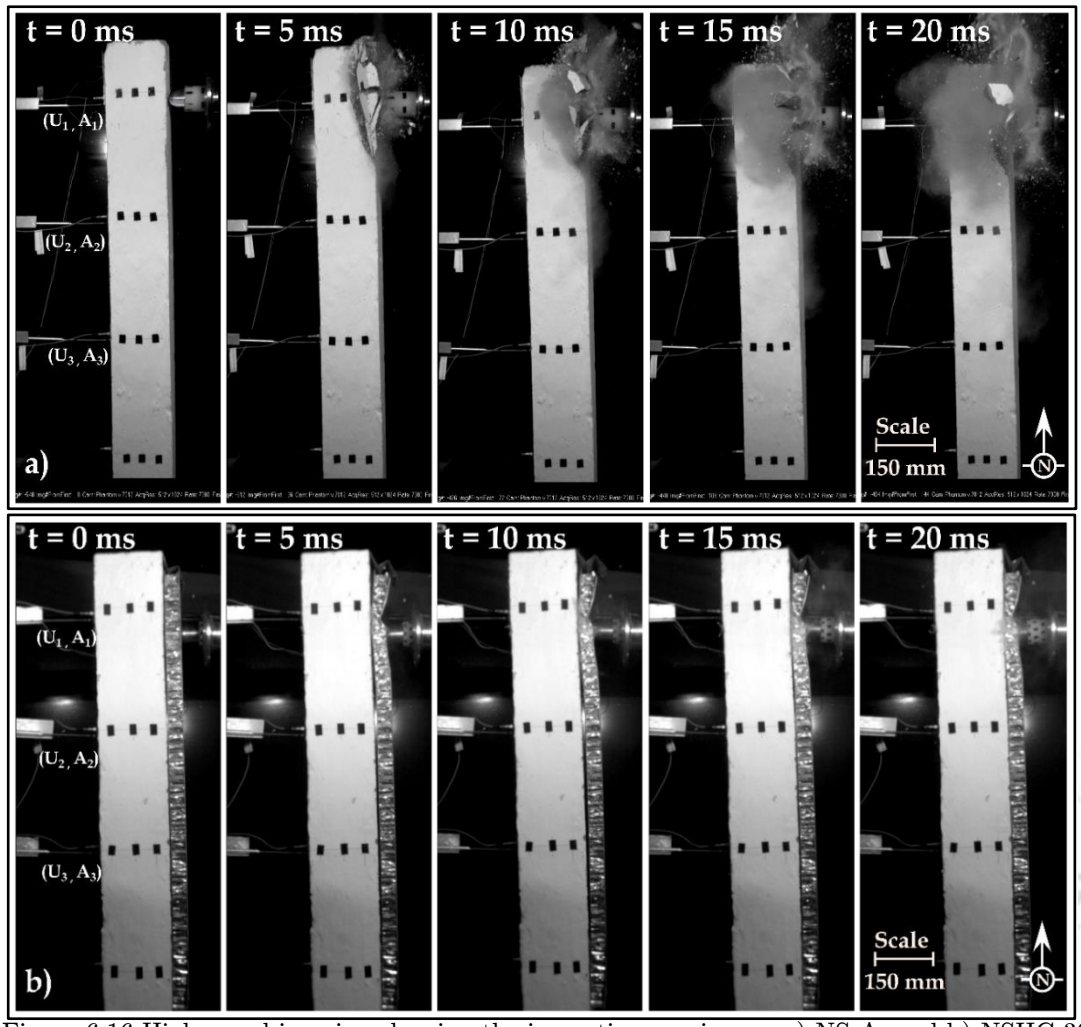

Figure 6.16 High-speed imaging showing the impacting specimens: a) NS-A, and b) NSHC-30A at an acquisition rate of 7,300 FPS

6.4 Experimental results and findings

The dynamic behavior of the exterior reinforced concrete beam-column joint was diagnosed using the following experimentally recorded data and observation:

1. Effect of impact velocity and energy absorption characteristics
2. Evaluation of target damage using crater analysis technique
3. Study of target morphology after impact
4. Evolution of cracks near beam-column joint
5. Transient displacement response
6. Acceleration time histories

The evaluated data was processed in order to determine the dynamic characteristics of the structure and for the better understanding of the dynamic response of exterior reinforced concrete beam-column joint under impact loading and the effects of the protecting aluminum honeycomb.

6.4.1 Effect of impact velocity and energy absorption characteristics

The projectile velocity was controlled by the number of Mylar sheets used in the diaphragm section. For the current set of experiments, one Mylar sheet is used for all set of experiments. The impact velocity and residual velocities of all the tests acquired from the image correlation analysis are summarized in Table 6.9. To ensure the consistency in the experiments, three specimens were tested for each type of beam-column joint under one impact loading condition. During the impact experiment, the specimens group without honeycomb shield has experienced the rebound of projectile and results in rebound velocities. Whereas, the velocities for the specimens with perforation failure shows the residual velocities as zero, that indicates the projectile has embedded into the specimen.

Table 6.9 Summary of experimental results: Ballistic velocity and perforation energy

Specimen Notation	Facesheet thickness	Core height	Core density	Impact velocity	Residual velocity	Ballistic limit	Perforation energy	Energy absorption/ Areal density
	d_f(mm)	h_c (mm)	ρ (kg/m^3)	V_i (m/s)	V_r(m/s)	V_b (m/s)	E_p(J)	E_p /A_D
NS-A	-	-	-	33.1	18.5	27.4	301.3	301.3
NS-B	-	-	-	32.8	18.9	26.8	287.5	287.5
NS-C	-	-	-	33.3	19.4	27.1	293.0	293.0
NSHC-30A	1.5	30	56	33.0	9.1	31.7	402.3	236.7
NSHC-30B	1.5	30	56	32.4	8.7	31.2	389.6	229.2
NSHC-30C	1.5	30	56	33.9	8.9	32.7	428.0	251.8
NSHC-50A	1.5	50	84	34.1	0.0	34.1	465.1	110.7
NSHC-50B	1.5	50	84	32.3	0.0	32.3	417.3	99.4
NSHC-50C	1.5	50	84	33.0	0.0	33.0	435.6	103.7
S-A	-	-	-	32.6	18.0	27.2	295.8	295.8
S-B	-	-	-	33.0	19.9	26.3	277.2	277.2
S-C	-	-	-	33.8	18.6	28.2	318.6	318.6
SHC-30A	1.5	30	56	33.2	8.2	32.2	414.7	243.9
SHC-30B	1.5	30	56	33.9	8.7	32.8	429.6	252.7
SHC-30C	1.5	30	56	32.7	8.3	31.6	400.2	235.4
SHC-50A	1.5	50	84	33.7	0.0	33.7	452.9	107.8
SHC-50B	1.5	50	84	33.5	0.0	33.5	449.2	106.9
SHC-50C	1.5	50	84	32.9	0.0	32.9	433.0	103.1

Two important computable results are considered in detail to evaluate the perforation resistant behavior and the energy absorption performance of the test specimens: (1) Ballistic limit velocity (V_b), which is well-defined as the minimum impact velocity required by the projectile to either penetrate into the specimen completely or stuck in the specimen; and (2) Perforation energy (E_p), which indicates the energy absorbed by the specimen during the perforation of projectile. To predict the ballistic limit and perforation energy, empirical equations were derived using

dimensionless analysis. The current approach is based on the assumption that the penetration is localized.

Energy absorption or perforation energy (E_p) is then equal to the difference of the initial impact kinetic energy and residual kinetic energy. Therefore,

$$E_p = \frac{1}{2} m_i V_i^2 - \frac{1}{2} m_i V_r^2 \tag{6.4}$$

Here 'm_i' is the mass of the projectile. Assuming that the kinetic energy of the projectile is all dissipated by the honeycomb absorbers and 'V_r' is significantly smaller, such that the energy loss due to the all other mechanisms are neglected and the corresponding perforation energy is given by

$$E_p = \frac{1}{2} m_i V_b^2 \tag{6.5}$$

From the above equations Eq.(6.4) and Eq.(6.5), ballistic limit (V_b) can be obtained. If the projectile gets embedded in the specimen, then the 'V_r' will be exterminated and $V_b = V_i$. Therefore, the energy absorption by the specimen would be the same as the projectile's initial kinetic energy, i.e. $(1/2)\ m_i V_i^2$. The summary of the estimated ballistic limit and perforation energy is listed in Table 6.9. The results of the residual velocity, ballistic limit, and energy absorption were compared in the groups of seismic and non-seismic specimens for both with and without honeycomb shielding. During the impact experiment, the specimens group without honeycomb shielding i.e. NS-A, B, C and S-A, B, C has experienced the rebound of projectile and results in minimum residual velocities. It was found that the specimens shielded with Group-II honeycomb i.e., 50 mm thick which possess higher areal density have a higher ballistic limit for both seismic and non-seismic specimens respectively. It demonstrates that the increase in the areal density of the honeycomb with higher ductility will enhance the energy absorption as well as ballistic velocity. The comparison plots of the ballistic limit of the non-seismic group specimens compared with seismic group specimens for with and without honeycomb shielding is shown in Figure 6.17. The ratio of the energy absorption to the areal density is minimum in the specimens shielded with 50 mm thick honeycomb. The research observation shows that the specimen shielded with higher areal density honeycomb exhibited a superior performance against the impact events. The comparison plots of the ratio of energy absorption to the areal density of the non-seismic group specimens compared with seismic group specimens for with and without honeycomb shielding is shown in Figure 6.18.

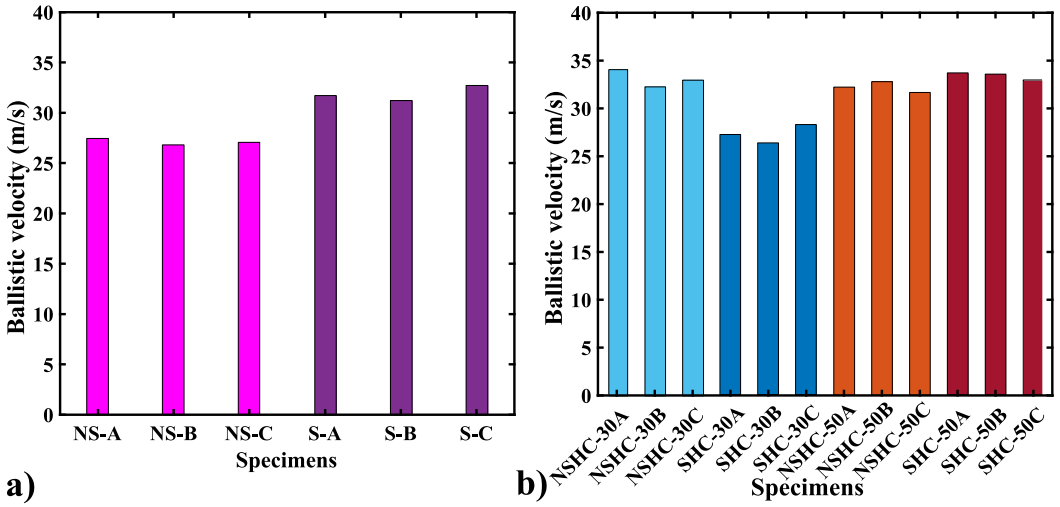

Figure 6.17 Comparison of Ballistic limit velocity results: a) Specimens group without honeycomb shielding, and b) Specimens group with honeycomb shielding

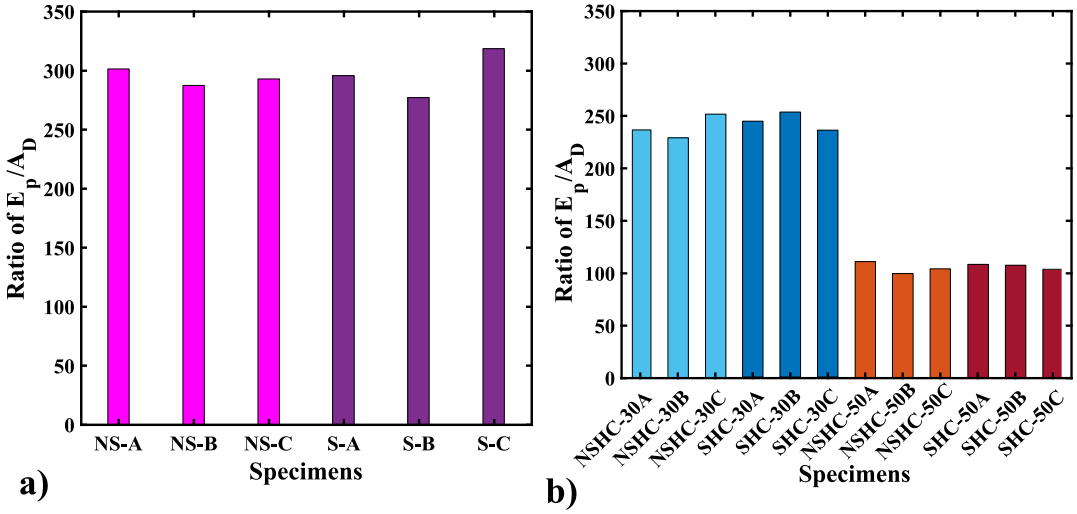

Figure 6.18 Comparison of Ratio of E_p/A_D results: a) Specimens group without honeycomb shielding, and b) Specimens group with honeycomb shielding

6.4.2 Evaluation of target damage using crater analysis technique

The failure of the specimen during the impact experiments occurs through the origination of radial cracks and fracture on the surface of specimens with and without honeycomb. The dimension of the surface craters formed on the specimen due to the impact were measured to determine the magnitude of the damage. The equivalent diameter of the surface crater was measured as the average of the four diameters in four different directions at 45 degree angle is represented with a schematic diagram in Figure 6.19. Therefore, the equivalent diameter of the surface crater is calculated for all the impacted specimens and the summary is detailed in Table 6.10.

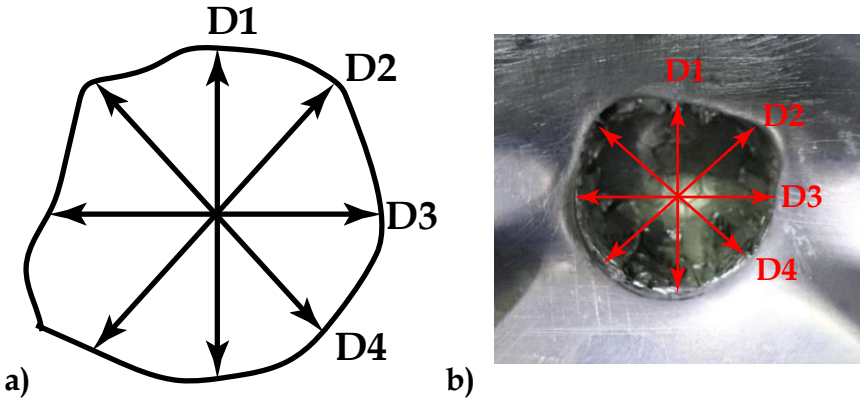

Figure 6.19 Measurement of equivalent diameter (D_{eq}) of surface crater: a) schematic diagram, and b) specimen NSHC-50A

It was observed that the specimens group of non-seismic (NS) i.e. beam-column joint without honeycomb shielding has undergone significant surface crater damage when compared to seismic (S) group specimens. It should be noted that the specimens shielded with honeycomb Group-I (30 mm) and Group-II (50 mm) experienced a variant surface crater but has protected the specimen from the impact in both seismic (SHC) and non-seismic (NSHC) specimens.

Table 6.10 Equivalent crater diameter on beam-column joint subjected by 0.80 kg projectile

Specimen Notation	D1 (mm)	D2 (mm)	D3 (mm)	D4 (mm)	Equivalent diameter D_{eq} (mm)	Depth of the crater T_d (mm)	Standard deviation (SD)	
							D_{eq}	T_d
NS-A	39	36	36	50	40.3	19.0		
NS-B	38	30	33	46	36.8	21.0	1.8	2.0
NS-C	40	32	33	53	39.5	17.0		
NSHC-30A	30	34	29	29	30.5	33.0		
NSHC-30B	27	30	29	28	28.5	32.5	1.1	1.3
NSHC-30C	28	29	27	31	28.8	35.0		
NSHC-50A	46	45	44	48	45.8	51.5		
NSHC-50B	46	43	44	43	44.0	52.0	1.6	0.3
NSHC-50C	48	49	45	47	47.3	52.0		
S-A	29	29	28	31	29.3	10.0		
S-B	27	28	27	29	27.8	8.0	0.8	2.5
S-C	29	31	28	27	28.8	13.0		
SHC-30A	34	29	28	27	29.5	28.0		
SHC-30B	30	31	27	27	28.8	27.0	0.6	1.3
SHC-30C	28	31	28	26	28.3	29.5		
SHC-50A	41	40	40	41	40.5	50.5		
SHC-50B	41	39	41	41	40.5	51.5	0.6	0.5
SHC-50C	42	40	43	41	41.5	51.0		

The extent of the crater damage on the impacted surface has significant variation with respect to the type of specimen (seismic and non-seismic), and projectile velocity for the specimens without the honeycomb. On the other hand, specimens shielded with honeycomb, the crater has been found to have insignificant influence with respect to the type of specimen and projectile velocity. A localization effect has been witnessed in all the test specimens against impact loading. The size of the crater in the Group-I (30 mm) specimens in both seismic and non-seismic case are relatively smaller compared to the other specimens. The equivalent diameter of the surface crater in the specimens with honeycomb (30 mm, 50 mm) for both seismic (SHC) and non-seismic (NSHC) varied from 28 to 42 mm and 28 to 48 mm respectively. However, both the core thicknesses of honeycomb shielded specimens experienced similar kind of crater damage. The detailed study of failure analysis is explained in the subsequent sections.

6.4.3 Study of target morphology after impact

The damage induced by the projectile is further studied in terms of target morphology that describes the failure modes of the specimen. Depending on the design category and impact energy, the specimens exhibit five types of failure modes, (1) Indentation-I; (2) Crack-C; (3) Fracture-F; (4) Penetration-P; and (5) Spalling-S. The schematic diagram of the various failure modes observed in this experiment is illustrated in Figure 6.20. It should be mentioned here that all the tests in the current study exhibits one of the distinct mode of failure out of five types of failure modes. The typical failure modes observed on the specimens impacted by hemispherical nosed projectile are shown in Figure 6.21.

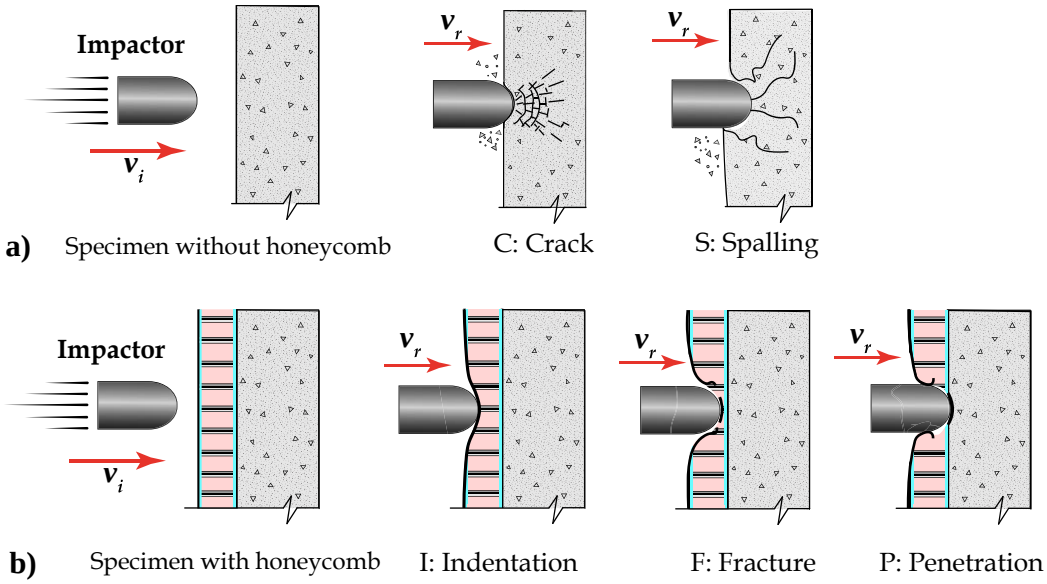

Figure 6.20 Schematic diagram of typical failure modes: a) specimen without honeycomb shielding, and b) specimen with honeycomb shielding

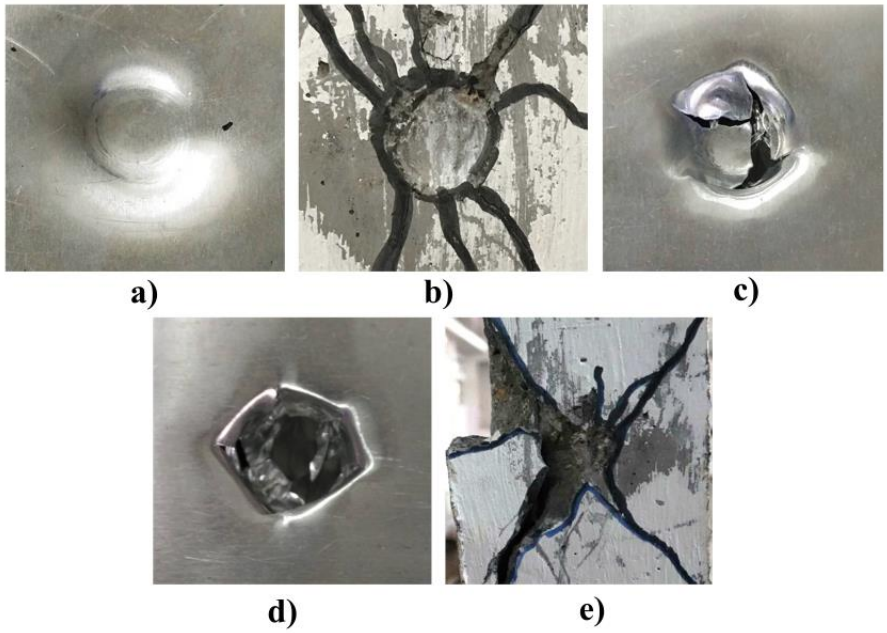

Figure 6.21 Typical failure modes of the front-face of honeycomb and concrete beam: a) Type I (Indentation), b) Type C (Crack), c) Type F (Fracture), d) Type P (Penetration), and e) Type S (Spalling)

A detailed summary of experimental failure modes for beam-column assembly subjected to impact considering seismic (S), non-seismic (NS) group without and with honeycomb (HC) sacrificial composite is shown in Figure 6.22.

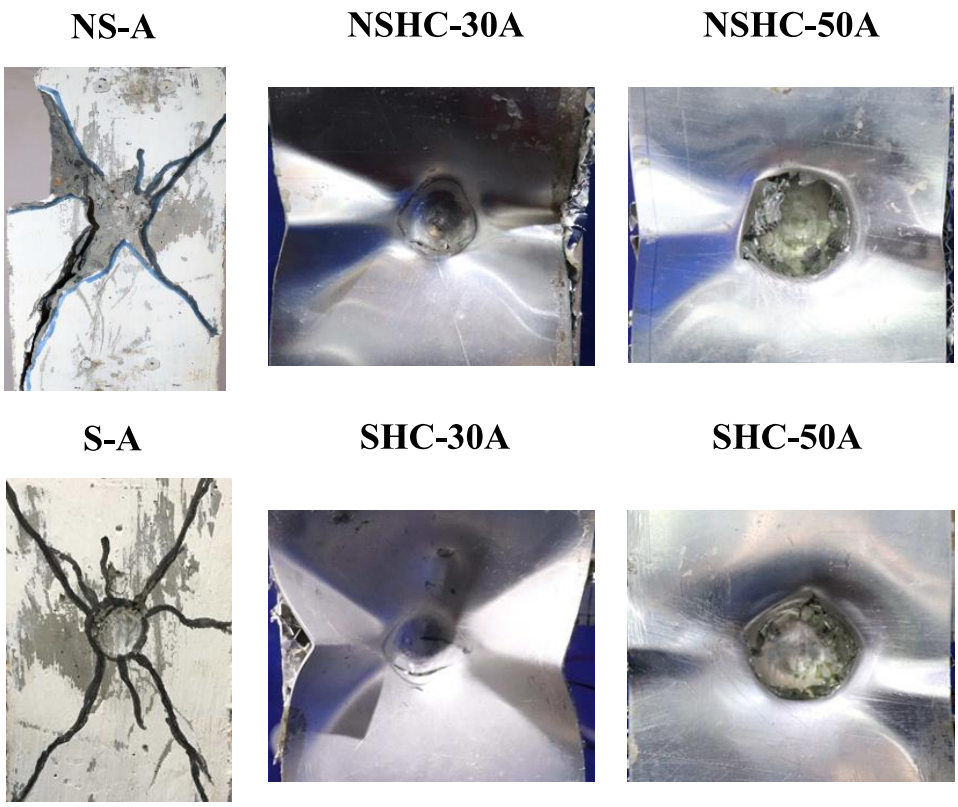

Figure 6.22 Summary of impact morphologies on various configuration of beam-column joint subjected to hemispherical nosed impactor

When the projectile contacts the specimen shielded with honeycomb, initially the front facesheet started to deform and subsequent the buckling of honeycomb cells walls occurs along the path of the front facesheet. This results in an indentation (I) on the front facesheet which is plastic deformation. Considering the test specimen shielded with 30 mm honeycomb (i.e. *NSHC-30A)*, the projectile breaks through the front facesheet of the honeycomb and results in the formation of fracture (F) and further crushes through the honeycomb core. There was no deformation observed in the back facesheet, implying that the smaller core height would lead to large bending deformation but smaller local indentation on the top facesheet. Whereas, for the test specimens shielded with 50 mm thick honeycomb core (*NSHC-50A),* the projectile fully penetrates (P) through the front facesheet as well as the core. Further, it came into contact with the back facesheet and forms a local indentation on it. Interesting results were observed regarding the relationship of the core thickness and the perforation. From both variants of honeycomb, it is confirmed that the increase in the core stiffness leads severe local indentation on the front facesheet which induces higher local stress and further failure of core. The obtained results that the core stiffness is more influential on the deformation of the front facesheet and perforation of the core. There was a noticeable amount of delamination between the core and the back facesheet that led the embedment of projectile in the core as shown in Figure 6.22. Similar findings have been observed for the seismic specimens shielded with honeycomb core thickness of 30 mm and 50 mm variant i.e. *SHC-30* and *SHC-50*.

The failure of the target specimen during impact experiment occurred through the origination of sudden radial cracks from the center of projectile nose. These cracks have propagated further that causes splitting of the concrete. It is important to identify the different types of modes of failure that can occur, in order to study the response of the specimen correctly. An impact load can results in different type of global and local damages which include radial cracks, scabbing, spalling, flexural penetration, perforation, and punching shear failure. In the current experiments, it is noticed that when the projectile contacts with the bare specimen, there was a progression of sudden radial cracks (C) originated on the surface of the concrete that results in spalling (S) of concrete. The test specimens (without honeycomb) of the seismic group (*S-A*), suffered from radial cracks on its surface. The surface of the concrete was spalled for all the test specimens in the non-seismic group (*NS-A*). The additional ductile reinforcement in the specimens provided additional strength and ductility to the concrete member and exhibits only radial cracking. Whereas, the non-seismic group specimens have undergone local damage at the impact face that consists of spalling of concrete due to the lack of ductile reinforcement.

The initial momentum and impulse per unit area generated by the projectile are calculated using Eq. (6.6) and Eq. (6.7) as proposed by Yahaya et al. (2015).

$$p_i = mv_i \tag{6.6}$$

$$\bar{I} = \rho_i l_i v_i \tag{6.7}$$

where, $'p_i'$ is initial momentum, $'m'$ is the mass of the projectile, $'v_i'$ is projectile velocity, $'\rho_i'$ is density of the projectile, $'l_i'$ is the length of the projectile, and $\bar{I}$ is impulse. The detailed summary of the experimental results of the projectile velocity, initial momentum, impulse per unit area and the failure mechanism of the both with and without honeycomb specimens are shown in Table 6.11.

Table 6.11 Summary of experimental results: Impact failure mechanism

Specimen Notation	Honeycomb			Impact velocity v_i (m/s)	Impact duration (ms)	Initial momentum p_i (kgm/s)	Standard deviation (SD)	Type of failure			
	Core height h_c (mm)	Cell size L_c (mm)	Cell wall thickness t (mm)					Front face	Core	Back face	Beam
NS-A	-	-	-	33.1	3.7	26.5		-	-	-	S
NS-B	-	-	-	32.8	4.1	26.2	0.2	-	-	-	S
NS-C	-	-	-	33.3	3.6	26.6		-	-	-	S
NSHC-30A	30	9	0.07	33.2	6.7	26.6		F	I	I	-
NSHC-30B	30	9	0.07	33.9	6.0	27.1	0.5	F	I	I	-
NSHC-30C	30	9	0.07	32.7	6.3	26.2		F	I	I	-
NSHC-50A	50	6	0.07	33.7	7.2	26.9		P	P	I	-
NSHC-50B	50	6	0.07	33.5	8.0	26.8	0.3	P	P	I	-
NSHC-50C	50	6	0.07	32.9	7.6	26.3		P	P	I	-
S-A	-	-	-	32.6	6.0	26.1		-	-	-	C
S-B	-	-	-	33.0	5.6	26.4	0.5	-	-	-	C
S-C	-	-	-	33.8	5.9	27.0		-	-	-	C
SHC-30A	30	9	0.07	33.0	6.5	26.4		F	I	I	-
SHC-30B	30	9	0.07	32.4	6.7	25.9	0.6	F	I	I	-
SHC-30C	30	9	0.07	33.9	6.0	27.1		F	I	I	-
SHC-50A	50	6	0.07	34.1	7.4	27.3		P	P	I	-
SHC-50B	50	6	0.07	32.3	7.8	25.8	0.7	P	P	I	-
SHC-50C	50	6	0.07	33.0	7.5	26.4		P	P	I	-

Note: I: Indentation; C: Crack; F: Fracture; P: Penetration; and S: Spalling

6.4.4 Evolution of cracks near beam-column joint

After conducting the experiments, a detailed visual inspection was carried to examine the evolution of cracks in the beam-column joint of all the specimens. The crack patterns were studied to evaluate the dynamic response of beam-column joint with and without honeycomb specimens. The discussion of the evolved crack pattern at the beam-column joints is as follows.

The crack pattern of the specimen NS-A and NS-B is presented in Figure 6.23. Interestingly, this work shows that the specimens shielded with honeycomb for both seismic and non-seismic do not have any kind of crack formation near the beam-column joint. It was observed that the cracks were propagating from the beam junction towards the column exterior face. The specimens designed with non-seismic detailing has a shear crack in the disturbed (D)-region due to lack of confining reinforcement.

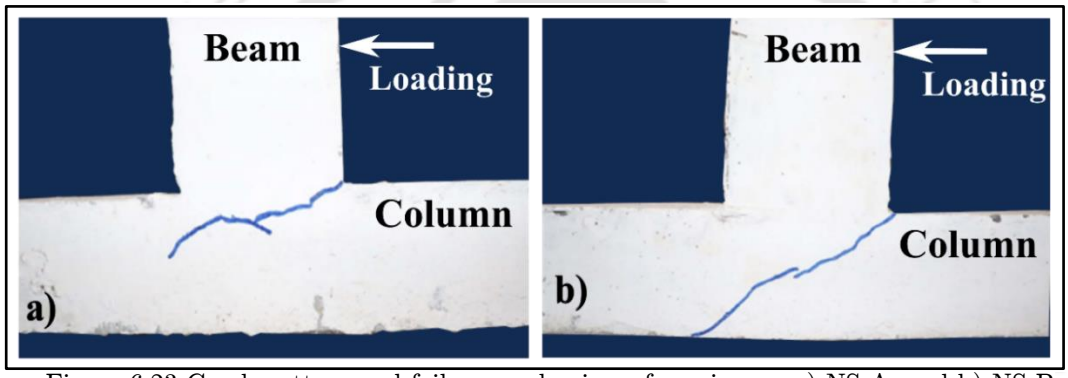

Figure 6.23 Crack pattern and failure mechanism of specimens: a) NS-A, and b) NS-B

The crack pattern of the specimen S-A and S-B is presented in Figure 6.24. In this case, the cracks initiate diagonally in the D-region and propagating further along the height of the column. Minor longitudinal crack propagation in the column is observed due to impact load. Therefore, it is inferred that the specimens designed with seismic detailing are more efficient against impact loads.

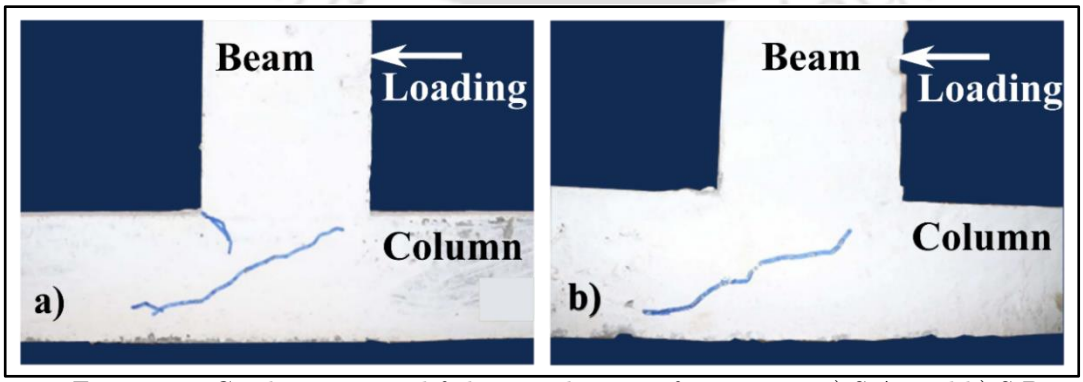

Figure 6.24 Crack pattern and failure mechanism of specimens: a) S-A, and b) S-B

6.4.5 Transient displacement response

The displacement response of all the specimens under impact loading has been acquired from the image analysis of the calibrated video data at three distinct locations along the beam as shown in Figure 6.13. The three displacements recorded along the beam length are labelled as U_1, U_2, and U_3 respectively. The displacement response for a duration of 150 ms for non-seismic specimen and seismic specimen from each group is plotted in Figure 6.25, Figure 6.26, and Figure 6.27. The summary of the maximum displacement and residual displacement for all the specimens is detailed in Table 6.12.

The magnitude of maximum and residual displacement in the seismic specimens with honeycomb (50 mm) i.e. *SHC-50* has been found to be smaller due to lower stiffness and a better energy absorption against the impact. It is observed that the additional ductility reinforcement provided in the seismic specimens was effective in reducing the residual displacement, enhances the residual capacity during the impact and minimizes the local damage at the impacted surface of the beam. From the obtained results it demonstrates that the residual displacements are very close in all the seismic specimens due to the additional ductility reinforcement. Whereas, the non-seismic specimen without honeycomb i.e. *NS* experienced higher maximum and residual displacement. The maximum and residual displacements of non-seismic group specimens (*NS, NSHC-30, NSHC-50*) was relatively higher than the seismic group specimens (*S, SHC-30, SHC-50*) respectively. The displacement has been reduced subsequently and stabilized at some permanent value which can be termed as residual displacement at the end of impact can be seen in Figure 6.25 (b). The residual displacement for the specimens with honeycomb (50mm) i.e. *NSHC-50* and *SHC-50* have found to be smaller due to its energy absorption efficiency. The reduction in residual displacement is consistent for the specimens shielded with honeycomb (30 mm and 50 mm). Thus, seismic detailing with honeycomb shielded beam-column joint enhances its impact resistance and energy absorption.

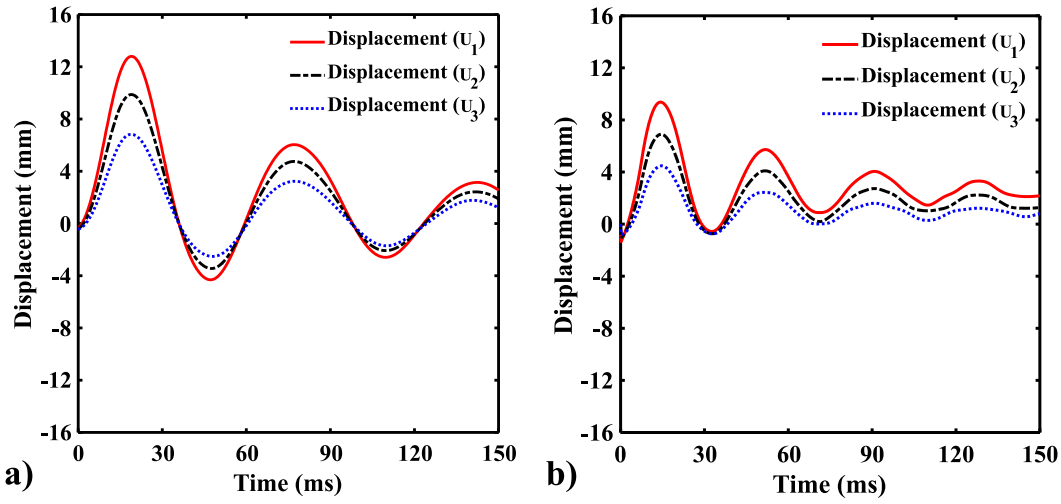

Figure 6.25 Transient displacement profile for specimens: a) NS-A, and b) S-A under impact loading

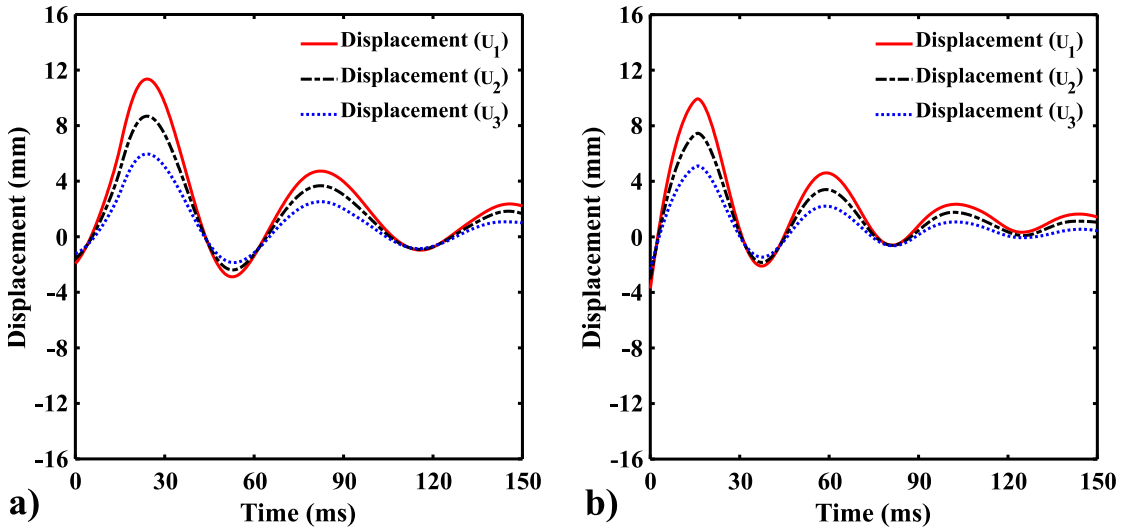

Figure 6.26 Transient displacement profile for specimens: a) NSHC-30A, and b) SHC-30A under impact loading

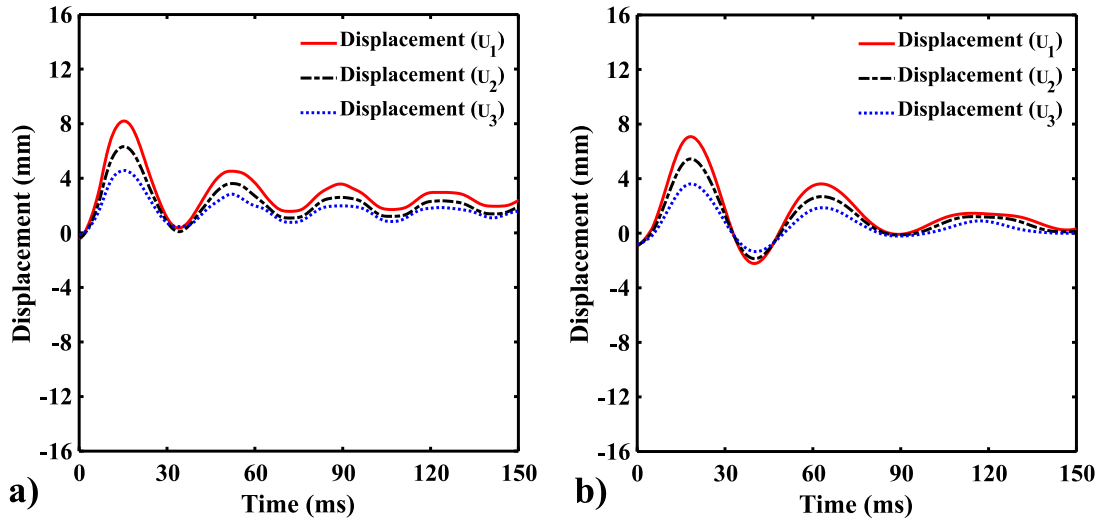

Figure 6.27 Transient displacement profile for specimens: a) NSHC-50A, and b) SHC-50A under impact loading

Table 6.12 Summary of experimental results: Displacement response

Specimen Notation	Maximum displacements			Residual displacements			Standard deviation (SD)	
	δ_1 (mm)	δ_2 (mm)	δ_3 (mm)	δ_1 (mm)	δ_2 (mm)	δ_3 (mm)	Maximum δ_1 (mm)	Residual δ_1 (mm)
NS-A	12.8	9.9	6.8	3.1	2.4	1.8		
NS-B	11.9	9.1	6.0	1.3	1.1	0.8	0.5	1.0
NS-C	12.1	9.3	_*	2.8	1.9	_*		
NSHC-30A	11.6	9.0	6.1	2.0	1.3	0.9		
NSHC-30B	11.4	8.7	6.0	1.1	0.9	0.3	0.2	0.4
NSHC-30C	11.8	9.2	6.3	1.6	1.2	0.5		
NSHC-50A	8.2	6.3	4.6	3.0	2.3	1.9		
NSHC-50B	7.6	6.0	4.3	1.5	1.0	0.6	0.3	0.8
NSHC-50C	7.9	6.1	4.7	1.9	1.4	0.9		
S-A	9.4	6.9	4.5	3.3	2.2	1.2		
S-B	8.0	5.9	3.7	1.3	1.0	0.2	0.7	1.1
S-C	8.6	6.2	4.1	1.8	1.3	0.5		
SHC-30A	9.9	7.5	5.1	1.6	1.1	0.5		
SHC-30B	8.8	6.6	4.5	0.9	0.3	0.1	0.6	0.4
SHC-30C	9.2	7.2	4.8	1.4	0.9	0.3		
SHC-50A	7.1	5.4	3.6	1.4	1.2	0.9		
SHC-50B	9.7	7.4	5.1	2.4	2.0	1.2	1.4	0.6
SHC-50C	7.3	5.2	3.3	1.2	0.8	0.6		

_* No data recorded

6.4.6 Acceleration time history

The acceleration time histories are obtained using shock accelerometers that are installed at three distinct locations along the length of the beam. The location of the three accelerometers is shown in Figure 6.13. The first accelerometer is located exactly at the rear face of the region of impact loading. The acceleration time histories near the inflection point of the beam for the non-seismic specimen along with a seismic specimen from each group are shown in Figure 6.28 to Figure 6.30.. The summary of the peak accelerations acquired from the recordings is presented in Table 6.13.

The seismic group specimens for both with and without honeycomb behave significantly stiffer compared to their non-seismic counterparts due to the ductile reinforcement detailing and thereby experienced higher accelerations. Correspondingly, the maximum displacements of the seismic group specimens is lower compared to that of their non-seismic counterparts.

It is interesting to note that the effect of 30 mm thick honeycomb sandwich panel shielded specimens shown relatively higher accelerations compared to the 50 mm thick honeycomb shielded in both the seismic and non-seismic group specimens. The honeycomb having 50 mm thick core has low stiffness compared to the 30 mm thick core and thus the damping is increased substantially. It highlights very clearly a viscous damping effect, as demonstrated from the decreasing trend of acceleration plots with

higher thickness of honeycomb (50 mm). It shows that the honeycomb with the higher thickness characterizes more viscoelastic damping effect and results in lesser acceleration. As the damping behavior is predominant in the energy dissipation mechanism, the thickness of the honeycomb is directly related to the perforation energy.

Table 6.13 Summary of experimental results: Acceleration time histories

Specimen Notation	Peak acceleration		
	A_1 (m/s^2)	A_2 (m/s^2)	A_3 (m/s^2)
NS-A	2479.4	2430.4	1666.0
NS-B	2712.5	2621.0	2136.2
NS-C	987.8	964.3	_*
NSHC-30A	5017.6	4939.2	4900.0
NSHC-30B	4860.8	3724.0	3410.4
NSHC-30C	5058.1	4731.3	4596.1
NSHC-50A	3733.8	3175.2	1411.2
NSHC-50B	2469.6	2469.6	1176.0
NSHC-50C	3012.2	2988.3	2143.2
S-A	4939.2	4900.0	4860.8
S-B	4641.5	4605.2	4198.0
S-C	4803.3	4609.3	4170.4
SHC-30A	9721.6	9643.2	9564.8
SHC-30B	9878.4	9329.6	9251.2
SHC-30C	9606.5	9372.3	9187.9
SHC-50A	7114.8	6409.2	6350.4
SHC-50B	4939.2	4782.4	4625.6
SHC-50C	7050.2	6540.1	6175.6

_* No data recorded

It was also noticed that the 50 mm thick honeycomb provided additional stiffness to both seismic and non-seismic group specimens and the experienced acceleration is almost in the same range of the specimens without honeycomb. These trends are observed from the summary of the peak accelerations presented in Table 6.13. Upon the application of honeycomb energy absorbers, the local damage induced on the beam-column joint was minimized and it enhanced the strength of the structural member. During the impact process of honeycomb panel shielded beam-column specimens, three stages of perforation are observed in the local damage as discussed in the aforementioned section. In stage-I (Indentation), the rapid dropping of the projectile's kinetic energy is observed, due to the resistance of the facesheet on the core which has contributed most of the energy absorption. In this stage, a very small amount of energy is absorbed by the buckling of honeycomb cells. In stage-II (Fracture), the front

facesheet reaches the plateau limit during the energy absorption since it has perforated by the projectile. In this stage, major energy absorption is attributed by the crushing of the honeycomb core during projectile penetration through it. In stage-III (Penetration), the projectile penetrated from the core and came into contact with the back facesheet, and most of the energy was absorbed by the honeycomb shield results in the beam-column specimen protected from the penetration. The obtained results demonstrate that the responses of the specimens shielded with honeycomb are significantly better than that of the non-shielded specimens, and was more efficient in mitigating impact effects on beam-column joint.

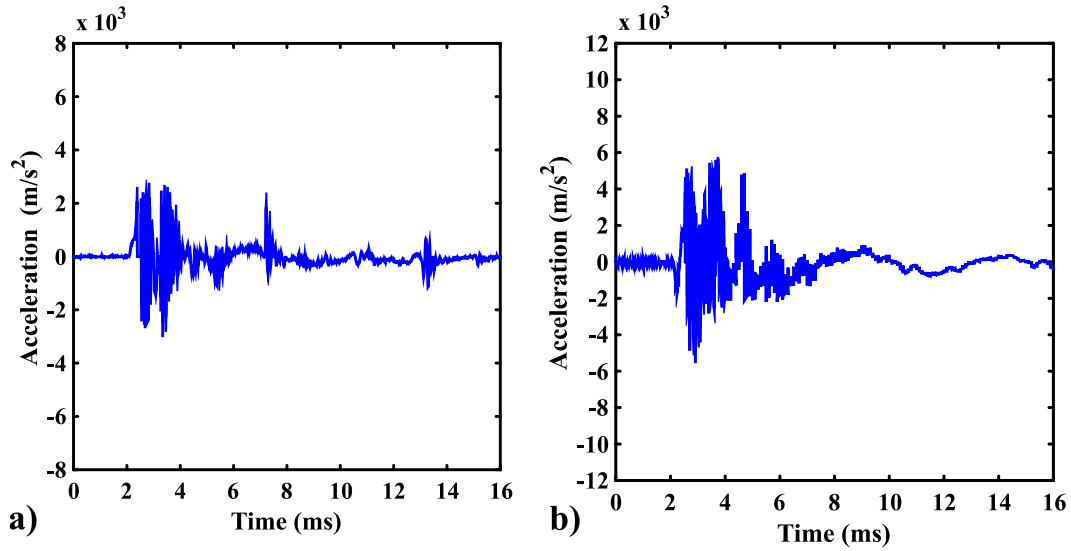

Figure 6.28 Acceleration–time histories for specimens: a) NS-A, and b) S-A under impact loading

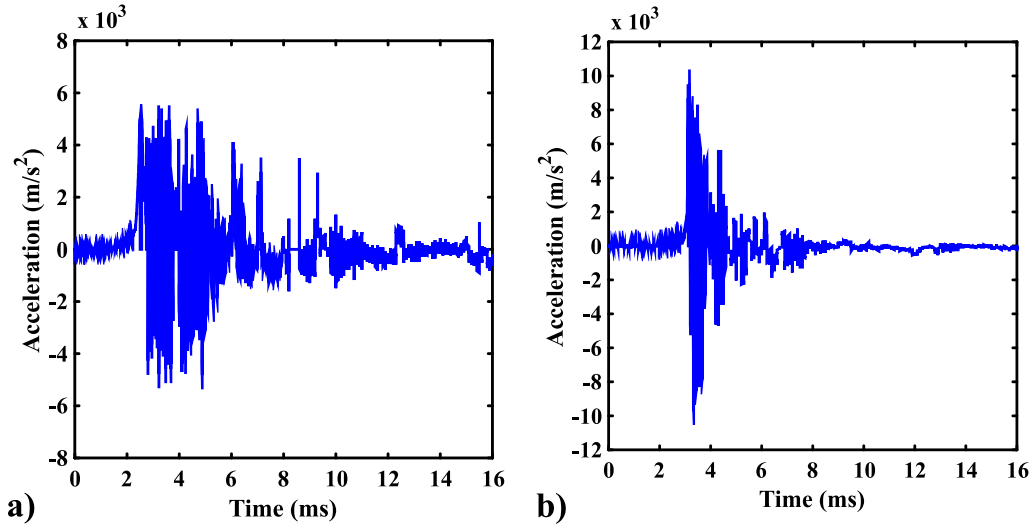

Figure 6.29 Acceleration–time histories for specimens: a) NSHC-30A, and b) SHC-30A under impact loading

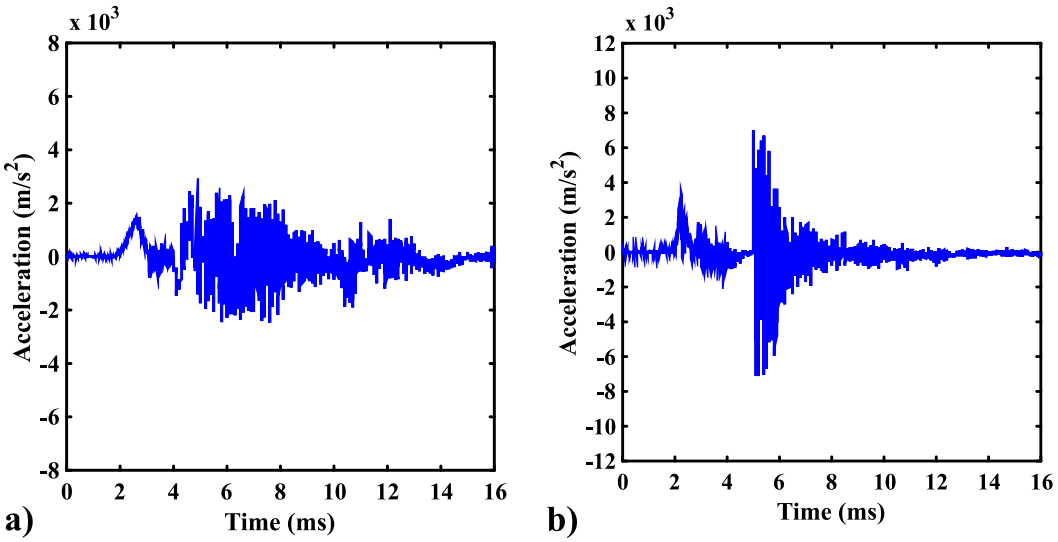

Figure 6.30 Acceleration–time histories for specimens: a) NSHC-50A, and b) SHC-50A under impact loading

6.5 Concluding remarks

The aim of the current study is to address the effectiveness of shielding honeycomb panels on exterior beam-column joint specimens under impact loading. A series of Aluminum honeycombs composite panels with variant thicknesses were tested under static compression as well as under impact loading. This includes both seismic and non-seismic detailing beam-column joint specimens shielded with honeycomb energy absorbers. Furthermore, a parametric investigation on the honeycomb with a variant thickness of 30 mm and 50 mm was adopted as a shielding material. The perforation process and energy absorption mechanisms were studied to characterize the dynamic response of the beam-column joint. The ballistic limit velocity, residual velocity, evaluation of target damage due to the impact, failure modes, energy absorption, and evolution of cracks near beam-column joints have been well investigated. Finally, the quantitative results for the protected structure were compared with the specimens without composite shielding panel.

The extensive experimental program has provided insights on the impact resistive behavior of exterior beam-column joint protected with honeycomb shielding. In the light of experimental results, the following conclusions are drawn:

(1) The maximum displacement response attained by the non-seismic specimens without honeycomb were found to have 26 % higher than that of respective seismic specimens without honeycomb.

(2) The maximum displacement response attained by the non-seismic specimens shielded with 30 and 50 mm honeycomb were found to have 16 % and 10 % higher than that of respective honeycomb shielded seismic specimens.

(3) The maximum acceleration experienced by the seismic specimens without honeycomb were found to have 45 % higher than that of respective non-seismic specimens without honeycomb.

(4) The maximum ballistic limit is achieved for the specimens shielded with 50 mm honeycomb that results in an increase in the perforation energy. The ballistic limit of seismic group specimens was found to have 22 % higher than that of respective honeycomb shielded specimens.

(5) The seismic specimens shielded with 50 mm thick honeycomb i.e. SHC-50 group which has higher areal density witnessed lesser peak displacement and residual displacements with a higher energy absorption capacity when compared with the other groups including non-seismic specimens.

(6) The maximum acceleration experienced by the seismic specimens shielded with 30 and 50 mm honeycomb were found to have 48 % and 47 % higher than that of respective honeycomb shielded non-seismic specimens.

(7) Peak acceleration was effectively reduced when the specimens were shielded with 50 mm thick honeycomb that further minimizes the impact damage and enhances its strength. Core stiffness of honeycomb plays a vital role in reducing the peak accelerations as well as residual displacement.

(8) Among the other findings, it is found that the specimens designed for non-seismic loading experiences low peak accelerations during the impact. Whereas, the specimens shielded with 50 mm honeycomb, show reduced peak accelerations and displacements. Interestingly, the current work shows that in the specimen group shielded with 30 mm honeycomb experiences higher peak accelerations.

(9) During the impact event, the projectile's kinetic energy is progressively absorbed by virtue of dynamic plastification of the honeycomb core. Within the tested specimen groups, the optimized specimen group SHC-50 shows the best energy absorption capability which is 49% higher than that of a seismic specimen without honeycomb shielding.

The key findings based on the impact test results indicate that the Aluminum honeycomb based protective systems are capable of mitigating damage induced by impact loading. It was found that the specimens fabricated using seismic design consideration protected with 50 mm thick honeycomb shielding possess to enhance the impact resistance. Finally, the results obtained from the current study provides guidelines and act as a valuable resource for the effective use of honeycomb panels as a sacrificial material to safeguard the engineering structures against impact. Further research will focus on validation of the proposed honeycomb shielded beam-column joint against impact, as well as the optimization of geometrical parameters of the honeycombs.

Chapter 7
Conclusions and future scope

7.1 Conclusions

The dissertation has aimed to investigate the effect of shock and impact loading on the exterior beam-column joints and the development of a sacrificial honeycomb composite structure to withstand against the aforementioned loads. The current research explores the response of the exterior reinforced concrete beam-column joints under quasi-static and dynamic loadings. The main aim of this dissertation is to study the efficacy of the honeycomb composite to act as an energy-absorbing protective and shielding system for safeguarding structural sub-assemblies under extreme loadings scenarios.

The output of this dissertation are summarized in the following conclusions:

1. A shock tube setup is designed for conducting the extreme loadings viz. shock and impact scenario, which can be performed under controllable conditions. Since conducting the blast experiments in an academic institution has many intricacies that require permission from the defense and other personnel. Therefore, employing the shock tube setup can be useful in experimenting with the shock and impact loads for working on the higher-pressure magnitudes for the research purposes. Further, the experimental results of the shock tube were calibrated with the numerical and analytical results.
2. A detailed experimental investigation of the dynamic response of the exterior beam-column joint specimens subjected to shock loading was conducted. The experimental and numerical results show that the specimens designed using seismic considerations undergo smaller displacements compared to their counterparts designed for gravity loading. For instance, the maximum dynamic displacement of the BSS is approximately 44 % smaller than BSNS. The specimens designed with ductile design considerations experience a higher magnitude of the acceleration due to the higher flexural and shear strength of the subassembly. The acceleration of the BSS specimen is 38 % greater than that of the BSNS specimen.
3. Furthermore, the evolution of failure modes and crack patterns in the beam-column sub-assembly due to shock loading is inspected. It was found that the failure and the crack pattern indicates that the beam-column joint mechanism is affected by the amount of longitudinal and transverse steel reinforcement in the D-region. The reinforcement in the beam-column junctions offers enhanced resistance by increasing the shear strength, which thereby results in the arrest

of shear cracks. The key finding of this study based on the detailed experimental and numerical investigation is that the structures designed with seismic criteria demonstrate better resistance to deformation and damage against shock loading. The obtained experimental results were validated with the combined numerical and theoretical approaches.

4. A lightweight aluminum honeycomb energy absorber panels were developed and conducted a series of static and impact tests. From the literature, it was found that the existing theoretical models which were based on the energy balance principle are incapable of predicting the contact force accurately. The theoretical prediction of the physical responses is always tedious due to the uncertainties involved in the quantification of materialistic and geometrical parameters. Moreover, from the experimental and numerical investigation, it was noticed that the impactor mass and velocity are profoundly influencing the contact force. Therefore, a probabilistic model to predict the peak contact force induced in the honeycomb sandwich structure subjected to low-velocity impact was proposed.
5. External beam-column joint specimens were experimentally investigated under impact loading and compared with specimen's façade with honeycomb energy absorbers. The maximum ballistic limit is achieved for the specimens shielded with a 50 mm honeycomb that results in an increase in the perforation energy. The ballistic limit of seismic group specimens was found to have 22 % higher than that of respective honeycomb shielded specimens. Peak acceleration was effectively reduced when the specimens were shielded with a 50 mm thick honeycomb that further minimizes the impact damage and enhances its strength.
6. Core stiffness of honeycomb plays a vital role in reducing the peak accelerations as well as residual displacement. It was found that the specimens fabricated using seismic design consideration protected with 50 mm thick honeycomb shielding possess to enhance the impact resistance. These energy absorbers offer a sustainable solution to shield and safeguard the parent structure against the blast and impact loading. The key findings based on the impact test results indicate that the energy absorption performance of the structure was enhanced when shielded with honeycomb energy absorbers.

7.2 Limitations of the current dissertation

1. The present dissertation incorporates only beam-column sub-assemblies designed for reduced scale (half-scale). However, implementations of full-scale specimens can be attempted for the study of shock and impact loading.
2. In the current study, experiments are conducted using shock tube imparting localized blast of relatively low-pressure intensity. For validating the proposed

response spectrum and investigate the collapse mechanism, a far-field blast loading at full scale is highly recommended.

3. A probabilistic contact force model is developed to predict impact force in the honeycomb impacted at a low-velocity. Similarly, the development of the probabilistic model for the honeycomb at high-velocity impact can be explored.
4. Due to the influence of the half-scaling effect, the designed beam-column joint specimens could not be strictly conforming to IS 13920: 2016, which can be investigated by accounting the code mentioned above.
5. In the current thesis, the beam-column joint impact study is aimed only for the moderately high-velocity regime. However, due to the instrumentation intricacies associated with the shock-tube setup, very high-velocity (>350 m/s) impact testing are not explored. Therefore, high-velocity impact experiments can be carried out for better insight into the dynamic response of sub-assemblies.

7.3 Scope of future work

The present research comprehends the development of impact mitigation sacrificial structures to safeguard the structural elements of the building. However, there is still considerable scope for future developments, and some recommendations for further studies are conferred below.

1. A detailed numerical investigation for the model verification and its validation for the beam-column joints subjected to the impact loading can be carried out.
2. A comprehensive numerical study with variant geometrical parameters of the honeycomb composite for structural optimization is needed to improve the efficacy of the honeycomb sacrificial system.
3. To develop constitutive modeling and for a better insight of sacrificial material behavior, the effect of high-strain rate loading, i.e., Split-Hopkinson bar tests are highly desirable.
4. To develop the material models, extensive material investigation at high strain rate for the reinforced concrete and honeycomb composites are needed.
5. Coating methods (epoxy, paint, spray, and pour) may influence the integrity performance of honeycomb sacrificial system, so the effects of coating methods on the impact and shock resistance of reinforced structural members shielded with honeycomb panels need to be investigated.
6. Furthermore, investigations on the application of honeycomb energy absorber on other structural elements, i.e., slab and shear wall subjected to blast and impact loading, can be studied.
7. There are various energy absorbing functional graded composite materials such as Aluminum foam, lattice structures, pyramidal, tetrahedral, and diamond textile. Feasibility study on these novel materials can be attempted for application as a sacrificial protective system to resist blast and impact loading.

List of Publications

Accepted

1. Parsi, Sai Sharath., Anupoju Rajeev., Ahsan Uddin., Amit Shelke., and Nasim Uddin., (2019). "Probabilistic contact force model for low-velocity impact on honeycomb structure." *Sustainable and Resilient Infrastructure*, 4(2), 51-65.

2. Anupoju Rajeev., Sai Sharath Parsi., Sudharshan N. Raman., Tuan Ngo., and Amit Shelke., (2020). "Experimental and numerical investigation of an exterior reinforced concrete beam-column joint subjected to shock loading." *International Journal of Impact Engineering*, 137, 103473.

3. Anupoju Rajeev., Damith Mohotti., and Amit Shelke., (2020). "Implications of impact experiments on honeycomb-shielded exterior beam-column joint." *Engineering Structures*, 212, 110470.

Under review

1. Anupoju Rajeev., Lavish Pamwani., and Amit Shelke. "Autoregressive modeling based structural health monitoring of RC beam-column joint subjected to shock loading." *Journal of Structural Engineering*.

Conference and proceedings

1. Anupoju Rajeev., Ayush Maheswari., and Amit Shelke., (2017). "Energy absorption of the smart hybrid honeycomb structure embedded with phononic crystals." *Proceedings of International Conference on Composite Materials and Structures*, pp. 2100-2108. Hyderabad, India.

Bibliography

Abedini, M., Mutalib, A. A., Raman, S. N., Alipour, R., and Akhlaghi, E. (2018). "Pressure–impulse (P–I) diagrams for reinforced concrete (RC) structures: a review." *Archives of Computational Methods in Engineering*, 26(3), 733-767.

Abrate, S. (2005). *Impact on composite structures*, Cambridge University Press, Cambridge.

Adhikary, S. D., Chandra, L. R., Christian, A., and Ong, K. C. G. (2017). "Influence of cylindrical charge orientation on the blast response of high strength concrete panels." *Engineering Structures*, 149, 35-49.

Agbabian, M., Higazy, E., Abdel-Ghaffar, A., and Elnashai, A., (1994). "Experimental observations on the seismic shear performance of RC beam-to-column connections subjected to varying axial column force." *Earthquake Engineering & Structural Dynamics*, 23(8), 859-876.

American Concrete Institute (ACI)-ASCE Committee 318. (2011). " Building code requirements for structural concrete and commentary." *ACI 318-11/318R-11, Farmington Hills, MI.*

American Concrete Institute (ACI)-ASCE Committee 352. (2010). "Recommendations for design of beam-column joints for design of beam column joints in monolithic reinforced concrete structures." *ACI 352R-02, Farmington Hills, MI.*

Ammann, W., Muhlematter, M., and Bachmann, H. (1982). "Stress-strain behaviour of non-prestressed and prestressed reinforcing steel at high strain rates." *Concrete Structures under impact and impulsive loading*.

Anderson Jr, J. D. (2010). *Fundamentals of aerodynamics*, Tata McGraw-Hill Education.

Anderson, T., and Madenci, E. (2000). "Experimental investigation of low-velocity impact characteristics of sandwich composites." *Composite Structures*, 50(3), 239-247.

Andreopoulos, Y., Xanthos, S., and Subramaniam, K. (2007). "Moving shocks through metallic grids: their interaction and potential for blast wave mitigation." *Shock Waves*, 16(6), 455-466.

Angioni, S., Meo, M., and Foreman, A. (2010). "Impact damage resistance and damage suppression properties of shape memory alloys in hybrid composites—a review." *Journal of Smart Materials Structures*, 20(1), 013001.

ANSYS. (2009). ANSYS FLUENT 12.0 user's guide. Canonsburg, PA.

Aoude, H., Dagenais, F. P., Burrell, R. P., and Saatcioglu, M. (2015). "Behavior of ultra-high performance fiber reinforced concrete columns under blast loading." *International Journal of Impact Engineering*, 80, 185-202.

ASCE (2011). "Blast protection of buildings." *ASCE/Structural Engineering Institute (SEI) 59-11*.

ASCE (2006). "Minimum design loads for buildings and other structures." *ASCE/SEI 7-05*, Reston, VA.

Ashby, M. F., Evans, T., Fleck, N. A., Hutchinson, J., Wadley, H., and Gibson, L. (2000). *Metal foams: a design guide*, Elsevier Science and Technology , Oxford.

Bai, Y., Nie, J., and Cai, C. S. (2008). "New connection system for confined concrete columns and beams. II: theoretical modeling." *Journal of Structural Engineering*, 134(12), 1800-1809.

Baker, W. E., Cox, P., Kulesz, J., Strehlow, R., and Westine, P. (2012). *Explosion hazards and evaluation*, Elsevier, London.

Baker, W. E., Kulesz, J. J., Westine, P. S., Cox, P. A., and Wilbeck, J. S. (1981). "*A manual for the prediction of blast and fragment loadings on structures*." Rep. No. DOE/TIC-11268, U.S., Department of Energy, Amarillo, Texas.

Bangash, T. (2006). *Explosion-resistant buildings: design, analysis, and case studies*, Springer Science & Business Media.

Bao, Y., Wang, W., and Zhou, Y. (2004). "Investigation of the relationship between elastic modulus and hardness based on depth-sensing indentation measurements." *Acta Materialia*, 52(18), 5397-5404.

Biggs, J. M. (1964). *Introduction to structural dynamics*, McGraw-Hill College.

Birtel, V., and Mark, P. (2006). "Parameterised finite element modelling of RC beam shear failure." *Proceedings of ABAQUS Users' Conference*, 95-108.

Bitzer, T. (2012). *Honeycomb technology: materials, design, manufacturing, applications and testing*, Springer Science & Business Media.

Brode, H. L. (1955). "Numerical solutions of spherical blast waves." *Journal of Applied Physics*, 26(6), 766-775.

Brown, M.D. and Loewe, A.S. (2003). "Reference manual to mitigate potential terrorist attacks against buildings." *FEMA*,4–19.

Buchan, P., and Chen, J. (2007). "Blast resistance of FRP composites and polymer strengthened concrete and masonry structures – a state-of-the-art review." *Composites Part B: Engineering*, 38(5-6), 509-522.

Buitrago, B. L., Santiuste, C., Sánchez-Sáez, S., Barbero, E., and Navarro, C. (2010). "Modelling of composite sandwich structures with honeycomb core subjected to high-velocity impact." *Composite Structures*, 92(9), 2090-2096.

Bull, P. H., and Hallstrom, S. (2004). "High-velocity and quasi-static impact of large sandwich panels." *Journal of Sandwich Structures and Materials*, 6(2), 97-113.

Bureau of Indian Standards (BIS). (2016). " Ductile detailing of reinforced concrete structures subjected to seismic forces-code of practice." IS: 13920, New Delhi, India.

Bureau of Indian Standards (BIS). (2016). " Plain and reinforced concrete-code of practice." IS: 456, New Delhi, India.

Bureau of Indian Standards (BIS). (2016). "Code of practice for criteria for earthquake resistant design of structures: Part 1: General provisions and buildings." IS: 1893, New Delhi, India.

Carta, G., and Stochino, F. (2013). "Theoretical models to predict the flexural failure of reinforced concrete beams under blast loads." *Engineering Structures*, 49, 306-315.

Castanié, B., Bouvet, C., Aminanda, Y., Barrau, J. J., and Thevenet, P. (2008). "Modelling of low-energy/low-velocity impact on Nomex honeycomb sandwich structures with metallic skins." *International Journal of Impact Engineering*, 35(7), 620-634.

Choe, D.-E., Gardoni, P., Rosowsky, D., and Haukaas, T. (2008). "Probabilistic capacity models and seismic fragility estimates for RC columns subject to corrosion." *Reliability Engineering & System Safety*, 93(3), 383-393.

Choi, H., and Kim, J. (2011). "Progressive collapse-resisting capacity of RC beam–column sub-assemblage." *Magazine of Concrete Research*, 63(4), 297-310.

Choi, I. H. (2006). "Contact force history analysis of composite sandwich plates subjected to low-velocity impact." *Composite Structures*, 75(1-4), 582-586.

Correia, J., Garrido, M., Gonilha, J., Branco, F., and Reis, L. (2012). "GFRP sandwich panels with PU foam and PP honeycomb cores for civil engineering structural applications: effects of introducing strengthening ribs." *International Journal of Structural Integrity*, 3(2), 127-147.

Crupi, V., and Montanini, R. (2007). "Aluminium foam sandwiches collapse modes under static and dynamic three-point bending." *International Journal of Impact Engineering*, 34(3), 509-521.

Crupi, V., Epasto, G., and Guglielmino, E. (2012). "Collapse modes in aluminium honeycomb sandwich panels under bending and impact loading." *International Journal of Impact Engineering*, 43, 6-15.

Cui, J., Hao, H., and Shi, Y. C. (2017). "Discussion on the suitability of concrete constitutive models for high-rate response predictions of RC structures." *International Journal of Impact Engineering*, 106, 202-216.

Database, G. T. (2017). "National consortium for the study of terrorism and responses to terrorism (START)." *[2006-2016]* Center of Excellence of the U.S. Department of Homeland Security, University of Maryland.

Davison, L. (2008). *Fundamentals of shock wave propagation in solids*, Springer Science & Business Media.

De Risi, M. T., and Verderame, G. M. (2017). "Experimental assessment and numerical modelling of exterior non-conforming beam-column joints with plain bars." *Engineering Structures*, 150, 115-134.

De Risi, M. T., Ricci, P., and Verderame, G. M. (2017) "Cyclic response and nonlinear modeling of exterior unreinforced rc beam-column joints with plain longitudinal bars." *6th ECCOMAS Thematic Conference on Computational Methods in Structural Dynamics and Earthquake Engineering*.

De Risi, M. T., Ricci, P., Verderame, G. M. (2017). "Modelling exterior unreinforced beam-column joints in seismic analysis of non-ductile RC frames." *Earthquake Engineering & Structural Dynamics* 46(6), 899-923.

De Risi, M. T., Ricci, P., Verderame, G. M., and Manfredi, G. (2016). "Experimental assessment of unreinforced exterior beam–column joints with deformed bars." *Engineering Structures*, 112, 215-232.

De Risi, M., Ricci, P., and Verderame, G. (2015). "Experimental assessment of RC exterior beam-column joints without transverse reinforcement." *Earthquake Resistant Engineering Structures X*, 152, 245-256.

De, S., and Thangadurai, M. (2011). "Numerical simulation of shock tube generated vortex: effect of numerics." *International Journal of Computational Fluid Dynamics*, 25(6), 345-354.

Deaton, J. B. (2013). "Nonlinear finite element analysis of reinforced concrete exterior beam-column joints with nonseismic detailing." PhD thesis Georgia Institute of Technology, Atlanta, GA.

Department of Defense (DOD). (2002). "Unified Facilities Criteria (UFC): Design and analysis of hardened structures to conventional weapons effects (UFC 3-340-01)." Unified Facilities Criteria (UFC) 3-340-01, Washington, DC.

Department of Defense (DOD). (2014). "Unified Facilities Criteria (UFC): Structures to resist the effects of accidental explosions (UFC 3–340–02)." Unified Facilities Criteria (UFC) 3-340-02, Washington, DC.

Department of Defense (DOD). (2013). "Unified Facilities Criteria (UFC): Minimum antiterrorism standards for buildings (UFC 4-010-01)." Unified Facilities Criteria (UFC) 4-010-01, Washington, DC.

Desai, S., Kulkarni, V., and Gadgil, H. (2016). "Delusive influence of nondimensional numbers in canonical hypersonic nonequilibrium flows." *International Journal of Aerospace Engineering*, 29(5), 04016030.

Deshpande, V., and Fleck, N. (2000). "High strain rate compressive behaviour of aluminium alloy foams." *International Journal of Impact Engineering*, 24(3), 277-298.

Dhakal, R. P., Pan, T.-C., Irawan, P., Tsai, K.-C., Lin, K.-C., and Chen, C.-H. (2005). "Experimental study on the dynamic response of gravity-designed reinforced concrete connections." *Engineering Structures*, 27(1), 75-87.

Dharmasena, K. P., Wadley, H. N. G., Xue, Z. Y., and Hutchinson, J. W. (2008). "Mechanical response of metallic honeycomb sandwich panel structures to high-intensity dynamic loading." *International Journal of Impact Engineering*, 35(9), 1063-1074.

Draganić, H., and Sigmund, V. (2012). "Blast loading on structures." *Tehnicki vjesnik/Technical Gazette*, 19(3).

Ebrahimi, H., Ghosh, R., Mahdi, E., Nayeb-Hashemi, H., and Vaziri, A. (2016). "Honeycomb sandwich panels subjected to combined shock and projectile impact." *International Journal of Impact Engineering*, 95, 1-11.

Edwards, D., McMenemy, L., Stapley, S., Patel, H., and Clasper, J. (2016). "40 years of terrorist bombings–a meta-analysis of the casualty and injury profile." *Injury*, 47(3), 646-652.

Ellis, B. D., DiPaolo, B. P., McDowell, D. L., and Zhou, M. (2014). "Experimental investigation and multiscale modeling of ultra-high-performance concrete panels subject to blast loading." *International Journal of Impact Engineering*, 69, 95-103.

Faleschini, F., Gonzalez-Libreros, J., Zanini, M. A., Hofer, L., Sneed, L., and Pellegrino, C. (2019). "Repair of severely-damaged RC exterior beam-column joints with FRP and FRCM composites." *Composite Structures*, 207, 352-363.

Fang, J., Sun, G., Qiu, N., Pang, T., Li, S., and Li, Q. (2017). "On hierarchical honeycombs under out-of-plane crushing." *International Journal of Solids and Structures*, 135, 1-13.

Fatt, M. S. H., and Park, K. S. J. C. S. (2001). "Dynamic models for low-velocity impact damage of composite sandwich panels–part A: deformation." *Composite Structures*, 52(3-4), 335-351.

Feli, S., and Pour, M. N. (2012). "An analytical model for composite sandwich panels with honeycomb core subjected to high-velocity impact." *Composites Part B: Engineering*, 43(5), 2439-2447.

Feng, D., and Aymerich, F. (2013). "Damage prediction in composite sandwich panels subjected to low-velocity impact." *Composites Part A: Applied Science and Manufacturing*, 52, 12-22.

Feng, D., and Aymerich, F. (2014). "Finite element modelling of damage induced by low-velocity impact on composite laminates." *Composite Structures*, 108, 161-171.

Foglar, M., and Kovar, M. (2013). "Conclusions from experimental testing of blast resistance of FRC and RC bridge decks." *International Journal of Impact Engineering*, 59, 18-28.

Foo, C. C., Seah, L. K., and Chai, G. B. (2008). "Low-velocity impact failure of aluminium honeycomb sandwich panels." *Composite Structures*, 85(1), 20-28.

Foo, C., Chai, G., and Seah, L. (2008). "A model to predict low-velocity impact response and damage in sandwich composites." *Composites Science and Technology*, 68(6), 1348-1356.

Fujikake, K., Li, B., and Soeun, S. (2009). "Impact response of reinforced concrete beam and its analytical evaluation." *Journal of Structural Engineering*, 135(8), 938-950.

Fujikura, S., and Bruneau, M. (2011). "Dynamic analysis of multihazard-resistant bridge piers having concrete-filled steel tube under blast loading." *Journal of Bridge Engineering*, 17(2), 249-258.

Fujikura, S., and Bruneau, M. (2010). "Experimental investigation of seismically resistant bridge piers under blast loading." *Journal of Bridge Engineering*, 16(1), 63-71.

Fujikura, S., Bruneau, M., and Lopez-Garcia, D. (2008). "Experimental investigation of multihazard resistant bridge piers having concrete-filled steel tube under blast loading." *Journal of Bridge Engineering*, 13(6), 586-594.

Gardoni, P., Der Kiureghian, A., and Mosalam, K. M. (2002). "Probabilistic capacity models and fragility estimates for reinforced concrete columns based on experimental observations." *Journal of Engineering Mechanics*, 128(10), 1024-1038.

Gardoni, P., Reinschmidt, K. F., and Kumar, R. (2007). "A probabilistic framework for Bayesian adaptive forecasting of project progress." *Computer-Aided Civil and Infrastructure Engineering*, 22(3), 182-196.

Gaydon, A. G., and Hurle, I. R. (1963). *The shock tube in high-temperature chemical physics*, Chapman and Hall.

Geretto, C., Yuen, S. C. K., and Nurick, G. N. (2015). "An experimental study of the effects of degrees of confinement on the response of square mild steel plates subjected to blast loading." *International Journal of Impact Engineering*, 79, 32-44.

Ghobarah, A., Aly, N., El-Attar, M. (1997). "Performance level criteria and evaluation. A critical review of proposed guidelines." *Seismic design methodology for the next generation of codes, Fajfar and Krawinkler, Editors, Balkema, Slovenia.*

Gibson, L. J., and Ashby, M. F. (1999). *Cellular solids: structure and properties*, Cambridge university press, Cambridge.

Gibson, L., Ashby, M., Zhang, J., and Triantafillou, T. (1989). "Failure surfaces for cellular materials under multiaxial loads—I. Modelling." *International Journal of Mechanical Sciences*, 31(9), 635-663.

Goel, M. D., and Matsagar, V. A. (2013). "Blast-resistant design of structures." *Practice Periodical on Structural Design and Construction*, 19(2), 04014007.

Goldsmith, W., and Sackman, J. L. (1992). "An experimental study of energy absorption in impact on sandwich plates." *International Journal of Impact Engineering*, 12(2), 241-262.

Gombeda, M. J., Naito, C. J., and Quiel, S. E. (2018). "Performance-based framework for evaluating the flexural response of precast concrete wall panels to blast loading." *Engineering Structures*, 168, 473-486.

Grady, D. (2017). *Physics of Shock and Impact, Volume 1*, IOP Publishing.

Grimsmo, E. L., Clausen, A. H., Aalberg, A., and Langseth, M. (2016). "A numerical study of beam-to-column joints subjected to impact." *Engineering Structures*, 120, 103-115.

Guan, D., Jiang, C., Guo, Z., and Ge, H.. (2018). "Development and seismic behavior of precast concrete beam-to-column connections." *Journal of Earthquake Engineering*, 22(2), 234-256.

Guo, X. E., and Gibson, L. J. (1999). "Behavior of intact and damaged honeycombs: a finite element study." *International Journal of Mechanical Sciences*, 41(1), 85-105.

Ha, J. H., Yi, N. H., Choi, J. K., and Kim, J. H. J. (2011). "Experimental study on hybrid CFRP-PU strengthening effect on RC panels under blast loading." *Composite Structures*, 93(8), 2070-2082.

Hakuto, S., Park, R., and Tanaka, H. (2000). "Seismic load tests on interior and exterior beam-column joints with substandard reinforcing details." *ACI Structural Journal*, 97(1), 11-25.

Hamra, L. (2016). "Development and analysis of low-order models of frame structures under blast loads." University of Liège, Liège, Belgium.

Harding, J., and Sneddon, I. (1945) "The elastic stresses produced by the indentation of the plane surface of a semi-infinite elastic solid by a rigid punch." *Mathematical Proceedings of the Cambridge Philosophical Society*, 41(1), 16-26.

Hayes Jr, J. R., Woodson, S. C., Pekelnicky, R. G., Poland, C. D., Corley, W. G., and Sozen, M. (2005). "Can strengthening for earthquake improve blast and progressive collapse resistance?" *Journal of Structural Engineering*, 131(8), 1157-1177.

Hazizan, M. A., and Cantwell, W. J. (2003). "The low-velocity impact response of an aluminium honeycomb sandwich structure." *Composites Part B: Engineering*, 34(8), 679-687.

He, Q., Feng, J., Chen, Y., and Zhou, H. (2018). "Mechanical properties of spider-web hierarchical honeycombs subjected to out-of-plane impact loading." *Journal of Sandwich Structures & Materials*, 1099636218772295.

Hertz, H. (1881). "On the contact of elastic solids." J. Reine und Anges. Mathematics, 92, 156-171.

Hetherington, J., and Smith, P. (2014). *Blast and ballistic loading of structures*, CRC Press,Oxford.

Holmberg, A. D. (2010). "Development and characterization of shock tubes for laboratory scale blast wave simulation." *University of Nebraska-Lincoln.*

Hou, J., Petrinic, N., Ruiz, C., and Hallett, S. (2000). "Prediction of impact damage in composite plates." *Composites Science and Technology*, 60(2), 273-281.

Hou, W. H., Zhu, F., Lu, G. X., and Fang, D. N. (2010). "Ballistic impact experiments of metallic sandwich panels with aluminium foam core." *International Journal of Impact Engineering*, 37(10), 1045-1055.

Hu, L. L., Wu, Z. J., and Fu, M. H. (2018). "Mechanical behavior of anti-trichiral honeycombs under lateral crushing." *International Journal of Mechanical Sciences*, 140, 537-546.

Huang, Q., Gardoni, P., and Hurlebaus, S. (2010). "Probabilistic seismic demand models and fragility estimates for reinforced concrete highway bridges with one single-column bent." *Journal of Engineering Mechanics*, 136(11), 1340-1353.

Huson, P. (2012). *Experimental and numerical simulations of explosive loading on structural components: composite sandwich connections*, University of California, San Diego.

Igra, D., and Igra, O. (2016). "Shock wave mitigation by different combination of plate barriers; a numerical investigation." *European Journal of Mechanics B-Fluids*, 59, 115-123.

Interagency Security Committee Standard (2010). "Physical security criteria for federal facilities." ,J Washington, DC).

Jen, Y.-M., and Chang, L.-Y. (2008). "Evaluating bending fatigue strength of aluminum honeycomb sandwich beams using local parameters." *International Journal of Fatigue*, 30(6), 1103-1114.

Jen, Y.-M., and Chang, L.-Y. (2008). "Evaluating bending fatigue strength of aluminum honeycomb sandwich beams using local parameters." *International Journal of Fatigue*, 30(6), 1103-1114.

Johnson, A. F., and Holzapfel, M. (2003). "Modelling soft body impact on composite structures." *Composite Structures*, 61(1), 103-113.

Johnson, K. L., and Johnson, K. L. (1987). *Contact Mechanics*, Cambridge university press, Cambridge.

Jourdan, G., Mariani, C., Houas, L., Chinnayya, A., Hadjadj, A., Del Prete, E., Haas, J. F., Rambert, N., Counilh, D., and Faure, S. (2015). "Analysis of shock-wave propagation in aqueous foams using shock tube experiments." *Physics of Fluids*, 27(5), 056101.

Karlos, V., and Solomos, G. (2013). "Calculation of blast loads for application to structural components." *Publications Office of the European Union, Luxembourg*.

Kelly, G., and Hallström, S. (2005). "Strength and failure mechanisms of composite laminates subject to localised transverse loading." *Composite Structures*, 69(3), 301-314.

Khatri, D., Ngo, D., and Daraio, C. (2012). "Highly nonlinear solitary waves in chains of cylindrical particles." *Granular Matter*, 14(1), 63-69.

Kim, H., Welch, D. A., and Kedward, K. T. (2003). "Experimental investigation of high-velocity ice impacts on woven carbon/epoxy composite panels." *Composites Part A: applied science and manufacturing*, 34(1), 25-41.

Kim, J., and LaFave, J. M. (2009). "Joint shear behavior of reinforced concrete beam-column connections subjected to seismic lateral loading." Newmark Structural Engineering Laboratory. University of Illinois at Urbana-Champaign, IL, Report No. NSEL-020.

Kingery, C. N., and Bulmash, G. (1984). *Airblast parameters from TNT spherical air burst and hemispherical surface burst*, US Army Armament and Development Center, Ballistic Research Laboratory, ARBRL-TR-02555.

Kinney, G. F., and Graham, K. J. (2013). *Explosive shocks in air*, Springer Science & Business Media.

Klintworth, J., and Stronge, W. (1988). "Elasto-plastic yield limits and deformation laws for transversely crushed honeycombs." *International Journal of Mechanical Sciences*, 30(3), 273-292.

Klintworth, J., and Stronge, W. (1989). "Plane punch indentation of a ductile honeycomb." *International Journal of Mechanical Sciences*, 31(5), 359-378.

Koccaz, Z., Sutcu, F., and Torunbalci, N. (2008). "Architectural and structural design for blast resistant buildings." *Proceedings of the 14th world conference on earthquake engineering October*, 12-17,China.

Koissin, V., Shipsha, A., and Rizov, V. (2004). "The inelastic quasi-static response of sandwich structures to local loading." *Composite Structures*, 64(2), 129-138.

Koissin, V., Skvortsov, V., Krahmalev, S., and Shilpsha, A.(2004). "The elastic response of sandwich structures to local loading." *Composite Structures*, 63(3-4), 375-385.

Koller, M. (1986). "Elastic impact of spheres on sandwich plates." *Journal of Applied Mathematics and Physics ZAMP*, 37(2), 256-269.

Komissarov, P., Borisov, A., Sokolov, G., and Lavrov, V. (2016). "Rigid polyurethane foam as an efficient material for shock wave attenuation." *Proceedings of Journal of Physics: Conference Series*, IOP Publishing,751, 012020.

Kong, X. Z., Fang, Q., Wu, H., and Peng, Y. (2016). "Numerical predictions of cratering and scabbing in concrete slabs subjected to projectile impact using a modified version of HJC material model." *International Journal of Impact Engineering*, 95, 61-71.

Kore, R., Waychal, A., Agarwal, S., Yadav, P., Uddin, A., Sahoo, N., and Shelke, A. (2016). "Impact induced solitary wave propagation through a woodpile structure." *Smart Materials and Structures*, 25(2), 025027.

Krauthammer, T. (2008). *Modern protective structures*, CRC Press, Oxford.

Krauthammer, T. (2017). "Recent observations on design and analysis of protective structures." *Engineering Structures*, 149, 78-90.

Krauthammer, T., Astarlioglu, S., Blasko, J., Soh, T., and Ng, P. (2008). "Pressure–impulse diagrams for the behavior assessment of structural components." *International Journal of Impact Engineering*, 35(8), 771-783.

Krehl, P. O. (2008). *History of shock waves, explosions and impact: a chronological and biographical reference*, Springer Science & Business Media, Berlin.

Kumar, C. S., Takayama, K., and Reddy, K. (2014). *Shock waves made simple*, Wiley-Blackwell.

Kyei, C., and Braimah, A. (2017). "Effects of transverse reinforcement spacing on the response of reinforced concrete columns subjected to blast loading." *Engineering Structures*, 142, 148-164.

Lal, K. (1983). "Residual strength assessment of low-velocity impact damage of graphite-epoxy laminates." *Journal of Reinforced Plastics And Composites*, 2(4), 226-238.

Lee, J. Y., Shin, H. O., Yoo, D. Y., and Yoon, Y. S. (2018). "Structural response of steel-fiber-reinforced concrete beams under various loading rates." *Engineering Structures*, 156, 271-283.

Lee, Y.-J., and Huang, C.-H. (2003). "Ultimate strength and failure process of composite laminated plates subjected to low-velocity impact." *Journal of Reinforced Plastics and Composites*, 22(12), 1059-1081.

Li, B., Nair, A., and Kai, Q. (2012). "Residual axial capacity of reinforced concrete columns with simulated blast damage." *Journal of Performance of Constructed Facilities*, 26(3), 287-299.

Li, J., Wu, C. Q., Hao, H., Su, Y., and Li, Z. X. (2017). "A study of concrete slabs with steel wire mesh reinforcement under close-in explosive loads." *International Journal of Impact Engineering*, 110, 242-254.

Li, Q. M., Magkiriadis, I., and Harrigan, J. J. (2006). "Compressive strain at the onset of densification of cellular solids." *Journal of Cellular Plastics*, 42(5), 371-392.

Li, Q., Liu, D., Templeton, D., and Raju, B. (2007). "A shock tube-based facility for impact testing." *Experimental Techniques*, 31(4), 25-28.

Lim, K. M., Shin, H. O., Kim, D. J., Yoon, Y. S., and Lee, J. H. (2016). "Numerical Assessment of Reinforcing Details in Beam-Column Joints on Blast Resistance." *International Journal of Concrete Structures and Materials*, 10(3), 87-96.

Limberger, E., Brandes, K., and Herter, J. (1982). "Influence of mechanical properties of reinforcing steel on the ductility of reinforced concrete beams with respect to high strain rates." *Proceedings of RILEM-CEB-IABSE-IASS Interassociation Symposium on Concrete Structures under Impact and Impulsive Loadin*g, G.Plauk, education., 134–145.

Liou, M. S., and Steffen Jr, C. J. (1993). "A new flux splitting scheme." *Journal of Computational Physics*, 107(1), 23-39.

Liu, J. G., Pattofatto, S., Fang, D. N., Lu, F. Y., and Zhao, H. (2015). "Impact strength enhancement of aluminum tetrahedral lattice truss core structures." *International Journal of Impact Engineering*, 79, 3-13.

Liverts, M., Ram, O., Sadot, O., Apazidis, N., and Ben-Dor, G. (2015). "Mitigation of exploding-wire-generated blast-waves by aqueous foam." *Physics of Fluids*, 27(7), 076103.

Lopatnikov, S. L., Gama, B. A., Haque, M. J., Krauthauser, C., and Gillespie, J. W. (2004). "High-velocity plate impact of metal foams." *International Journal of Impact Engineering*, 30(4), 421-445.

Lopatnikov, S. L., Gama, B. A., Haque, M. J., Krauthauser, C., Gillespie, J. W., Guden, M., and Hall, I. W. (2003). "Dynamics of metal foam deformation during Taylor cylinder–Hopkinson bar impact experiment." *Composite Structures*, 61(1), 61-71.

Lowes, L. N., Mitra, N., and Altoontash, A. (2003). "A beam-column joint model for simulating the earthquake response of reinforced concrete frames." Report no. PEER 2003/10. Pacific Earthquake Engineering Research Center, University of Berkeley.

Lubliner, J., Oliver, J., Oller, S., and Onate, E. (1989). "A plastic-damage model for concrete." *International Journal of Solids and Structures*, 25(3), 299-326.

Luccioni, B. M., Ambrosini, R. D., and Danesi, R. F. (2004). "Analysis of building collapse under blast loads." *Engineering Structures*, 26(1), 63-71.

Luccioni, B., Ambrosini, R., and Danesi, R. (2004). "Analysis of building collapse under blast loads." *Engineering Structures*, 26(1), 63-71.

Luccioni, B., Isla, F., Codina, R., Ambrosini, D., Zerbino, R., Giaccio, G., and Torrijos, M. C. (2018). "Experimental and numerical analysis of blast response of high strength fiber reinforced concrete slabs." *Engineering Structures*, 175, 113-122.

MacGregor, J. G., Wight, J. K., Teng, S., and Irawan, P. (1997). *Reinforced concrete: Mechanics and design*, Prentice Hall Upper Saddle River, NJ.

Magnusson, J., and Hallgren, M. (2003). "High performance concrete beams subjected to shock waves from air blast." Part 2. Report no. FOI-R–1116–SE, Swedish Defence Research Agency (FOI), Tumba, Sweden

Magnusson, J., Hallgren, M., and Ansell, A. (2010). "Air-blast-loaded, high-strength concrete beams. Part I: Experimental investigation." *Magazine of Concrete Research*, 62(4), 235-242.

Mander, J. B., Priestley, M. J. N., and Park, R. (1988). "Theoretical stress-strain model for confined concrete." *Journal of Structural Engineering-ASCE*, 114(8), 1804-1826.

Marthong, C., Dutta, A., and Deb, S. K. (2013). "Seismic rehabilitation of rc exterior beam-column connections using epoxy resin injection." *Journal of Earthquake Engineering*, 17(3), 378-398.

Masi, F., Stefanou, I., and Vannucci, P. (2018). "A study on the effects of an explosion in the Pantheon of Rome." *Engineering Structures*, 164, 259-273.

Mattock, A. H. (1967). "Discussion of Rotational capacity of reinforced concrete beams." *Journal of the Structural Division,ASCE*, 93(2), 519-522.

Mays, G., Smith, P. D. (1995). *Blast effects on buildings: Design of buildings to optimize resistance to blast loading*, Thomas Telford, London.

Meo, M., Vignjevic, R., and Marengo, G. (2005). "The response of honeycomb sandwich panels under low-velocity impact loading." *International Journal of Mechanical Sciences*, 47(9), 1301-1325.

Meyer, L. W., Herzig, N., Pursche, F., and Abdel-Malek, S. (2011). "Impact Testing and Dynamic Behavior of Materials." *Time Dependent Constitutive Behavior and Fracture/Failure Processes*, Springer, *3*, 67-74.

Mirgal, P. G., Tikate, P. D., Suryawanshi, S. G., and Tande, S. (2014). "Architectural and Structural Design for Blast Resistant Buildings." *Journal of Civil Engineering and Environmental Technology*.

Mohotti, D., Ngo, T., Mendis, P., and Raman, S. N. (2013). "Polyurea coated composite aluminium plates subjected to high-velocity projectile impact." *Materials & Design*, 52, 1-16.

Mohotti, D., Ngo, T., Raman, S. N., and Mendis, P. (2015). "Analytical and numerical investigation of polyurea layered aluminium plates subjected to high-velocity projectile impact." *Materials & Design*, 82, 1-17.

Montgomery, D. C. (2017). *Design and analysis of experiments*, John wiley & sons, New York

Montgomery, D. C., and Runger, G. C. (2010). *Applied statistics and probability for engineers*, John Wiley & Sons, New York.

Murty, C., Rai, D. C., Bajpai, K., and Jain, S. K. (2003). "Effectiveness of reinforcement details in exterior reinforced concrete beam-column joints for earthquake resistance." *Structural Journal*, 100(2), 149-156.

Muszynski, L. C., and Purcell, M. R. (2003). "Composite reinforcement to strengthen existing concrete structures against air blast." *Journal of Composites for Construction*, 7(2), 93-97.

Muszynski, L. C., and Purcell, M. R. (2003). "Use of composite reinforcement to strengthen concrete and air-entrained concrete masonry walls against air blast." *Journal of Composites for Construction*, 7(2), 98-108.

Naito, C., Wheaton, K. (2006). "Blast assessment of load-bearing reinforced concrete shear walls. "*Practice Periodical on Structural Design and Construction*, 11(2), 112-121.

Nam, J. W., Kim, H. J., Kim, S. B., Yi, N. H., and Kim, J. H. J. (2010). "Numerical evaluation of the retrofit effectiveness for GFRP retrofitted concrete slab subjected to blast pressure." *Composite Structures*, 92(5), 1212-1222.

Nanda, S. R., Agarwal, S., Kulkarni, V., and Sahoo, N. (2017). "Shock tube as an impulsive application device." *International Journal of Aerospace Engineering*, 2010476.

Nassr, A. A., Razaqpur, A. G., and Campidelli, M. (2017). "Effect of initial blast response on RC beams failure modes." *Nuclear Engineering and Design*, 320, 437-451.

Nassr, A. A., Razaqpur, A. G., Tait, M. J., Campidelli, M., and Foo, S. (2012). "Single and multi degree of freedom analysis of steel beams under blast loading." *Nuclear Engineering and Design*, 242, 63-77.

Nassr, A. A., Razaqpur, A. G., Tait, M. J., Campidelli, M., and Foo, S. (2013). "Strength and stability of steel beam columns under blast load." *International Journal of Impact Engineering*, 55, 34-48.

Nassr, A. A., Razaqpur, A. G., Tait, M. J., Campidelli, M., and Foo, S. J. (2011). "Experimental performance of steel beams under blast loading." *Journal of Performance of Constructed Facilities*, 26(5), 600-619.

Nassr, A. A., Razaqpur, A. G., Tait, M. J., Campidelli, M., and Foo, S. (2013). "Dynamic response of steel columns subjected to blast loading." *Journal of Structural Engineering*, 140(7), 04014036.

Newmark, N., and Hansen, R. J. (1961). "Design of blast resistant structures." *Shock and vibration handbook*, C. M. Harris, ed., Vol. 3, McGraw-Hill, New York.

Ngo, T., Mendis, P., and Krauthammer, (2007). "Behavior of ultrahigh-strength prestressed concrete panels subjected to blast loading." *Journal of Structural Engineering*, 133(11), 1582-1590.

Ngo, T., Mendis, P., Gupta, A., and Ramsay, J. (2007). "Blast loading and blast effects on structures–an overview." *Electronic Journal of Structural Engineering*, 7(S1), 76-91.

Ngo, T., Mohotti, D., Remennikov, A., and Uy, B. (2015). "Numerical simulations of response of tubular steel beams to close-range explosions." *Journal of Constructional Steel Research*, 105, 151-163.

Nie, J., Bai, Y., and Cai, C. (2008). "New connection system for confined concrete columns and beams. I: Experimental study." *Journal of Structural Engineering*, 134(12), 1787-1799.

NTC (2008). "Norme tecniche per le costruzioni." *e dei Trasporti, Ministero delle Infrastrutture %J Ministero delle Infrastrutture e dei Trasporti, Decreto Ministeriale del*, 14.

Nystrom, U., and Gylltoft, K. (2011). "Comparative numerical studies of projectile impacts on plain and steel-fibre reinforced concrete." *International Journal of Impact Engineering*, 38(2-3), 95-105.

Ohtsu, M., Uddin, F. A. K. M., Tong, W., and Murakami, K. (2007). "Dynamics of spall failure in fiber reinforced concrete due to blasting." *Construction and Building Materials*, 21(3), 511-518.

Olsson, R. (1992). "Impact response of orthotropic composite plates predicted from a one-parameter differential equation." *American Institute of Aeronautics and Astronautics Journal*, 30(6), 1587-1596.

Olsson, R., and McManus, H. L. (1996). "Improved theory for contact indentation of sandwich panels." *American Institute of Aeronautics and Astronautics journal*, 34(6), 1238-1244.

Olsson, R., Donadon, M. V., and Falzon, B. G. (2006). "Delamination threshold load for dynamic impact on plates." *International Journal of Solids and Structures*, 43(10), 3124-3141.

Pandey, A., Kumar, R., Paul, D., and Trikha, D. (2006). "Non-linear response of reinforced concrete containment structure under blast loading." *Nuclear Engineering and Design*, 236(9), 993-1002.

Pantelides, C. P., Clyde, C., and Reaveley, L. D. (2002). "Performance-based evaluation of reinforced concrete building exterior joints for seismic excitation." *Earthquake Spectra*, 18(3), 449-480.

Pantelides, C., Hansen, J., Ameli, M., Reaveley, L (2017). "Seismic performance of reinforced concrete building exterior joints with substandard details." *Journal of Structural Integrity and Maintenance* 2(1), 1-11.

Parisi, F., and Augenti, N. (2012). "Influence of seismic design criteria on blast resistance of RC framed buildings: A case study." *Engineering Structures*, 44, 78-93.

Park, J., Ha, S., Kang, K., Kim, C., and Kim, H. (2008). "Impact damage resistance of sandwich structure subjected to low-velocity impact." *Journal of Materials Processing Technology*, 201(1), 425-430.

Park, R., and Paulay, T. (1975). *Reinforced concrete structures*, John Wiley & Sons, New York.

Peng, Y., Wu, H., Fang, Q., Liu, J. Z., and Gong, Z. M. (2016). "Residual velocities of projectiles after normally perforating the thin ultra-high performance steel fiber reinforced concrete slabs." *International Journal of Impact Engineering*, 97, 1-9.

Petras, A., and Sutcliffe, M. (1999). "Failure mode maps for honeycomb sandwich panels." *Composite Structures*, 44(4), 237-252.

Petras, A., and Sutcliffe, M. (2000). "Indentation failure analysis of sandwich beams." *Composite Structures*, 50(3), 311-318.

Prasanna Kumar, S., Patnaik, B., and Ramamurthi, K. (2018). "Prediction of air blast mitigation in an array of rigid obstacles using smoothed particle hydrodynamics." *Physics of Fluids*, 30(4), 046105.

Prasanna Kumar, S., Ramamurthi, K., and Patnaik, B. (2018). "Numerical study of a foam-shock trap based blast mitigation strategy." *Physics of Fluids*, 30(8), 086102.

Priestley, M. N., Verma, R., and Xiao, Y. (1994). "Seismic shear strength of reinforced concrete columns." *Journal of Structural Engineering* , 120(8), 2310-2329.

Qi, C., Jiang, F., Yu, C., and Yang, S. (2019). "In-plane crushing response of tetra-chiral honeycombs." *International Journal of Impact Engineering*, 130, 247-265.

Quintero, R., Wei, J., Galati, N., Nanni, A. (2007). "Failure modeling of bridge components subjected to blast loading part II: estimation of the capacity and critical charge." *International Journal of Concrete Structures and Materials,* 1(1), 29-36.

Radford, D., Fleck, N., and Deshpande, V. (2006). "The response of clamped sandwich beams subjected to shock loading." *International Journal of Impact Engineering*, 32(6), 968-987.

Radford, D., McShane, G., Deshpande, V., and Fleck, N. (2006). "The response of clamped sandwich plates with metallic foam cores to simulated blast loading." *International Journal of Solids and Structures*, 43(7), 2243-2259.

Ramamoorthy, S. K., Gardoni, P., and Bracci, J. M. (2006). "Probabilistic demand models and fragility curves for reinforced concrete frames." *Journal of Structural Engineering*, 132(10), 1563-1572.

Ramanjaneyulu, K., Novak, B., Sasmal, S., Roehm, C., Lakshmanan, N., and Iyer, N. R. (2013). "Seismic performance evaluation of exterior beam-column sub-assemblages designed according to different codal recommendations." *Structure and Infrastructure Engineering*, 9(8), 817-833.

Razaqpur, A. G., Contestabile, E., and Tolba, A. (2009). "Experimental study of the strength and deformations of carbon fibre reinforced polymer (CFRP) retrofitted reinforced concrete slabs under blast load." *Canadian Journal of Civil Engineering*, 36(8), 1366-1377.

Remennikov, A. M. (2003). "A review of methods for predicting bomb blast effects on buildings." *Journal of Battlefield Technology*, 6(3), 5-10.

Remennikov, A. M., and Rose, T. A. (2005). "Modelling blast loads on buildings in complex city geometries." *Computers & Structures*, 83(27), 2197-2205.

Remennikov, A., Ngo, T., Mohotti, D., Uy, B., and Netherton, M. (2017). "Experimental investigation and simplified modeling of response of steel plates subjected to close-in blast loading from spherical liquid explosive charges." *International Journal of Impact Engineering*, 101, 78-89.

Rhymer, J., Kim, H., and Roach, D. (2012). "The damage resistance of quasi-isotropic carbon/epoxy composite tape laminates impacted by high-velocity ice." *Composites Part A: Applied Science and Manufacturing*, 43(7), 1134-1144.

Ricci, P., De Risi, M. T., Verderame, G. M., and Manfredi, G. (2016). "Experimental tests of unreinforced exterior beam–column joints with plain bars." *Engineering Structures*, 118, 178-194.

Rodriguez-Nikl, T. (2006). "Experimental simulations of explosive loading on structural components: reinforced concrete columns with advanced composite jackets." Ph.D. thesis

Roehm, C., Sasmal, S., Novák, B., and Karusala, R. (2015). "Numerical simulation for seismic performance evaluation of fibre reinforced concrete beam–column sub-assemblages." *Engineering Structures,* 91, 182-196.

Saatcioglu, M., and Baingo, D. (1999). "Circular high-strength concrete columns under simulated seismic loading." *Journal of Structural Engineering*, 125(3), 272-280.

Saatcioglu, M., Mitchell, D., Tinawi, R., Gardner, N. J., Gillies, A. G., Ghobarah, A., Anderson, D. L., and Lau, D. (2001). "The august 17, 1999, kocaeli (Turkey) earthquake - damage to structures." *Canadian Journal of Civil Engineering*, 28(4), 715-737.

Saatcioglu, M., Ozbakkaloglu, T., Naumoski, N., and Lloyd, A. (2009). "Response of earthquake-resistant reinforced-concrete buildings to blast loading." *Canadian Journal of Civil Engineering*, 36(8), 1378-1390.

Saha, P., Meesaraganda, L. V. (2019). "Experimental investigation of reinforced SCC beam-column joint with rectangular spiral reinforcement under cyclic loading." *Construction and Building Materials,* 201, 171-185.

Sarkar, P., Agrawal, R., and Menon, D. (2007). "Design of RC beam-column joints under seismic loading-A review." *Journal of Structural Engineering,* 33(6), 449-457.

Sasmal, S. (2009). "Performance evaluation and strengthening of deficient beam-column sub-assemblages under cyclic loading." Ph.D. Thesis, Institute for Lightweight Structures and Conceptual Design (ILEK), University of Stuttgart, Germany.

Sasmal, S., Novák, B., and Ramanjaneyulu, K. (2011). "Numerical analysis of fiber composite-steel plate upgraded beam–column sub-assemblages under cyclic loading." *Composite Structures,* 93(2), 599-610.

Schenker, A., Anteby, I., Gal, E., Kivity, Y., Nizri, E., Sadot, O., Michaelis, R., Levintant, O., and Ben-Dor, G. (2008). "Full-scale field tests of concrete slabs subjected to blast loads." *International Journal of Impact Engineering*, 35(3), 184-198.

Schenker, A., Anteby, I., Nizri, E., Ostraich, B., Kivity, Y., Sadot, O., Haham, O., Michaelis, R., Gal, E., and Ben-Dor, G. (2005). "Foam-protected reinforced concrete structures under impact: Experimental and numerical studies." *Journal of Structural Engineering-ASCE*, 131(8), 1233-1242.

Schofield, H., Ingham, J. M., and Pampanin, S. (2006). "Critical earthquake risk detailing in New Zealand's multistorey building stock: understanding and improving the current perception." *Proceedings of NZSEE Conference*.

Sezen, H., Elwood, K., Whittaker, A., Mosalam, K., Wallace, J., and Stanton, J. F. (2000). "Structural engineering reconnaissance of the august 17, 1999 kocaeli (izmit), Turkey earthquake." *Technical Rep. No., PEER 2000*, 9.

Sharma, A., Reddy, G. R., Eligehausen, R., and Vaze, K. K. (2011). "Strength and ductility of RC beam-column joints of non-safety related structures and recommendations by national standards." *Nuclear Engineering and Design*, 241(5), 1360-1370.

Sharma, H., Gardoni, P., and Hurlebaus, S. (2014). "Probabilistic demand model and performance-based fragility estimates for RC column subject to vehicle collision." *Engineering Structures*, 74, 86-95.

Sharma, H., Gardoni, P., and Hurlebaus, S. (2015). "Performance-based probabilistic capacity models and fragility estimates for rc columns subject to vehicle collision." *Computer-Aided Civil and Infrastructure Engineering*, 30(7), 555-569.

Sharma, N., Gibson, R. F., and Ayorinde, E. O. (2006). "Fatigue of foam and honeycomb core composite sandwich structures: a tutorial." *Journal of Sandwich Structures and Materials*, 8(4), 263-319.

Shelke, A., Uddin, A., and Yang, J. Y. (2014). "Impact identification in sandwich structures using solitary wave-supporting granular crystal sensors." *American Institute of Aeronautics and Astronautics Journal*, 52(10), 2283-2290.

Shi, Y., Hao, H., and Li, Z.-X. (2008). "Numerical derivation of pressure–impulse diagrams for prediction of RC column damage to blast loads." *International Journal of Impact Engineering*, 35(11), 1213-1227.

Shin, K. B., Lee, J. Y., and Cho, S. H. (2008). "An experimental study of low-velocity impact responses of sandwich panels for Korean low floor bus." *Composite Structures*, 84(3), 228-240.

Shivakumar, K., Elber, W., and Illg, W. (1985). "Prediction of impact force and duration due to low-velocity impact on circular composite laminates." *Journal of Applied Mechanics*, 52(3), 674-680.

Shukla, A., Ravichandran, G., and Rajapakse, Y. (2010). *Dynamic failure of materials and structures*, Springer, New York.

Shvetsov, A., Shvetsova, S., Kozyrev, V. A., Spharov, V. A., and Sheremet, N. M. (2017). "The "car-bomb" as a terrorist tool at metro stations, railway terminals and airports." *Journal of Transportation Security*, 10(1-2), 31-43.

Skews, B. W., Atkins, M. D., and Seitz, M. W. (1993). "The Impact of a Shock-Wave on Porous Compressible Foams." *Journal of Fluid Mechanics*, 253, 245-265.

Smith, P., and Hetherington, J. (1994). *Blast and ballistic loading of structures*, Butterworth-Heinemann Ltd, Great Britain.

Sokolinsky, V. S., Von Bremen, H. F., Lavoie, J. A., and Nutt, S. R. (2004). "Analytical and experimental study of free vibration response of soft-core sandwich beams." *Journal of Sandwich Structures and Materials*, 6(3), 239-261.

Spence, D. A. (1975). "The Hertz contact problem with finite friction." *Journal of Elasticity*, 5(3-4), 297-319.

Staudhammer, K. P., Murr, L. E., and Meyers, M. A. (2001). *Fundamental issues and applications of shock-wave and high-strain-rate phenomena*, Elsevier.

Stewart, L. K., and Durant, B. J. (2016). "Experimental and analysis methods for blast mitigating designs in civil infrastructure." *Multi-hazard approaches to civil infrastructure engineering*, Springer, 265-287.

Stolz, A., Fischer, K., Roller, C., and Hauser, S. (2014). "Dynamic bearing capacity of ductile concrete plates under blast loading." *International Journal of Impact Engineering*, 69, 25-38.

Subramaniam, K. V., Nian, W., and Andreopoulos, Y. (2009). "Blast response simulation of an elastic structure: Evaluation of the fluid–structure interaction effect." *International Journal of Impact Engineering*, 36(7), 965-974.

Subramanian, N. (2013). *Design of reinforced concrete structures*, Oxford University Press.

Suemasu, H., Kerth, S., and Maier, M. (1994). "Indentation of spherical head indentors on transversely isotropic composite plates." *Journal of Composite Materials*, 28(17), 1723-1739.

Sun, G., Chen, D., Huo, X., Zheng, G., and Li, Q. (2018). "Experimental and numerical studies on indentation and perforation characteristics of honeycomb sandwich panels." *Composite Structures*, 184, 110-124.

Sun, G., Huo, X., Chen, D., and Li, Q. (2017). "Experimental and numerical study on honeycomb sandwich panels under bending and in-panel compression." *Materials & Design*, 133, 154-168.

Sun, G., Jiang, H., Fang, J., Li, G., and Li, Q. (2016). "Crashworthiness of vertex based hierarchical honeycombs in out-of-plane impact." *Materials & Design*, 110, 705-719.

Swanson, S. R. (1992). "Limits of quasi-static solutions in impact of composite structures." *Composites Engineering*, 2(4), 261-267.

Syed, Z., Raman, S., Ngo, T., Mendis, P., and Pham, T. (2018). Tthe failure behaviour of reinforced concrete panels under far-field and near-field blast effects." *Structures*,14, 220-229.

Systèmes, D. (2010). "Abaqus 6.10 online documentation." *Abaqus User Subroutines Reference Manual*.

Szuladzinski, G. (2009). *Formulas for mechanical and structural shock and impact*, CRC Press.

Tabatabaei, Z. S., Volz, J. S., Baird, J., Gliha, B. P., and Keener, D. I. (2013). "Experimental and numerical analyses of long carbon fiber reinforced concrete panels exposed to blast loading." *International Journal of Impact Engineering*, 57, 70-80.

Tan, T. M., and Sun, C. (1985). "Use of statical indentation laws in the impact analysis of laminated composite plates." *Journal of Applied Mechanics*, 52(1), 6-12.

TEC (2007) Turkish earthquake code-specification for structures to be built in disaster areas, Government of Republic of Turkey. Ministry of Public Works and Settlements.

Thiagarajan, G., Kadambi, A. V., Robert, S., and Johnson, C. F. (2015). "Experimental and finite element analysis of doubly reinforced concrete slabs subjected to blast loads." *International Journal of Impact Engineering*, 75, 162-173.

Thomas, R. J., Steel, K., and Sorensen, A. D. (2018). "Reliability analysis of circular reinforced concrete columns subject to sequential vehicular impact and blast loading." *Engineering Structures*, 168, 838-851.

Timoshenko, S. P., and Woinowsky-Krieger, S. (1959). *Theory of plates and shells*, McGraw-hill, New York.

TM5-1300. Structures to resist the effect of accidental explosions. (1990). U.S. Department of the Army, Navy and Air Force Technical Manual.

Tolba, A. F. F. (2002). "Response of FRP-Retrofitted Reinforced concrete panels to Blast loading." Doctoral thesis, Carleton University, Ottawa, Canada.

Uddin, N. (2013). *Developments in fiber-reinforced polymer (FRP) composites for civil engineering*, Woodhead publishing, Cambridge.

Uma, S., Jain, S. K. (2006). "Seismic design of beam-column joints in RC moment resisting frames-Review of codes." *Structural Engineering and Mechanics*, 23(5), 579-597.

Vaidya, A. S., Vaidya, U. K., and Uddin, N. (2008). "Impact response of three-dimensional multifunctional sandwich composite." *Materials Science and Engineering: A*, 472(1-2), 52-58.

Verderame, G. M., De Risi, M. T., and Ricci, P. (2018). "Experimental Investigation of Exterior Unreinforced Beam-Column Joints with Plain and Deformed Bars." *Journal of Earthquake Engineering*, 22(3), 404-434.

Vivek, P., and Sitharam, T. G. (2018). "Laboratory scale investigation of stress wave propagation and vibrational characteristics in sand when subjected to air-blast loading." *International Journal of Impact Engineering*, 114, 169-181.

Wada, Y., and Liou, M. S. (1997). "An accurate and robust flux splitting scheme for shock and contact discontinuities." *Journal on Scientific Computing*, 18(3), 633-657.

Wadley, H., Dharmasena, K., Chen, Y. C., Dudt, P., Knight, D., Charette, R., and Kiddy, K. (2008). "Compressive response of multilayered pyramidal lattices during underwater shock loading." *International Journal of Impact Engineering*, 35(9), 1102-1114.

Wang, W., Zhang, D., Lu, F. Y., Wang, S. C., and Tang, F. J. (2012). "Experimental study on scaling the explosion resistance of a one-way square reinforced concrete slab under a close-in blast loading." *International Journal of Impact Engineering*, 49, 158-164.

Wei, J., Quintero, R., Galati, N., Nanni, A. (2007). "Failure modeling of bridge components subjected to blast loading part I: strain rate-dependent damage model for concrete." *International Journal of Concrete Structures and Materials*, 1(1), 19-28.

Wierzbicki, T. (1983). "Crushing analysis of metal honeycombs." *International Journal of Impact Engineering*, 1(2), 157-174.

Wierzbicki, T., and Abramowicz, W. (1983). "On the crushing mechanics of thin-walled structures." *Journal of Applied mechanics*, 50(4a), 727-734.

Williams, G., Holland, C., Williamson, E. B., Bayrak, O., Marchand, K. A., and Ray, J. (2010). *Blast-resistant highway bridges: Design and detailing guidelines*, Transportation Research Board, Washington D.C.

Wu, C. Q., and Sheikh, H. (2013). "A finite element modelling to investigate the mitigation of blast effects on reinforced concrete panel using foam cladding." *International Journal of Impact Engineering*, 55, 24-33.

Wu, C., Huang, L., and Oehlers, D. J. (2010). "Blast testing of aluminum foam–protected reinforced concrete slabs." *Journal of Performance of Constructed Facilities*, 25(5), 464-474.

Wu, C., Oehlers, D. J., Rebentrost, M., Leach, J., and Whittaker, A. S. (2009). "Blast testing of ultra-high performance fibre and FRP-retrofitted concrete slabs." *Engineering Structures*, 31(9), 2060-2069.

Wu, E., and Jiang, W.-S. (1997). "Axial crush of metallic honeycombs." *International Journal of Impact Engineering*, 19(5), 439-456.

Xia, Y., Wu, C., Liu, Z.-X., Yuan, Y. J. C., and Materials, B. (2016). "Protective effect of graded density aluminium foam on RC slab under blast loading–An experimental study." *Construction and Building Materials*, 111, 209-222.

Xiao, W., Andrae, M., and Gebbeken, N. (2019). "Experimental investigations of shock wave attenuation performance using protective barriers made of woven wire mesh." *International Journal of Impact Engineering*, 131, 209-221.

Xu, J. C., Wu, C. Q., Xiang, H. B., Su, Y., Li, Z. X., Fang, Q., Hao, H., Liu, Z. X., Zhang, Y. D., and Li, J. (2016). "Behaviour of ultra high performance fibre reinforced concrete columns subjected to blast loading." *Engineering Structures*, 118, 97-107.

Yahaya, M. A., Ruan, D., Lu, G., and Dargusch, M. S. (2015). "Response of aluminium honeycomb sandwich panels subjected to foam projectile impact–An experimental study." *International Journal of Impact Engineering*, 75, 100-109.

Yang, Y., Liou, W. W., Sheng, J., Gorsich, D., and Arepally, S. (2013). "Shock wave impact simulation of a vehicle occupant using fluid/structure/dynamics interactions." *International Journal of Impact Engineering*, 52, 11-22.

Yankelevsky, D., Schwarz, S., and Brosh, B. (2013). "Full scale field blast tests on reinforced concrete residential buildings–from theory to practice." *International Journal of Protective Structures*, 4(4), 565-590.

Yu, J., and Tan, K. H. (2013). "Experimental and numerical investigation on progressive collapse resistance of reinforced concrete beam column sub-assemblages." *Engineering Structures*, 55, 90-106.

Yu, J., Wang, E., Li, J., and Zheng, Z. (2008). "Static and low-velocity impact behavior of sandwich beams with closed-cell aluminum-foam core in three-point bending." *International Journal of Impact Engineering*, 35(8), 885-894.

Yuan, S. J., Hao, H., Zong, Z. H., and Li, J. (2017). "A study of RC bridge columns under contact explosion." *International Journal of Impact Engineering*, 109, 378-390.

Yungwirth, C. J., Radford, D. D., Aronson, M., and Wadley, H. N. G. (2008). "Experiment assessment of the ballistic response of composite pyramidal lattice truss structures." *Composites Part B-Engineering*, 39(3), 556-569.

Yurdakul, Ö., and Avsar, Ö. (2015). "Structural repairing of damaged reinforced concrete beam-column assemblies with CFRPs." *Structural Engineering Mechanics*, 54(3), 521-543.

Yurdakul, O., and Avsar, O. (2016). "Strengthening of substandard reinforced concrete beam-column joints by external post-tension rods." *Engineering Structures*, 107, 9-22.

Yusof, M. A., Norazman, N., Ariffin, A., Zain, F. M., Risby, R., Ng, C. (2011). "Normal strength steel fiber reinforced concrete subjected to explosive loading." *International Journal of Sustainable Construction Engineering and Technology*, 1(2), 127-136.

Zener, C. (1941). "The intrinsic inelasticity of large plates." *Physical Review*, 59(8), 669.

Zhang, D., Yao, S. J., Lu, F. Y., Chen, X. G., Lin, G. H., Wang, W., and Lin, Y. L. (2013). "Experimental study on scaling of RC beams under close-in blast loading." *Engineering Failure Analysis*, 33, 497-504.

Zhang, G. Q., Wang, B., Ma, L., Wu, L. Z., Pan, S. D., and Yang, J. S. (2014). "Energy absorption and low-velocity impact response of polyurethane foam filled pyramidal lattice core sandwich panels." *Composite Structures*, 108, 304-310.

Zhang, G., Wang, B., Ma, L., Xiong, J., and Wu, L. (2013). "Response of sandwich structures with pyramidal truss cores under the compression and impact loading." *Composite Structures*, 100, 451-463.

Zhao, D. B., Yi, W. J., and Kunnath, S. K. (2017). "Shear mechanisms in reinforced concrete beams under impact loading." *Journal of Structural Engineering*, 143(9), 04017089.

Zhong, J., Gardoni, P., Rosowsky, D., and Haukaas, T. (2008). "Probabilistic seismic demand models and fragility estimates for reinforced concrete bridges with two-column bents." *Journal of Engineering Mechanics*, 134(6), 495-504.

Zhou, D., and Stronge, W. (2006). "Low-velocity impact denting of HSSA lightweight sandwich panel." *International Journal of Mechanical Sciences*, 48(10), 1031-1045.

Zhou, D., and Stronge, W. J. (2006). "Low-velocity impact denting of HSSA lightweight sandwich panel." *International Journal of Mechanical Sciences*, 48(10), 1031-1045.

Zhu, F., and Lu, G. (2007). "A review of blast and impact of metallic and sandwich structures." *EJSE Special Issue: Loading on Structures*, 8, 92-101.

Zhu, F., Zhao, L. M., Lu, G. X., and Gad, E. (2009). "A numerical simulation of the blast impact of square metallic sandwich panels." *International Journal of Impact Engineering*, 36(5), 687-699.

Zhu, F., Zhao, L., Lu, G., and Wang, Z. (2008). "Deformation and failure of blast-loaded metallic sandwich panels—experimental investigations." *International Journal of Impact Engineering*, 35(8), 937-951.

Zhu, S., and Chai, G. B. (2013). "Damage and failure mode maps of composite sandwich panel subjected to quasi-static indentation and low-velocity impact." *Composite Structures*, 101, 204-214.

Zou, Z., Reid, S., Tan, P., Li, S., and Harrigan, J. (2009). "Dynamic crushing of honeycombs and features of shock fronts." *International Journal of Impact Engineering*, 36(1), 165-176.

Appendix A

User defined function (UDF) for shock tube analysis

User define function (UDF) to initialize the computation domain into driver and driven sections (Shock tube):

A User-defined function (UDF) is profoundly a C program or C function that can be dynamically loaded with ANSYS FLUENT to enhance its standard characteristics. Initially, the UDF is used to define the shock tube zone, which consists of nitrogen gas particles. For performing a numerical simulation, all the initial state properties of the shock tube and the gas's boundary conditions are given by the help of UDF.

The UDF used in this simulation

```
DEFINE_INIT(name,d)
{
cell_t c;
Thread *t;
real xc[ND_ND];
thread_loop_c(t,d)
{
begin_c_loop_all(c,t)
{
C_CENTROID(xc,c,t);
if (xc[0] < 2.0 )
{
C_U(c,t) = 0.;
C_V(c,t) = 0.;
C_P(c,t) = 723949.8; /*Initial Bursting Pressure at driver section
C_T(c,t) = 300.; /*Initial Temperature at driver section
C_YI(c,t,0)= 1.0; /*This will fulfill the first part with nitrogen*/
C_YI(c,t,1)= 0.0; /*This will ensure there is no air in the first part*/
}
else
```

```
{
C_U(c,t) = 0.;
C_V(c,t) = 0.;
C_P(c,t) = 10.; /*Initial Bursting Pressure at driver section
C_T(c,t) = 300.; /*Initial Temperature at driver section
C_YI(c,t,0)= 0.0; /*This will ensure there is no helium in the second part*/
C_YI(c,t,1)= 1.0; /*This will fulfill the second part with air*/
}
}
end_c_loop_all(c,t)
}
}
```

Appendix B

Design of a beam for blast load as per UFC 3–340–02 (2014)

According to UFC 3–340–02 (2014), an interior roof beam subjected to an overhead blast load is designed as follows. Structural configuration is shown in Figure B-1.

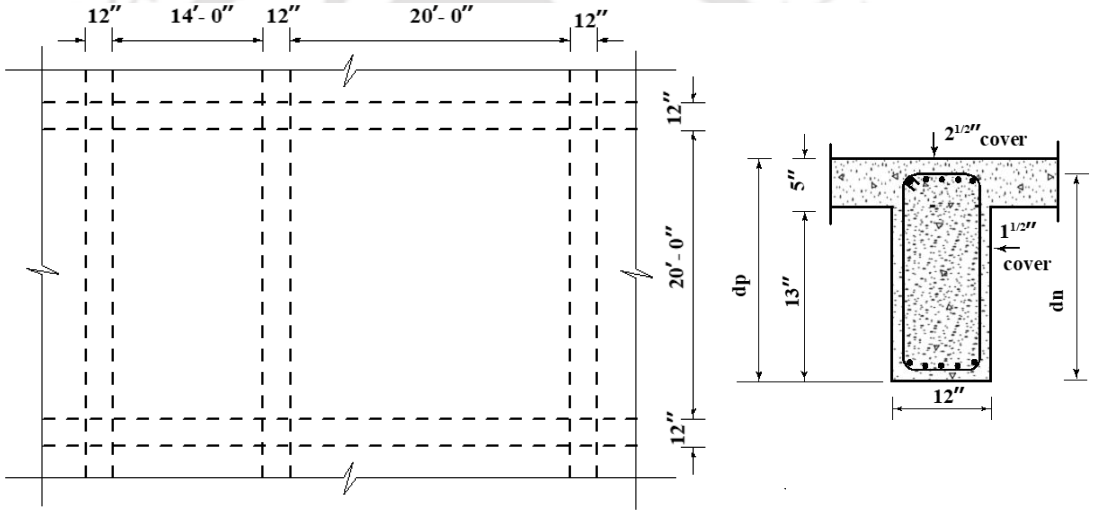

Figure B-1 Structural configuration: a) slab, and b) cross-section of beam

1) a. Dimensions of beam are shown in Figure B-1.

1) Width of beam (b) = 300 mm = 12 inch
2) Depth of beam (d) = 450 mm = 18 inch
3) Thickness of slab (t) = 125 mm = 5 inch

b. Pressure-time loading is shown in Figure B-2

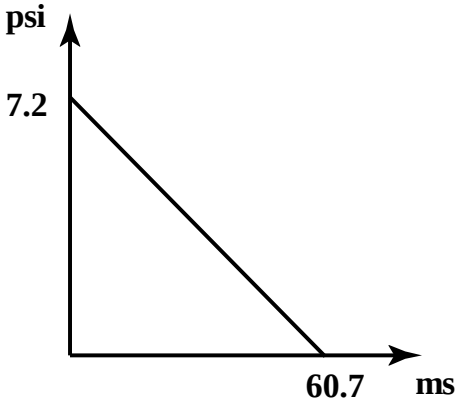

Figure B-2 Pressure profile of blast loading

c. Support rotation is considered as one degree (Maximum).

d. Yield stress of reinforcing steel, $f_y = 66,000$ psi

e. Concrete compressive strength, $f_c^{'} = 4,000$ psi

f. Weight of concrete, $w = 150$ lbs/ft^3

2) a. Dynamic increase factors from Table B-1 for intermediate and low-pressure range.

Table B-1 Dynamic increase factor (DIF) for design of reinforced concrete elements

Type of stress	Far design range			Close-in design range		
	Reinforcing bars		Concrete	Reinforcing bars		Concrete
	f_{dy}/f_y	f_{du}/f_u	$f_{dc}^{'}/f_c^{'}$	f_{dy}/f_y	f_{du}/f_u	$f^{'}_{dc}/f^{'}_c$
Bending	1.17	1.05	01.19	1.23	1.05	1.25
Diagonal tension	1.00	-	1.00	1.10	1.00	1.00
Direct shear	1.10	1.00	1.10	1.10	1.00	1.10
Bond	1.17	1.05	1.00	1.23	1.05	1.00
Compression	1.10	-	1.12	1.13	-	1.16

Reinforcing steel - bending, DIF = 1.17

Direct shear, DIF = 1.10

Concrete - compression, DIF = 1.19

Direct shear, DIF = 1.10

Diagonal tension, DIF = 1.00

b. From Table B-2, for $\Theta_m \le 2^o$: $f_{ds} = f_{dy}$

Table B-2 Dynamic design stresses for design of reinforced concrete elements

Type of stress	Type of reinforcement	Maximum support rotation (Degrees)	Dynamic design stress	
			Reinforcement	Concrete
Bending	Tension and Compression	$0 < \Theta_m \le 2$	f_{dy} (1)	f'_{dc}
		$2 < \Theta_m \le 6$	$f_{dy} + (f_{du} - f_{dy})/4$	(2)
		$6 < \Theta_m \le 12$	$(f_{dy} + f_{du})/2$	(2)
Diagonal tension	Stirrups	$0 < \Theta_m \le 2$	f_{dy}	f'_{dc}
		$2 < \Theta_m \le 6$	f_{dy}	f'_{dc}
		$6 < \Theta_m \le 12$	f_{dy}	f'_{dc}
Diagonal tension	Lacing	$0 < \Theta_m \le 2$	f_{dy}	f'_{dc}
		$2 < \Theta_m \le 6$	$f_{dy} + (f_{du} - f_{dy})/4$	f'_{dc}
		$6 < \Theta_m \le 12$	$(f_{dy} + f_{du})/2$	f'_{dc}
Direct shear	Diagonal bars	$0 < \Theta_m \le 2$	f_{dy}	f'_{dc}
		$2 < \Theta_m \le 6$	$f_{dy} + (f_{du} - f_{dy})/4$	(3)
		$6 < \Theta_m \le 12$	$(f_{dy} + f_{du})/2$	(3)
Compression	Column	(4)	f_{dy}	f'_{dc}

Tension reinforcement only.

Concrete crushed and not effective in resisting moment.

Concrete is considered not effective and shear is resisted by the reinforcement only.

Capacity is not a function of support rotation.

c. Dynamic design stresses from Table B-3.

Table B-3 Minimum area of flexural reinforcement

Cross-Section	Reinforcement	One and Two-Way Slabs
Type I	Main direction	$A_s = 1.875\frac{\sqrt{f_c'}}{f_y}bd$
		$A_s' = 1.25\frac{\sqrt{f_c'}}{f_y}bd$
	Secondary direction	$A_s = 1.25\frac{\sqrt{f_c'}}{f_y}bd$
		$A_s' = 1.25\frac{\sqrt{f_c'}}{f_y}bd$
Type II and Type III	Main direction	$A = A_s' = 1.875\frac{\sqrt{f_c'}}{f_y}bd_c$
	Second direction	$A = A_s' = 1.875\frac{\sqrt{f_c'}}{f_y}bd_c$

* but not less than $A_s/4$ used in the main direction

Reinforcing steel

Bending	$f_{dy} = 1.17 \times 66,000 = 77,220$ psi
Diagonal tension	$f_{dy} = 1.00 \times 66,000 = 66,000$ psi
Concrete compression	$f_{dc}' = 1.19 \times 4000 = 4,760$ psi
Direct shear	$f_{dc}' = 1.10 \times 4,000 = 4,400$ psi
Diagonal tension	$f_{dy} = 1.00 \times 4,000 = 4,000$ psi

3) Assume 5 No. 6 bars for bending: $A_s = 5 \times 0.44 = 2.20$ in^2

For concrete cover and beam section can be seen in Figure B-1.

4) Check reinforcement requirements:

a. Calculate '*d*' negative (support) and positive (mid-span) for checking bending reinforcement ratios.

$$d = h - d'(\text{cover}) - \phi'(\text{tie}) - \frac{\phi}{2}(\text{Bending bar})$$

$$d_N = 23 - 2 - 0.5 - 0.75/2 = 20.125 \text{ in}$$

$$d_p = 23 - 1.5 - 0.5 - 0.75/2 = 20.625 \text{ in}$$

b. Calculate reinforcement ratio:

$$p_s = A_s / bd$$

$$p_N = 2.2/(12 \text{ x } 20.125) = 0.0919$$

$$p_p = 2.2/(12 \text{ x } 20.625) = 0.0088$$

c. Maximum reinforcement:

Maximum reinforcing ratio $p_{\max} = 0.075 \text{ x } p_b$

$$p_b = \left[\frac{0.85 k_1 f'_{dc}}{f_{dy}}\right] \cdot \left[\frac{87{,}000}{87{,}000 + f_{dy}}\right]$$

where :

$$k_1 = 0.85 - \frac{0.05\left(f'_{dc} - 4000\right)}{1{,}000} = 0.812$$

$$p_b = \frac{0.85 \text{ x } 0.812 \text{ x } 4760}{77{,}220}\left(\frac{87{,}000}{87{,}000 + 77{,}220}\right) = 0.0225$$

$p_{\max} = 0.75 \text{ x } 0.0225 = 0.0169 > p_N = 0.0045$ and $p_p = 0.0044$ OK.

d. Checking minimum reinforcing ratio against the larger value from the following equations:

$$p_{\min} = \frac{200}{f_y} = \frac{200}{66{,}000} = 0.0030$$

$$p_{\min} = \frac{3\sqrt{f'_c}}{f_y} = \frac{3\sqrt{4{,}000}}{66{,}000} = 0.0029$$

$$p_{\min} = 0.0030 < p_N = 0.0045$$

$$< p_p = 0.0044 \text{ OK.}$$

5) Moment capacity of the beam:

$$M_u = A_s f_{dy}\left(d - a/2\right)$$

where:

$$a = \frac{A_s f_{dy}}{0.85 b f'_{dc}}$$

$$a = \frac{2.20 \text{ x } 77{,}220}{0.85 \text{ x } 12 \text{ x } 4{,}760} = 3.4990 \text{ in}$$

at support:

$$M_N = A_s \text{ x } f_{dy} \text{ x } \left(d_N - a/2\right)$$

$$M_N = 2.20 \text{ x } 77{,}220 \text{ x } (20.125 - 3.4990/2)$$

$$= 3{,}121{,}703 \text{ in-lbs}$$

at mid-span:

$$M_p = 2.20 \text{ x } 77,220 \text{ x } (20.625 - 3.4990/2)$$

$$= 3,206,645 \text{ in-lbs}$$

6) Ultimate resistance of uniformly loaded beam with fixed end condition is:

$$r_u = \frac{8(M_N + M_p)}{L^2}$$

$$r_u = \frac{8(3,121,703 + 3,206,645)}{240^2} = 878.93 \text{ lbs/in}$$

7) Calculating the average moment of inertia of the beam section.

a. Concrete modulus of elasticity:

$$E_c = w^{1.5} \text{ x } 33 \text{ x } \left(f_c^{'}\right)^{1/2}$$

$$E_c = 150^{1.5} \text{ x } 33 \text{ x } (4,000)^{1/2} = 3.8 \text{ x } 10^6 \text{ psi}$$

b. Steel modulus of elasticity:

$$E_s = 29 \text{ x } 10^6 \text{ psi}$$

c. Modular ratio

$$n = \frac{E_s}{E_c}$$

$$n = \frac{29 \text{ x } 10^6}{3.8 \text{ x } 10^6} = 7.6$$

d. From Figure B-3, with the obtained values of n, p_N and p_p, the coefficients for moment of inertia of cracked sections are:

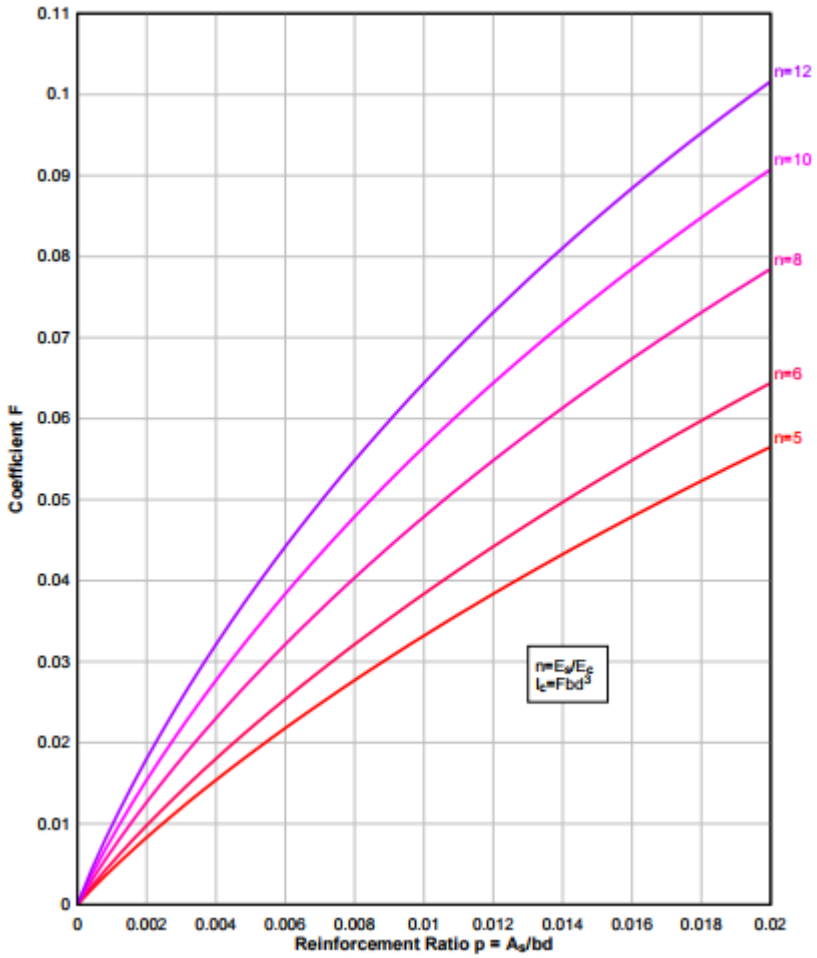

Figure B-3 Coefficient for moment of inertia cracked sections with tension reinforcement only [from ref. UFC 3–340–02 (2014)]

$F_N = 0.040$ at support

$F_p = 0.035$ at mid-span

e. Cracked moment of inertia:

$$I_c = Fbd^3$$

$$I_{cN} = 0.040 \text{ x } 12 \text{ x } 20.125^3 = 3{,}192 \text{ in}^4$$

$$I_{cP} = 0.035 \text{ x } 12 \text{ x } 20.625^3 = 3{,}684 \text{ in}^4$$

Average:

$$I_c = (I_{cN} + I_{cP})/2$$

$$I_c = (3{,}192 + 3{,}684)/2 = 3{,}438 \text{ in}^4$$

f. Gross moment of inertia:

$$I_g = \frac{bh^3}{12}$$

$$I_g = \frac{12 \text{ x } 23^3}{12} = 12{,}167 \text{ in}^4$$

g. Average moment of inertia of the beam:

$$I_a = \frac{I_g + I_c}{2}$$

$$I_a = \frac{12{,}167 + 3{,}438}{2} = 7{,}802.5 \text{ in}^4$$

8) K_E of a uniformly loaded beam with fixed ends is:

$$K_E = \frac{307 E_c I_a}{L^4}$$

$$K_E = \frac{307 \text{ x } 3.8 \text{ x } 10^6 \text{ x } 7{,}802.5}{240^4} = 2{,}743.53 \text{ lbs/in/in}$$

9) **Equivalent elastic deflection:**

$$X_E = \frac{r_u}{K_E} = \frac{873.93}{2{,}743.53} = 0.318 \text{ in}$$

10) Load-mass factor for a plastic range of a uniformly loaded beam with fixed ends:

K_{LM} - elastic = 0.77

- elastic = 0.78

- plastic = 0.66

K_{LM} for plastic mode deflections

$$K_{LM} = \left[\left[\frac{0.77 + 0.78}{2}\right] + 0.66\right] \Big/ 2 = 0.72$$

11) Natural period of the beam:

$$T_N = 2\pi \left(K_{LM}\, m / K_E\right)^{1/2}$$

Where, m is the mass of the beam plus 20% of the slabs span perpendicular to the beam:

$$m = \frac{w}{g}$$

$$= (18 \text{ x } 12 + 2 \text{ x } 5 \text{ x } 108 \text{ x } 0.20) \text{ x } \frac{150}{12^3} \text{ x } \frac{1{,}000^2}{32.2 \text{ x } 12}$$

$$= 97{,}043.478 \text{ lbs-ms}^2/\text{in/in}$$

$$T_N = 2\pi \left[\frac{0.72 \text{ x } 97{,}043.478}{2{,}743.53}\right]^{1/2} = 31.7 \text{ ms}$$

12) Finding μ, ductility ratio from Figure B-4

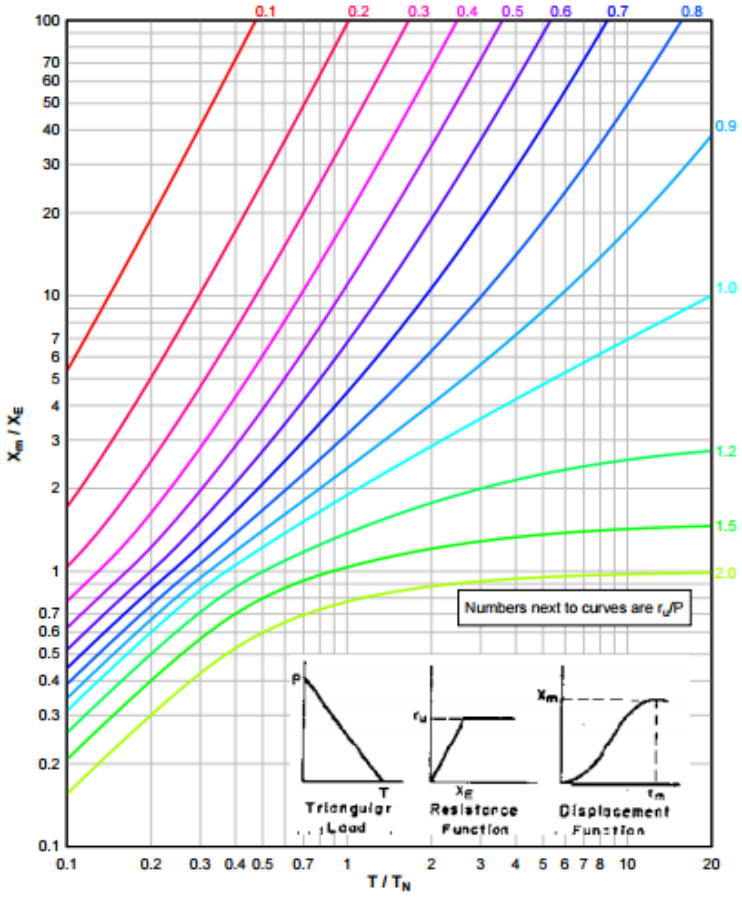

Figure B-4 Maximum deflection of elasto-plastic, one-degree-of-freedom system for triangular load [from ref. UFC 3–340–02 (2014)]

From 1):

$$T/T_N = 60.7/31.7 = 1.92$$

$$P = (12+54+120)\text{x}7.2$$

$$= 1339.2 \text{ lbs/in}$$

$$r_u/P = \frac{878.93}{1339.2} = 0.656$$

$$\mu = 13.0$$

13) Support rotation (X_m) for the fixed end support beam is:

$$X_m = \frac{L \tan\Theta}{2}$$

$$= \mu \text{ x } X_E$$

$$\mu \text{ x } X_E = 13.0 \text{ x } 0.3303$$

$$\mu \text{ x } X_E = 13.0 \text{ x } 0.3303$$

$$= 4.2939 \text{ in}$$

$$\tan\Theta = \frac{2 \text{ x } 4.2939}{240} = 0.0357$$

$$\Theta = 0.0357° < 1° \text{ OK.}$$

14) Direct Shear (V_s) for the fixed end one-way element:

$$V_s = \frac{r_u L}{2} = \frac{878.93 \text{ x } 240}{2} = 105,471 \text{ lbs}$$

Section capacity in direct shear:

$$V_d = 0.18 f_{dc}^{'} bd$$

$$V_d = 0.18 \text{ x } 4,400 \text{ x } 12 \text{ x } 20.125$$

$$= 191,268 \text{ lbs} > v_s = 105,471 \text{ OK.}$$

15) Diagonal tension stress:

$$v_u = \frac{V_u}{bd} \le 10\left(f_c^{'}\right)^{1/2}$$

Total shear d distance from the face of support:

$$V_u = (L/2 - d) r_u$$

$$= \left(\frac{240}{2} - 20.125\right) 878.93 = 87,783.13 \text{ lbs}$$

$$v_u = \frac{87,783.13}{12 \text{ x } 20.125} = 363.49 \text{ psi}$$

$$10\left(f_{dc}^{'}\right)^{1/2} = 10 \text{ x } (4,000)^{1/2}$$

$$632.5 \text{ psi} > 363.49 \text{psi}, \text{ OK.}$$

16) Unreinforced web shear capacity:

$$v_c = \left[1.9\left(f_{dc}^{'}\right)^{1/2} + 2,500p\right]$$

$$< 3.5\left(f_{dc}^{'}\right)^{1/2}$$

$$v_c = \left[1.9(4,000)^{1/2} + 2,500 \text{ x } 0.0045\right]$$

$$= 131.4 \text{ psi}$$

$$< 3.5(4,000)^{1/2}$$

$$= 221.4 \text{ psi} > 131.4 \text{ psi OK.}$$

17) Area of web reinforcing:

$$A_V = \left[\left(v_u - v_c\right) \text{ x b x } s_s\right] / \phi \text{ x } f_{dy} \text{ ; } v_u - v_c \ge v_c$$

$$v_u - v_c = 363.49 - 131.4 = 232.09 v_c \text{ use } v_c$$

Assuming, $s_s = 9$ in

$$A_v = 131.4 \text{ x } 12 \text{ x } 9/(0.85 \text{ x } 66,000)$$

$$= 0.2529 \text{ in}/9 \text{ in}^2$$

Use No. 4 tie: $A_v = 0.40 \text{ in}^2$

18) Minimum tie reinforcing area:

$$A_v(\min) = 0.0015 b s_s$$

$$= 0.0015 \text{ x } 12 \text{ x } 9$$

$$= 0.162 \text{ in}^2 < 0.40 \text{ in}^2 \text{ OK.}$$

Maximum tie spacing:

$$\left(f'_{dc}\right)^{1/2} = 4 \text{ x } (4{,}000)^{1/2}$$

$$= 253 \text{ psi} > v_c = 131.4 \text{ psi}$$

$$> v_u - v_c = 232.09 \text{ psi}$$

$$s_{\max} = d/2$$

$$= 20.125/2 = 10.0625 \text{ in} > 9 \text{ in OK.}$$

19) Determining required resistance for rebound r^- from Figure B-5

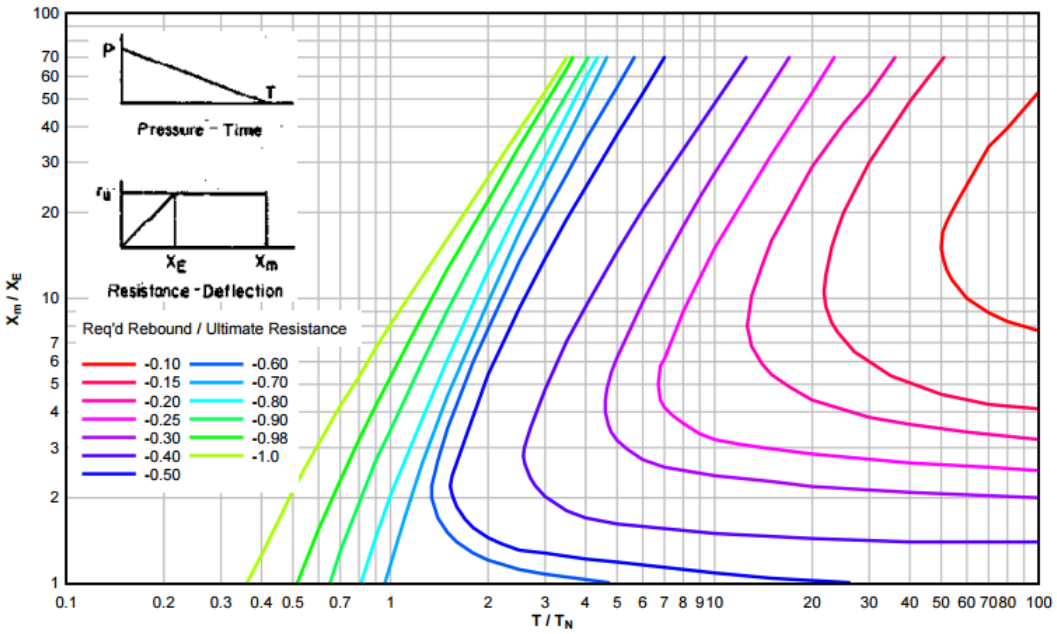

Figure B-5 Elastic rebound of simple spring-mass system [from ref. UFC 3–340–02 (2014)]

$$r^-/r_u = 0.50 \text{ for } T/T_N = 2.40 \text{ and } X_m/X_E = 9.0$$

Required:

$$r^- = 0.50 \text{ x } 878.93 = 439.46 \text{ lbs}$$

20) Repeat steps 3 to 6:

Assume:

$$A_S^- = 1.64 \text{ in}^2 \text{ , } 2 \text{ No. } 7 + 1 \text{ No. } 6$$

$$p_N^- = 1.64/(12 \text{ x } 20.125) = 0.0068$$

$$\bar{p}_N \text{ at support} = 0.0068 = 200/f_y$$

$$p_p^- = 1.64/(12 \text{ x } 20.625) = 0.0066$$

$$\bar{p}_N \text{ at mid span} = 0.0066 > 200/f_y$$

$$M_N^- = 1.64 \text{ x } 77{,}220 \text{ x } \left(20.125 - 3.4990/2\right)$$

$$M_N^- \quad \text{at support} \quad = 2{,}327{,}088 \text{ in-lbs}$$

$$M_p^- = 1.64 \text{ x } 77{,}220 \text{ x } \left(20.625 - 3.4499/2\right)$$

$$M_N^- \quad \text{at mid-span} \quad = 2{,}390{,}408 \text{ in-lbs}$$

$$r^- = 655.20 \text{ lbs/in}$$

$$> 439.6 \text{ lbs/in OK.}$$